

**Searches for new phenomena using events with three or more charged leptons
in pp collisions at $\sqrt{s} = 8$ TeV with the ATLAS detector at the LHC**

by

David Ren-Hwa Yu

A dissertation submitted in partial satisfaction of the

requirements for the degree of

Doctor of Philosophy

in

Physics

in the

Graduate Division

of the

University of California, Berkeley

Committee in charge:

Professor Beate E. Heinemann, Chair

Professor Yury G. Kolomensky

Professor Karl A. van Bibber

Summer 2015

**Searches for new phenomena using events with three or more charged leptons
in pp collisions at $\sqrt{s} = 8$ TeV with the ATLAS detector at the LHC**

Copyright 2015
by
David Ren-Hwa Yu

Abstract

Searches for new phenomena using events with three or more charged leptons in pp collisions at $\sqrt{s} = 8$ TeV with the ATLAS detector at the LHC

by

David Ren-Hwa Yu

Doctor of Philosophy in Physics

University of California, Berkeley

Professor Beate E. Heinemann, Chair

This dissertation presents two searches for phenomena beyond the Standard Model using events with three or more charged leptons. The searches are based on 20.3 fb^{-1} of proton-proton collision data with a center-of-mass energy of $\sqrt{s} = 8$ TeV collected by the ATLAS detector at the CERN Large Hadron Collider in 2012. The first is a model-independent search for excesses beyond Standard Model expectations in many signal regions. The events are required to have least three charged leptons, of which at least two are electrons or muons, and at most one is a hadronically decaying τ lepton. The selected events are categorized based on the flavor and charge of the leptons, and the signal regions are defined using several kinematic variables sensitive to beyond the Standard Model phenomena. The second search looks for new heavy leptons decaying resonantly to three electrons or muons, two of which are produced through an intermediate Z boson. The resonant decay produces a narrowly-peaked excess in the trilepton mass spectrum. In both cases, no significant excess beyond Standard Model expectations is observed, and the data are used to set limits on models of new physics. The model-independent trilepton search is used to confront a model of doubly charged scalar particles decaying to $e\tau$ or $\mu\tau$, excluding masses below 400 GeV at 95% confidence level. The trilepton resonance search is used to test models of vector-like leptons and the type III neutrino seesaw mechanism. The vector-like lepton model is excluded for most of the mass range 114 GeV – 176 GeV, while the type III seesaw model is excluded for most the mass range 100 GeV – 468 GeV. Both searches also present tools to facilitate reinterpretations in the context of other models predicting the production of three or more charged leptons.

Dedicated to my family.

Contents

Contents	ii
List of Figures	iv
List of Tables	xvi
1 Introduction	1
2 Theoretical Motivation	3
2.1 The Standard Model	3
2.2 Beyond the Standard Model	14
3 The Experimental Apparatus	28
3.1 The Large Hadron Collider	28
3.2 The ATLAS Experiment	36
4 Luminosity Measurement	65
4.1 Run I Luminosity	65
4.2 Measurement Overview	65
4.3 Luminosity Detectors	66
4.4 Luminosity Calibration: van der Meer Scans	69
4.5 Systematic Uncertainties	73
4.6 Vertex-Based Luminosity Measurement	73
5 Event Reconstruction	86
5.1 Track and Vertex Reconstruction	86
5.2 Electrons	87
5.3 Muons	90
5.4 τ Leptons	92
5.5 Jets	98
5.6 Invisible Particles	103
5.7 Object Selection	104

6 Background Estimation	110
6.1 Prompt Backgrounds	110
6.2 Reducible Backgrounds	113
7 Model-Independent Trilepton Search	130
7.1 Event Selection	130
7.2 Analysis Strategy	131
7.3 Systematic Uncertainties	133
7.4 Background Validation	135
7.5 Results and Limits	139
7.6 Model Testing	145
8 Trilepton Resonance Search	151
8.1 Signal Models	151
8.2 Search Strategy	155
8.3 Systematic Uncertainties	163
8.4 Background Validation	171
8.5 Signal and Background Fit Model	175
8.6 Results	184
8.7 Interpretation	186
9 Conclusion	194
A Author Contributions	195
B Trilepton Resonance Search	196
C Statistical Methods	206

List of Figures

2.1	Schematic picture of a collision between two protons, labeled A and B . Partons a and b , which are gluons in this picture, participate in the hard scatter interaction, $gg \rightarrow q\bar{q}$. The beam remnants, the remainder of the two protons, do not participate in the hard scatter interaction, but can interact with the final state partons from the hard scatter interaction and with each other, forming the underlying event. The outgoing colored partons undergo fragmentation and hadronization to form jets, not shown here.	8
2.2	Example parton distribution functions at $\mu = 2 \text{ GeV}$ and $\mu = 85 \text{ GeV}$, from the CT10 PDF set.	9
2.3	One-loop Feynman diagrams involving fermions (left) and bosons (right) leading to the quadratic divergence of the Higgs mass.	17
2.4	Feynman diagram showing the production of a chargino, $\tilde{\chi}_1^\pm$, and a neutralino, $\tilde{\chi}_2^0$, decaying to two neutralino LSPs, $\tilde{\chi}_1^0$, plus three leptons and a neutrino. The chargino/neutralino subscript indicates mass ordering, with 1 being the lightest.	19
2.5	Example of the pair production of two vector-like leptons, L^\pm . The L^\pm decay via mixing with Standard Model leptons. In this example, one vector-like lepton is shown decaying to three leptons via an intermediate Z boson.	20
3.1	The LHC and the four interaction points where the beams are brought into collision. The ATLAS experiment is located at interaction point 1.	28
3.2	Schematic picture of an RF bucket.	30
3.3	The LHC accelerator complex. The proton injection chain begins at LINAC2, proceeding through the booster, PS, and SPS before reaching the LHC. The facility also provides ions to the LHC, as well as a variety of particles to other experiments.	30
3.4	Layout of the LHC. The ring consists of eight arcs and eight long straight sections (LSS). Each junction between an arc and a LSS contains a dispersion suppressor cell (DSL, DSR). TI2 and TI8 are the two injection tunnels (“tunnel d’injection”) leading from the SPS to the LHC.	32
3.5	Two views of the LHC superconducting dipole magnet. The magnets are 15 m long and have two bores, one for each of the counter-rotating beams.	33
3.6	The LHC RF cryomodules.	33

3.7	The geometry of the magnet windings and tile calorimeter steel. The three toroids and solenoid are shown in red. The remaining colors show layers of the tile calorimeter with different magnetic properties and an outside return yoke.	37
3.8	The central solenoid in the factory after completion of the coil winding.	38
3.9	Left: the solenoid magnetic field in the radial (B_r) and longitudinal (B_z) directions, shown as a function of z for $\phi = 20\pi/16$ at different values of R . The field determined from a fit of the field model to measurements using an array of Hall probes. Right: The predicted toroid magnetic field integral as a function of $ \eta $. The integral is taken over a straight line through the interaction point, from the innermost to the outermost muon detector.	39
3.10	Images of the barrel (left) and end-cap toroid (right) magnets during installation.	39
3.11	Left: 3D model of the inner detector, showing the arrangement of the pixel detector, SCT, and TRT in the barrel and end-caps. Right: layout of the inner detector in the $R - z$ plane.	40
3.12	Drawings of the inner detector sensors and structural elements traversed by 10 GeV charged particles originating from the interaction point at various angles. Trajectories of particles traversing the barrel elements at $\eta = 0.3$ (left) and both the barrel and end-cap elements at $\eta = 1.4$ and $\eta = 2.2$ (right) are shown.	41
3.13	Comparison of depletion zones in n^+ -in- n pixel sensors before and after type inversion. Before type inversion, the electrical field grows from the bottom side, reaching the pixel implants at full depletion. After type inversion, the depletion zone grows from the pixel side, allowing operation even if the bulk is not fully depleted.	42
3.14	Schematic pictures of a barrel pixel module. The top diagram shows the assembly of a module, consisting of the front-end electronics chips (FEs), the pixel sensor elements, and the flex-hybrid, which bears the module control chip (MCC) and NTC thermistors. The bottom is a photograph of a barrel pixel module.	43
3.15	Diagrams of the SCT barrel (left) and end-cap (right) modules.	44
3.16	Layout of the TRT barrel modules in the R - ϕ plane.	46
3.17	A 3D model of the ATLAS calorimeters, showing the electromagnetic barrel and end-caps, hadronic barrel and end-caps, and the forward calorimeter.	47
3.18	Cumulative amounts of material versus $ \eta $ in front of and within the LAr electromagnetic calorimeter, in terms of radiation lengths, X_0 . (a) show the material before the calorimeters. (b) shows the material in the crack region between the barrel and end-cap cryostats. (c) shows the material in and before the barrel LAr calorimeter. (d) shows the material in and before the end-cap LAr calorimeters.	48
3.19	Cumulative amounts of material versus $ \eta $ due to each calorimeter in terms of interaction lengths, λ . The material in front of the calorimeters is also shown in tan.	49

3.20	The LAr calorimeter uses an accordion geometry to provide uniform coverage in ϕ . Steel-clad lead plates are interleaved with electrodes, consisting of three copper layers separated by polyimide sheets. (a) shows a schematic drawing of a LAr barrel module, illustrating the accordion geometry and the three layers in depth, with fine segmentation in η in the layer closest the interaction point. (b) shows a photograph of the accordion geometry.	49
3.21	Left: Schematic view of a tile calorimeter module, showing assembly of the steel absorber, the inserted scintillator tiles, and the readout of lighting through wavelength-shifting fibers to the photomultiplier tubes. Right: Layout of the tile calorimeter cells, defined by the grouping of the readout fibers connecting the scintillating tiles to the photomultiplier tubes.	51
3.22	Schematic $R - \phi$ (left) and $R - z$ (right) views of the hadronic end-cap calorimeters.	52
3.23	Schematic diagram showing the layout of the forward calorimeter in the R - z plane.	53
3.24	Left: the electrode structure of FCal1, showing the matrix of copper tubes and rods. The Molière radius, R_M , is shown for reference. Right: the absorber matrix in FCal2 and FCal, made from tungsten rods and copper tubes.	53
3.25	3D model of the ATLAS muon spectrometer. The four different types of detector (MDTs, CSCs, RPCs, and TGCs) and the toroid magnets are shown.	54
3.26	Layout of the chambers of the muon spectrometer.	55
3.27	The mechanical structure of a MDT chamber. Two multilayers, each consisting of three or four rows of drift tubes, are separated by aluminum spacers. Four optical alignment rays continuously monitor the geometry of the chamber.	55
3.28	Cross section of a drift tube, showing the cathode tube, the anode wire, and an illustration of a muon ionizing the gas as it traverses the tube.	56
3.29	Left: Layout of the eight large and eight small CSC chambers. Right: Schematic view of the CSC anode wires and perpendicular cathode strips, showing the deposition of charge from a track on several adjacent strips.	57
3.30	Cross section of an RPC, showing two units joined to form a single chamber. Each unit has two sets of two resistive plates (gray) separated by insulating spacers (green). The readout strips (magenta) are on the opposite side of the resistive plates from the gas gap. Outside the detecting elements, the volume of the RPC chamber is filled with paper honeycomb. The dimensions are given in millimeters.	58
3.31	The construction of the TGCs.	59
3.32	Block diagram of the L1 trigger system.	60
4.1	Left: The cumulative delivered, recorded, and physics-ready integrated luminosity versus time in 2011-2011. Right: Distribution of the number of interactions per bunch crossing in events recorded in 2011-2012.	66

4.2	An example of a scan curve measured by BCMV_OR from the van der Meer scans on 15 May 2011. The specific visible interaction rate $\mu_{\text{vis}}^{\text{sp}} \equiv \mu_{\text{vis}}/(n_1 n_2)$ is shown as a function of transverse beam separation in the x direction for a single scan and BCID. The data are fitted with Gaussian plus constant. The bottom plot shows the residual deviation of the data from the fit, divided by the uncertainty on the data.	71
4.3	Measured σ_{vis} values from the vdm scans performed in May 2011. The error bars represent statistical uncertainties only. The vertical dashed lines indicate the weighted average over BCIDs from the two sets of scans. The yellow band shows a variation of $\pm 0.9\%$ from the total weighted average, equal to the systematic uncertainty due to the observed BCID-to-BCID and scan-to-scan variations.	72
4.4	Left: Comparison of luminosities measured by different algorithms as a function of time in 2011. Right: Comparison of luminosities measured by different algorithms as a function of the average number of interactions per bunch cross, μ , as measured by BCM_VOR. The data were taken during a single run by separating the beams in the transverse direction, similar to a van der Meer scan.	74
4.5	Average number of fake vertices per event as a function of the number of generated pp interactions.	76
4.6	Δz distribution between pairs of vertices in the same event, with data from the May 2011 van der Meer scan.	77
4.7	Calibration of the masking correction method on data, using run 182013. Left: Δz distributions and template fits using expected Δz distributions in the range $30 \text{ mm} \leq \Delta z \leq 300 \text{ mm}$. Right: pairwise vertex masking probability as a function of the longitudinal distance Δz between the vertices.	78
4.8	Calibration of the masking correction method on simulation, using 8 TeV minimum bias Monte Carlo (PYTHIA 8, tune A2M). Left: Δz distributions and template fits using expected Δz distributions in the range $30 \text{ mm} \leq \Delta z \leq 300 \text{ mm}$. Right: pairwise vertex masking probability as a function of the longitudinal distance Δz between the vertices.	78
4.9	$\mu_{\text{vis}}^{(\text{sp})}$ vs. beam separation, with single Gaussian plus constant fits, and pulls.	80
4.10	Ratio of luminosity values from vertexing to the reference value from BCM_VOR during the pileup scan in September 2011. The black points show the vertex-based luminosity with ≥ 5 tracks, the red with ≥ 7 tracks, and the green with ≥ 10 tracks. The different shapes show the application of each successive pileup correction: the hollow squares show the vertex-based luminosity with no pileup corrections applied, the hollow triangles are corrected for fake vertices, and the solid circles are corrected for both fake and masked vertices.	82
4.11	Percent difference between luminosities measured by vertex counting and BCM_VOR during the pileup scan in September 2011. Vertices are required to have at least five tracks. The black points show the central values, taken to be the average between the two colliding BCIDs. The gray bars show the spread between BCIDs and between different track cuts (≥ 5 , ≥ 7 , and ≥ 10), summed in quadrature.	83

4.12 Luminosities measured by BCM, LUCID, and vertex counting during the $\beta^* = 90\text{ m}$ ALFA run in October 2011.	84
5.1 The combined reconstruction and identification efficiencies with respect to electrons detected as a cluster in the electromagnetic calorimeter, shown as a function of E_T (left) and η (right). The error bars show the statistical uncertainty (inner) and the statistical plus systematic uncertainty (outer). The <i>multilepton</i> identification cuts are optimized for low energy electrons in the $H \rightarrow ZZ^* \rightarrow 4\ell$ analysis, and are not used in this dissertation.	89
5.2 Electron energy resolution as a function of E_T for various values of $ \eta $. The shaded band shows the uncertainty on the resolution.	91
5.3 Muon reconstruction efficiencies as a function of η for muons with $p_T > 10\text{ GeV}$ (left), and as a function of p_T for muons with $0.1 < \eta < 2.5$ (right). The uncertainty bars on the points indicate statistical uncertainties. The bottom plots show the ratio between the measured and simulated efficiencies, with the combination of statistical and systematic uncertainties indicated by the uncertainty bars.	92
5.4 Dimuon invariant mass distribution of $Z \rightarrow \mu\mu$ events, using CB muons. The top panel shows the invariant mass distribution for data (black points), expected $Z \rightarrow \mu\mu$ signal from MC simulation (green), and expected background from MC simulation (yellow). The muon momentum corrections are applied to the MC simulation, and the total MC prediction is normalized to the data. The dashed histogram shows the background plus signal without muon momentum corrections. The bottom panel shows the ratio of the data to the normalized MC prediction, with the systematic uncertainty on the momentum corrections shown in the yellow band.	93
5.5 Dimuon invariant mass resolution for combined muons as a function of the average muon p_T in three pseudorapidity regions. The resolution is determined from $J/\Psi \rightarrow \mu\mu$, $\Upsilon \rightarrow \mu\mu$, and $Z \rightarrow \mu\mu$ events. Both muons are required to be in the same pseudorapidity region. The J/Ψ and Υ data are plotted as a function of $\bar{p}_T = \frac{p_{T1}+p_{T2}}{2}$, while Z data are plotted as a function of $p_T^* = m_Z \sqrt{\frac{\sin \theta_1 \sin \theta_2}{2(1-\cos \alpha_{12})}}$, where $\theta_{1,2}$ are the polar angles of the two muons and α_{12} is the angle between the two muons, which removes the correlation between $m_{\mu\mu}$ and \bar{p}_T . The lower panels show the ratio between data and the corrected MC, with bands representing the uncertainty on the MC corrections for the three calibration samples.	94

5.6	Inverse background efficiency (rejection power) versus signal efficiency for the BDT-based offline τ identification algorithm. (a) shows the efficiency for τ leptons with $20 \text{ GeV} < p_T < 40 \text{ GeV}$, and (b) shows the efficiency for τ leptons with $p_T > 40 \text{ GeV}$. The three points on each curve correspond to the BDT-tight , BDT-medium , and BDT-loose working points, in order of increasing signal efficiency and decreasing background rejection power. The background consists of simulated multijet events, while the signal consists of simulated Z , W , and Z' events decaying to τ leptons.	96
5.7	Correction factors applied to simulation to equalize the efficiency to that measured in data, as measured in Z tag-and-probe data. The error bars show the combined statistical and systematic uncertainty.	96
5.8	Electron rejection power versus 1-track τ_{had} efficiency for the electron rejection BDT.	97
5.9	Energy resolution for hadronically decaying τ leptons with one associated track in various pseudorapidity regions. The resolution is the standard deviation of a Gaussian fit to the distribution of $\frac{E_{\text{reco}} - E_{\text{true-vis}}}{E_{\text{true-vis}}}$ in bins of $E_{\text{true-vis}}$ and $ \eta_{\text{true-vis}} $.	97
5.10	Overview of the jet reconstruction, showing the inputs to and outputs from the jet finding algorithms. The bottom two rows show the reconstruction of calorimeter jets, while the top two rows show jets built from truth particles in simulation and from tracks.	99
5.11	Overview of the jet calibration scheme.	100
5.12	Sample-dependent fractional jet energy scale (JES) systematic uncertainty as a function of p_T^{jet} (top) and η (bottom), at fixed values of η or p_T^{jet} , respectively. The jets are reconstruction using the anti- k_T algorithm with a radius parameter of $R = 0.4$ from clusters at the LCW scale, and are calibrated as described in the text. The shaded area shows the total systematic uncertainty, while the colored lines show the contribution of various individual sources of uncertainty.	101
5.13	Schematic representation of the jet vertex fractions in the case of two jets and two primary vertices. f is the fraction of track p_T in jet 1 due to tracks associated with vertex PV2.	102
5.14	Performance of the MV1 b -tagging algorithm. The inclusive signal efficiency versus background rejection is shown at left. The signal and background efficiencies at the 70% working point are shown as a function of p_T at right.	103
6.1	Example tree-level Feynman diagrams of Standard Model processes leading to trilepton final states.	111
6.2	Numerator and denominator electron object counts. The data sample consists of all single-electron events in the 2012 dataset, with cuts to reduce prompt contamination as described in the text. The markers represent object counts from 2012 data, and the colored histograms indicate the prompt subtractions estimated from MC.	118
6.3	Electron fake factors parametrized in p_T and η .	119

6.4	Electron fake factors projected in p_T . The discontinuity at 24 GeV is due to a change in the the denominator requirements; below 24 GeV, where electron triggers are used, additional requirements are imposed on the track-cluster matching, which cause a drop in the denominator counts, and an increase in the fake factor values.	119
6.5	Electron numerator and denominator object counts versus η for $p_T < 24$ GeV.	120
6.6	Electron fake factors vs. p_T , with systematic and total uncertainties. The statistical uncertainty includes both the data and prompt subtraction Monte Carlo statistics. The total uncertainty is the sum in quadrature of the statistical and systematic uncertainty.	120
6.7	p_T spectrum of muons used in fake factor measurement. The left plots show events with zero jets, the middle plots show events with one jet, and the right plots show events with two or more jets. All numerator events require both numerator and denominator be separated from a jet by $\Delta R > 0.3$; the same requirement is applied to denominators in the second row of plots, while the third row shows denominators that are not required to be isolated from nearby jets.	122
6.8	Ratio between the fake factors for muons with $ d_0 /\sigma(d_0) > 3$ compared to fake factors with nominal numerator and denominator definitions. These fake factors are derived from a POWHEG $t\bar{t}$ sample.	123
6.9	Muon fake factors as a function of p_T . Two sets of fake factors are plotted, with and without the “dR” requirement. The vertical dashed line at 40 GeV indicates the point at which the fake factors switch from the “dR” points, where the denominators are required to be separated from nearby jets, to the lower, non-“dR” points where the jet-isolation requirement is dropped to improve the statistics.	123
6.10	Muon fake factors as functions of p_T and $ \eta $. The left plot shows fake factors measured in the inclusive control sample and applied to events with zero jets. The right plot shows fake factors measured in events with two jets, and applied to events with at least one jet.	124
6.11	Systematic uncertainties on muon fake factor as a function of $p_T(\mu)$. The left plot shows the uncertainties for the inclusive fake factor, while the right shows the uncertainty for the two-jet fake factor.	125
6.12	Invariant mass of the muon and $\tau_{\text{had-vis}}$ pair (left) and p_T of the τ candidate (right). The top plots show the distributions for numerator $\tau_{\text{had-vis}}$ candidates, while the bottom plots show the distributions for denominator $\tau_{\text{had-vis}}$ candidates. The filled histograms show the prompt contamination estimated from simulation.	126
6.13	τ lepton fake factors binned in p_T and $ \eta $ (left), and the corresponding statistical uncertainty (right). The correction for the maximum MV1 b -tag weight of all jets in the event is also shown (bottom). The fake factors are derived from $W+\text{jets}$ events.	127

6.14 Results of the closure test, comparing the data to the fake factor-based background estimate in a $t\bar{t}$ validation region. The $\tau_{\text{had-vis}} p_T$ (left), $ \eta $ (right), and the dilepton invariant mass (bottom) are shown.	128
7.1 Dilepton invariant mass distributions for the ee (left) and $\mu\mu$ (right) validation regions. The shaded bands on the ratio plots show the systematic uncertainty on the background estimate due to the MC sample statistical uncertainties and normalizations. The disagreement between data and simulation in the ee mass distribution is covered by the electron energy scale uncertainties, not shown in the plot.	136
7.2 Ratios of efficiencies between data and simulation for electrons (top) and muons (bottom) as functions of p_T (left) and $ \eta $ (right).	137
7.3 p_T distribution of the $\tau_{\text{had-vis}}$ candidates in the $\mu\tau_{\text{had}}$ validation region. The shaded band on the ratio plot shows the total systematic uncertainty on the background estimate.	138
7.4 $t\bar{t}$ validation regions for all flavor (e, μ) combinations. The shaded band on the ratio plot shows the total systematic uncertainty on the background estimate.	138
7.5 p_T (left) and η (right) distributions of the off- Z electron (top) or muon (bottom) satisfying the intermediate selection criteria. The other two leptons in the event are required to satisfy the numerator selection criteria and form an opposite-sign, same-flavor pair, with different flavor from the intermediate lepton. The shaded bands on the ratio plots show the systematic uncertainty on the background estimate due to the MC sample statistical uncertainties and normalizations.	140
7.6 p_T and η distributions of the intermediate τ_{had} in the on- Z , off- Z /OSSF, and off- Z /mixed intermediate validation regions.	141
7.7 H_T^{leptons} distributions in the six categories: (a) $2e/\mu+ \geq 1\tau_{\text{had}}$, on- Z , (b) $\geq 3e/\mu$, on- Z , (c) $2e/\mu+ \geq 1\tau_{\text{had}}$, off- Z , no-OSSF, (d) $3e/\mu$, off- Z , no-OSSF, (e) $2e/\mu+ \geq 1\tau_{\text{had}}$, off- Z , OSSF, and (f) $\geq 3e/\mu$, off- Z , OSSF. The expected signal from an excited τ neutrino with mass $m(\nu_\tau^*) = 0.5$ TeV is shown to illustrate the sensitivity of the different signal regions. The lower panel shows the ratio of the observed data to the background prediction.	143
7.8 95% CL upper limits on the visible cross section of trilepton event production from new physics, σ_{95}^{vis} , in each signal region.	144
7.9 Deviations between the observed event counts and the background expectations in each signal region divided by the total uncertainty on the background prediction.	144
7.10 Observed and expected 95% CL limits on the cross section times branching ratio for $H^{\pm\pm}$ decaying to $e^\pm\tau^\pm$ (left) and $\mu^\pm\tau^\pm$ (right). The solid and dashed red lines show the expected cross section times branching ratio for left- and right-handed $H^{\pm\pm}$, respectively.	148
8.1 Production and decay of new heavy leptons to final states with a trilepton resonance.	152

8.2	Production cross sections at $\sqrt{s} = 8$ TeV for heavy lepton pair production for the type III seesaw model (left) and the vector-like leptons model (right).	153
8.3	Branching ratios of a L^\pm (left) or N^0 (right) decaying via mixing with Standard Model leptons.	154
8.4	Expected $\Delta R(Z, \ell_3)$ distributions for background and signal for events containing a Z candidate plus an electron.	158
8.5	Expected upper limits on the heavy lepton production cross section times branching ratio to final states with least one $Z(\ell\ell) + \ell$ decay for different cuts on the maximum value of $\Delta R(Z, \ell_3)$.	158
8.6	Fraction of events with various activity on the opposite side of the event, for $L^\pm L^\mp$ events at left, and $L^\pm N^0$ events at right. The left plot, showing the opposite side activity for a $L^\pm L^\mp$ final state, is identical for the type III seesaw and vector-like lepton models.	162
8.7	Comparison of the Δm distributions between POWHEG and SHERPA for the WZ backgrounds. The top panels show the Δm distributions, normalized to unity, and the bottom panels show the ratio of POWHEG to SHERPA. The shaded bands and error bars represent the statistical uncertainties. The 4ℓ signal region is omitted due to the negligible number of WZ events with four leptons.	167
8.8	Comparison of the Δm distributions between POWHEG and SHERPA for the ZZ backgrounds. The top panels show the Δm distributions, normalized to unity, and the bottom panels show the ratio of POWHEG to SHERPA. The shaded bands and error bars represent the statistical uncertainties. The POWHEG events are weighted to account for the <code>m114</code> filter.	168
8.9	Systematics summary plots for each signal region in the $Z + e$ flavor channel. The contribution from each source of systematic uncertainty is shown in 20 GeV bins, along with the total systematic uncertainty and the expected statistical uncertainty. Note that these uncertainties reflect bin-by-bin uncertainties on the Monte Carlo predictions, and do not necessarily correspond to the final uncertainty after fitting the background shapes.	169
8.10	Systematics summary plots for each signal region in the $Z + \mu$ flavor channel. The contribution from each source of systematic uncertainty is shown in 20 GeV bins, along with the total systematic uncertainty and the expected statistical uncertainty. Note that these uncertainties reflect bin-by-bin uncertainties on the Monte Carlo predictions, and do not necessarily correspond to the final uncertainty after fitting the background shapes.	170
8.11	Δm distributions for the high ΔR validation regions.	172
8.12	Δm distributions for the ZZ validation regions.	173
8.13	Δm distributions for the off- Z validation regions.	173
8.14	Δm distributions for the WZ validation regions.	174
8.15	Fit of a Landau and a Voigtian to the inclusive distribution of the Δm at 300 GeV for the vector-like leptons model for $Z + e$ final states (a) and $Z + \mu$ final states (b).	176

- 8.16 Scatter plot showing the correlation between σ_p and x_p (left) and ξ_p and x_p (right), determined from 100 toy experiments on the WZ background sample in the inclusive signal region. The line shows the linear least squares fit used to constrain the parameter on the y -axis. 177
- 8.17 Scatter plot showing the correlation between σ_p and x_p (left) and ξ_p and x_p (right), determined from 100 toy experiments on the ZZ background sample in the inclusive signal region. The line shows the linear least squares fit used to constrain the parameter on the y -axis. 178
- 8.18 Comparison of $ZZ \Delta m$ shapes between the inclusive signal region and the categorized signal regions, with empirical distribution functions. 179
- 8.19 Comparison of $WZ \Delta m$ shapes between the inclusive signal region and the categorized signal regions, with empirical distribution functions. The 4ℓ signal regions are not shown due to the lack of WZ events with four leptons. 180
- 8.20 Δm distributions from Monte Carlo and Bukin function fits for the WZ background. The $Z + e$ and $Z + \mu$ events are combined. The inclusive (left) and $3\ell + jj$ (right) signal regions are shown. 181
- 8.21 Δm distributions from Monte Carlo and Bukin function fits for the ZZ background. The $Z + e$ and $Z + \mu$ events are combined. The inclusive (left) and $3\ell + jj$ (right) signal regions are shown. 181
- 8.22 Δm distributions from Monte Carlo and Landau function fits for the reducible backgrounds in the inclusive signal region, for $Z + e$ (left) and $Z + \mu$ (right) events. 182
- 8.23 Δm distributions from Monte Carlo and Landau function fits for the $Z + \gamma$ (left) and $t\bar{t} + V$ plus $VVV^{(*)}$ (right) backgrounds. For the $Z + \gamma$ background, the inclusive, $Z + e$ signal region is shown; the background is negligible in the $Z + \mu$ signal regions. For the $t\bar{t} + V$ plus $VVV^{(*)}$ backgrounds, the inclusive signal region is shown, with the $Z + e$ and $Z + \mu$ channels combined. 183
- 8.24 The Δm distributions for the 4ℓ (top), $3\ell + jj$ (middle), and 3ℓ -only (bottom) categories, divided into the $Z + e$ (left) and $Z + \mu$ (right) flavor channels. The data are shown as black points, while the pre-fit background expectations are shown in the solid histograms. Signal contributions from a 140 GeV L^\pm in the VLL model and a 300 GeV L^\pm in the seesaw model are also shown. The error bars on the points represent statistical uncertainties, and the shaded bands represent the systematic uncertainties on the background predictions. 185
- 8.25 Projections onto the Δm variable of the background-only unbinned maximum-likelihood fits, shown superimposed on the data with the three categories in each flavor channel added together. The $Z + e$ flavor channel is shown in (a), and the $Z + \mu$ channel is shown in (b). The contributions of the separate background components to the total background-only fit are also shown. The error bars on the data points represent statistical uncertainties. Good agreement is observed between the background model and the data. 186

8.26 p_0 -values for the background-only hypothesis as a function of the heavy lepton mass and the corresponding expected p_0 -values for the vector-like lepton model (blue) and the type-III seesaw model.	187
8.27 95% CL upper limits on the vector-like lepton cross section. The left (right) plot shows the limits assuming 100% branching fraction to e/ν_e (μ/ν_μ). The solid line shows the observed limit. The dashed line shows the median expected limit for a background-only hypothesis, with green and yellow bands indicating the expected fluctuations at the $\pm 1\sigma$ and $\pm 2\sigma$ levels. The limit is evaluated in 3 GeV intervals.	188
8.28 95% CL upper limits on the type III seesaw production cross section. The left (right) plot shows the limits assuming 100% branching fraction to e/ν_e (μ/ν_μ). The solid line shows the observed limit. The dashed line shows the median expected limit for a background-only hypothesis dataset, with green and yellow bands indicating the expected fluctuations at the $\pm 1\sigma$ and $\pm 2\sigma$ levels. The limit is evaluated in 3 GeV intervals.	188
8.29 Upper limits at 95% CL on σ_{vis} for the $Z + e$ (left) and $Z + \mu$ (right) flavor channels, derived without dividing events into the three categories. The limits are evaluated in 3 GeV intervals.	190
8.30 Efficiencies for reconstructing and correctly identifying the $L^\pm \rightarrow Z(\ell\ell)\ell^\pm$ decay in events within the fiducial volume for the type III seesaw model. The left (right) plot shows the efficiencies for events containing a $L^\pm \rightarrow Z(\ell\ell)e$ ($L^\pm \rightarrow Z(\ell\ell)\mu$) decay. The decay of the second heavy lepton is specified in the legend. The shaded bands show the statistical uncertainty.	190
B.1 $m_{3\ell}$ distributions for $Z + e$ and $Z + \mu$ candidates, for the inclusive and 4ℓ signal regions (linear scale).	198
B.2 $m_{3\ell}$ distributions for $Z + e$ and $Z + \mu$ candidates, for the $3\ell + jj$ and 3ℓ -only signal regions (linear scale).	199
B.3 $\Delta R(Z, \ell_3)$ distributions for $Z + e$ and $Z + \mu$ candidates, for the inclusive and 4ℓ signal regions (linear scale).	200
B.4 $\Delta R(Z, \ell_3)$ distributions for $Z + e$ and $Z + \mu$ candidates, for the $3\ell + jj$ and 3ℓ -only signal regions (linear scale).	201
B.5 Transverse mass of the missing energy and bachelor lepton (m_T^W) for $Z + e$ and $Z + \mu$ candidates, for the inclusive and 4ℓ signal regions.	202
B.6 Transverse mass of the missing energy and bachelor lepton (m_T^W) for $Z + e$ and $Z + \mu$ candidates, for the $3\ell + jj$ and 3ℓ -only signal regions.	203
B.7 Missing energy (E_T^{miss}) for $Z + e$ and $Z + \mu$ candidates, for the inclusive and 4ℓ signal regions.	204
B.8 Missing energy (E_T^{miss}) for $Z + e$ and $Z + \mu$ candidates, for the $3\ell + jj$ and 3ℓ -only signal regions.	205

C.1 Two example of pdfs for \tilde{q}_μ for the $S + B$ and B hypotheses. The left plot shows pdfs where the two hypotheses are well separated, while the right plot shows a case where the experiment has little sensitivity to the signal.

207

List of Tables

2.1	Matter particles (fermions) in a single generation of the Standard Model, their representations under $SU(3)_c$ and $SU(2)_L$, and their charges under $U(1)_Y$. The left- and right-handed fermions are distinguished by the subscripts L and R .	5
2.2	List of particles in the Standard Model. The mass, spin, and electric charge of each particle is shown.	6
2.3	Branching fractions of W^\pm and Z^0 bosons to leptons and other final states.	14
3.1	Summary of typical beam parameters in 2011 and 2012.	35
3.2	Main parameters of the ATLAS magnet system.	37
3.3	Parameters of the pixel detector.	42
3.4	The dimensions and arrangement of modules in the four SCT layers. The tilt angle is between the normal to the module surface and \hat{r} , in the $\hat{\phi}$ direction.	44
3.5	Layout and straw counts of the TRT barrel modules and end-cap wheels. The totals for the barrel and end-caps, shown in bold, include services and electronics.	45
3.6	The rates of recording events from the event filter for different data streams.	62
4.1	Visible cross sections for pp luminosity measurement algorithms used in 2011. The corresponding efficiency of detecting an inelastic pp collision is also shown for $\sigma_{\text{inel}} = 71.34 \text{ mb}$.	72
4.2	Systematic uncertainties on the integrated luminosity measured in 2011 using the BCM_VOR algorithm. The uncertainties are separated into uncertainties on the visible cross section (1.5%) and measurement uncertainties over the year (0.9%).	74
5.1	Leading branching fractions of the τ lepton to final states with leptons or pions. Most of the remaining decays are to final states with kaons.	94
5.2	Electron and muon selection criteria.	106
5.3	τ lepton selection criteria.	106
6.1	Configurations of the background MC samples used in this dissertation. The generator, parton shower and hadronization, PDF, and underlying event tune are shown for each sample.	112

6.2	Cross section times filter efficiencies, NLO K -factors (if used), equivalent integrated luminosities, and number of events simulated for the background MC samples used in this dissertation. The filter efficiencies account for filters applied to the samples to remove events outside the phase space relevant for the analyses, e.g. imposing cuts on lepton p_T .	112
6.3	Data-to-MC scale factors for photon conversions.	114
6.4	Electron denominator definitions. The denominators are taken to be an exclusive OR combination of the two selection inversions. Additionally, denominator objects must pass the tight requirement on the $\Delta\eta$ and $\Delta\phi$ between the track and the cluster.	116
6.5	Triggers used to collect electron numerator and denominator objects in various p_T ranges, along with the average trigger prescale in 2012. Electron triggers are denoted by <code>EF_e</code> , and photon triggers by <code>EF_g</code> . The number indicates the E_T cut in GeV. Triggers labeled <code>loose</code> or <code>loose0</code> impose shower shape requirements similar to the offline <code>loose++</code> electron identification criteria. The trigger labeled <code>etcut</code> only imposes the E_T cut, with no shower shape requirement.	117
7.1	Kinematic signal regions defined in the analysis.	133
7.2	Systematic uncertainties on the normalizations of the background contributions estimated with simulation.	134
7.3	Expected and observed event yields for the H_T^{leptons} signal regions.	142
7.4	The fiducial efficiency for electrons, muons, and τ leptons in different p_T ranges ($\epsilon_{fid}(p_T)$). For electrons and muons from τ decays, the p_T is that of the electron or muon, not the τ . The uncertainties shown reflect the statistical uncertainties of the simulated samples only.	146
7.5	The fiducial efficiency for electrons and τ leptons in different η ranges ($\epsilon_{fid}(\eta)$). For electrons from τ decays, the η is that of the electron, not the τ . The uncertainties shown reflect the statistical uncertainties of the simulated samples only.	146
8.1	Mass values, production cross sections, and equivalent luminosities of the signal Monte Carlo samples.	156
8.2	Production modes and decays of the two heavy leptons simulated for the type III seesaw signal samples.	156
8.3	Comparison of the full-width, half-maxima of the signal peaks between the Δm and $m_{3\ell}$ variables. The signal peaks are modeled using a Voigtian function, a convolution of a Gaussian and a Lorentzian, fit to the Monte Carlo simulation. The fit is described in section 8.5.1. The full-width, half-maximum of a Voigtian is given approximately by $\text{FWHM} \approx 0.5346 f_L + \sqrt{0.02166 f_L^2 + f_G^2}$, where $f_L = 2\gamma$ is the FWHM of the Lorentzian and $f_G = 2\sigma\sqrt{2\log 2}$ is the FWHM of the Gaussian.	159

8.4	Percent of fiducial events remaining at various stages in the cutflow for the $Z + e$ signal regions. Only statistical uncertainties due to finite Monte Carlo statistics are shown. The preselection cut requires three selected leptons, with one OSSF pair, as well as the general event selection cuts listed above.	160
8.5	Percent of fiducial events remaining at various stages in the cutflow for the $Z + \mu$ signal regions. Only statistical uncertainties due to finite Monte Carlo statistics are shown. The preselection cut requires three selected leptons, with one OSSF pair, as well as the general event selection cuts listed above.	161
8.6	The impact of different sources of uncertainty on the background prediction in each signal region, in terms of percent of the total background normalization.	165
8.7	The impact of different sources of systematic uncertainty on the signal prediction for the type III seesaw model with $m_{L^\pm} = 160$ GeV, in terms of percent of the total signal normalization.	165
8.8	The impact of different sources of systematic uncertainty on the signal prediction for the type III seesaw model with $m_{L^\pm} = 300$ GeV, in terms of percent of the total signal normalization.	166
8.9	The impact of different sources of systematic uncertainty on the signal prediction for the type III seesaw model with $m_{L^\pm} = 500$ GeV, in terms of percent of the total signal normalization.	166
8.10	Definitions and targeted backgrounds of the four validation regions.	171
8.11	Summary of the number of events observed and predicted for each validation region. The uncertainty on the background prediction is the total systematic uncertainty. The difference between the observed and predicted number of events divided by the combined statistical and systematic uncertainty on the prediction is also shown.	172
8.12	Comparison of the interpolated and directly fitted parameters of the signal fits. The comparison is shown for the 120 GeV and 160 GeV mass points of the vector-like lepton model.	176
8.13	Results of Kolmogorov-Smirnov tests comparing the $ZZ \Delta m$ shapes between the categorized signal regions and the inclusive signal regions. The Kolmogorov-Smirnov probability and test statistic are shown.	178
8.14	Results of Kolmogorov-Smirnov tests comparing the $WZ \Delta m$ shapes between the categorized signal regions and the inclusive signal regions. The Kolmogorov-Smirnov probability and test statistic are shown.	182
8.15	Observed and expected number of events in the six signal regions, before and after the combined unbinned maximum-likelihood fit. The pre-fit uncertainties represent the total systematic uncertainties on the background estimates. The post-fit uncertainties are determined by the maximum-likelihood fit.	184

- B.1 Fit parameters for the type III seesaw model in the $Z + e$ flavor channel and inclusive category. m_V , γ_V , and σ_V represent the mean, Lorentzian width, and Gaussian width of the Voigt function, and m_L and σ_L represent the mean and width of the Landau function. Note that the absence of the intrinsic width of the Z boson in the simulation leads to smaller values than expected for the width of the Voigtian peak for masses below ~ 250 GeV. 196
- B.2 Fit parameters for the type III seesaw model in the $Z + \mu$ flavor channel and inclusive category. m_V , γ_V , and σ_V represent the mean, Lorentzian width, and Gaussian width of the Voigt function, and m_L and σ_L represent the mean and width of the Landau function. Note that the absence of the intrinsic width of the Z boson in the simulation leads to smaller values than expected for the width of the Voigtian peak for masses below ~ 250 GeV. 197
- B.3 Fit parameters for the VLL model in the $Z + e$ flavor channel and inclusive category. m_V , γ_V , and σ_V represent the mean, Lorentzian width, and Gaussian width of the Voigt function, and m_L and σ_L represent the mean and width of the Landau function. 197
- B.4 Fit parameters for the VLL model in the $Z + \mu$ flavor channel and inclusive category. m_V , γ_V , and σ_V represent the mean, Lorentzian width, and Gaussian width of the Voigt function, and m_L and σ_L represent the mean and width of the Landau function. 197

Acknowledgments

This dissertation could not have happened without the help of many friends, family, teachers, and mentors. I am deeply grateful for their support, guidance, and camaraderie, which made my time in graduate school as enjoyable as it was educational.

I am fortunate to have been a member of the LBNL ATLAS group, whose wide range of expertise makes it a great place for a newcomer to ATLAS. My adviser, Beate Heinemann, is a tireless source of inspiration. Her suggestions have led to many interesting projects, and her quick insights often pointed me back on course when I ran into difficulty. I thank her for her dedication to her students, despite often being a continent away.

The LBNL postdocs have been a wonderful source of support, particularly Simone Pagan Griso, Mark Tibbetts, and Mike Hance. One could write a textbook, or perhaps a very helpful twiki page, with all the questions they've answered over the years. From the workings of the ATLAS detector to programming style, much of the knowledge I've gained in graduate school is due to them.

Moving to CERN, I thank the luminosity task force for supporting my first project on ATLAS. I am especially grateful to Witold Kozanecki for his mentorship, and the many espressos at our weekly lunch meetings. I was fortunate to work with two talented analysis teams within the ATLAS exotics group. It was a pleasure to work with Sourabh Dube, Pier-Olivier DeViveiros, Olya Igolkina, and Joern Mahlstedt on the model-independent trilepton analysis, and Jochen Dingfelder, Benedict Winter, and especially Liv Wiik-Fuchs on the trilepton resonance analysis. Thanks also to the editorial board for the trilepton resonance analysis, Stefania Spagnolo, Kenji Hamano, Xin Wu, and Ed Moyse, for their dedication and patience.

Transportation graduate students across the Atlantic Ocean is no easy task, but Alexia Leyval makes it possible. Thank to her for making our transitions to Geneva as smooth as possible.

I am extremely grateful to all my friends and fellow students at Berkeley and CERN. Though we are dispersing around the world, I hope our futures will share many trails, fondue pots, and physics pun(che)s. Thanks to the Strawberries, especially Carl Rose, for making Berkeley feel like home for the last six years.

Finally, my deepest thanks are saved for Mom, Dad, Emily, and Paul, for making me who I am today.

Chapter 1

Introduction

This dissertation presents two searches for phenomena beyond the Standard Model in proton-proton collision data with a center-of-mass collision energy of $\sqrt{s} = 8 \text{ TeV}$. The dataset contains 20.3 fb^{-1} of integrated luminosity recorded by the ATLAS detector at the Large Hadron Collider (LHC) in 2012. Both searches look for an excess above the predicted Standard Model backgrounds of events containing at least three charged leptons. Such events are produced rarely in Standard Model processes, and consequently provide a useful low-background sample in which to search for new physics.

Since its development in the 1970s, the Standard Model of particle physics has successfully described most phenomena observed in high energy physics. With the discovery of the Higgs boson at the LHC in 2012, all of the Standard Model particles have been observed, with their properties and interactions largely agreeing with predictions. A small number of observations, however, cannot be explained by the Standard Model; neutrino oscillations, dark matter, and the overabundance of matter over antimatter in the universe suggest that the content of the Standard Model is incomplete. Together with several theoretical concerns, these discrepancies have inspired a multifaceted effort to discover and understand physics beyond the Standard Model. The Standard Model, its shortcomings, and several proposed remedies are described in chapter 2.

The experimental techniques of particle physics are roughly divided into three “frontiers”: intensity, cosmology, and energy. The intensity frontier investigates rare processes using intense particle beams. The cosmic frontier analyzes the contents of the universe, such as the distribution of matter or the cosmic microwave background, to determine the physics responsible for the evolution of the universe from the Big Bang to today. The energy frontier uses particle accelerators to produce new particles in high-energy collisions. The three frontiers offer complementary approaches to searching for beyond the Standard Model phenomena.

The Large Hadron Collider, or LHC, is the current flagship experiment of the energy frontier, capable of producing proton-proton collisions with a center-of-mass energy of up to $\sqrt{s} = 14 \text{ TeV}$. The first data-taking run of the LHC, spanning 2011–2012, delivered integrated luminosities of $\int \mathcal{L} dt = 5.46 \text{ fb}^{-1}$ at $\sqrt{s} = 7 \text{ TeV}$ and $\int \mathcal{L} dt = 22.8 \text{ fb}^{-1}$ at

$\sqrt{s} = 8$ TeV to the ATLAS detector, one of two general-purpose detectors at the LHC. The LHC and the ATLAS detector are described in chapter 3. The data collected are potentially sensitive to new phenomena up to roughly the TeV scale. The measurement of the integrated luminosity and the algorithms used to process the data are described in chapters 4 and 5, respectively.

Events containing three or more charged leptons are a useful probe of new physics due to the small expected Standard Model backgrounds. The backgrounds and the techniques for their estimation are described in chapter 6. This dissertation presents two signature-driven searches for new physics using trilepton events. The first, presented in chapter 7, is a generic search for deviations from Standard Model predictions in many signal regions sensitive to new physics. The second, presented in chapter 8, searches for resonant trilepton production via an intermediate Z boson. In both cases, no significant deviations from Standard Model predictions are observed. The data are used to set limits on several models of new physics.

Chapter 2

Theoretical Motivation

The LHC is capable of producing proton-proton collisions with a center-of-mass energy of up to $\sqrt{s} = 14$ TeV. Accounting for the composite nature of the proton, these collisions give access to phenomena with characteristic energies approximately up to the TeV scale which couple in some fashion to quarks or gluons. To date, the Standard Model (SM) of Particle Physics has accurately described most phenomena observed in collider experiments up to this energy scale. A small number of observations, however, as well as a few technical and aesthetic concerns, reveal deficiencies in the theory. Numerous theories have been proposed to remedy the deficiencies, many of which make testable predictions for the LHC.

This chapter describes the theories underlying the LHC’s exploration of physics at the TeV scale. The Standard Model physics is described first, followed by its known shortcomings and their possible consequences at the LHC. Emphasis is placed on theories predicting the production of several charged leptons, which are the subject of the searches described in chapters 7 and 8.

2.1 The Standard Model

The Standard Model of particle physics is a theoretical framework describing the dynamics and interactions of the known elementary particles under the electromagnetic, weak, and strong forces. The theory is a gauge theory describing a wide range of phenomena in the language of Quantum Field Theory. Particles are described as excitations of quantum fields, whose properties are defined by their representations under the Lorentz group and the gauge groups associated with the electroweak and strong forces. This section briefly introduces the Standard Model in the context of proton-proton collisions at the LHC.

2.1.1 Gauge Theory

A *gauge theory* is a quantum field theory in which the Lagrangian is invariant under local transformations under a gauge group G [1]. To give a simple example, consider a single

massless fermion field $\psi(x)$, with kinetic term,

$$\mathcal{L} = i\bar{\psi}(x)\not{\partial}\psi(x), \quad (2.1)$$

where $\not{\partial} \equiv \gamma^\mu \partial_\mu$ and γ^μ are the γ -matrices associated with the Lorentz group. To introduce a gauge group G , the Lagrangian is required to be invariant under local transformations under the action of G :

$$\begin{aligned} \psi(x) &\rightarrow V(x)\psi(x), \\ V(x) &= e^{i\alpha(x)^a t^a} \end{aligned}$$

where t^a are the generators of the Lie algebra of G , and $\alpha(x)_a$ are arbitrary continuous functions. The kinetic term in the Lagrangian, $i\bar{\psi}(x)\gamma^\mu \partial_\mu \psi(x)$, can be made invariant by promoting the simple derivate ∂_μ to a *covariant derivative*, D_μ , defined as:

$$D_\mu = \partial_\mu - igt^a A_\mu^a, \quad (2.2)$$

where g is a coupling constant associated with the gauge interaction and $A_\mu^a(x)$ are vector fields associated with the gauge bosons of G , which transform under the action of G as:

$$A_\mu^a(x)t_a \rightarrow V(x) \left(A_\mu^a(x)t^a + \frac{i}{g}\partial_\mu \right) V^\dagger(x) \quad (2.3)$$

For infinitesimal $\alpha(x)^a$, the transformations can be expressed as:

$$\psi(x) \rightarrow (1 + i\alpha^a t^a + \mathcal{O}(\alpha^2))\psi(x) \quad (2.4)$$

$$A_\mu^a \rightarrow A_\mu^a + \frac{1}{g}\partial_\mu \alpha^a(x) + f^{abc}A_\mu^b \alpha^c + \mathcal{O}(\alpha^2), \quad (2.5)$$

where f^{abc} are the structure constants of G , defined by

$$[t^a, t^b] = if^{abc}t^c. \quad (2.6)$$

Note that the structure constants are zero for abelian gauge groups, such as $G = U(1)$. The Lagrangian for the gauge theory, including gauge-invariant terms involving $A_\mu^a(x)$ itself, is:

$$\mathcal{L} = \bar{\psi}(x)(i\not{\partial})\psi(x) - \frac{1}{4}(F_{\mu\nu}^a)^2, \quad (2.7)$$

where

$$F_{\mu\nu}^a = \partial_\mu A_\nu^a(x) - \partial_\nu A_\mu^a(x) + gf^{abc}A_\mu^b A_\nu^c \quad (2.8)$$

is the field strength tensor of $A_\mu^a(x)$.

The interactions of the fields $\psi(x)$ and $A_\mu^a(x)$ are manifest in the Lagrangian. In this example, the interaction of ψ with A^a is described by the interaction term

$$\mathcal{L}_{\text{int}} = \bar{\psi}\gamma^\mu A_\mu^a t^a \psi. \quad (2.9)$$

For non-abelian gauge groups with nonzero structure constants f^{abc} , the square of the field strength tensor also yields cubic and quartic self-interaction terms amongst the $A_\mu^a(x)$.

2.1.2 Particle Content

The Standard Model is a gauge theory constructed to describe the known fundamental particles and their interactions. The gauge group is $G_{\text{SM}} = \text{SU}(3)_c \times \text{SU}(2)_L \times \text{U}(1)_Y$, roughly corresponding to the strong, weak, and electromagnetic forces, respectively¹. The theory contains a vector gauge boson for each generator of G_{SM} , as described in section 2.1.1: eight gluons (g) for $\text{SU}(3)_c$ and four electroweak gauge bosons (W^\pm , Z^0 , and the photon, γ) for $\text{SU}(2)_L \times \text{U}(1)_Y$.

A fermion field is included for every observed matter particle: six quarks, three leptons, and three neutrinos. The fermions can be grouped into three generations, which are identical except for the particles' masses. Each generation contains an up-type quark with electric charge $\pm\frac{2}{3}$, a down-type quark with charge $\pm\frac{1}{3}$, a lepton with charge ± 1 , and a neutrino with charge 0. The representations of the particles are shown in table 2.1. The quarks carry a quantum number called *color* (e.g. red, green, and blue), which transforms under the fundamental representation of $\text{SU}(3)_c$; the leptons and neutrinos, on the other hand, are assigned to the trivial representation. The left-handed components of all particles are grouped into doublets, transforming in the fundamental representation of $\text{SU}(2)_L$, while the right-handed components are $\text{SU}(2)_L$ singlets. Finally, each particle is assigned a *hypercharge*, Y , describing the coupling to $\text{U}(1)_Y$.

Finally, the theory contains a single $\text{SU}(2)_L$ doublet of complex scalar fields, ϕ , which explains the nonzero masses of the fermions and the W^\pm and Z^0 bosons via the Higgs mechanism, as described in section 2.1.4. The Higgs mechanism predicts a single scalar boson, the Higgs boson, which interacts with the fermions and the W^\pm and Z^0 bosons.

The Standard Model particle content is summarized in table 2.2.

	$Q_L = \begin{pmatrix} u_L \\ d_L \end{pmatrix}$	u_R	d_R	$E_L = \begin{pmatrix} \nu_L \\ e_L \end{pmatrix}$	e_R
$\text{SU}(3)_c$	3	3	3	1	1
$\text{SU}(2)_L$	2	1	1	2	1
$\text{U}(1)_Y$	$\frac{1}{6}$	$\frac{2}{3}$	$-\frac{1}{3}$	$-\frac{1}{2}$	-1

Table 2.1: Matter particles (fermions) in a single generation of the Standard Model, their representations under $\text{SU}(3)_c$ and $\text{SU}(2)_L$, and their charges under $\text{U}(1)_Y$. The left- and right-handed fermions are distinguished by the subscripts L and R .

2.1.3 Strong Sector

The strong sector of the Standard Model is a non-abelian $\text{SU}(3)_c$ gauge theory, describing the interactions of quarks under the strong force. The theory, called *quantum chromodynamics*

¹The fourth force, gravity, has yet to be incorporated successfully. Due to the strength of the interaction, many orders of magnitude weaker than the other three interactions, gravity has a negligible effect on high energy collisions.

	Name	Mass	Spin	Electric Charge
Quarks	Up (u)	2.3 MeV	$\frac{1}{2}$	$+\frac{2}{3}$
	Down (d)	4.8 MeV		$-\frac{1}{3}$
	Charm (c)	1.275 GeV		$+\frac{2}{3}$
	Strange (s)	95 MeV		$-\frac{1}{3}$
	Top (t)	173.21 GeV		$+\frac{2}{3}$
	Bottom (b)	4.18 GeV		$-\frac{1}{3}$
Leptons	Electron (e)	511 keV	$\frac{1}{2}$	-1
	Electron Neutrino (ν_e)	< 2 eV		0
	Muon (μ)	106 MeV		-1
	Muon Neutrino (ν_μ)	< 0.19 MeV		0
	Tau (τ)	1.78 GeV		-1
	Tau Neutrino (ν_τ)	< 18.2 MeV		0
Bosons	Photon (γ)	0	1	0
	W^\pm	80.4 GeV	1	± 1
	Z^0	91.1876 GeV	1	0
	Gluon (g)	0	1	0
	Higgs boson (H)	125.0 GeV	0	0

Table 2.2: List of particles in the Standard Model [2]. The mass, spin, and electric charge of each particle is shown.

(QCD), contains the six observed quarks, called the up, down, charm, strange, top, and bottom quarks, as well as eight massless force carriers called gluons.

QCD describes drastically different phenomena at high and low energies. At low energies, the most tangible consequence of the strong interaction, perhaps, is that most of the matter in the universe is composed of protons and neutrons, not individual quarks. Indeed, free quarks have never been observed in nature, except for the short-lived top quark; rather, quarks are always confined into hadrons, bound states of quarks that are neutral under the strong interaction. On the other hand, in the high energy limit, the strength of the interaction becomes small, and quarks and gluons behave as nearly free particles.

This behavior, called *asymptotic freedom*, was described in 1973 by Wilczek and Gross, and independently Politzer [3, 4]. Asymptotic freedom is a particular case of a more general phenomenon: coupling “constants” change with the energy scale of the interaction, Q , due to the participation of virtual particles in the interaction. Once the coupling is known at some scale μ_R (the *renormalization scale*), the dependence on Q can be computed using the *renormalization group equations*. In the case of QCD, the strong coupling constant, $\alpha_s = \frac{g_s}{4\pi}$, is small at high energies, so calculations can be performed using perturbation theory, expanding to a small number of orders in α_s . To order first order in α_s , the dependence on

Q is given by:

$$\alpha_s(Q) = \frac{\alpha_s(\mu_R)}{1 + (b_0\alpha_s/2\pi)\log(Q/\mu_R)}, \quad (2.10)$$

where $b_0 = 11 - \frac{2}{3}n_f$ for n_f fermion fields. With $n_f = 6$, corresponding to the six quark flavors, $\frac{d\alpha_s(Q)}{dQ} < 0$; hence the coupling decreases as Q increases. At high energies, $Q \gtrsim 1 \text{ GeV}$, quarks interact weakly, and perturbative calculations are reliable. On the other hand, as Q decreases, $\alpha_s(Q)$ increases. Equation 2.10 diverges at

$$Q = M \exp\left(\frac{8\pi^2}{b_0 g^2}\right) \equiv \Lambda_{\text{QCD}}. \quad (2.11)$$

Note that this calculation is perturbative in α_s , and becomes unreliable once α_s becomes large in the vicinity of the divergence. Experimental measurements indicate $\Lambda_{\text{QCD}} \approx 200 \text{ MeV}$ [5].

Proton-Proton Collisions

The proton-proton collisions at the LHC involve several characteristic energy scales, such as the scale of the interaction between constituents of the protons, Q^2 , or the masses of the various particles participating in the interactions. Calculations rely on QCD factorization [6]: hard, perturbative processes, namely the hard scattering between constituents of the protons, factorize from soft, non-perturbative processes, such as the description of the behavior of those constituents within the proton.

The composite nature of the colliding protons is described by the *parton model*, developed in the context of deep inelastic scattering experiments and generalized to hadron-hadron collisions [7–9]. Protons are described as collections of pointlike particles, or partons, bound together by their interactions. In the center-of-mass reference frame, the incoming protons are highly boosted. The time scale of the collision is very short due to Lorentz contraction, while the internal interactions among partons are time dilated and do not influence the hard scattering. The essence of factorization is that while the interactions of the remaining partons can affect the eventual outcome of the collision, they do not interfere quantum mechanically with the hard scattering, and hence their effect can be factorized at the level of probabilities, rather than amplitudes.

Over the short duration of the collision, the colliding parton can be assigned a definite fraction x of the total proton momentum. The partons are characterized by universal *parton distribution functions* (PDFs), $f_{a/A}(x_a, \mu_F^2)$, which describe the probability that parton a within hadron A carries a fraction x_a of the total hadron momentum. The factorization scale, μ_F , roughly represents the scale dividing long- and short-distance processes, and is usually chosen to be near the scale of the hard scattering interaction, $\mu_F \sim Q^2$ [10]. Cross

sections for a given interaction are calculated by summing over the relevant partons and integrating over the PDFs:

$$\sigma_{AB \rightarrow X} = \sum_{a \in A, b \in B} \int dx_a dx_b f_{a/A}(x_a, \mu_F^2) f_{b/B}(x_b, \mu_F^2) \hat{\sigma}_{ab \rightarrow X}, \quad (2.12)$$

where a and b represent partons within protons A and B with momentum fractions x_a and x_b , respectively, and $\hat{\sigma}_{ab \rightarrow X}$ is the hard scattering cross section for those partons. The process is shown schematically in figure 2.1. Note that this calculation requires the choice of two unphysical scales, μ_F and the renormalization scale, μ_R used to compute $\hat{\sigma}_{ab \rightarrow X}$. In principle, the results should be independent of the choice of μ_F and μ_R ; however, the truncation of computations at finite order in α_s introduces some dependence on the choice of scales. Systematic uncertainties are assigned by varying μ_F and μ_R about their nominal values, e.g. up and down by factors of two.

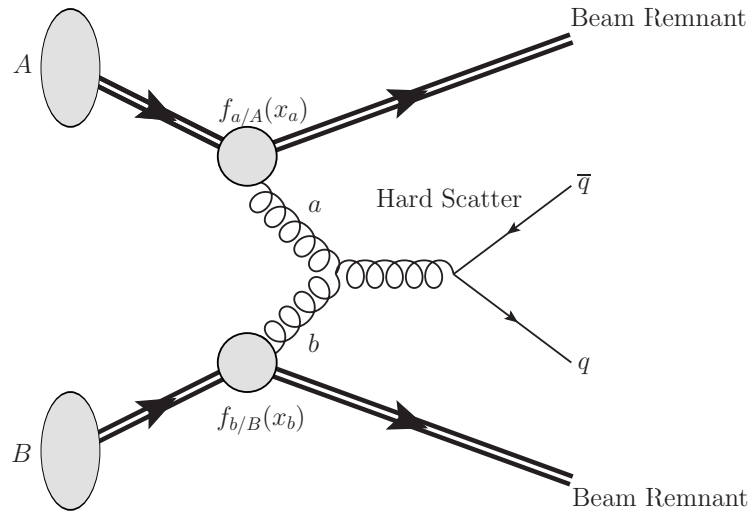


Figure 2.1: Schematic picture of a collision between two protons, labeled A and B . Partons a and b , which are gluons in this picture, participate in the hard scatter interaction, $gg \rightarrow q\bar{q}$. The beam remnants, the remainder of the two protons, do not participate in the hard scatter interaction, but can interact with the final state partons from the hard scatter interaction and with each other, forming the underlying event. The outgoing colored partons undergo fragmentation and hadronization to form jets, not shown here.

The PDFs are determined from fits to existing data; the dependence on x must be determined from the data, while the dependence on the factorization scale can be derived from the DGLAP equations [11–13]. Uncertainties on the PDFs take into account the experimental uncertainties on the input data, as well as various assumptions used in the PDF extraction, such as the value of α_s used in the fit. An example is shown in figure 2.2. At high x , the PDFs are dominated by the three valence quarks (uud), while at low x , gluons and sea

quarks (quark-antiquark pairs formed from the splitting of a gluon) are more prominent. At higher energy scales, the sea quark distributions are more flavor-symmetric, and the gluon and sea quark distributions are larger with respect to the valence quarks.

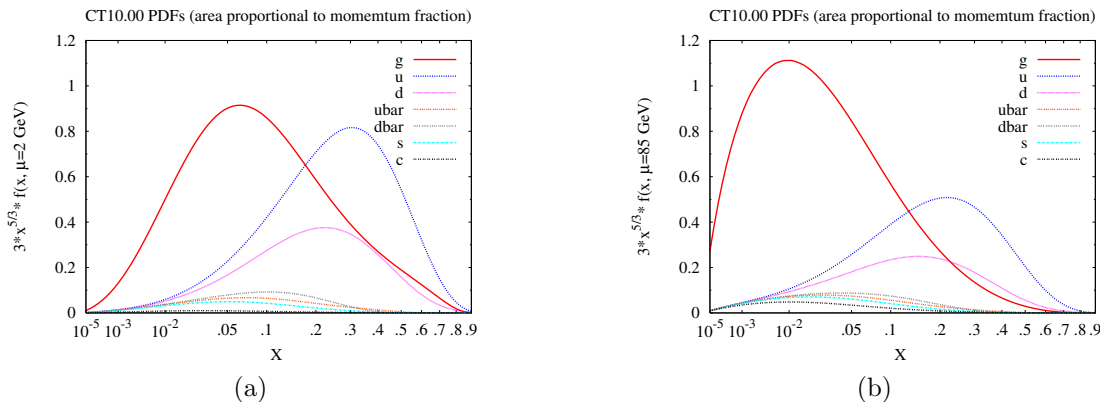


Figure 2.2: Example parton distribution functions at $\mu = 2$ GeV and $\mu = 85$ GeV, from the CT10 PDF set [14].

Jets

A typical proton-proton collision will typically produce several colored partons, from the hard scattering interaction itself or from QCD radiation from initial or final state partons. Free quarks are not observed in nature due to confinement, and hence the colored partons are not directly observed. Rather, the partons transform into a collection of color-neutral hadrons, which are observed as clusters of particles called *jets*. Quarks and gluons emerging from the collision radiate additional gluons, and the gluons split into quark-antiquark pairs (*fragmentation*). The splittings, which are dominated by the emission of soft and collinear radiation, continue until the local momentum scales reach $\mathcal{O}(1 \text{ GeV})$, at which point QCD becomes strongly interacting and confines the partons into hadrons (*hadronization*).

The perturbative part of jet formation can be modeled using a *parton shower* algorithm, which describes probabilistically the creation soft or collinear partons due to splittings [15]. Hadronization is a non-perturbative process, and hence cannot be computed from QCD. It is instead described by phenomenological models, such as the Lund string model [16] or the cluster model [17], which incorporate many free parameters to tune to data.

2.1.4 Electroweak Sector

The electroweak sector is a unified description of electromagnetism and weak decays as a gauge theory with gauge group $SU(2)_L \times U(1)_Y$. The theory models a number of phenomena, including:

- The weak decays of heavy quarks and leptons.
- The nonzero masses of the weak gauge bosons, quarks, and charged leptons.
- Flavor violation in weak decays involving charged currents.
- Violation of C -, P -, and CP -symmetry observed in certain decay processes [18–21].

The underlying theory of the electroweak sector is rather more complicated than the strong sector. C violation is manifest in the construction of the theory: the gauge couplings are *chiral*, with the left- and right-handed components of fermions belonging to different representations of $SU(2)$. Such a symmetry forbids mass terms for the fermions and gauge bosons, in clear conflict with observations. To accommodate fermion and gauge boson masses without abandoning the symmetry, a scalar Higgs field is added with a quartic potential arranged such that the ground state spontaneously breaks the $SU(2)_L$ symmetry. The resulting theory contains a large number of free parameters: two gauge couplings g and g' , two constants in the quartic Higgs potential, nine Yukawa couplings between the fermions and the Higgs field, and three mixing angles and one phase in the CKM matrix.

In this and the following sections, $W^{a\mu}$ represents the three $SU(2)_L$ gauge fields, B^μ the $U(1)_Y$ gauge field, and ϕ the Higgs scalar field, which is a complex $SU(2)_L$ doublet. Assigning the left-handed components of fermions to the doublet $SU(2)_L$ representation and the right-handed components to the singlet presentation, the Standard Model quarks are denoted by $Q_L^i \equiv \begin{pmatrix} u_L^i \\ d_L^i \end{pmatrix}$, u_R^i , and d_R^i , where $i = 1, 2, 3$ indicates the generation. Similarly, the leptons are denoted by $E_L^i \equiv \begin{pmatrix} \nu_L^i \\ e_L^i \end{pmatrix}$ and e_R^i . There is no corresponding right-handed neutrino in the theory.

The Higgs Mechanism

Much of the phenomenology of the electroweak sector can be derived starting from the observation that the W^\pm and Z^0 bosons have masses of nearly 100 GeV, as heavy as entire krypton or molybdenum atoms. Straightforwardly adding explicit gauge boson masses in the Lagrangian, e.g. $m_W^2 (W_\mu^a)^2$, fails immediately due to the requirement of gauge invariance. It is easy to see that such terms are not invariant under equation 2.4.

The solution to this quandary is that the ground state of the theory need not exhibit the same symmetries as the underlying Lagrangian. This phenomenon, known as spontaneous symmetry breaking, underlies the Higgs mechanism [22–24], and is realized in the model of Glashow, Salam, and Weinberg [25–27].

The model introduces an $SU(2)$ doublet of scalar fields, ϕ , with Lagrangian,

$$\mathcal{L}_{\text{Higgs}} = |D_\mu \phi|^2 - V(\phi^\dagger \phi), \quad (2.13)$$

where the potential energy term given by:

$$V(\phi^\dagger \phi) = \frac{1}{2}\mu^2\phi^\dagger \phi + \frac{1}{4}\lambda(\phi^\dagger \phi)^2. \quad (2.14)$$

The quartic potential induces electroweak symmetry breaking if the quadratic coefficient is negative, i.e. $\mu^2 < 0$. The potential is then minimized for a nonzero value of ϕ . Using the $SU(2)_L$ symmetry, we can take vacuum expectation value of ϕ to be:

$$\langle \phi \rangle = \frac{1}{\sqrt{2}} \begin{pmatrix} 0 \\ v \end{pmatrix}. \quad (2.15)$$

Solving for v ,

$$0 = \frac{dV}{dv} = -\frac{1}{2}\mu^2v + \frac{1}{4}\lambda v^3 \quad (2.16)$$

$$v = \frac{2\mu^2}{\lambda}. \quad (2.17)$$

Expanding the Higgs field about its expectation value, ϕ can be written:

$$\phi = U \frac{1}{\sqrt{2}} \begin{pmatrix} 0 \\ v + H \end{pmatrix}, \quad (2.18)$$

where U is a local $SU(2)$ gauge transformation that can be set to **1** by choice of gauge.

The masses and interactions of various particles are described by expanding the Higgs field about $\langle \phi \rangle$ and identifying the relevant physical states. For the Higgs field itself, the potential energy terms are:

$$\Delta \mathcal{L} = -\frac{1}{2}m_H^2 H^2 - \sqrt{\frac{\lambda}{2}} m_H H^3 - \frac{1}{4}\lambda H^4, \quad (2.19)$$

where $m_H = \sqrt{2}\mu$. The theory thus predicts a massive scalar boson with cubic and quartic self interactions.

Gauge Bosons

The mass terms for the gauge bosons arise from the covariant derivative terms in equation 2.13. Expanding the covariant derivatives, the relevant mass terms are:

$$\Delta \mathcal{L} = \frac{1}{8}v^2 \left(g^2(W_\mu^1 W^{1\mu} + W_\mu^2 W^{2\mu}) + (g'B_\mu - gW_\mu^3)^2 \right). \quad (2.20)$$

The physical states are the gauge- and mass-eigenstates,

$$W_\mu^\pm = \frac{W^1 \mp iW^2}{\sqrt{2}} \quad (2.21)$$

$$Z_\mu^0 = -\sin \theta_w B_\mu + \cos \theta_w W_\mu^3 \quad (2.22)$$

$$A_\mu = \cos \theta_w B_\mu + \sin \theta_w W_\mu^3, \quad (2.23)$$

where $\tan \theta_w = \frac{g'}{g}$. The corresponding masses are:

$$m_{W^\pm} = \frac{gv}{2} \quad (2.24)$$

$$m_{Z^0} = \frac{gv}{2 \cos \theta_w} \quad (2.25)$$

$$m_A = 0. \quad (2.26)$$

The theory thus predicts a nontrivial relationship between the masses of the gauge bosons, m_{W^\pm} and m_{Z^0} , and the gauge coupling constants g and g' .

In addition to the Higgs terms in equation 2.13, the Standard Model Lagrangian contains the pure gauge term shown in equation 2.7,

$$\Delta\mathcal{L} = -\frac{1}{4}(F_{\mu\nu}^a)^2, \quad (2.27)$$

where $F_{\mu\nu}^a$ is the field strength tensor (equation 2.8). The structure constants are given by $f^{abc} = i\epsilon^{abc}$, where ϵ^{abc} is the Levi-Civita symbol. In addition to the quadratic kinetic term for the electroweak gauge bosons, the Lagrangian contains cubic and quartic terms, which correspond to interactions between three or four bosons: WWZ , $WW\gamma$, WWW , $WWZZ$, $WW\gamma\gamma$, and $WWZ\gamma$.

Fermion Masses

The fermion masses arise from the Yukawa coupling terms between the fermions and the Higgs field,

$$-\Delta\mathcal{L} = -\left(\lambda_d^{ij}\bar{Q}_L^i \cdot \phi d_R^j - \lambda_u^{ij}\epsilon^{ab}\bar{Q}_{La}^i u_R^j + \text{h.c.}\right) - \left(\lambda_l^{ij}\bar{E}_L^i \cdot \phi e_R^j + \text{h.c.}\right). \quad (2.28)$$

The $\lambda_{u,d,l}^{ij}$ are complex matrices of coupling constants. These are, in general, not symmetric or Hermitian, and to identify the physical mass eigenstates, the matrices must be diagonalized. The Yukawa matrices can be decomposed using the singular value decomposition as:

$$\lambda_u = U_u D_u W_u^\dagger, \quad \lambda_d = U_d D_d W_d^\dagger, \quad \lambda_l = U_l D_l W_l^\dagger, \quad (2.29)$$

where $U_{u,d,l}$ and $W_{u,d,l}$ are unitary matrices, and $D_{u,d,l}$ are diagonal, non-negative matrices. Making a change of variables,

$$u_L^i \rightarrow U_u^{ij} u_L^j, \quad d_L^i \rightarrow U_d^{ij} d_L^j, \quad (2.30)$$

$$u_R^i \rightarrow W_u^{ij} u_R^j, \quad d_R^i \rightarrow W_d^{ij} d_R^j, \quad (2.31)$$

$$e_L^i \rightarrow U_l^{ij} e_L^j, \quad \nu_L^i \rightarrow U_l^{ij} \nu_L^j, \quad (2.32)$$

$$e_R^i \rightarrow W_l^{ij} e_R^j, \quad (2.33)$$

the off-diagonal Yukawa couplings vanish as intended, while the kinetic terms remain invariant. The masses of the fermions are:

$$m_u^i = \frac{1}{\sqrt{2}} D_u^{ii} v, \quad m_d^i = \frac{1}{\sqrt{2}} D_d^{ii} v, \quad m_l^i = \frac{1}{\sqrt{2}} D_l^{ii} v, \quad m_\nu^i = 0. \quad (2.34)$$

Electroweak Interactions of Fermions

The Lagrangian describing the interactions of fermions and gauge bosons is:

$$\mathcal{L}_{\text{sym}} = -\frac{1}{4} \sum_{i=1}^3 \bar{E}_L(iD) E_L + \bar{e}_R(iD) e_R + \bar{Q}_L(iD) Q_L + \bar{u}_R(iD) u_R + \bar{d}_R(iD) d_R, \quad (2.35)$$

where, similarly to equation 2.2, the covariant derivative D_μ is given by:

$$D_\mu = \partial_\mu - ig\tau^a W_\mu^a - ig'YB_\mu, \quad (2.36)$$

$$(2.37)$$

where the τ^a are operators corresponding to the action of a given generator of the $SU(2)_L$ Lie algebra, and Y is an operator corresponding to the action of the generator of $U(1)_Y$, which simply returns the hypercharge. For the left-handed doublets in the fundamental representation of $SU(2)_L$, the τ^a can be taken to be the Pauli matrices, $\tau^a = \frac{1}{2}\sigma^a$. For right-handed singlets in the trivial representation of $SU(2)_L$, the τ^a are zero. In other words, the right-handed fermions do not interact with the $W^{a\mu}$.

In terms of the physical gauge bosons, given in equations 2.21–2.23,

$$D_\mu = \partial_\mu - i\frac{g}{\sqrt{2}} (W_\mu^+ \tau^+ + W_\mu^- \tau^-) - i\frac{g}{\cos\theta_w} Z_\mu (\tau^3 - \sin^2\theta_w Q) - ieA_\mu Q, \quad (2.38)$$

where $e = \frac{gg'}{\sqrt{g^2+g'^2}}$, $\tau^\pm = (\tau^1 \pm i\tau^2)$, and $Q = \tau^3 + Y$.

The fermion couplings to the gauge bosons are complicated by the fact that the mass eigenstates do not necessarily coincide with the gauge eigenstates, due to the off-diagonal Yukawa couplings in section 2.1.4. The diagonalization procedure alters the couplings of the quarks to the W^\pm bosons. The quark- W^\pm couplings can be written in terms of the current $J^{\mu\pm} = \sum_i \frac{1}{\sqrt{2}} (\bar{u}_L^i \gamma^\mu d_L^i)$ as:

$$\Delta\mathcal{L} = g(W_\mu^+ J_W^{\mu+} + W_\mu^- J_W^{\mu-}) \quad (2.39)$$

Under the transformation in equation 2.30, $J^{\mu\pm} \rightarrow \sum_{ij} \frac{1}{\sqrt{2}} \bar{u}_L^i \gamma^\mu V^{ij} d_L^j$, where V^{ij} is a 3×3 unitary matrix known as the *Cabibbo-Kobayashi-Maskawa* (CKM) matrix, $V = U_u^\dagger U_d$. The non-zero off-diagonal elements of V imply that weak decays mix the three generations

of quarks; quark flavor is not conserved in weak decays, as is readily observed in hadron decays, e.g. $K^\pm \rightarrow \pi^\pm + \pi^0$. Further, V contains one nontrivial complex phase, allowing for CP violation in weak decays. Note that the lepton sector does not contain an analogous mixing matrix for weak decays, due to the presence of only a single Yukawa matrix λ_l^{ij} . Hence lepton flavor and CP are conserved in leptonic weak decays.

The decays of W^\pm and Z^0 bosons are shown in table 2.3. Approximately 33% of W^\pm bosons decay to a lepton plus a neutrino. The branching fraction of the Z^0 boson to a lepton-antilepton pair is roughly 10%. In both cases, the decays are distributed nearly equally between the three lepton flavors.

Decay	Branching Fraction	Decay	Branching Fraction
$e\nu$	10.71 ± 0.16 [%]	e^+e^-	3.363 ± 0.004 [%]
$\mu\nu$	10.63 ± 0.15 [%]	$\mu^+\mu^-$	3.366 ± 0.007 [%]
$\tau\nu$	11.38 ± 0.21 [%]	$\tau^+\tau^-$	3.370 ± 0.008 [%]
Hadrons	67.41 ± 0.27 [%]	Invisible	20.00 ± 0.06 [%]
		Hadrons	69.91 ± 0.06 [%]
		4ℓ ($\ell = e, \mu$)	$(3.20 \pm 0.28) \times 10^{-6}$ [28]
(a) W		(b) Z	

Table 2.3: Branching fractions of W^\pm and Z^0 bosons to leptons and other final states [2].

2.2 Beyond the Standard Model

Though quite successful as a description of most observed phenomena in particle physics, the Standard Model is deficient in several ways. Several observations indicate that the particle content is incomplete; additionally, the theory has a few unsatisfying constructional aspects which, while not technically inconsistent, suggest that there remains underlying physics to be discovered. Many theories have been proposed to solve these issues, and confronting these theories is a major goal of the ATLAS experiment. This section describes the motivations for searching for physics beyond the Standard Model (BSM), and lists several of the leading BSM theories which can be confronted at the LHC.

2.2.1 Shortcomings of the Standard Model

Several observations over the last few decades, largely from astrophysics and cosmology, are not described by the Standard Model. These include:

- **Neutrino mass:** Due to the lack of right-handed neutrinos and left-handed antineutrinos, neutrinos are massless in the Standard Model. However, observation of neutrino flavor oscillations indicate that at least two of the three neutrinos have nonzero mass.

The phenomenon of oscillation was first observed by the Homestake solar electron neutrino detector [29], in the form of a deficit of electron neutrinos detected from the sun. Later experiments observed oscillation among other types of neutrinos and antineutrinos, from a variety of sources including the sun, nuclear reactors, cosmic rays interacting with the atmosphere, and particle accelerators [2]. The data imply that the three neutrino mass eigenstates have different masses, with differences given by:

$$|\Delta m_{21}^2| \cong 7.5 \times 10^{-5} \text{ eV}^2 \quad (2.40)$$

$$|\Delta m_{31}^2| \cong 2.5 \times 10^{-3} \text{ eV}^2. \quad (2.41)$$

These relations hold only if at least two of the neutrino masses are nonzero. On the other hand, β -decay experiments and cosmological observations indicate an upper bound on the neutrino mass scale of order $m_{v_i} \lesssim \mathcal{O}(0.1 - 1 \text{ eV})$ [30–32].

- **Dark matter:** Astrophysical observations suggest the existence of a large amount of non-Standard Model matter which interacts only gravitationally with baryonic matter. The earliest tension with known physics comes from galactic rotation curves, the distribution of rotational velocities of stars about the galactic center as a function of radius [33]. The rotational velocities $v(r)$ can be compared with the expectation from the observed matter distribution, $\tilde{v}(r) = \sqrt{\frac{M(r)}{r}}$, where $M(r)$ is the observed mass at radius less than r . At large distances from the galactic center, the observed rotation curve behaves like $v(r) \sim \text{constant}$, while the expected rotation curves behaves like $v(r) \sim \frac{1}{\sqrt{r}}$.

At present, the leading explanation for the discrepancy is the presence of a large amount of gravitationally interacting, non-luminous matter in galaxies, known as *dark matter*. The hypothesis is supported by cosmological observations: measurements of anisotropies in the cosmic microwave background (CMB) are sensitive to the relative amounts of baryonic matter (which interacts with photons), dark matter (which does not), and dark energy. A recent combination of CMB measurements gives the following values [34]:

$$\Omega_c h^2 = 0.1198 \pm 0.0026, \quad (2.42)$$

$$\Omega_b h^2 = 0.02207 \pm 0.00027, \quad (2.43)$$

$$\Omega_\Lambda = 0.685^{+0.017}_{-0.016}, \quad (2.44)$$

$$(2.45)$$

where Ω_c and Ω_b are the density parameters for cold dark matter and baryonic matter, respectively, h is the Hubble constant, and Ω_Λ is the cosmological constant.

Many candidates have been proposed as the constituents of dark matter, such as primordial black holes, sterile neutrinos, axions, and weakly interacting massive particles (WIMPs). WIMPs are a particularly interesting candidate for LHC phenomenology:

in the so-called “freeze-out” model of dark matter evolution, Ω_c is fixed when dark matter falls out of thermal equilibrium with conventional matter. $\Omega_c \sim 0.1$ is achieved with $m_\chi \sim \mathcal{O}(100 \text{ GeV})$ and couplings of order $g_X \sim \mathcal{O}(0.1 - 1)$; such a particle could be produced and detected at the LHC.

- **Matter-Antimatter Asymmetry:** The observable universe is made up of matter and photons, with very little antimatter. Astrophysical observations measure the ratio of baryons (minus antibaryons) to photons,

$$\eta \equiv \frac{n_B - n_{\bar{B}}}{n_\gamma}, \quad (2.46)$$

to be in the range $5.7 \times 10^{-10} \leq \eta \leq 6.7 \times 10^{-10}$ at 95% confidence level [2]. However, assuming symmetrical initial conditions and conservation of baryon number, the Big Bang would produce baryons and antibaryons in equal number². Due to inefficient annihilation after freeze-out, the present abundances would be $\frac{n_B}{n_\gamma} = \frac{n_{\bar{B}}}{n_\gamma} \approx 10^{-20}$ [35]. The generation of a large baryon-antibaryon asymmetry is known as the *baryogenesis* problem.

- **Gravity:** Gravity is not described by the Standard Model.

2.2.2 Theoretical Issues

Besides not describing the phenomena listed above, the Standard Model has a number of theoretical issues related to its parameters and structure.

- **Hierarchy problem:** The hierarchy problem refers to the large discrepancy between the electroweak scale, $\mathcal{O}(10^2 \text{ GeV})$, and the Planck scale, $\mathcal{O}(10^{19} \text{ GeV})$. Due to fermion and gauge boson loops like those shown in figure 2.3, the Higgs boson mass receives quantum corrections proportional to Λ^2 , where Λ is the scale up to which the theory is valid. For example, due to a fermion f with Yukawa coupling λ_f , the physical Higgs mass at one loop order is:

$$m_{H,\text{phys}}^2 \approx m_H^2 - \frac{|\lambda_f|^2}{8\pi^2} \Lambda^2, \quad (2.47)$$

where m_H^2 is the bare Higgs mass parameter in the Lagrangian. In practice, the contribution from the top quark, with $\lambda_t \sim 1$, dominates this expression. If Λ is near the Planck scale, $\Lambda \sim 10^{19} \text{ GeV}$, then with $m_H(\text{phys}) = 125.1 \text{ GeV}$, the bare Higgs mass and Δm_H^2 must cancel to some 30 orders of magnitude, an unsavory coincidence referred to as *fine tuning*. Turning the problem on its head, if nature is not finely tuned, then Λ should be not too far above the electroweak scale, $\Lambda \lesssim 10 \text{ TeV}$. The physics responsible for such a cutoff scale could be accessible at the LHC.

²Asymmetric initial conditions are disfavored due to inflation, which would dilute any initial asymmetry [35].

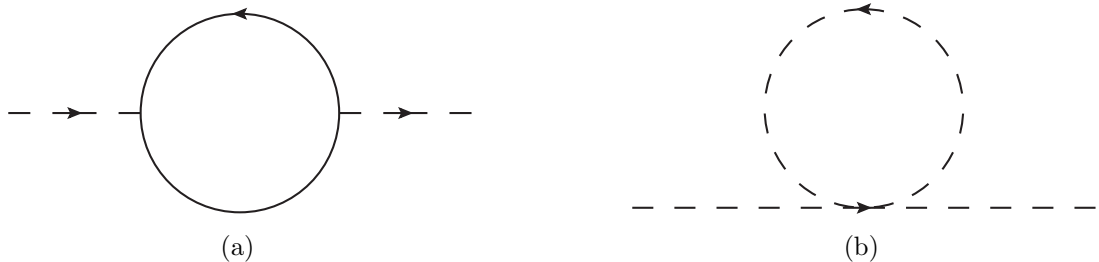


Figure 2.3: One-loop Feynman diagrams involving fermions (left) and bosons (right) leading to the quadratic divergence of the Higgs mass.

- **Strong CP problem:** The strong sector of the Standard Model potentially contains a CP -violating term,

$$\mathcal{L}_\Theta = \theta_{\text{QCD}} \frac{\alpha_s}{8\pi} G^{\mu\nu a} \tilde{G}_{\mu\nu}^a, \quad (2.48)$$

where $-\pi \leq \theta_{\text{QCD}} \leq \pi$ is the effective Θ parameter after diagonalizing the quark mass matrix, $G_{\mu\nu}^a = \partial_\mu A_\mu^a - \partial_\nu A_\mu^a - g_s f^{abc} A_\mu^b A_\nu^c$ is the gluon field strength tensor, and $\tilde{G}_{\mu\nu}^a = \epsilon_{\mu\nu\alpha\beta} G^{\alpha\beta a}$ is its dual [2]. However, this term is severely constrained by measurements of the neutron dipole moment [36], with a limit of $|\theta_{\text{QCD}}| \lesssim 10^{-10}$.

Axions are a leading candidate for the resolution of the strong CP problem [37]. These are typically very weakly coupled, and would not be observable at the LHC.

- **Free parameters:** The Standard Model contains 19 free parameters. In terms of measured quantities, these are the 6 quark masses m_{q_i} , 3 lepton masses m_{l_i} , 3 CKM mixing angles θ_{ij} and 1 CKM phase δ , 3 gauge couplings g_i , the QCD vacuum angle θ_{QCD} , the Higgs field vacuum expectation value v , and the Higgs mass, m_H . These parameters are measured; their values are not predicted by the theory. It remains unknown why the Yukawa couplings range over six orders of magnitude, for example, nor why the fermions fall into three identical generations. A more complete theory might explain the patterns observed among the parameters and predict their values.
- **Gauge Unification:** The origin of the Standard Model gauge group, $G_{SM} = SU(3)_c \times SU(2)_L \times U(1)_Y$, is not understood. Remarkably, the Standard Model fermion content can be described as a **5*** \oplus **10** representation of $SU(5)$, the smallest simple group containing G_{SM} , with all of the Standard Model quantum numbers correctly predicted. Unfortunately, simply augmenting the gauge group to $SU(5)$ leads to an unacceptable rate of proton decay, but deriving G_{SM} from a larger, “unified” gauge group remains a topic of active investigation.

2.2.3 Theories of BSM Physics

A large number of theories have been developed to address the problems in the previous section, many of which yield testable predictions for the LHC. This section describes three examples of such theories: supersymmetry, extra fermions beyond the three Standard Model generations, and the neutrino seesaw mechanism. These theories are capable of producing three or more charged leptons in pp collisions through the production and decay of heavy new particles, and can thus be confronted against the analyses described in chapters 7 and 8.

Supersymmetry

The hierarchy problem described above motivates the consideration of additional symmetries. Consider again the Higgs mass quadratic divergence (equation 2.47). The divergence could be avoided by introducing scalar partners to the fermions to counteract the divergence, due to the relative (-) sign between scalar and fermion loops in figure 2.3. Canceling the divergence at all orders suggests the introduction of an extra symmetry to the Standard Model.

The forms that such a symmetry could take are quite restricted. In 1967, Coleman and Mandula demonstrated that, under a small set of physically assumptions, the symmetry algebra of the S -matrix must be isomorphic to a direct product of the Poincaré group and an internal symmetry group (i.e. whose generators commute with those of the Poincaré group). This *no-go* theorem appeared to establish that it is impossible to “[combine] space-time and internal symmetries in any but a trivial way.” However, a loophole was found in 1975, formalized in the theorem of Haag, Lopuszanski, and Sohnius: the Poincaré group can be extended nontrivially in the context of graded Lie algebras, allowing the symmetry generators to be commuting or anticommuting [38]. These so-called “supersymmetries”, first proposed in by Wess and Zumino [39], transform bosons to fermions and vice-versa, and combine nontrivially with the Poincaré group in that the anticommutator of two supersymmetry generators is a spacetime translation.

By itself, supersymmetry predicts a partner for every Standard Model particle with identical mass and quantum numbers, except that the spin differs by 1/2. The symmetry is assumed to be spontaneously broken at some high mass scale, giving additional mass to the superpartners to account for the fact that superpartners have not yet been observed. The minimal implementation, called the *minimal supersymmetric Standard Model* (MSSM), contains 178 free parameters, although simplifying assumptions are almost always used to reduce this enormous parameter space to manageable size.

Supersymmetry addresses a number of the shortcomings of the standard model described above. First, it provides a boson-fermion symmetry to cancel the quadratic divergence in the Higgs mass. Second, the superpartners are typically assigned an extra quantum number, R -parity, under with the SM particles are neutral, in order to stabilize the proton; this extra symmetry has the consequence of making the lightest supersymmetric particle (LSP) stable, providing a dark matter candidate. Third, the supersymmetry breaking sector

contains numerous CP-violating parameters, which could provide the necessary CP violation to explain the matter-antimatter asymmetry in the universe. Finally, the superpartners modify the running of the three gauge couplings such that they approach similar values in the UV, supporting the notion of gauge unification.

Trilepton events are a useful tool in MSSM searches. A common scenario is that the heavy supersymmetric particles decay back to Standard Model particles plus an LSP, often producing three or more leptons in the decay chains. Figure 2.4 shows an example involving the production of charginos and neutralinos, the superpartners of the W^\pm , Z^0 , and H bosons. ATLAS has performed several dedicated searches for such scenarios [40–42], which are not discussed in this dissertation.

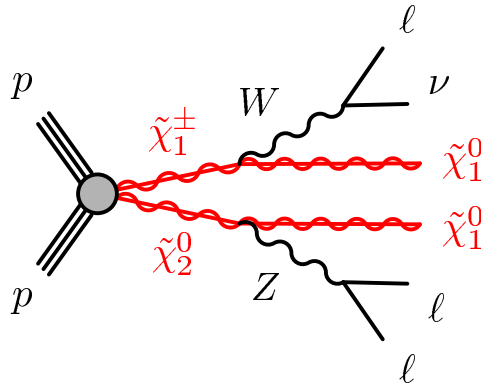


Figure 2.4: Feynman diagram showing the production of a chargino, $\tilde{\chi}_1^\pm$, and a neutralino, $\tilde{\chi}_2^0$, decaying to two neutralino LSPs, $\tilde{\chi}_1^0$, plus three leptons and a neutrino. The chargino/neutralino subscript indicates mass ordering, with 1 being the lightest.

Extra Generations of Matter

Given that the origin of the three generations of fermions is not understood, an obvious question is whether additional generations might exist. A review of extra fermions can be found at [43]. A fourth chiral generation, i.e. another copy of the three known generations, is strongly constrained, though not completely excluded [44–47]. The number of neutrinos coupling to the Z boson with $m_\nu < \frac{1}{2}m_Z$ can be determined from the invisible width of the Z , giving $N_\nu = 2.9840 \pm 0.0084$. Further, additional chiral fermions coupling to the Higgs boson would significantly alter its production rate and decay patterns. In particular, an additional pair of quarks would increase the production cross section for $gg \rightarrow H$ by roughly a factor of 9.

Additional non-chiral, or *vector-like*, fermions are less constrained. Such fermions are defined as having identical left- and right-handed interactions under the Standard Model gauge group, particularly under $SU(2)_L$. Consequently, explicit mass terms, $m\bar{\psi}\psi$, are not forbidden by gauge invariance, and the fermions need not couple to the Higgs field to ac-

quire mass. The impact on Higgs production and decay, as well as precision electroweak observables, are small. Further, the pattern of extra vector-like fermions is less restricted compared to chiral generations, where a spectacular cancellation between the fields of each generation is needed to avoid chiral anomalies [48].

Vector-like fermions are a feature of many model of BSM physics. Additional quarks are present in some models addressing the hierarchy problem, such as the little Higgs model [49] or composite Higgs models [50]. Vector-like leptons can appear alongside quarks in SU(5) multiplets [51], and are predicted in models explaining the fermion mass hierarchy [52], composite Higgs models, models with warped extra dimensions [53, 54], and the type III neutrino seesaw mechanism, discussed in section 2.2.3.

In order to render the vector-like fermions unstable, mixing terms involving the Standard Model fermions can be introduced. This enables decays to a W^\pm , Z^0 , or H boson, plus a Standard Model quark or lepton. Three or more leptons can be produced if the bosons decay leptonically. In the case of vector-like leptons, the three leptons can also be produced resonantly, allowing the use of a trilepton mass constraint. An example Feynman diagram is shown in figure 2.5. The collider phenomenology of vector-like leptons is discussed in more detail in section 8.1.

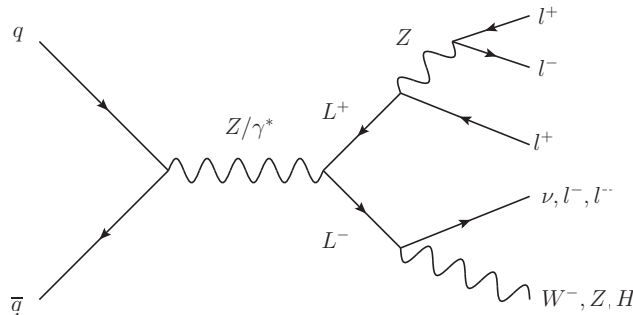


Figure 2.5: Example of the pair production of two vector-like leptons, L^\pm . The L^\pm decay via mixing with Standard Model leptons. In this example, one vector-like lepton is shown decaying to three leptons via an intermediate Z boson.

Neutrino Seesaw

Due to the lack of right-handed neutrinos in the Standard Model, neutrinos are exactly massless. A neutrino mass term, $m_\nu \bar{\nu}_L \nu_L^c$ violates $SU(2)_L$ gauge invariance. An effective mass term arising perturbatively, e.g. $\frac{Y_{ij}}{v} \phi \phi L_i L_j$, would be a good candidate to explain the small size of neutrino masses due to suppression from the mass scale v , but turns out to be forbidden as well due to the accidental conservation of lepton number, L , and also baryon minus lepton number, $B - L$ [55].

If neutrinos are their own antiparticle, i.e. are Majorana fermions rather than Dirac fermions, a leading candidate to explain the small but nonzero neutrino masses is the *neutrino*

seesaw mechanism [56–58]. The Standard Model is augmented with heavy, sterile neutrinos, N_i , which have both Majorana masses and Yukawa interactions with the Standard Model neutrinos:

$$\mathcal{L}_N = \frac{1}{2} M_{N_{ij}} \bar{N}_i^c N_j + Y_{ij}^\nu \bar{L}_i \tilde{\phi} N_j + \text{h.c.} \quad (2.49)$$

where $L_i = \begin{pmatrix} \nu_i \\ \ell_i \end{pmatrix}$. The resulting mass matrix takes the form:

$$M_\nu = \begin{pmatrix} 0 & Y^\nu \frac{v}{\sqrt{2}} \\ (Y^\nu)^T \frac{v}{\sqrt{2}} & M_N \end{pmatrix} \quad (2.50)$$

in the basis $\begin{pmatrix} \nu_i \\ N_j \end{pmatrix}$. If $M_N \gg v$, then diagonalizing the mass matrix gives three eigenstates will light masses, $m_{\nu_{L_i}} \sim \frac{Yv^2}{M_N}$. With $v = 246$ GeV, a light neutrino mass of $m_\nu = 0.1$ eV gives a heavy neutrino mass of:

$$M_N \sim Y \times 10^{15} \text{ GeV}. \quad (2.51)$$

Hence Yukawa couplings of order 1 predict heavy, sterile neutrinos around the GUT scale, while smaller couplings predict a proportionally smaller mass scale. New mass scales accessible at the LHC can be achieved with more complicated models, such as the inverse seesaw model [59], which introduce more mass scales and high powers of the suppression factors.

At tree level, there are three possible implementations of the seesaw mechanism:

- **Type I:** The simplest realization of the seesaw mechanism, at least two sterile neutrinos N_i are introduced as described above. This scenario is not likely to be testable at the LHC, due to the combination of small Yukawa couplings and large sterile neutrino masses required for $\mathcal{O}(0.1)$ eV neutrino masses.
- **Type II:** The seesaw mechanism is generated by an $SU(2)_L$ triplet of scalars, Δ , with hypercharge $Y = 2$. This allows the construction of the following Yukawa term:

$$-\mathcal{L} = Y_{ij}^\Delta L_i^T C \sigma_2 \Delta L_j + \text{h.c.}, \quad (2.52)$$

where i ranges over the three lepton flavors. Assuming diagonal Yukawa couplings for simplicity, the neutral component of the triplet, Δ^0 , acquires a vacuum expectation value,

$$v_\Delta = \frac{\mu v^2}{\sqrt{2} m_\Delta^2}, \quad (2.53)$$

where m_Δ is the mass term for Δ , $\mu \sim m_\Delta$ is a coefficient of the cubic Higgs- Δ interaction with mass dimension 1, and v is the Standard Model Higgs vacuum expectation value. The light neutrinos acquire mass:

$$m_{\nu_i} \sim Y_i^\Delta v_\Delta = Y_i^\Delta \frac{\mu v^2}{\sqrt{2} m_\Delta^2}. \quad (2.54)$$

The triplet of scalars can potentially be produced via gauge interactions at the LHC, if their masses are below the TeV scale. The new particle content consists of Δ^0 , Δ^\pm , and $\Delta^{\pm\pm}$. Same-sign dilepton final states have been used to search for the doubly charged scalar [60], and $\Delta^{\pm\pm}\Delta^{\mp\mp}$ pair production is used as a benchmark model for the model-independent trilepton search presented in chapter 7.

- **Type III:** The seesaw mechanism is generated by at least two $SU(2)_L$ triplets of fermions with hypercharge $Y = 0$,

$$\Sigma = \Sigma^a \sigma^a = \begin{pmatrix} \Sigma^0/\sqrt{2} & \Sigma^+ \\ \Sigma^- & -\Sigma^0/\sqrt{2} \end{pmatrix}. \quad (2.55)$$

The Lagrangian is:

$$\mathcal{L}_\Sigma = \text{Tr}[i\bar{\Sigma}\not{D}\Sigma] - \frac{1}{2}\text{Tr}[\bar{\Sigma}M_\Sigma\Sigma^c + \bar{\Sigma}^c M_\Sigma^*\Sigma] - \tilde{\phi}^\dagger\bar{\Sigma}\sqrt{2}Y_\Sigma L - \bar{L}\sqrt{s}Y_\Sigma^\dagger\Sigma\tilde{\phi}, \quad (2.56)$$

where $L = (\nu, l)^T$, $\phi = (\phi^+, \phi^0)^T$, $\tilde{\phi} = i\sigma_2\phi^*$, and $\Sigma^c = C\bar{\Sigma}^T$. Summation over lepton flavor is implicit. The neutral fermion Σ^0 generates the seesaw mechanism in much the same way as in the type I implementation, giving neutrino masses:

$$m_\nu = -v^2 Y_\Sigma^T \cdot M_\Sigma^{-1} \cdot Y_\Sigma \quad (2.57)$$

Like the scalar triplet, the heavy fermion triplet can also be produced at detectable rates at the LHC via gauge interactions. The collider phenomenology of the fermions, which are vector-like, is described in more detail in section 8.1.

Bibliography

- [1] M. Peskin and D. Schroeder, *An Introduction to Quantum Field Theory*, Advanced book program, Boulder (Colo.): Westview Press Reading (Mass.), 1995.
- [2] K. Olive et al., *Review of Particle Physics*, Chin.Phys. **C38** (2014) p. 090001.
- [3] D. J. Gross and F. Wilczek, *Ultraviolet Behavior of Nonabelian Gauge Theories*, Phys.Rev.Lett. **30**.26 (1973) pp. 1343–1346.
- [4] H. D. Politzer, *Reliable Perturbative Results for Strong Interactions?*, Phys.Rev.Lett. **30**.26 (1973) pp. 1346–1349.
- [5] J. M. Campbell, E. W. N. Glover, and C. J. Maxwell, *Determination of the QCD Parameter $\Lambda_{\overline{MS}}^{(5)}$ from the Measured Energy Dependence of the Average Value of 1-Thrust*, Phys.Rev.Lett. **81** (1998) pp. 1568–1571.
- [6] J. C. Collins, D. E. Soper, and G. Sterman, *Factorization of Hard Processes in QCD* (2004), arXiv: hep-ph/0409313v1 [hep-ph].
- [7] J. D. Bjorken and E. A. Paschos, *Inelastic Electron Proton and gamma Proton Scattering, and the Structure of the Nucleon*, Phys.Rev. **185**.5 (1969) pp. 1975–1982.
- [8] R. P. Feynman, “The Behavior of Hadron Collisions at Extreme Energies”, *Special Relativity and Quantum Theory*, ed. by M. Noz and Y. Kim, vol. 33, Fundamental Theories of Physics, Springer Netherlands, 1988 pp. 289–304.
- [9] S. D. Drell and T.-M. Yan, *Partons and their Applications at High-Energies*, Annals Phys. **66**.2 (1971) pp. 578–623.
- [10] J. M. Campbell, J. W. Huston, and W. J. Stirling, *Hard interactions of quarks and gluons: a primer for LHC physics*, Reports on Progress in Physics **70**.1 (2006) pp. 89–193.
- [11] V. N. Gribov and L. N. Lipatov, *Deep inelastic e p scattering in perturbation theory*, Sov. J. Nucl. Phys. **15** (1972) pp. 438–450.
- [12] Y. L. Dokshitzer, *Calculation of the Structure Functions for Deep Inelastic Scattering and e+ e- Annihilation by Perturbation Theory in Quantum Chromodynamics.*, Sov. Phys. JETP **46** (1977) pp. 641–653.
- [13] G. Altarelli and G. Parisi, *Asymptotic Freedom in Parton Language*, Nucl.Phys. **B126**.2 (1977) pp. 298–318.

- [14] H.-L. Lai et al., *New parton distributions for collider physics*, Phys. Rev. **D 82** (2010) p. 074024, arXiv: 1007.2241 [hep-ph].
- [15] A. Buckley et al., *General-purpose event generators for LHC physics*, arXiv **504.5** (2011) pp. 145–233.
- [16] B. Andersson et al., *Parton Fragmentation and String Dynamics*, Phys. Rept. **97.2-3** (1983) pp. 31–145.
- [17] B. R. Webber,
A QCD Model for Jet Fragmentation Including Soft Gluon Interference, Nucl.Phys. **B238.3** (1984) pp. 492–528.
- [18] C. S. Wu et al., *Experimental Test of Parity Conservation in Beta Decay*, Phys.Rev. **105.4** (1957) pp. 1413–1414.
- [19] J. H. Christenson et al., *Evidence for the 2π Decay of the K_2^0 Meson*, Phys.Rev.Lett. **13.4** (1964) pp. 138–140.
- [20] V. Fanti et al. (NA48 Collaboration),
A new measurement of direct CP violation in two pion decays of the neutral kaon, Physics Letters B **465** (1999) pp. 335–348.
- [21] A. Alavi-Harati et al., *Observation of direct CP violation in $K_{S,L} \rightarrow \pi\pi$ decays*, Phys.Rev.Lett. **83** (1999).
- [22] P. W. Higgs, *Broken Symmetries and the Masses of Gauge Bosons*, Phys.Rev.Lett. **13.16** (1964) pp. 508–509.
- [23] F. Englert and R. Brout, *Broken Symmetry and the Mass of Gauge Vector Mesons*, Phys.Rev.Lett. **13.9** (1964) pp. 321–323.
- [24] G. S. Guralnik, C. R. Hagen, and T. W. B. Kibble,
Global Conservation Laws and Massless Particles, Phys.Rev.Lett. **13.20** (1964) pp. 585–587.
- [25] S. L. Glashow, *Partial Symmetries of Weak Interactions*, Nucl.Phys. **22.4** (1961) pp. 579–588.
- [26] S. Weinberg, *A Model of Leptons*, Phys.Rev.Lett. **19.21** (1967) pp. 1264–1266.
- [27] A. Salam, *Weak and Electromagnetic Interactions*, Conf. Proc. **C680519** (1968) pp. 367–377.
- [28] ATLAS Collaboration, *Measurements of Four-Lepton Production at the Z Resonance in pp Collisions at $\sqrt{s} = 7$ and 8 TeV with ATLAS*, Phys. Rev. Lett. **112** (2014), arXiv: 1403.5657 [hep-ex].
- [29] B. Cleveland et al., *Measurement of the solar electron neutrino flux with the Homestake chlorine detector*, Astrophys.J. **496** (1998) pp. 505–526.

- [30] V. N. Aseev et al.,
Upper limit on the electron antineutrino mass from the Troitsk experiment,
Physical Review D **84**.11 (2011) pp. 112003–9.
- [31] K. N. Abazajian et al., *Cosmological and astrophysical neutrino mass measurements*,
Astroparticle Physics **35**.4 (2011) pp. 177–184.
- [32] P. Ade et al., *Planck 2013 results. XVI. Cosmological parameters*,
Astron.Astrophys. **571** (2014) A16, arXiv: 1303.5076 [astro-ph.CO].
- [33] V. C. Rubin, W. K. Ford, and N. . Thonnard,
Rotational properties of 21 SC galaxies with a large range of luminosities and radii, from NGC 4605 ($R = 4\text{kpc}$) to UGC 2885 ($R = 122\text{ kpc}$),
The Astrophysical Journal **238** (1980) pp. 471–487.
- [34] P.A.R. Ade et al. (Planck Collab. 2013),
Planck 2013 results. XVI. Cosmological parameters, A&A **571** (2014) A16,
arXiv: 1303.5076 [astro-ph.CO].
- [35] J. M. Cline, *Baryogenesis*, arXiv **hep-ph** (2006).
- [36] C. A. Baker et al.,
Improved Experimental Limit on the Electric Dipole Moment of the Neutron,
Phys. Rev. Lett. **97** (13 2006) p. 131801.
- [37] R. D. Peccei and H. R. Quinn, *CP conservation in the presence of pseudoparticles*,
Phys.Rev.Lett. **38**.25 (1977) pp. 1440–1443.
- [38] R. Haag, J. T. Lopuszanski, and M. Sohnius,
All possible generators of supersymmetries of the S-matrix,
Nuclear Physics B **88**.2 (1975) pp. 257–274, ISSN: 0550-3213.
- [39] J. Wess and B. Zumino, *Supergauge transformations in four dimensions*,
Nuclear Physics B **70**.1 (1974) pp. 39–50, ISSN: 0550-3213.
- [40] ATLAS Collaboration, *Search for direct production of charginos and neutralinos in events with three leptons and missing transverse momentum in $\sqrt{s} = 8\text{ TeV}$ pp collisions with the ATLAS detector*, JHEP **2014**.04 (2014).
- [41] ATLAS Collaboration, *Search for supersymmetry in events with four or more leptons in $\sqrt{s} = 8\text{ TeV}$ pp collisions with the ATLAS detector*,
Physical Review D **90**.5 (2014).
- [42] ATLAS Collaboration, *Search for supersymmetry at $\sqrt{s} = 8\text{ TeV}$ in final states with jets and two same-sign leptons or three leptons with the ATLAS detector*,
JHEP **2014**.6 (2014) pp. 35–50.
- [43] P. H. Frampton, P. Q. Hung, and M. Sher,
Quarks and Leptons Beyond the Third Generation, Physics Reports **330**.5-6 (2000),
arXiv: hep-ph/9903387v2 [hep-ph].

- [44] M. Buchkremer, J.-M. Gérard, and F. Maltoni,
Closing in on a perturbative fourth generation, JHEP **2012**.06 (2012) pp. 135–23,
arXiv: 1204.5403 [hep-ph].
- [45] A. Djouadi and A. Lenz, *Sealing the fate of a fourth generation of fermions*,
Physics Letters B **715**.4–5 (2012) pp. 310–314.
- [46] M. S. Chanowitz, *Electroweak constraints on the fourth generation at two loop order*,
Physical Review D **88**.1 (2013) pp. 015012–9, arXiv: 1212.3209 [hep-ph].
- [47] S. Banerjee, M. Frank, and S. K. Rai,
Higgs data confronts sequential fourth generation fermions in the Higgs triplet model,
Physical Review D **89**.7 (2014) pp. 075005–16, arXiv: 1312.4249 [hep-ph].
- [48] C. Q. Geng and R. E. Marshak, *Uniqueness of Quark and Lepton Representations in the Standard Model From the Anomalies Viewpoint*, English,
Phys. Rev. **D39**.2 (1989) pp. 693–696.
- [49] N. Arkani-Hamed et al., *The Littlest Higgs*, JHEP **2002**.07 (2002) p. 34,
arXiv: 0206021 [hep-ph].
- [50] D. B. Kaplan, H. M. Georgi, and S. K. Dimopoulos, *Composite Higgs scalars*,
Phys. Lett. B **136**.HUTP-83-A-079 (1983) 187. 10 p.
- [51] S. P. Martin and J. D. Wells, *Implications of gauge-mediated supersymmetry breaking with vector-like quarks and a 125 GeV Higgs boson*,
Phys. Rev. D **86** (3 2012) p. 035017, arXiv: 1206.2956 [hep-ph].
- [52] A. Falkowski, D. M. Straub, and A. Vicente,
Vector-like leptons: Higgs decays and collider phenomenology,
JHEP **2014**.5 (2014) pp. 92–18, arXiv: 1312.5329 [hep-ph].
- [53] M. Redi, *Leptons in composite MFV*, JHEP **2013**.9 (2013) pp. 60–17,
arXiv: 1306.1525 [hep-ph].
- [54] R. Contino et al., *Warped/Composite Phenomenology Simplified*,
JHEP **2007**.05 (2006) p. 74, arXiv: 0612180 [hep-ph].
- [55] M. C. Gonzalez-Garcia and Y. Nir,
Neutrino masses and mixing: evidence and implications,
Rev. Mod. Phys. **75** (2 2003) pp. 345–402.
- [56] R. N. Mohapatra and G. Senjanovic, *Neutrino Masses and Mixings in Gauge Models with Spontaneous Parity Violation*, English,
Physical Review D **23** (1981) pp. 165–180.
- [57] M. Gell-Mann, P. Ramond, and R. Slansky, *Complex Spinors and Unified Theories*,
Conf. Proc. **C790927** (1979) pp. 315–321, arXiv: 1306.4669 [hep-th].
- [58] T. Yanagida, *Horizontal Symmetry and Masses of Neutrinos*, English,
Prog.Theor.Phys. **64**.3 (1980) pp. 1103–1105.

- [59] F. Deppisch and J. W. F. Valle,
Enhanced lepton flavor violation in the supersymmetric inverse seesaw model,
Physical Review D **72** (2005), arXiv: 0406040 [[hep-ph](#)].
- [60] ATLAS Collaboration, *Search for anomalous production of prompt same-sign lepton pairs and pair-produced doubly charged Higgs bosons with $\sqrt{s} = 8$ TeV pp collisions using the ATLAS detector*, JHEP **2015**.3, 41 (2015).

Chapter 3

The Experimental Apparatus

3.1 The Large Hadron Collider

The Large Hadron Collider (LHC) is a particle accelerator designed to explore the physics of particles at the energy scale of electroweak symmetry breaking. The accelerator occupies a 26.7 km tunnel beneath the Switzerland-France border near Geneva, which previously housed the Large Electron Positron Collider (LEP). Protons are accelerated in two counter-rotating beams up to a design momentum of $7 \text{ TeV}/c$. The beams collide at four interaction points (IPs), shown in figure 3.1, where four collider detectors, ATLAS, CMS, LHCb, and ALICE, analyze the remnants of the collisions.

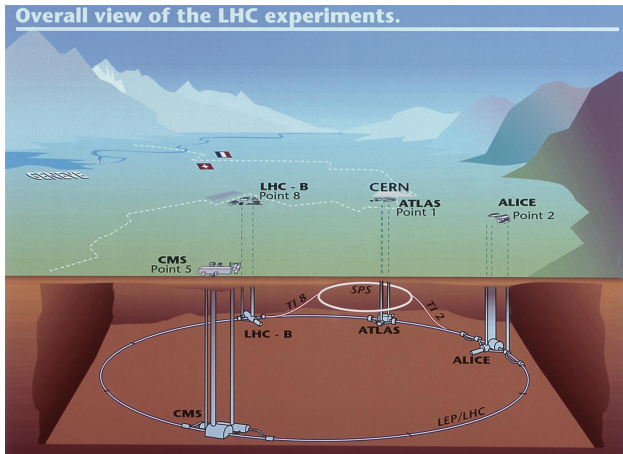


Figure 3.1: The LHC and the four interaction points where the beams are brought into collision. The ATLAS experiment is located at interaction point 1.

The LHC project was approved in 1994 by the CERN Council, and construction proceeded over the ensuing 14 years [1]. The collider detectors were constructed in parallel, beginning with the excavation of two additional caverns at IP1 and IP5 for the ATLAS and CMS detectors (LHCb and ALICE occupied the existing caverns at IP2 and IP8, which

previously housed the DELPHI and L3 LEP experiments). The first beam was circulated on 10 September 2008; however, on 19 September, the LHC sustained severe damage due to an incident stemming from a faulty joint between magnets¹. Repairs took an extra year, and the energy of the beams was reduced to 3.5-4 TeV for the first data-taking run, to mitigate the risk of another possible faulty joint.

Proton-proton collisions at a center-of-mass energy of $\sqrt{s} = 7 \text{ TeV}$ commenced in early 2010. The LHC delivered an integrated luminosity of $\int \mathcal{L} dt = 48.1 \text{ pb}^{-1}$ to the ATLAS detector in 2010, and $\int \mathcal{L} dt = 5.46 \text{ fb}^{-1}$ in 2011. In 2012, the collision energy was increased to $\sqrt{s} = 8 \text{ TeV}$, and a dataset of $\int \mathcal{L} dt = 22.8 \text{ fb}^{-1}$ was delivered.

3.1.1 Accelerator Components

The primary devices used for acceleration are synchrotrons, circular accelerators comprised of magnets and radio frequency (RF) cavities [3]. The magnets are used to manipulate the particle beams: dipole magnets bend the beams in a circle and steer the beams down transfer lines between the accelerators, while quadrupole and higher moment magnets focus the beams. RF cavities are hollow metallic structures used for particle acceleration. The RF cavities are driven by klystrons, radio frequency amplifiers that act as power sources, at their resonant frequency, creating an oscillating electric field inside the structure. The frequency of the RF cavities is matched to the rotation frequency of the particle beams.

The RF oscillations cause the particle beam to bunch longitudinally into so-called RF buckets, shown schematically in figure 3.2. The center of the bucket corresponds to particles with the reference energy, determined by the magnets, which arrive in phase with the RF oscillations so that they experience no force. During *flat-top* operation, where the particle are held at fixed energy in the synchrotron, particles at the center of the RF bucket remain stationary at that point (neglecting energy losses due to synchrotron radiation), while nearby particles oscillate around the fixed point. During a *ramp*, where particles are accelerated, the magnetic fields of the dipoles are slowly increased, shifting the RF bucket and causing the particle bunches to fall on the accelerating edge of the electric field oscillations.

¹A postmortem analysis implicated a bad splice between the superconducting cables of adjacent magnets as the source of the incident, with a resistance about 10^3 times above specification. The joint melted, and 275 MJ of energy in the magnets dissipated in electric arcs, which vaporized beam pipes and breached the cryogenic vessel containing the magnets. A large amount of liquid helium entered the vacuum vessel and heated rapidly, breaking several vacuum barriers of the cryostats with a force of up to 56 tons. Ultimately, 30 dipoles and 7 quadrupoles were damaged beyond repair, and another 9 dipoles and 7 quadrupoles required repairs; 9 magnet interconnections were destroyed; 26 magnets were pushed down the tunnel; 276 MJ of energy were dissipated in electrical faults and arcs; 6 tons of helium were lost; and 2.8km of both beam pipes were contaminated with fragments of insulation, with 1km also contaminated with soot from molten copper and insulation. [2]

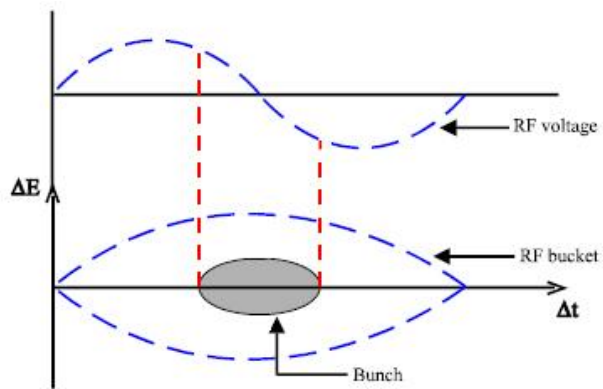


Figure 3.2: Schematic picture of an RF bucket.

3.1.2 The Accelerator Complex

Injection Chain

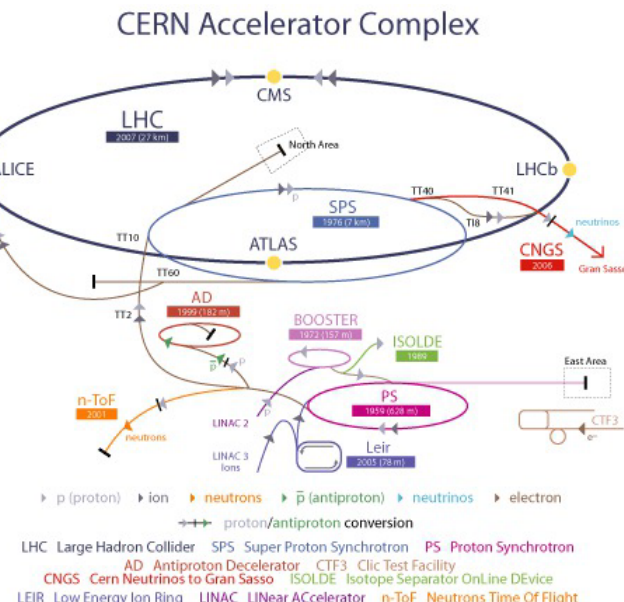


Figure 3.3: The LHC accelerator complex. The proton injection chain begins at LINAC2, proceeding through the booster, PS, and SPS before reaching the LHC. The facility also provides ions to the LHC, as well as a variety of particles to other experiments.

The LHC itself is the last stage of a chain of lower-energy accelerators, shown in figure 3.3 [4]. The staged acceleration chain preserves the high-quality of the beam over many decades of energy. It consists of a linear accelerator and three synchrotrons which were used for previous generations of experiments at CERN. The reuse of the older accelerators is eco-

nomical while still meeting the stringent performance requirements of the LHC, providing up to 2808 proton bunches with a very small transverse emittance, the area occupied by the beam in position-momentum phase space, and controllable longitudinal emittance.

Protons are produced from hydrogen gas using a duoplasmatron source, which strips electrons from protons in a high electric field. After passing through a 90 kV pre-injector, a radio frequency quadrupole (RFQ) focuses and accelerates the protons to 750 kV. A linear accelerator (LINAC2) then accelerates the protons to 50 MeV using RF cavities. The protons then pass through an 80 m-long transfer line into the the Proton Synchrotron Booster (PSB) and Proton Synchrotron (PS).

The PSB consists of four stacked circular synchrotrons, 157 m in circumference, and accelerates the protons to 1.4 GeV. The use of four separate rings mitigates the space charge effects caused by the repulsion of protons within a bunch, which scale as $N_b/(\beta\gamma^2)$, where N_b is the number of protons per bunch. The protons are then injected into the single-ring PS, where the higher injection energy reduces the space charge effect. The RF cavities of the PS, operating at several frequencies, accelerate the beams to 26 GeV, and also split the protons into the bunches eventually inject into the LHC. Nominally, this yields 72 bunches separated by 25 ns, but for Run I, 50 ns spacing was used instead.

The protons are extracted from the PS at intervals of 3.6 s and injected into the third synchrotron in the chain, the 7 km-circumference Super Proton Synchrotron (SPS). Immediately prior to extraction, the bunches are rotated by increasing the RF voltage, reducing the longitudinal emittance in order to ease capture in the SPS RF buckets, which have a frequency of 200 MHz. Up to four PS batches are injected per SPS cycle, after which the particle are accelerated at an average of 78 GeV/s to the LHC injection energy of 450 GeV. Flat-top is maintained for about one second, during which the injection is prepared:

- The magnets used for the beam extraction are ramped, safety checks are performed, and the SPS phase is tuned to match that of the LHC.
- The bunch length is compressed using an RF voltage increase, as in the PS-SPS transfer.
- The tails of the bunches are removed, down to $3-3.5\sigma$.

The SPS cycle takes 21.6 seconds, leading to a total LHC filling time of about nine minutes.

LHC Main Ring

The LHC main ring accelerates protons from the injection energy of 450 GeV to the collision energy, which ranged from 3.5 TeV to 4 TeV for proton-proton collisions during Run I [5]. The 26.7 km ring consists of eight arcs and eight straight sections, shown in figure 3.4. Each straight section is called an *insertion region* (IR), and contain either collider experiments or important services. IRs 1, 2, 5, and 8 contain the ATLAS, LHCb, CMS, and ALICE

experiments, respectively; IR 4 contains two independent 400 MHz RF systems, one for each of the counter-rotating beams; IR 6 contains the beam dump system; and IRs 3 and 7 contain collimation systems. The beams are contained in separate beam pipes except near the collision points.

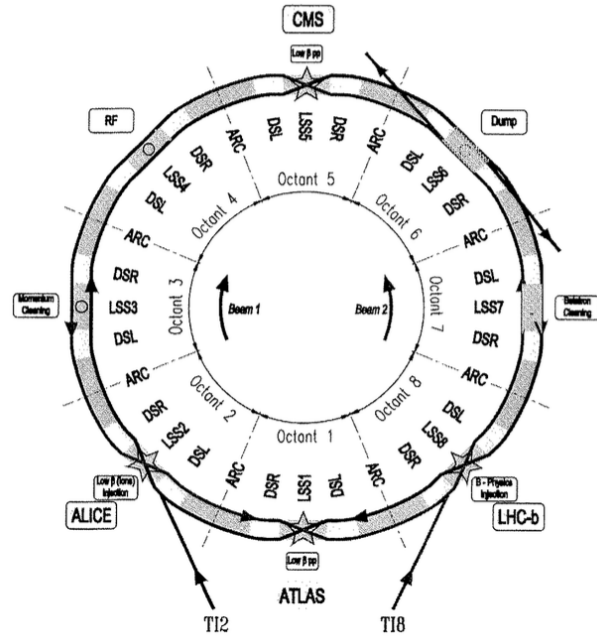


Figure 3.4: Layout of the LHC. The ring consists of eight arcs and eight long straight sections (LSS). Each junction between an arc and a LSS contains a dispersion suppressor cell (DSL, DSR). TI2 and TI8 are the two injection tunnels (“tunnel d’injection”) leading from the SPS to the LHC.

The beams are controlled by over 7,000 magnets. The primary bending and focusing are performed by 1232 superconducting dipole and 392 superconducting quadrupole magnets. The dipole magnets, shown in figure 3.5, have a nominal maximum field of 8.33 T and a length of 15 m. The conducting coils are constructed from Nb-Ti Rutherford cables, and are cooled to 1.9 K using superfluid helium. The dipoles have a double-bore structure, so that a single magnet provides the bending field for both beams.

The acceleration is provided by two superconducting RF systems, one for each beam. The RF cavities are constructed from copper with a thin (1 μm -2 μm) layer of niobium, and operate at 4.5 K. The single-cell cavities, each nominally providing 2 MV, are arranged into cryomodules containing eight cells, for a total peak voltage of 16 MV. A module consisting of two cells is shown in figure 3.6. The RF frequency is 400 MHz, giving an RF bucket length of 2.5 ns, or 75 cm.

At the collision points, the two beams converge in a single pipe for approximately 130 m. A steering dipole directs the beams into collision, and a triplet of quadrupoles on each side

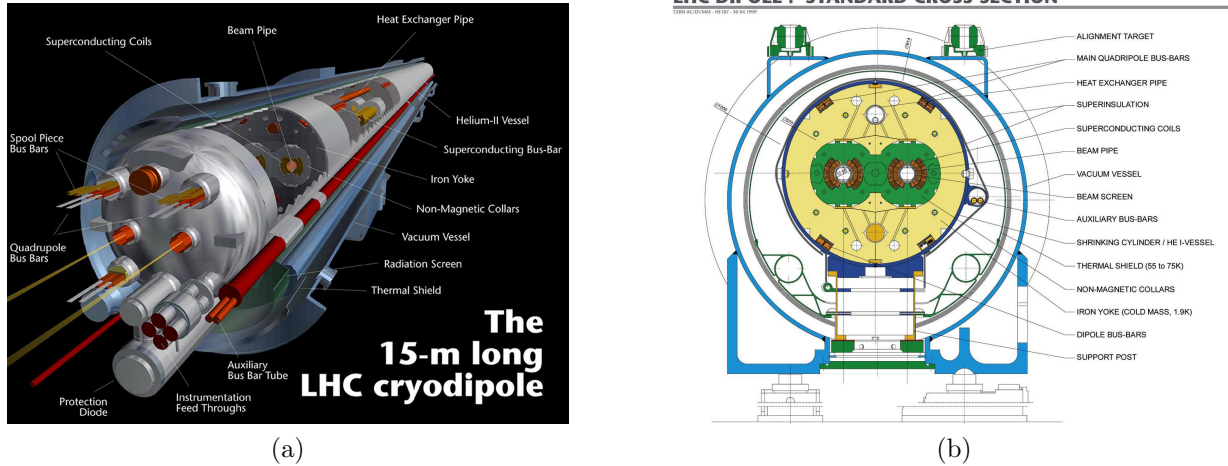
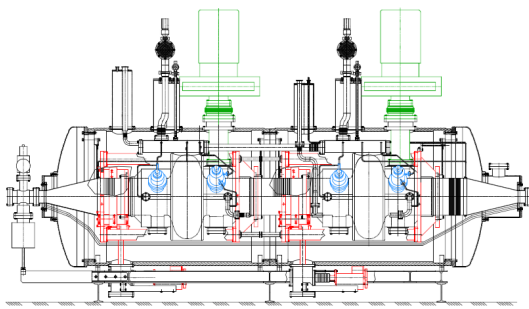


Figure 3.5: Two views of the LHC superconducting dipole magnet. The magnets are 15 m long and have two bores, one for each of the counter-rotating beams.



(a) A prototype cryomodule containing two cavities.



(b) The RF cryomodules installed at IR4.

Figure 3.6: The LHC RF cryomodules.

of the interaction region focus the beam onto the interaction point, squeezing the beams in the transverse directions from a typical orbiting width of $\mathcal{O}(1\text{ mm})$ to a collision width of $\mathcal{O}(10\text{ }\mu\text{m})$.

3.1.3 Beam Parameters

From the experiments' point of view, there are two main parameters to optimize in order to maximize sensitivity to new physics: the collision energy, \sqrt{s} , and the integrated luminosity, $L = \int \mathcal{L} dt$. The collision energy is limited to $\sqrt{s} = 14\text{ TeV}$ by the bending power of the dipole magnets, which have a nominal field strength of 8.33 T; however, due to the faulty splice design mentioned above, the energy was limited to $\sqrt{s} = 7\text{--}8\text{ TeV}$ in Run I.

The optimization of the integrated luminosity is somewhat more complicated. For simplicity, assume that the two beams have the same transverse dimensions. The instantaneous luminosity of two colliding bunches is given by,

$$\mathcal{L} = \frac{f_r N_1 N_2}{4\pi\sigma_x\sigma_y} F(\alpha), \quad (3.1)$$

where $f_r = 11\,245.5\text{ Hz}$ is the LHC revolution frequency; $N_{1,2}$ are the numbers of protons in the two beams; α is the cross angle between the beams; and $\sigma_{x,y}$ are the RMS widths of the beam. $F(\alpha)$ is the reduction in luminosity due to a nonzero beam crossing half-angle of α , given by

$$F(\alpha) = \frac{\cos \alpha}{\sqrt{1 + (\tan \alpha \frac{\sigma_z}{\sigma^*})^2}}, \quad (3.2)$$

where σ_z is the RMS bunch length and σ^* is the transverse beam width at the collision point in the plane of the crossing angle. The RMS widths are determined by two beam parameters: the transverse emittance ϵ_i^2 , defined as the area of the ellipse occupied by the beam in position-momentum space, and β_i^* , which characterizes the focusing of the beams by the quadrupole triplet magnets. Specifically, at a distance z from the collision point, the widths are equal to

$$\sigma_i^2(z) = \epsilon_i \beta_i^* \left(1 + \frac{z^2}{\beta_i^{*2}}\right). \quad (3.3)$$

The total instantaneous luminosity is given by the sum of all colliding bunch pairs. In general, a higher total integrated luminosity is desired. This depends on a number of factors:

- The instantaneous luminosity per bunch, $\mathcal{L} = \frac{f_r N_1 N_2}{4\pi\epsilon_n\beta_*}$. A higher \mathcal{L} increases the number of simultaneous collisions per bunch crossing (*pileup*), $\mu = \mathcal{L}/(f_r\sigma_{\text{inel}})$, where σ_{inel} is the total inelastic proton-proton cross section. A higher amount of pileup degrades the performance of the detectors.

²this is sometimes quoted as the normalized transverse emittance, $\epsilon_n = \epsilon\gamma_b\beta_b$, where γ_b and β_b are the relativistic gamma and beta factors.

- The crossing angle, α . A nonzero crossing angle is required to prevent parasitic collisions between bunches away from the nominal collision point. For bunches spaced by 25 ns, there are 34 unwanted parasitic collision points inside the common beam pipe at each interaction region. The reduction in luminosity is given by equation 3.2; during normal 2012 running conditions, the crossing half-angle was $\alpha = 145 \mu\text{rad}$, and the luminosity reduction factor was about 18%.
- The number of bunches in the LHC, n_b . During Run I, the LHC was filled with 1380 bunches with 50 ns spacing between bunches, as opposed to the nominal 2808 bunches with 25 ns spacing. The advantages of 50 ns spacing include smaller transverse emittances, a smaller cross angle needed to avoid parasitic collisions, and less buildup of electrons in the LHC vacuum (the so-called *electron cloud* effect) [6]. The primary disadvantage is a higher pileup for the experiments.
- The fill schedule of the LHC. The instantaneous luminosity of the LHC decreases over time. The dominant source of the decrease is the loss of protons from the collisions themselves, with a typical decay constant of $\tau_{\text{nuclear},1/e} = 29 \text{ h}$. Luminosity is also lost to emittance growth, caused by sources such as intra-bunch scattering, scattering from collisions with gas in the beam pipe, beam-beam effects, and RF noise. In total, the typical luminosity lifetime is $\tau_L = 14.9 \text{ h}$.

The fill schedule can be optimized to maximize the luminosity based on τ_L and the average turnaround time to refill the LHC after a beam dump, $T_{\text{turnaround}}$. This can be quantified using the *Hübner factor*, HF_{peak} , defined as the ratio of the delivered integrated luminosity to the hypothetical integrated luminosity with $\tau_L = \infty$ and $T_{\text{turnaround}} = 0$. In 2011, this was typically in the range 15%–20%.

Typical values of the beam parameters in 2011 and 2012 are summarized in table 3.1. The delivered luminosity will be discussed in chapter 4.

Parameter	Value in 2011	Value in 2012
Beam energy	3.5 TeV	4 TeV
β^*	1.0 m	0.6 m
Initial ϵ_n	2.6 mm mrad	2.5 mm mrad
$N_{1,2}$	1.5×10^{11}	$1.6\text{--}1.7 \times 10^{11}$
Peak luminosity	$3.6 \times 10^{33} \text{ cm}^{-2} \text{ s}^{-1}$	$7.7 \times 10^{33} \text{ cm}^{-2} \text{ s}^{-1}$
Maximum average pileup	≈ 17	≈ 40
Stored beam energy	$\approx 115 \text{ MJ}$	$\approx 140 \text{ MJ}$

Table 3.1: Summary of typical beam parameters in 2011 and 2012 [7].

3.2 The ATLAS Experiment

The ATLAS detector [8] is a large, cylindrical collider detector located at IR1 on the LHC ring (figure 3.1). The detector measures the energy and momenta of particles produced in the collisions provided by the LHC. It consists of several subsystems occupying a cylinder with a diameter of 25 m and a length of 46 m, with a combined weight of approximately 7,000 tons. Closest to the interaction region, the inner detector measures the momenta of charged particles by tracking their movement through a solenoidal magnetic field. Outside the inner detector solenoid magnet, electromagnetic and hadronic calorimeters measure the energy of electrons, photons, and hadrons. Finally, the muon spectrometer provides additional tracking and particle identification for muons in large toroidal magnetic field.

This section describes the design of the magnets, inner detector, calorimeters, and muon spectrometer. The reconstruction of physics objects from the detector measurements is described in chapter 5.

3.2.1 Coordinate System

The ATLAS detector uses a right-handed coordinate system, with \hat{x} pointing from the interaction point towards the center of the LHC ring, \hat{y} pointing up, and \hat{z} pointing along the ring towards IR2. Due to the symmetry of the detector, cylindrical coordinates (r, θ, ϕ) are often used, with r the transverse distance from the beam line, θ the polar angle from the beamline, and ϕ the azimuthal angle in the x - y plane. The polar angle can also be expressed in term of the pseudorapidity, $\eta = -\log \tan \frac{\theta}{2}$, which is useful for describing the geometry of particles in part because differences in pseudorapidity, $\Delta\eta$, are invariant under longitudinal Lorentz boosts along \hat{z} . For massless particles, the pseudorapidity is equal to the rapidity, $y = \frac{1}{2} \log \frac{E+p_z}{E-p_z}$.

3.2.2 Magnets

ATLAS relies on four powerful superconducting magnets to bend the trajectories of charged particles, allowing the tracking detectors to provide measurements of their momenta. The solenoid provides a 2 T axial magnetic field in the volume of the inner detector, with particle trajectories bending in the R - ϕ plane. The barrel and two end-cap toroids provide a toroidal magnetic field ranging from 0.5–1 T for the muon spectrometer, with bending in the R - z plane. The geometry of the magnets is shown in figure 3.7. Key parameters for the magnet system are shown in table 3.2.

Solenoid

The central solenoid, shown in figure 3.8, occupies the volume between the inner detector and the electromagnetic calorimeter, with an inner radius of 2.46 m, an outer radius of 2.56 m, and a length of 5.8 m. The single coil has 1154 windings made of high strength Al-stabilized

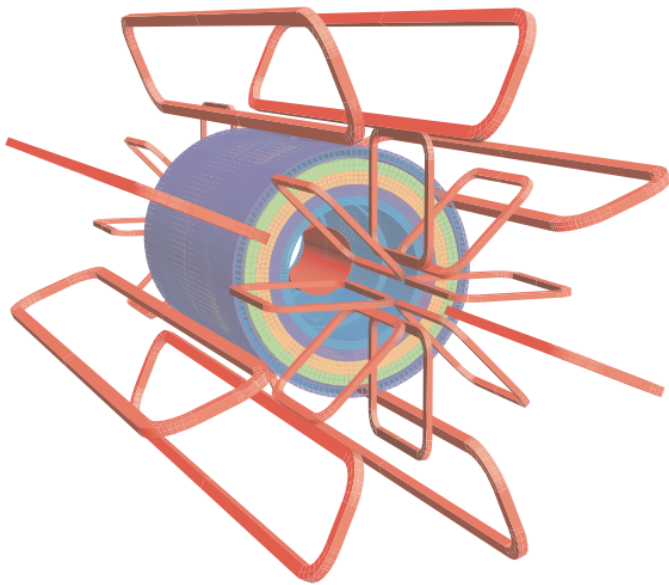


Figure 3.7: The geometry of the magnet windings and tile calorimeter steel. The three toroids and solenoid are shown in red. The remaining colors show layers of the tile calorimeter with different magnetic properties and an outside return yoke [9].

Property	Feature	Unit	Solenoid	Barrel toroid	End-cap toroids
Size	Inner diameter	m	2.46	9.4	1.65
	Outer diameter	m	2.56	20.1	10.7
	Axial length	m	5.8	25.3	5.0
	Number of coils		1	8	2×8
Mass	Conductor	t	3.8	118	2×20.5
	Cold mass	t	5.4	370	2×140
	Total assembly	t	5.7	830	2×239
Coils	Turns per coil		1154	120	116
	Nominal current	kA	7.73	20.5	20.5
	Magnet stored energy	GJ	0.04	1.08	2×0.25
	Peak field in the windings	T	2.6	3.9	4.1
	Field range in the bore	T	0.9-2.0	0.2-2.5	0.2-3.5

Table 3.2: Main parameters of the ATLAS magnet system [8].

NbTi conductor. With a nominal current of 7.73 kA, the magnetic field is 1.998 T at the center of the solenoid, falling to 1.8 T at $z = 1.7$ m and 0.9 T at the end of the inner detector cavity. The magnetic flux is returned via the steel in the hadronic calorimeter and its support structures. Liquid helium is used to cool the superconducting coil to an operating temperature of 4.5 K. At nominal current, the stored energy is 40 MJ.

The longitudinal and radial magnetic field components are shown for different R and z values in figure 3.9a.



Figure 3.8: The central solenoid in the factory after completion of the coil winding [9].

Toroid

The magnetic field for the muon spectrometer is provided by three large toroid magnets, each with eight superconducting coils. The magnets are shown in figure 3.10. The barrel toroid measures 25.3 m in length, with inner and outer diameters of 9.4 m and 20.1 m, respectively. The two end-cap toroids are 5.0 m in length, with inner and outer diameters of 1.65 m and 10.7 m, respectively. Both types of toroid contain eight coils, with 120 windings per coil in the barrel and 116 windings per coil in the end-caps. The end-cap coils are rotated by 22.5° from the barrel coils to optimize the bending power in the overlap region between the magnets. Like the solenoid, the conductor is Al-stabilized NbTi, operated at 4.5 K. The nominal current is 20.5 kA, producing a magnetic field that varies from 0.15 T to 2.5 T in the barrel region, and 0.2 T to 3.5 T in the end-caps. The total stored energy at nominal current is 1.58 GJ.

The field integral of the toroid is shown as a function of η in figure 3.9b. The field integral drops at the boundary between the barrel and end-caps, where the fields from the two magnets partially cancel.

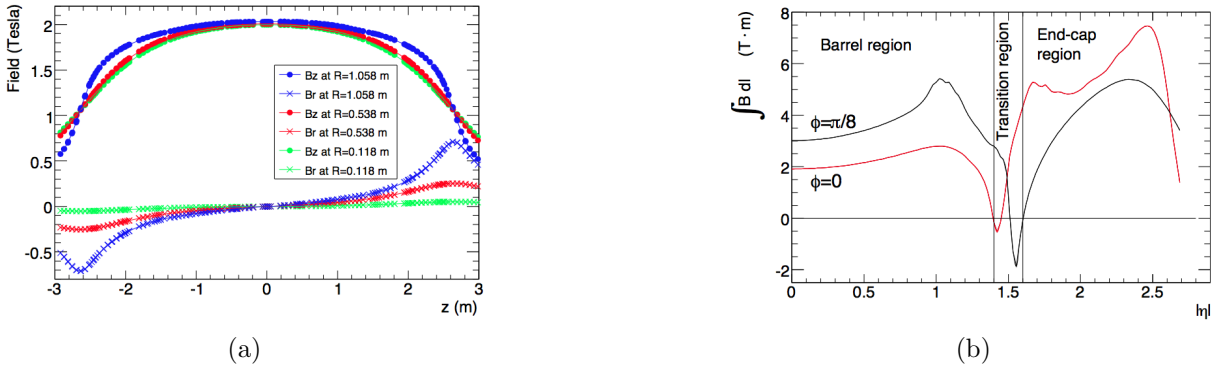


Figure 3.9: Left: the solenoid magnetic field in the radial (B_r) and longitudinal (B_z) directions, shown as a function of z for $\phi = 20\pi/16$ at different values of R . The field determined from a fit of the field model to measurements using an array of Hall probes [10]. Right: The predicted toroid magnetic field integral as a function of $|\eta|$. The integral is taken over a straight line through the interaction point, from the innermost to the outermost muon detector.

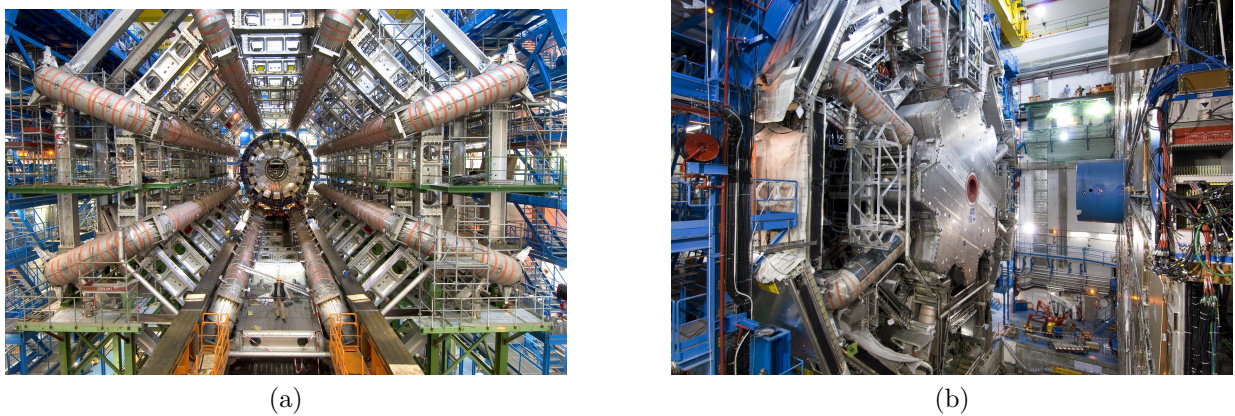


Figure 3.10: Images of the barrel (left) and end-cap (right) toroid magnets during installation [9].

3.2.3 Inner Detector

The inner detector performs tracking of charged particles traversing the 2 T solenoidal magnetic field in the pseudorapidity range $|\eta| < 2.5$. It also performs electron identification in the range $|\eta| < 2.0$. It consists of three subdetectors occupying the volume closest to the interaction region, directly outside the beam pipe, as shown in figure 3.11. Proceeding outwards from the interaction point, these are the pixel detector, the semiconductor tracker (SCT), and the transition radiation tracker (TRT). The pixel detector provides three track measurements with high spatial resolution using silicon pixels. The SCT provides an additional four measurements using silicon strips. Finally, for particles with $|\eta| < 2.0$, the TRT provides an average of 36 measurements per track using gas-filled straw tubes, which aids the pattern recognition and improves the momentum resolution. The use of transition radiation also enables the TRT to perform electron identification. Examples of trajectories of 10 GeV particles through the barrel and end-cap layers are shown in figure 3.12.

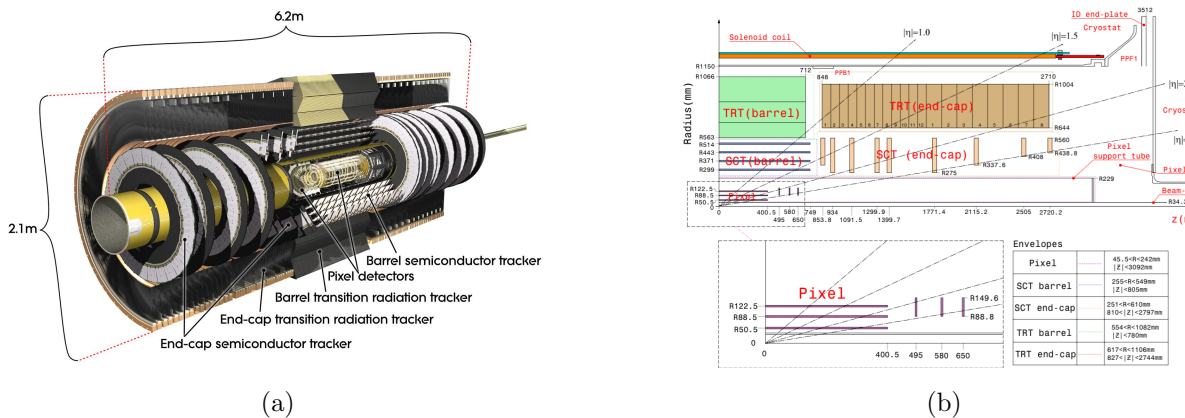


Figure 3.11: Left: 3D model of the inner detector, showing the arrangement of the pixel detector, SCT, and TRT in the barrel and end-caps. Right: layout of the inner detector in the $R - z$ plane.

Pixel Detector

The pixel detector consists of 1744 identical pixel sensors, each measuring $19 \times 63 \text{ mm}^2$ and containing $144 \times 328 = 47232$ pixels, for a total of 80.4×10^6 pixels. The size of the pixels is dictated by the front-end electronics: in 128 of the 144 columns, the pixels have a pitch of $50 \times 400 \mu\text{m}^2$, while the remaining 16 columns have a pitch of $50 \times 600 \mu\text{m}^2$. For space reasons, eight pairs of pixels in each column are ganged to a common readout, giving a total of 46080 readout channels per sensor.

The sensors are $256 \mu\text{m}$ -thick detectors utilizing n -in- n technology, constructed from n -type wafers with high dose positive (p^+) and negative (n^+) dose regions implanted on each

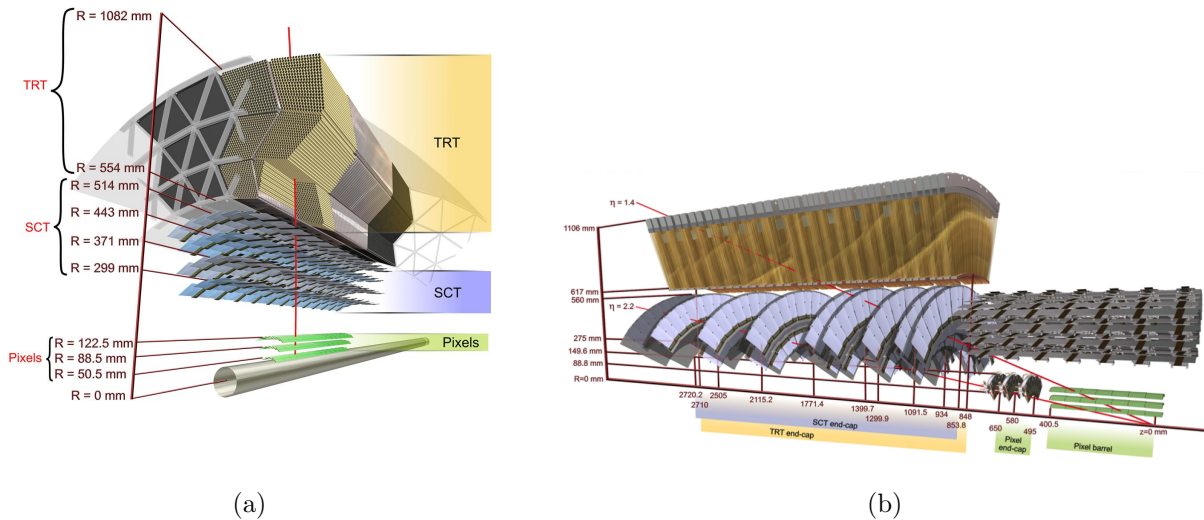


Figure 3.12: Drawings of the inner detector sensors and structural elements traversed by 10 GeV charged particles originating from the interaction point at various angles. Trajectories of particles traversing the barrel elements at $\eta = 0.3$ (left) and both the barrel and end-cap elements at $\eta = 1.4$ and $\eta = 2.2$ (right) are shown.

side of a wafer. Initially, the asymmetric depletion region at the $p^+ - n$ junction is operated in reverse bias with a voltage of 150 V, and fills the sensor bulk volume, shown in figure 3.13a. The charge carriers generated by the passage of an ionizing particle through the bulk are collected at the n^+ side of the sensor, where the readout electronics are bump-bonded to the pixel. The nominal threshold for readout is about 3,500 electrons, while a minimally ionizing particle crossing a pixel at normal incidence produces a signal of about 20,000 electrons. A “hit” is recorded if the signal exceeds the threshold, and the pulse height is measured using a time-over-threshold (ToT) technique. Over time, radiation damage induces type inversion in the bulk, after which the junction moves to the n^+ side of the sensor and the depletion zone grows from the pixel side, as shown in figure 3.13b. The double-sided construction thus allows the pixel sensors to continue operating after type inversion.

The pixel sensors are assembled into pixel modules, shown in figure 3.14. Each module contains 16 front-end electronics chips each with 2880 electronics channels. The front-ends are bump bonded to the pixel sensor elements. The other side of the pixel sensor tile is glued to a flexible polyimide printed circuit board (*flex-hybrid*) that houses the module control chip.

The layout of the pixel detector is summarized in table 3.3. The modules are assembled into staves in the barrel region, each with 13 pixel modules, and sectors in the end-caps, each with 6 pixel modules. The barrel layers consist of 22, 38, and 52 staves for layers 0, 1, and 2, respectively, while the end-caps each contain eight sectors³. In the barrel, to provide

³During the shutdown following Run I, a fourth layer of barrel pixel detectors, known as the insertable

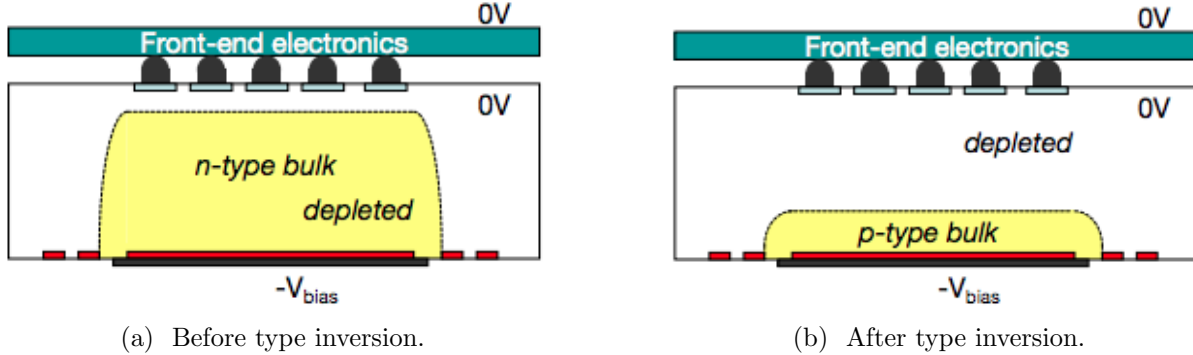


Figure 3.13: Comparison of depletion zones in n^+ -in- n pixel sensors before and after type inversion. Before type inversion, the electrical field grows from the bottom side, reaching the pixel implants at full depletion. After type inversion, the depletion zone grows from the pixel side, allowing operation even if the bulk is not fully depleted.

complete coverage, the pixel staves overlap and are mounted with a tilt angle of 20° between the normal to the module surface and \hat{r} , in the $\hat{\phi}$ direction.

In the barrel, the pixels have an intrinsic accuracy of $10\text{ }\mu\text{m}$ in the $R - \phi$ direction and $115\text{ }\mu\text{m}$ in the z direction, while in the end-caps, the intrinsic accuracy is $10\text{ }\mu\text{m}$ in the $R - \phi$ direction and $115\text{ }\mu\text{m}$ in the R direction.

Barrel	Radius (mm)	Staves	Modules	Pixels
Layer-0	50.5	22	286	13.2×10^6
Layer-1	88.5	38	494	22.8×10^6
Layer-2	112.5	52	676	31.2×10^6
End-cap (one side)	z (mm)	Sectors	Modules	Pixels
Disk 1	495	8	48	2.2×10^6
Disk 2	495	8	48	2.2×10^6
Disk 3	495	8	48	2.2×10^6
Barrel and both end-caps			1744	80.4×10^6

Table 3.3: Parameters of the pixel detector [8].

SCT

The SCT consists of 15912 sensors using single-sided, p -in- n type silicon strips. The use of single-sided strips lowers both the cost and the number of readout channels of the detector, which covers significantly more area than the pixel detector (61.1 m^2 versus 2.3 m^2). In the

B-layer (IBL), was added between the beam pipe and the innermost pixel layer. The data used in this dissertation predate the inclusion of the IBL.

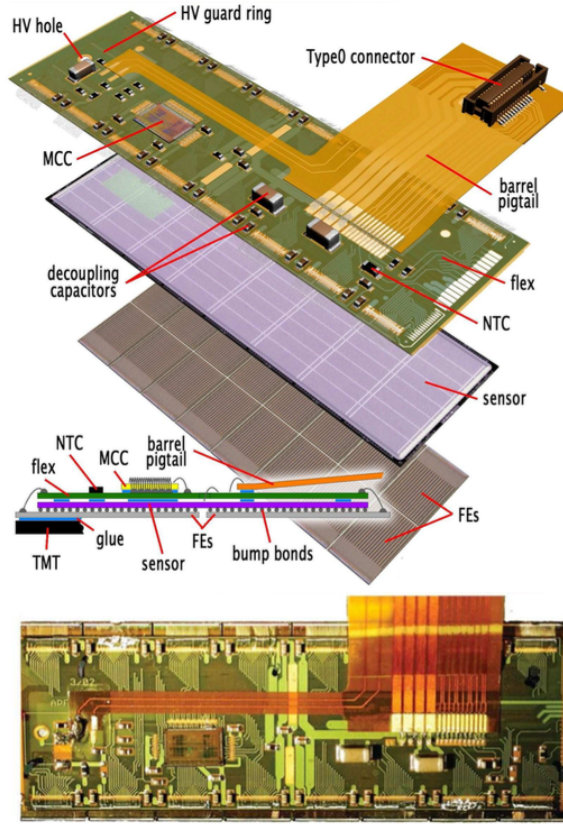


Figure 3.14: Schematic pictures of a barrel pixel module. The top diagram shows the assembly of a module, consisting of the front-end electronics chips (FEs), the pixel sensor elements, and the flex-hybrid, which bears the module control chip (MCC) and NTC thermistors. The bottom is a photograph of a barrel pixel module.

barrel, the strips have a pitch of $80\text{ }\mu\text{m}$ and a length of 12 cm. In the end-caps, the sensors are trapezoidal with radially arranged strips, with a mean strip pitch of $80\text{ }\mu\text{m}$ and a length of 12 cm. Each sensor has 768 active strips. Like the pixel sensors, the operating voltage is initially $\sim 150\text{ V}$, but will require an increase to $250\text{ V}-350\text{ V}$ after several years of irradiation, depending on the location of the sensor.

SCT barrel and end-cap modules are shown in figure 3.15. The 2112 barrel modules contain four sensors, while the 1976 end-cap modules contain two sensors. In both cases, the sensors are glued to a $380\text{ }\mu\text{m}$ -thick thermal pyrolytic graphite (TPG) base-board. The sensors are assembled in two layers with a rotation of $\pm 20\text{ mrad}$ about the center of the sensors. The stereo angle between the two sensors allows for a measurement of the position along the length of the sensors.

The intrinsic accuracy of the SCT sensors is $17\text{ }\mu\text{m}$ along the strip pitch, corresponding

to the $R - \phi$ direction. Along the length of the strips, the stereo angle allows for position measurement with an accuracy of $580\text{ }\mu\text{m}$, corresponding to the z direction in the barrel and the R direction in the end-caps.

Barrel layer	Radius (mm)	Length (mm)	Module tilt angle	Number of modules
3	299	1498	11.00°	384
4	371		11.00°	480
5	443		11.25°	576
6	514		11.25°	672

Table 3.4: The dimensions and arrangement of modules in the four SCT layers. The tilt angle is between the normal to the module surface and \hat{r} , in the $\hat{\phi}$ direction.

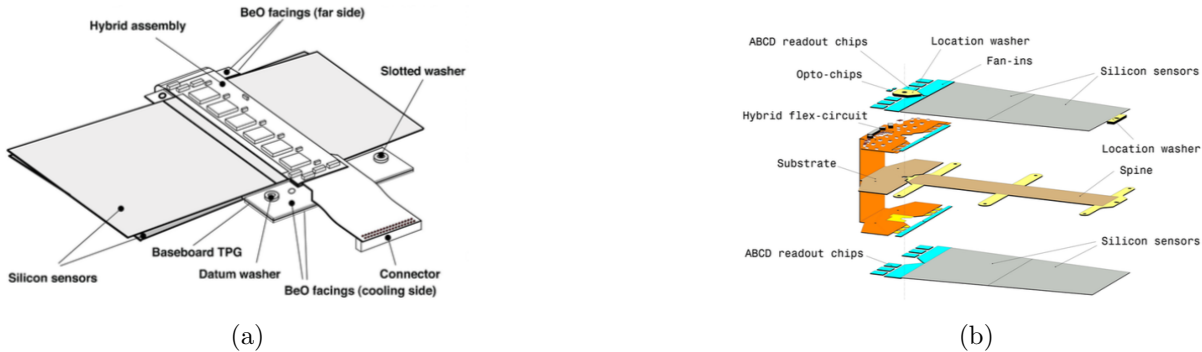


Figure 3.15: Diagrams of the SCT barrel (left) and end-cap (right) modules.

TRT

The TRT detector elements are polyimide drift (straw) tubes. A charged particle traversing a straw ionizes the gas along its trajectory, and the resulting electrons are drawn to the axial anode wire. The primary electrons induce an avalanche due to the high electric field in the straw, and the resulting signal is read out from the end of the straws. The straws are arranged such that charged particles with $p_T > 500\text{ MeV}$ and $|\eta| < 2.0$ traverse at least 36 straws, except in the barrel/end-cap transition region where particles traverse as few as 22 straws. The intrinsic resolution of the straws is $130\text{ }\mu\text{m}$ in the transverse direction, with no measurement provided in the z direction.

In addition to measuring particle trajectories, the TRT also uses transition radiation to distinguish electrons from charged hadrons. Charged particles crossing between materials with different dielectric constants emit transition radiation photons with probability proportional to $\gamma = \frac{E}{m}$. In the TRT, the transition radiation is produced by interleaving the straws with polypropylene fibers in the barrel and polypropylene foils in the end-caps to provide transition radiation. Consequently, particles can produce a stronger, “high-threshold” signal

in the straw tubes, with much greater probability for electrons than hadrons. Electrons typically leave 7-10 high-threshold hits.

The straws measure 4 mm in diameter and 144 cm (37 cm) in length in the barrel (end-caps). The straw walls consist of two 35 μm aluminum-coated polyimide films bonded back-to-back. The anodes of the detectors are gold-plated tungsten wires running down the axis of the tubes, with 31 μm diameter. The wires are supported at the end of the straw by an end plug, where they connect to the front-end electronics. At the middle of the straw, the wires are supported by a plastic insert, and are also split electrically by a fused glass capillary to reduce occupancy. The active length of each half of the wire is 71.2 cm, with a 2 cm inefficient section at the middle. The straws are filled with a mixture of 70% Xe, 27% CO₂, and 3% O₂. With a cathode voltage of -1530 V , the gain in the straws is 2.5×10^4 .

The layout of the straws in the barrel and end-caps is summarized in table 3.5. In the barrel, the straws are arranged into three layers of modules as shown in figure 3.16, with different dimensions and straw counts depending on the layer. The straws are interleaved with transition radiation material, polypropylene fibers measuring 19 μm in diameter. The module shell is made from 400 μm thick carbon fiber, and serve not only as a support structure, but also as a gas manifold for CO₂, which prevents high-voltage discharges, flushes any Xe leaking from the straws, and conducts heat away from the straws.

The end-caps consist of 160 layers of 768 straws, arranged radially into 20 wheels with 8 layers each. The inner 12 wheels (type-A) are spaced 8 mm in z , while the outer 8 wheels (type-B) are spaced by 15 mm. Each successive layer in a wheel is separated by a 15 μm thick polypropylene radiator foil, and is rotated by 3/8 of the azimuthal straw spacing to optimize the uniformity of the number of straw crossed.

	z (mm)	R (mm)	Modules	Layers	Straws/Module
Barrel (both sides)	0-780	554-1082	96	73	52544
Type-1 module (inner)	400-712.1	563-624		9	
Type-1 module (outer)	7.5-712.1	625-694	32	10	329
Type-2 module	7.5-712.1	697-860	32	24	520
Type-3 module	7.5-712.1	863-1066	32	30	793
End-cap (one side)	827-2744	615-1106	20	160	122880
Type-A wheels	848-1705	644-1004	12	8	6144
Type-B wheels	1740-2710	644-1004	8	8	6144

Table 3.5: Layout and straw counts of the TRT barrel modules and end-cap wheels. The totals for the barrel and end-caps, shown in bold, include services and electronics.

3.2.4 Calorimetry

The calorimeter system occupies the volume directly exterior to the solenoid magnet, and measures the energy of electrons, photon, and hadrons up to a pseudorapidity of $|\eta| = 4.9$.

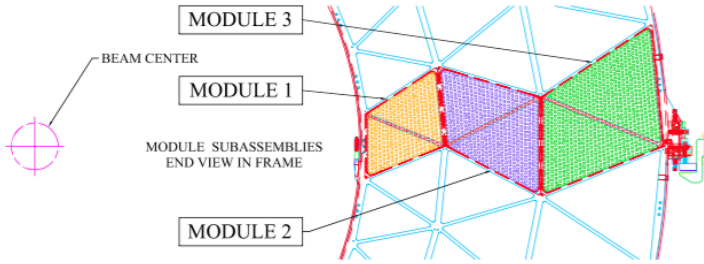


Figure 3.16: Layout of the TRT barrel modules in the $R\text{-}\phi$ plane.

The system consists of a number of independent sampling calorimeters, shown in figure 3.17. Each calorimeter contains alternating layers of dense absorber material, which induces particle showers from incoming particles, and active material, which measures the energy of the secondary particles in the showers. The active layers typically measure only few percent of the initial particle's energy, so the energy measurement must be calibrated based on particles of known energy.

The electromagnetic calorimeter measures the energy of electrons and photons using lead and liquid argon (LAr) to measure the energy of electrons and photons. The hadronic calorimeter measures the energy of hadrons using steel and scintillator tiles in the barrel and copper and LAr in the end-caps. Finally, electromagnetic and hadronic calorimetry is performed in the forward region using copper-LAr and tungsten-LAr technology. Besides performing energy measurements, the calorimeters stop electrons, photons, and hadrons, providing shielding for the muon spectrometer. The total amount of material in front of and in the calorimeters is shown in terms of radiation lengths, X_0 , and interaction lengths, λ , in figures 3.18 and 3.19.

Electromagnetic Calorimeter

The electromagnetic calorimeter consists of two half-barrels ($0 < \eta < \pm 1.475$), two end-caps ($\pm 1.375 < \eta < \pm 3.2$), and a presampler ($|\eta| < 1.8$). The half-barrels and end-caps use LAr as the active material and steel-clad lead plates as the absorber. The lead plates are arranged in an accordion geometry to provide a uniform, gapless coverage in ϕ , shown for a barrel module in figure 3.20. The plates are interleaved with electrodes built from copper etchings on polyimide, consisting of three conducting layers. The outer conductive layers of the electrodes distribute the 2 000 V high voltage over the electrode surface, which drifts the charges induced by ionization in the LAr towards the electrodes with a drift time of 450 ns. The inner layer of the electrode, separated from the outer layers by isolating foils, collects the signals via capacitive coupling.

The two half-barrels occupy the region $1.4 \text{ m} < R < 2 \text{ m}$ and $0 \text{ m} < z < \pm 3.2 \text{ m}$, which covers up to $|\eta| < 1.52$ depending on the layer. Each half-barrel has 1024 lead plates with a thickness of 1.53 mm for $|\eta| < 0.8$ and 1.13 mm for $|\eta| > 0.8$. The cells are divided into

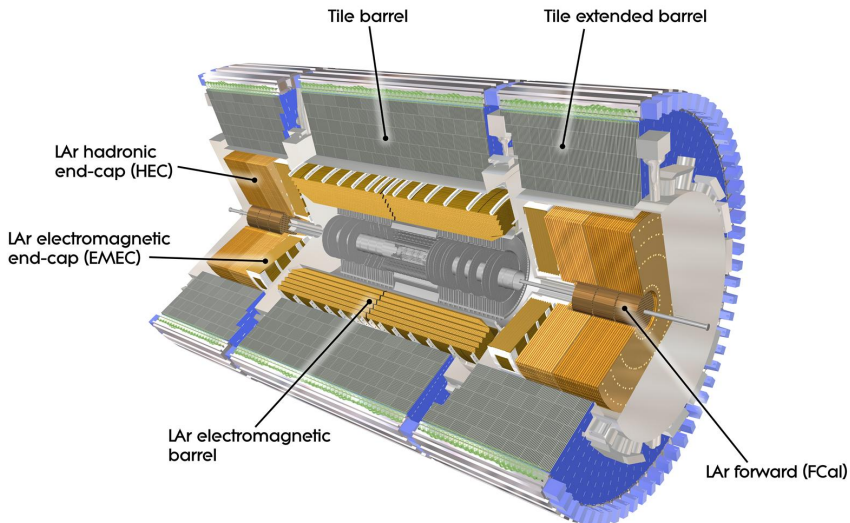


Figure 3.17: A 3D model of the ATLAS calorimeters, showing the electromagnetic barrel and end-caps, hadronic barrel and end-caps, and the forward calorimeter.

three layers, and have variable size in η and ϕ :

- The first layer is finely segmented in η to improve the spatial resolution; this improves the particle identification, helps resolve nearby particles (in particular photon pairs from π^0 decays), and, in combination with the second layer, allows for a measurement of the polar angle of electromagnetic showers. The majority of the cells measure $\Delta\eta \times \Delta\phi = 0.025/8 \times 0.1$. Cells in the barrel-end-cap overlap region, $1.40 < |\eta| < 1.475$, have a coarser granularity of $\Delta\eta \times \Delta\phi = 0.025 \times 0.025$.
- The second layer absorbs most of the energy of the electromagnetic showers. Most of the cells have size $\Delta\eta \times \Delta\phi = 0.025 \times 0.025$, except for cells with $1.40 < |\eta| < 1.475$, which measure $\Delta\eta \times \Delta\phi = 0.075 \times 0.025$.
- The third layer absorbs the tails of electromagnetic showers, and has a coarse granularity of $\Delta\eta \times \Delta\phi = 0.050 \times 0.025$.

The number of radiation lengths presented by each layer is shown in figure 3.18c.

The end-caps, one on either side of the interaction region, measure 63 cm in thickness with inner and outer radii of 33 cm and 209.8 cm, respectively. Each end-cap consists of 1024 lead absorbers with the same accordion geometry as used in the barrel. In the region $1.5 < |\eta| < 2.5$, the end-caps present three layers in the longitudinal direction, with fine η segmentation in the front layer. At $|\eta| = 1.5$, the granularity of each layer is the same as in the barrel, becoming coarser in the first layer with increasing $|\eta|$. Elsewhere, there are

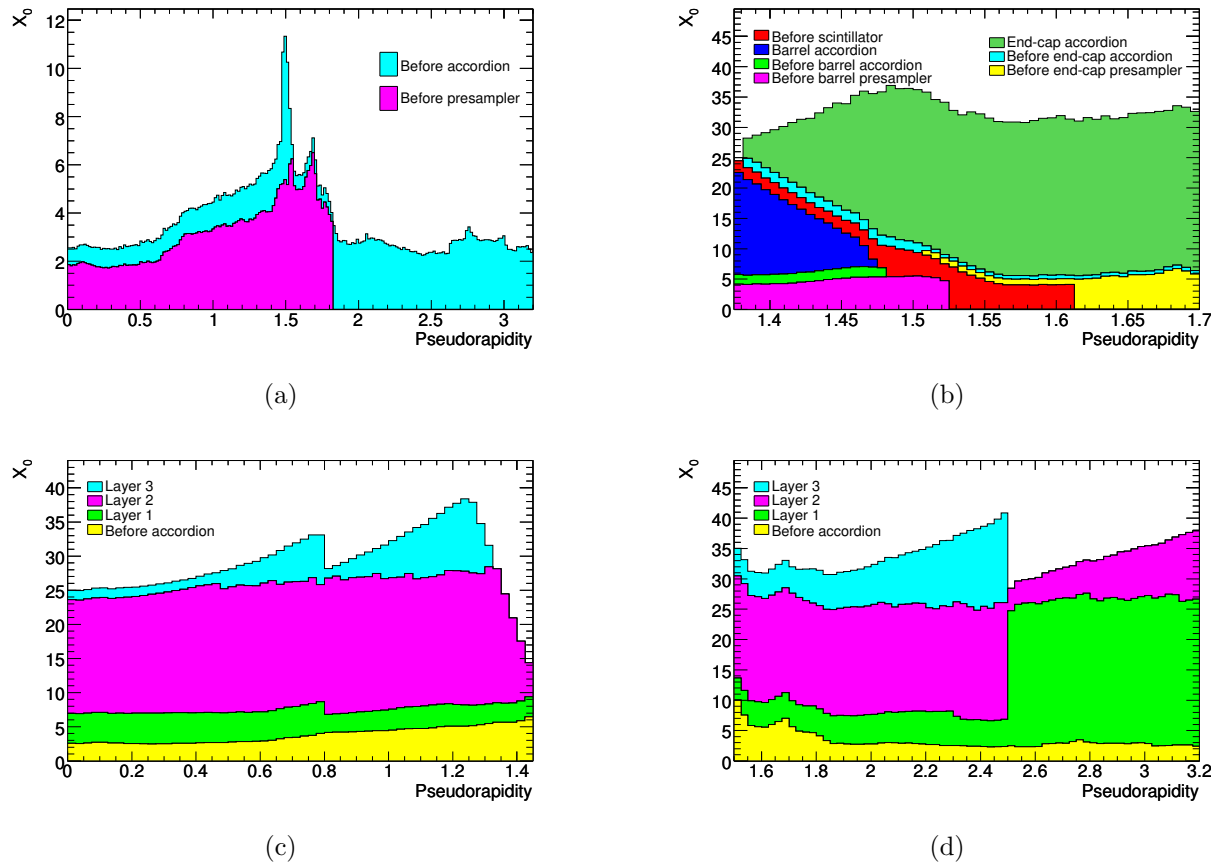


Figure 3.18: Cumulative amounts of material versus $|\eta|$ in front of and within the LAr electromagnetic calorimeter, in terms of radiation lengths, X_0 . (a) show the material before the calorimeters. (b) shows the material in the crack region between the barrel and end-cap cryostats. (c) shows the material in and before the barrel LAr calorimeter. (d) shows the material in and before the end-cap LAr calorimeters.

two longitudinal layers with coarser transverse granularity. Figure 3.18c shows the number of radiation lengths in each layer of the end-cap.

Finally, the presampler is an instrumented layer of LAr installed in front of the first layer calorimeter, with a thickness of 11 mm in the barrel ($|\eta| < 1.5$) and 2×2 mm in the end-caps ($1.5 < |\eta| < 1.8$). The presampler is sensitive to energy lost due to interactions with material between the interaction region and the calorimeters (the beam pipe, inner detector, solenoid, cryostates, and other services and support structures). The total amount of material in front of the the electromagnetic calorimeters is shown in figures 3.18a and 3.18b in terms of radiation lengths, X_0 . The cells have a granularity of $\Delta\eta \times \Delta\phi = 0.025 \times 0.1$.

In total, the electromagnetic calorimeter has 101,760 readout channels for the barrel, 62,208 channels for the end-caps, 7,808 channels for the barrel presampler, and 1,536 channels

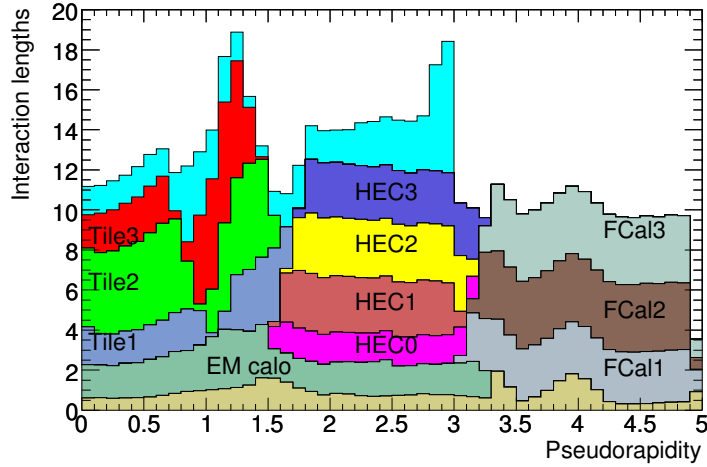


Figure 3.19: Cumulative amounts of material versus $|\eta|$ due to each calorimeter in terms of interaction lengths, λ . The material in front of the calorimeters is also shown in tan.

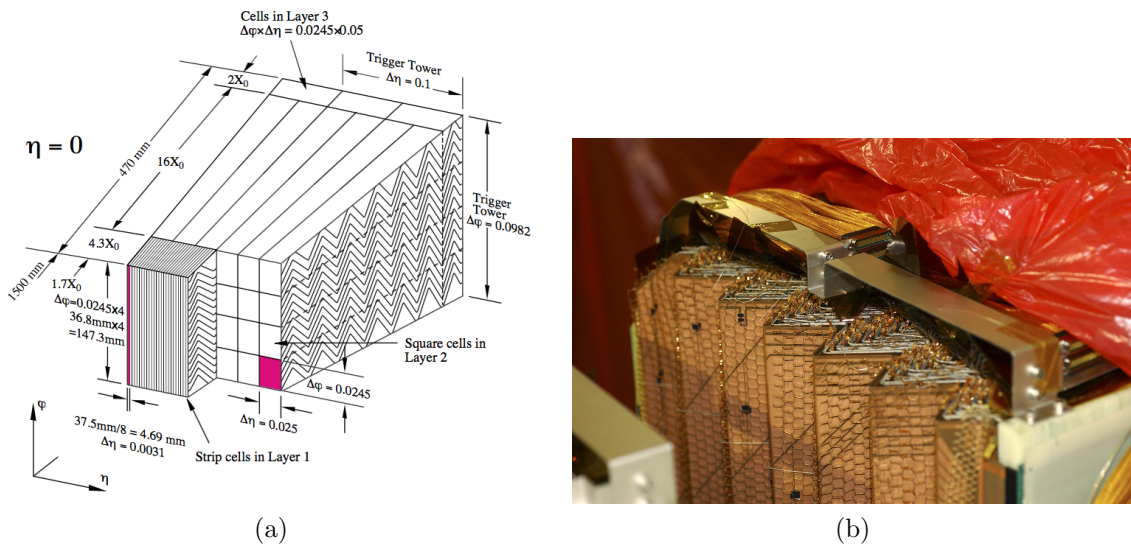


Figure 3.20: The LAr calorimeter uses an accordion geometry to provide uniform coverage in ϕ . Steel-clad lead plates are interleaved with electrodes, consisting of three copper layers separated by polyimide sheets. (a) shows a schematic drawing of a LAr barrel module, illustrating the accordion geometry and the three layers in depth, with fine segmentation in η in the layer closest the interaction point. (b) shows a photograph of the accordion geometry.

for the end-cap presamplers. The energy resolution of the calorimeter is parametrized as:

$$\frac{\sigma(E)}{E} = \frac{a}{\sqrt{E}} \oplus \frac{b}{E} \oplus c, \quad (3.4)$$

where a , b , and c are the sampling, noise, and constant terms, respectively, and generally vary with η . The design value of the sampling term is 9–10% GeV $^{1/2}$ in the central region, and worsens at higher pseudorapidities due to the increased material in front of the calorimeters. The noise term, due to electronics noise and pileup effects, is approximately $b = 350 \times \cosh \eta$ MeV. The constant term dominates the resolution at high energies, with a design value of $c = 0.7\%$.

Tile Calorimeter

The tile calorimeter measures the energy of hadrons in the region $|\eta| < 1.7$, occupying the radial range $2.28 \text{ m} < R < 4.25 \text{ m}$. Divided into a 5.8 m-long central barrel and two 2.6 m-long extended barrels on either side, it uses steel as the absorber and scintillating tiles as the active material. The total depth is approximately 7.4λ .

Each of the three calorimeter sections is divided azimuthally into 64 modules, each spanning $\Delta\phi = 5.625$. A module is shown schematically in figure 3.21a. The outer edge of a module is a steel girder which houses the tile calorimeter readout electronics and also provides flux return for the solenoidal magnetic field. The body of the module is a self-supporting structure built from steel absorber plates, with 4 mm-thick spacer plates glued in staggered fashion to 5 mm-thick master plates. The staggered spacing creates the gaps into which the scintillating tiles are inserted, with a steel-to-scintillator volume ratio of approximately 4.7 : 1.

The scintillating tiles use polystyrene as the base material, in which ionizing particles induce the production of ultraviolet light. The polystyrene is doped with wavelength-shifting fluors, 1.5% PTP and 0.044% POPOP, which convert the scintillation light into the visible light. The tiles measure 3 mm thick, and vary between 97 mm and 187 mm in radial length and 200 mm and 400 mm in azimuthal length. A plastic sleeve envelops each tile, both for the protection of the tile during installation and also to improve the scintillation light collection efficiency due to a reflectivity of $\sim 95\%$. At the tile edges, wavelength-shifting fibers transmit the light to photomultiplier tubes housed in the girder. The grouping of the fibers determines the readout cell size, as shown in figure 3.21b; the cells measure $\Delta\eta \times \Delta\phi = 0.1 \times 0.1$ in the transverse direction, and are segmented into three layers longitudinally corresponding to depths of approximately 1.5λ , 4.1λ , and 1.8λ .

Hadronic End-Cap Calorimeters

Two hadronic end-cap calorimeters (HEC) perform hadronic calorimetry in the pseudorapidity range $1.5 < |\eta| < 3.2$. The HECs use copper and LAr arranged into a flat plate geometry, as shown in figure 3.22. Each HEC consists of two wheels (HEC1 and HEC2),

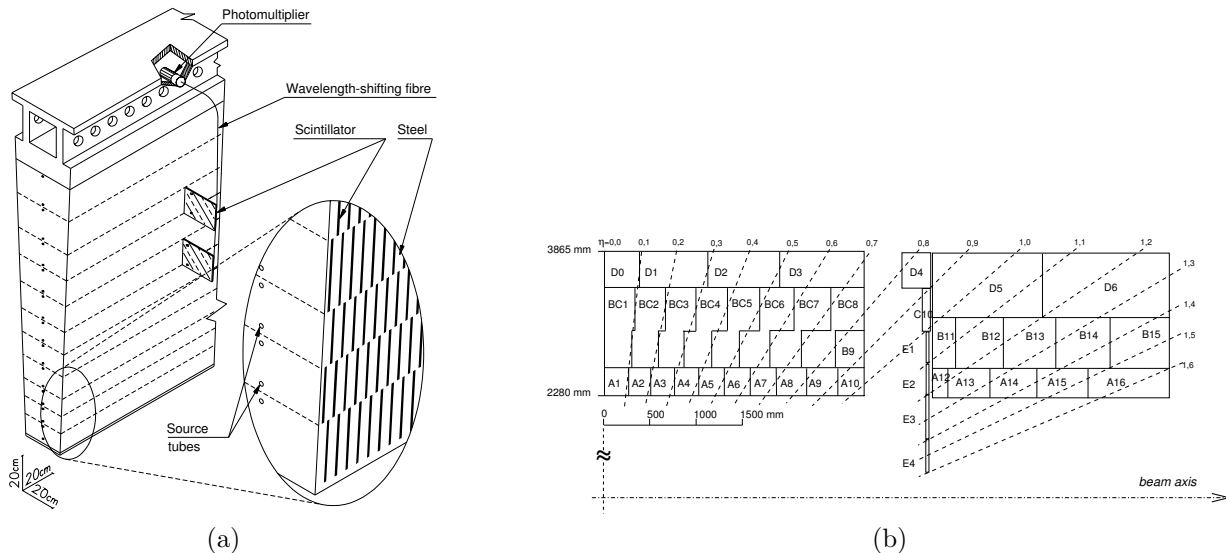


Figure 3.21: Left: Schematic view of a tile calorimeter module, showing assembly of the steel absorber, the inserted scintillator tiles, and the readout of lighting through wavelength-shifting fibers to the photomultiplier tubes. Right: Layout of the tile calorimeter cells, defined by the grouping of the readout fibers connecting the scintillating tiles to the photomultiplier tubes.

which are further divided into two longitudinal segments. The plates have an inner radius of 372 mm or 475 mm depending on z , and an outer radius of 2030 mm. HEC1 contains 24 copper plates, each 24 mm thick and spaced by 8.5 mm, plus a 12.5 mm-thick front plate. HEC2 contains 16 copper plates measuring 50 mm in thickness, with a 25 mm-thick front plate. The sampling fractions are thus 4.4% for HEC1 and 2.2% for HEC2.

The gaps contain 3 electrodes spaced by 1.8 mm, the outer two of which supply a nominal operating voltage of 1800 V, and the middle of which performs the readout. The readout pads provide a transverse segmentation of $\Delta\eta \times \Delta\phi = 0.1 \times 0.1$ for $|\eta| < 2.5$, and $\Delta\eta \times \Delta\phi = 0.2 \times 0.2$ for $2.5 < |\eta| < 3.2$. In total, 5,632 channels are read from the HEC.

Forward Calorimeter

The forward calorimeter (FCal) performs both electromagnetic and hadronic calorimetry in the very forward region, $3.2 < |\eta| < 4.9$, and also shields the muon system from high particle fluxes. On each side, the FCal is divided into three layers measuring 45 cm in depth, an electromagnetic layer (FCal1) and two hadronic layers (FCal2 and FCal3). All three layers use LAr as the active medium, with very thin gaps due to avoid ion buildup due to the high particle flux. FCal1 uses copper absorbers to optimize the resolution and heat removal. FCal2 and FCal3 use tungsten absorbers, which provides good containment and reduces the lateral spread of hadronic showers. Finally, a passive brass plug behind FCal3 provides

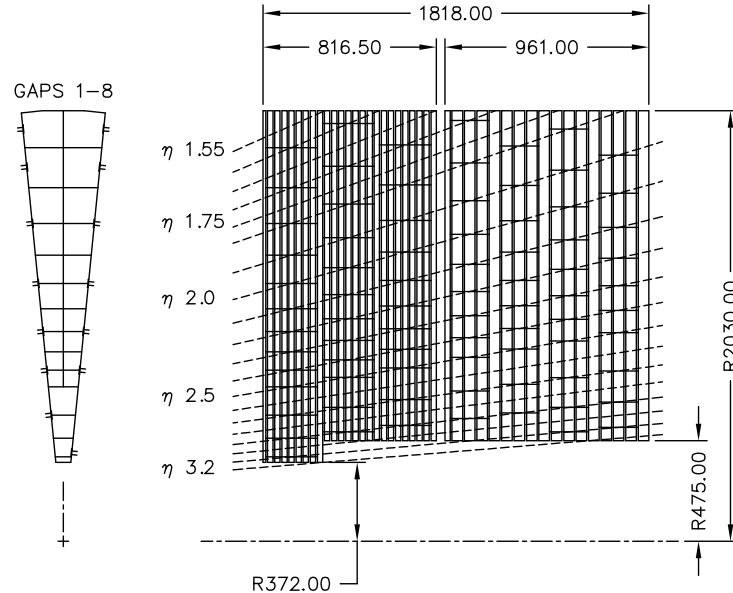


Figure 3.22: Schematic $R - \phi$ (left) and $R - z$ (right) views of the hadronic end-cap calorimeters.

shielding for the muon system. The layout of the three layers and shielding plug is shown in figure 3.23.

FCal1 consists of stacked copper plates with 0.27 mm LAr gaps. The electrodes occupy 12,260 holes drilled through the copper plates, and consist of a copper rod coaxial with a copper tube, as shown in figure 3.24a. FCal2 and FCal3 consist of two 2.35 cm-thick copper end-plates spanned by an array electrodes similar to those in FCal1, except with tungsten rods, as shown in figure 3.24b. The arrays contains 10,200 and 8,224 electrodes in FCal2 and FCal3, respectively. In total, the three layers, FCal1, FCal2, and FCal3, contain 1008, 500, and 254 readout channels, respectively, and constitute 208.1 radiation lengths and 9.94 interaction lengths.

3.2.5 Muon Spectrometer

The muon spectrometer detects charged particles that penetrate the barrel or end-cap calorimeters. It forms the exterior of the ATLAS detector, occupying the volume of the barrel toroid with four large wheels on each side of the interaction point. Using a combination of several technologies, the muon spectrometer performs precision measurements of muon momenta in the region $|\eta| < 2.7$, with a design resolution of 10% for 1 TeV tracks, and also provides triggering on muons for $|\eta| < 2.4$.

The structure of the muon spectrometer is shown in figures 3.25 and 3.26. The barrel systems are arranged in three layers with radii of approximately 5 m, 7.5 m, and 10 m, mounted inside and on the eight coils of the barrel toroid magnet with approximate octagonal sym-

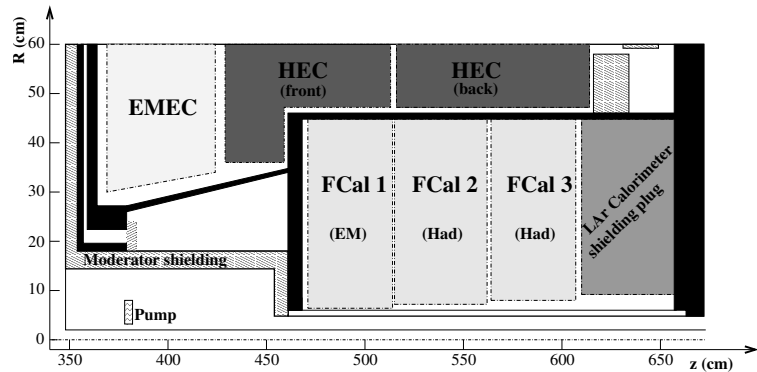


Figure 3.23: Schematic diagram showing the layout of the forward calorimeter in the R - z plane.

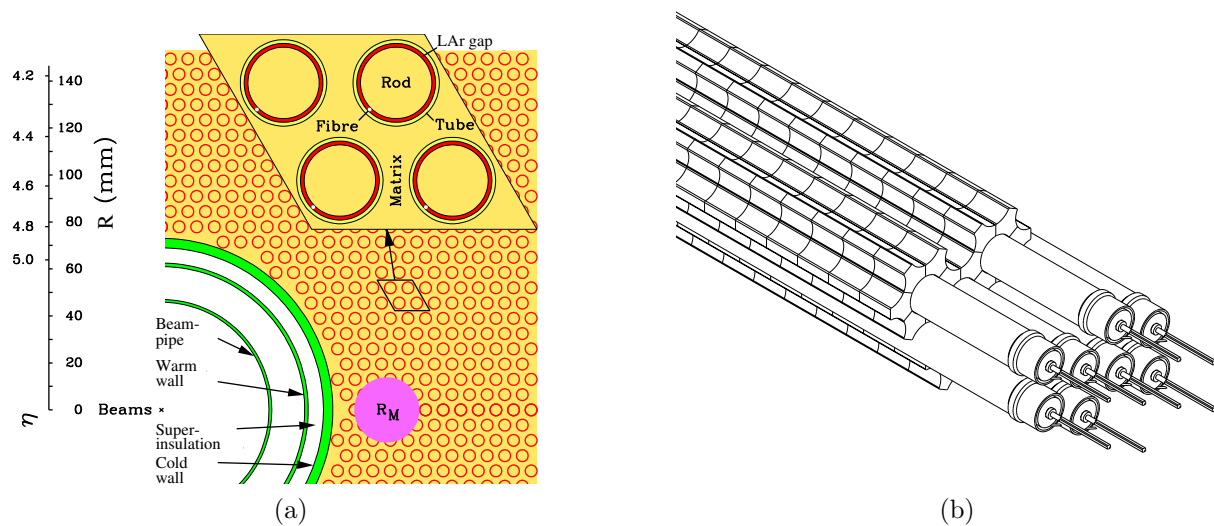


Figure 3.24: Left: the electrode structure of FCal1, showing the matrix of copper tubes and rods. The Molière radius, R_M , is shown for reference. Right: the absorber matrix in FCal2 and FCal, made from tungsten rods and copper tubes.

metry. The end-cap systems form four large wheels, located before and after the end-cap toroid magnets at positions of $|z| \approx 7.4$ m, 10.8 m, 14 m, and 21.5 m.

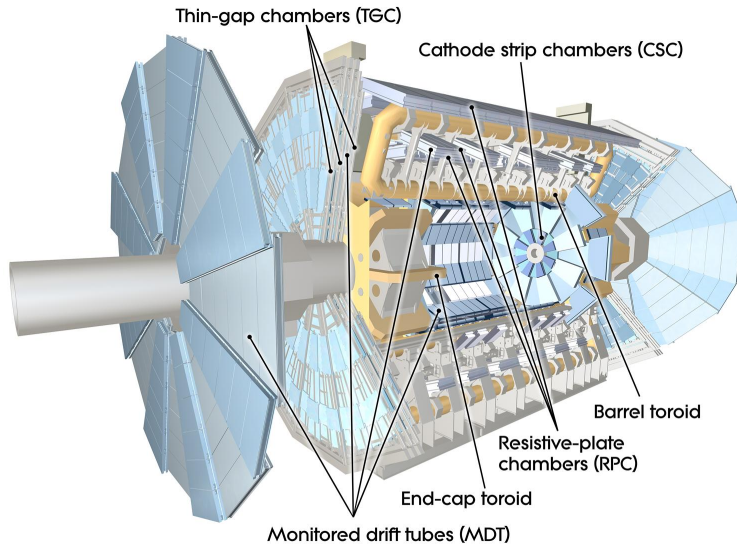


Figure 3.25: 3D model of the ATLAS muon spectrometer. The four different types of detector (MDTs, CSCs, RPCs, and TGCs) and the toroid magnets are shown.

Four different technologies are used for precision measurements and triggering, depending on the location in the detector. Monitored drift tubes (MDTs) perform the precision measurements over most of the volume with $|\eta| < 2.7$. Cathode strip chambers (CSCs) replace the MDTs in the innermost wheel for $2.0 < |\eta| < 2.7$, to handle the high particle flux. Triggering is performed by resistive plate chambers (RPCs) in the barrel ($|\eta| < 1.05$) and thin gap chambers (TGCs) in the end-caps. The trigger chambers also supplement the MDT position measurements with the hit coordinate in the non-bending plane.

Monitored Drift Tubes

Similarly to the TRT, the MDTs measure the trajectories of muons using gas-filled tubes with an axial anode wire. Muons traversing a tube ionize the gas, and the resulting electrons drift to the anode wire in an electric field. The tubes are arranged into 1088 MDT chambers, covering a total area of ~ 550 m². The majority of the MDT chambers are rectangular in the barrel and trapezoidal in the end-caps, and are laid out to optimize the solid angle coverage under the constraints of the magnet coils and other structures in the vicinity of the toroid magnet. Each chamber contains several layers of drift tubes, as shown in figure 3.27. The innermost chambers are divided into two groups of tube layers, called *multilayers*, each with four layers of tubes, while the remaining chambers have two groups of three layers of tubes.

The aluminum drift tubes have a radius of 29.97 mm, with a 50 μm -diameter tungsten-rhenium wire forming the anode along the axis of the tube. A cross section of a tube is

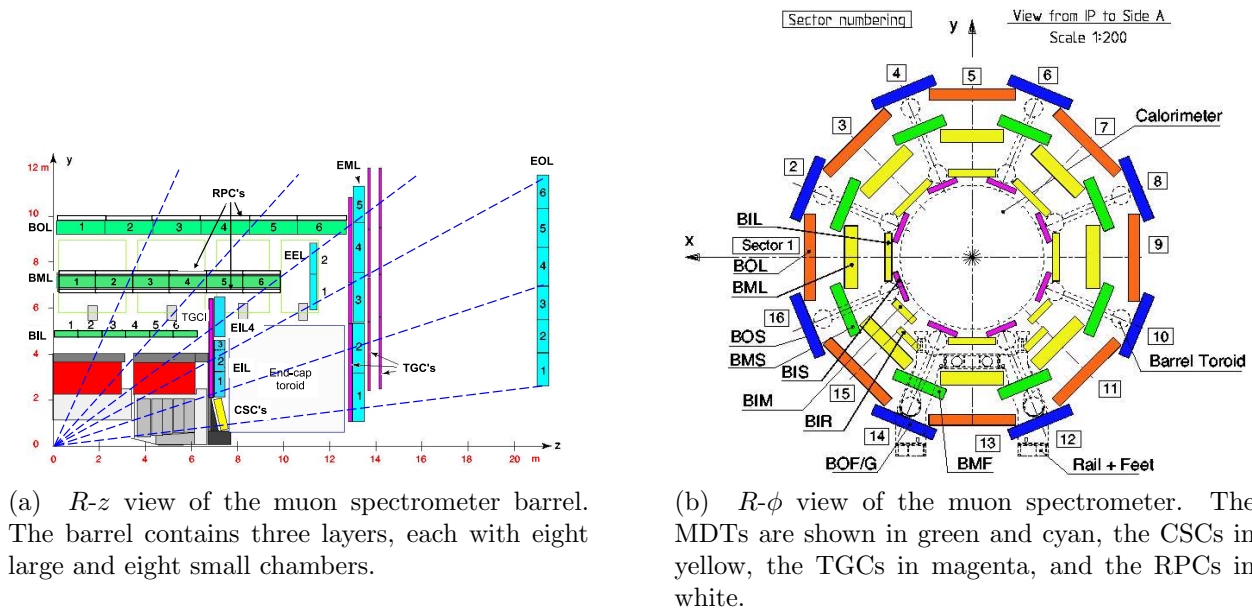


Figure 3.26: Layout of the chambers of the muon spectrometer.

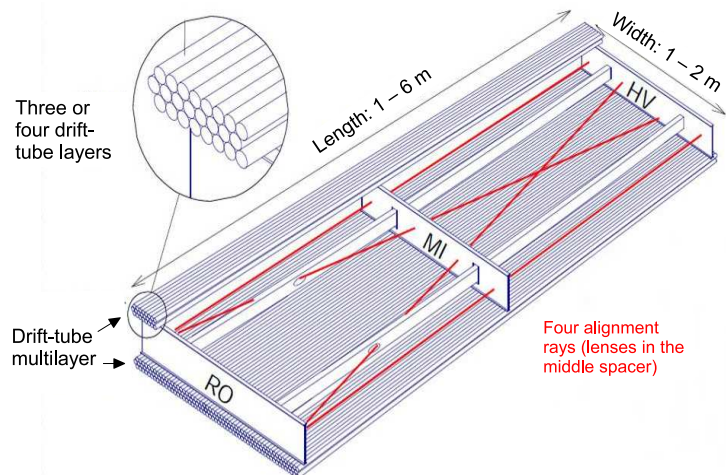


Figure 3.27: The mechanical structure of a MDT chamber. Two multilayers, each consisting of three or four rows of drift tubes, are separated by aluminum spacers. Four optical alignment rays continuously monitor the geometry of the chamber.

shown in figure 3.28. The tubes are filled with a mixture of argon and CO₂ (93:7) with a high pressure of 3 bar, and are operated with a voltage of 3 080 V. The average resolution of a single drift tube is 80 μm , and the combined resolution of a chamber is 35 μm . To achieve this precision, the position of the drift tubes and wires must be known to less than 30 μm . Four optical alignment rays inside each MDT chamber continuously monitor the geometry of the chamber with a precision of a few microns, shown in figure 3.27. An inter-chamber optical alignment network monitors the relative positions of chambers relative to their neighbors with a precision of approximately 20 μm . The optical alignment is supplemented with track-based alignment algorithms to align the chambers with poor or absent connection to the optical network, the end-caps with respect to the barrel, and the muon spectrometer with respect to the inner detector.

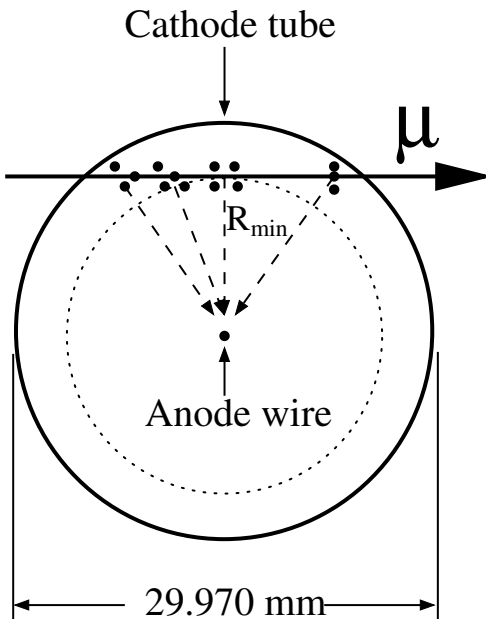


Figure 3.28: Cross section of a drift tube, showing the cathode tube, the anode wire, and an illustration of a muon ionizing the gas as it traverses the tube.

Cathode Strip Chambers

The rate limit for the safe operation of the MDTs is about 150 Hz/cm², which is exceeded for $|\eta| > 2$ in the first layer of the end-cap at $|z| \approx 7\text{ m}$. Accordingly, CSCs are used in this volume of the detector, which can operate up to rates of about 1 kHz/cm². Eight large and eight small trapezoidal chambers give full coverage in ϕ , as shown in figure 3.29a.

The CSCs are multiwire proportional chambers, with parallel wires running in the radial direction and the two cathodes finely segmented in perpendicular directions to provide measurements in both the η and ϕ directions. Muons passing through the chamber ionize the gas, and the resulting electrons form an avalanche as they drift to the anode wire, inducing a

charge distribution on the cathode strips. The perpendicular cathode segmentation provides position measurements in two dimensions, which helps distinguish hits from nearby particles. In the bending direction, the segmentation corresponds to a readout pitch of 5.31 mm and 5.56 mm for the large and small chambers, respectively. The track coordinate is determined from a relative measurement of the charge induced on 3-5 adjacent strips at the peak of the charge distribution. The resolution, dominated by electronic noise in the pre-amplifiers and by the spread of charge along the anode wire due inclined tracks, delta electrons, or a Lorentz force along the wire, is roughly 60 μm per CSC plane. In the non-bending direction, a coarser segmentation leads to a resolution of 5 mm.

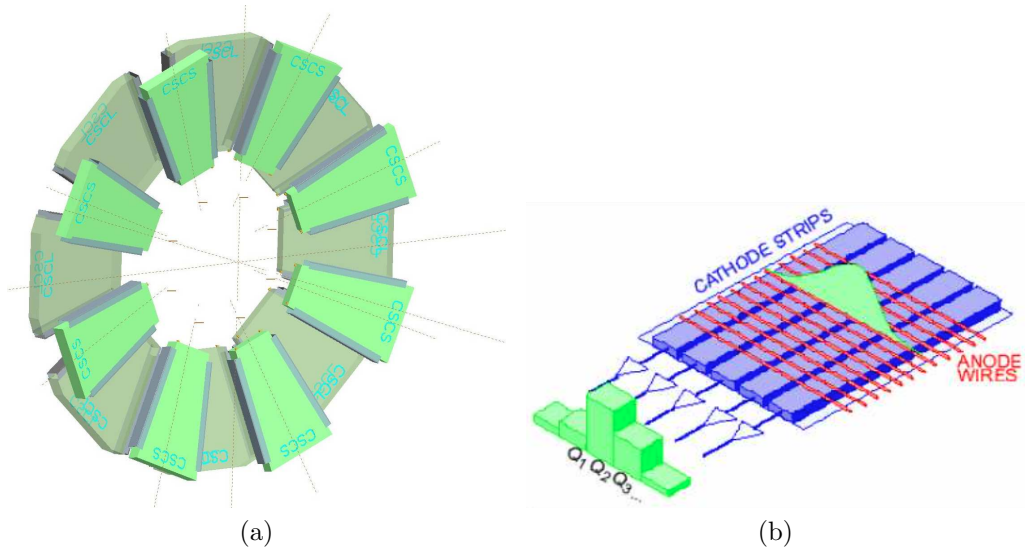


Figure 3.29: Left: Layout of the eight large and eight small CSC chambers. Right: Schematic view of the CSC anode wires and perpendicular cathode strips, showing the deposition of charge from a track on several adjacent strips.

Resistive Plate Chambers

Muon triggering in the barrel ($|\eta| < 1.05$) is performed by 544 RPCs, which exhibit good spatial and timing resolution and an adequate rate capability of $\sim 1 \text{ kHz/cm}^2$. The RPCs form three layers, or *stations*, with two on either side of the middle MDT layer and the third on the inner or outer side of the outer MDT layer, for the small and large sectors, respectively. Each station has two independent layers, each providing a measurement of η and ϕ , resulting in six possible measurements for muons passing through three stations.

An RPC unit consists of two sets of two parallel resistive plates (2 mm-thick phenolic-melaminic plastic laminate) separated by 2 mm by insulating spacers, shown in figure 3.30. The interior is filled with a gas mixture of $\text{C}_2\text{H}_2\text{F}_4/\text{Iso-C}_4\text{H}_{10}/\text{SF}_6$ (94.7/5/0.3). With an electric field of 4.9 kV/mm, muons traversing the gas induce an avalanche towards the anode,

which is read out via capacitive coupling to 25–35 mm-wide copper strips on the exterior face of the RPC. The RPCs achieve a spatial resolution of approximately 10 mm in z and ϕ , a timing resolution of 1.5 ns, and a detection efficiency of $\sim 98\%$.

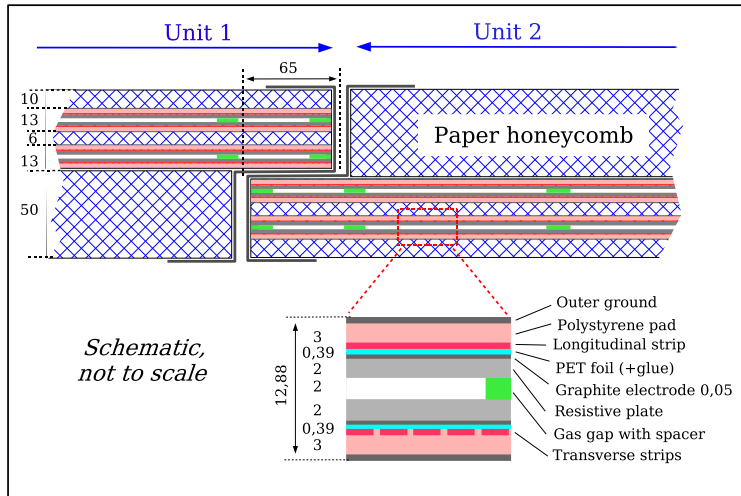


Figure 3.30: Cross section of an RPC, showing two units joined to form a single chamber. Each unit has two sets of two resistive plates (gray) separated by insulating spacers (green). The readout strips (magenta) are on the opposite side of the resistive plates from the gas gap. Outside the detecting elements, the volume of the RPC chamber is filled with paper honeycomb. The dimensions are given in millimeters.

Thin Gap Chambers

TGCs provide muon triggering in the end-caps, due to their good timing resolution and high rate capability. The TGCs also provide an azimuthal coordinate measurement, which complements the MDT measurement in the radial direction. Nine TGC disks are installed in total: a doublet mounted near the inner MDT end-cap layer, and a triplet and two doublets near the middle MDT end-cap layer. The disks are divided into two concentric annuli, one covering $1.05 \leq |\eta| \leq 1.92$ and the other covering $1.92 \leq |\eta| \leq 2.4$.

The TGCs are multiwire proportional chambers filled with a gas mixture of CO₂ and *n*-pentane. The principle of operation is similar to the CSCs. The cathode planes are 1.6 mm-thick FR4 (Flame Resistant 4) plates, with the interior faces coated with graphite and exterior faces cladded with copper. The triplet TGCs have three layers of wires and two layers of copper readout strips, while the doublet TGCs have two layers each of wires and strips, as shown in figure 3.31a. The radial coordinate is measured by the anode wire groups and the azimuthal coordinate by the radial cathode strips. The chambers are “thin” in that the wire to cathode distance, 1.4 mm, is shorter than the wire to wire distance of 1.8 mm, as shown in figure 3.31b. The anode wires have a diameter of 50 μm and are operated at a

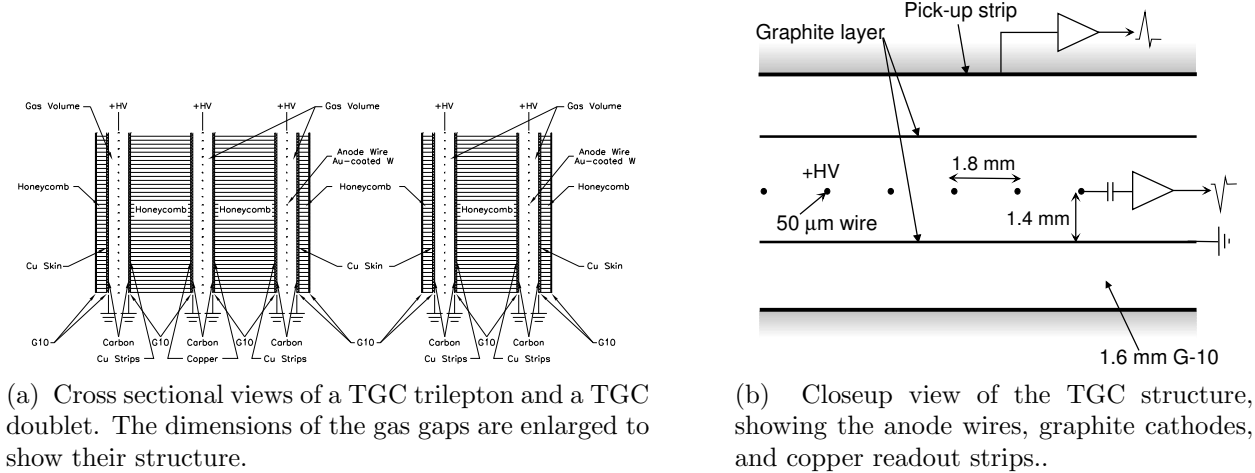


Figure 3.31: The construction of the TGCs.

potential of 2.9 kV. The small wire-to-wire distance and high electric field near the anode wires contribute to a good timing resolution of 4 ns. The spatial resolution, 2–6 mm in R and 3–7 mm in ϕ , is determined by the ganging of readouts: due to the direction of the magnetic field, achieving the required momentum resolution at fixed transverse momentum requires finer resolution at larger pseudorapidities.

3.2.6 Trigger and Data Acquisition

During a typical data-taking run during 2012, the LHC beam contains 1377 bunches with a typical bunch spacing of 50 ns, giving an event rate of ~ 20 MHz. In contrast, the ATLAS data acquisition system records events at roughly 400 Hz. The filtering of events is performed by the three-level ATLAS triggering system. The first level, L1, is implemented in hardware, and reduces the event rate to less than 75 kHz. The second level, L2, is implemented in software, and reduces the event rate to less than 3.5 kHz using regions of interest (RoIs) identified by the L1 trigger. The final level of the trigger, the Event Filter, is also implemented in software, and reduce the event rate to less than 400 Hz using the full event information.

L1 Trigger

The L1 trigger reduces the event rate from 20 MHz to 75 kHz using a limited subset of the event data. While the L1 trigger is processing an event, the full event data is stored in buffers on the detector. Due to the limited buffer size, the L1 latency must be less than 2.5 μ s, of which 1 μ s is used by the cable propagation time. Therefore, the trigger is implemented in custom hardware processors. The block diagram for the trigger is shown in figure 3.32. The inputs to the trigger include the RPC and TGC detectors in the muon spectrometer

and all of the calorimeter system. Two primary systems, the L1 Calorimeter Trigger and the L1 Muon Trigger, select events based on the presence of high- E_T objects or significant total event activity. These include high- p_T muons, electron and photons, jets, hadronically decaying tau leptons, large missing transverse energy, and large total transverse energy.

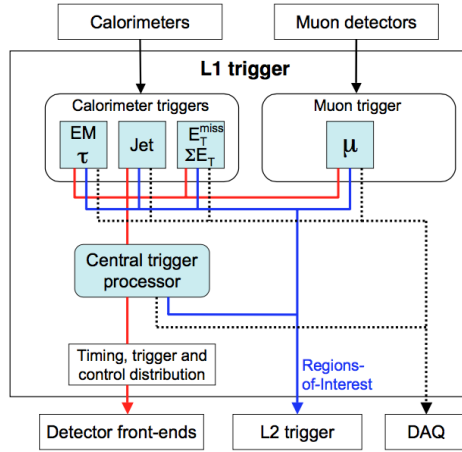


Figure 3.32: Block diagram of the L1 trigger system.

The L1 Calorimeter Trigger uses about 7,000 analogue trigger towers with a reduced granularity, $\Delta\eta \times \Delta\phi = 0.1 \times 0.1$ for most of the detector. Two subsystems run in parallel: the cluster processor identifies electrons/photon and hadronically decaying tau lepton candidates with E_T above a programmable set of thresholds, while the jet/energy-sum processor identifies jets and calculates the total scalar transverse energy and E_T^{miss} using $\Delta\eta \times \Delta\phi = 0.2 \times 0.2$ blocks of calorimeter cells. Isolation cuts can be applied as well, limiting the energy allowed in the towers surrounding the object of interest and, in the case of electrons/photon, in the hadronic towers behind the electromagnetic towers.

The L1 Muon Trigger searches for a coincidence of hits in consecutive muon trigger stations within a *road*, roughly corresponding to the path of a muon from the interaction point through the detector. The p_T threshold is encoded in the width of the road, with a narrower road corresponding to a higher p_T threshold. For low- p_T muons in the RPCs, the algorithm begins with hits in the second RPC doublet, called the *pivot plane*. The trigger requires a hit in the first RPC doublet, within the road defined by the interaction point and the hit in the pivot plane. The high- p_T algorithm is similar, requiring a hit along the road in the third RPC doublet as well as the first two. In the end-caps, the pivot plane is established by the outermost layer of TGCs, with the road corresponding to the path of an infinite-momentum muon originating from the interaction point. To reject backgrounds from random coincidences, stricter requirements are imposed on the number of coincident hits in the TGC doublets and triplets.

The muon and calorimeter triggers pass their decisions along with the corresponding data to the Central Trigger Processor (CTP). The CTP communicates the total trigger decision

to the front ends on the detector, including special triggers such as random triggers or the minimum bias trigger based on scintillator counters. In the event of a passed trigger, the event data is passed to the L2 trigger. The CTP also manages the *luminosity blocks*, an index representing the time at which an event was recorded with coarse (~ 1 minutes) granularity. A luminosity block is the shortest time interval for which the integrated luminosity can be determined such that the total uncertainty is dominated by systematic effects, rather than limited statistics. In the event of a detector failure, this index allows the rejection of a minimal set of affected events.

High Level Trigger

The L2 trigger reduces the event rate from a maximum of 75 kHz from the L1 trigger to less than 3.5 kHz. The trigger is implemented in software, and uses only the subset of the event data within the RoIs identified by the L1 trigger, typically 1%-2% of the total. After a successful L1 trigger, the data corresponding to the RoIs, stored in the detector-specific front end electronics, are accumulated in the ROI builder via 1574 readout links. The ROI builder combines the 1574 event fragments into a single data structure, which is passed to the L2 processing farm. At each step of a given trigger algorithm targeting particular signatures, only the relevant RoIs are analyzed. If no signatures remain valid, the event is rejected. Hence the full ROI information is transferred only for events which pass the L2 selection criteria. The typical L2 latency is about 40 ms.

Finally, the event filter reduces the event rate to the final \sim 400 Hz read out from the detector to disk. Also implemented in software, it runs the same algorithms as used in the offline event reconstruction using the full event information. Based on the objects used for triggering, the triggered events are categorized into one or more *data streams*. The data streams and other data computed by the event filter are appended to the event data, which are then transferred to CERN’s central data-recording facility for storage. An example of the event filter rates from the various streams during a single data-taking run is shown in figure 3.6a. The monthly average rates of each stream during 2012 are shown in figure 3.6b.

3.2.7 Simulation

In order to interpret the data collected by the detector, an accurate understanding of proton-proton collisions and their interactions with the detector is essential. The collisions are complex events, typically involving hundreds of particles and interactions with energy scales across many orders of magnitude. In the context of a search, predictions for the signal and the Standard Model backgrounds are produced using Monte Carlo simulation, making use of QCD factorization (section 2.1.3) to separate the problem into tractable pieces.

The modeling of the collision is handled by event generators, with various tools addressing different parts of the collision [11]. The matrix element for the hard scattering process is calculated perturbatively to fixed finite order. The perturbative part of the evolution of outgoing partons into jets is modeled using a parton shower algorithm, which leads into

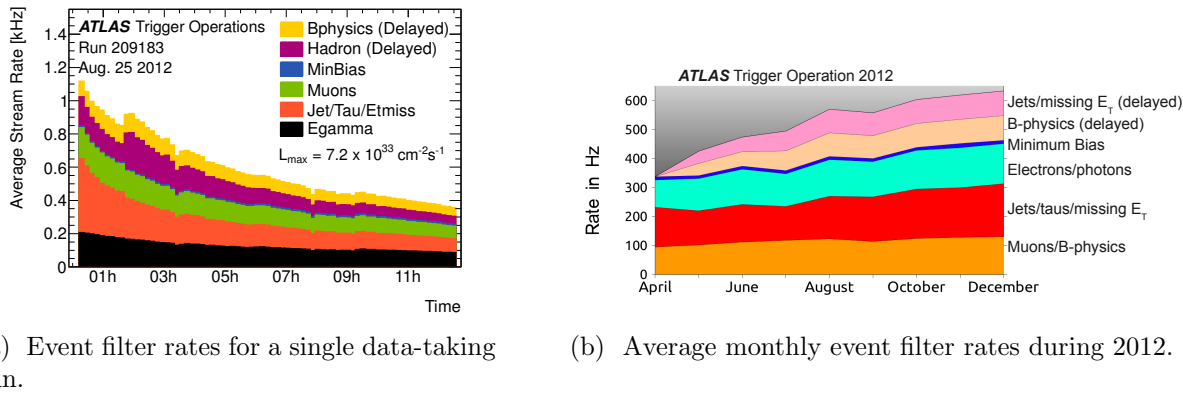


Table 3.6: The rates of recording events from the event filter for different data streams.

a non-perturbative hadronization model. Additional tools describe the underlying event, the behavior of the remainder of the protons which did not participate in the hard scatter. The generators used to model the backgrounds are described in section 6.1; these include SHERPA [12] and POWHEG [13] for the diboson backgrounds, MADGRAPH [14] other rare background processes, and PYTHIA [15, 16] for pileup interactions. Parton shower algorithms are implemented in PYTHIA and SHERPA.

The interactions of the particles from the event generator with the detector are modeled using the ATLAS simulation framework [17], a model of the ATLAS detector based on the GEANT4 toolkit [18]. The simulation describes the passage of particles through the detector, resulting in energy deposit, or ‘‘hits,’’ in the various sensitive elements of the detector. The hits are then digitized and passed to the same reconstruction algorithms used for the data (see chapter 5).

Bibliography

- [1] L. Evans, *History of the LHC* (2010) pp. 1–87.
- [2] L. Rossi, *Superconductivity: its role, its success and its setbacks in the Large Hadron Collider of CERN*, Superconductor Science and Technology **23**.3 (2010) p. 034001.
- [3] H. Wiedemann, *Particle Accelerator Physics*, SpringerLink: Springer e-Books, Springer Berlin Heidelberg, 2007.
- [4] M. Benedikt et al., *LHC Design Report. 3. The LHC injector chain* (2004).
- [5] O. S. Bruning et al., *LHC Design Report. 1. The LHC Main Ring* (2004).
- [6] G. Papotti et al., *Observations of beam-beam effects at the LHC* (2014), arXiv: 1409.5208 [physics.acc-ph].
- [7] M. Lamont, *Status of the LHC*, Journal of Physics: Conference Series **455** (2013) pp. 012001–10.
- [8] ATLAS Collaboration, *The ATLAS Experiment at the CERN Large Hadron Collider*, Journal of Instrumentation **3**.08 (2008) S08003–438.
- [9] ATLAS Collaboration, *ATLAS Photos*, URL: <http://www.atlas.ch/photos/>, 2015.
- [10] M. Alekseev et al., *Results of the ATLAS solenoid magnetic field map*, Journal of Physics: Conference Series **110**.9 (2008) pp. 092018–5.
- [11] A. Buckley et al., *General-purpose event generators for LHC physics*, arXiv **504**.5 (2011) pp. 145–233.
- [12] T. Gleisberg et al., *Event generation with SHERPA 1.1*, JHEP **0902** (2009) p. 007, arXiv: 0811.4622 [hep-ph].
- [13] T. Melia et al., *W^+W^- , WZ and ZZ production in the POWHEG BOX*, JHEP **11** (2011) p. 078, arXiv: 1107.5051 [hep-ph].
- [14] J. Alwall et al., *The automated computation of tree-level and next-to-leading order differential cross sections, and their matching to parton shower simulations*, JHEP **1407** (2014) p. 079, arXiv: 1405.0301 [hep-ph].
- [15] T. Sjöstrand, S. Mrenna, and P. Z. Skands, *PYTHIA 6.4 Physics and Manual*, JHEP **0605** (2006) p. 026, arXiv: hep-ph/0603175.

- [16] T. Sjöstrand, S. Mrenna, and P. Z. Skands, *A Brief Introduction to PYTHIA 8.1*, Comput. Phys. Commun. **178** (2008) pp. 852–867, arXiv: 0710.3820 [hep-ph].
- [17] ATLAS Collaboration, *The ATLAS Simulation Infrastructure*, The European Physical Journal C **70**.3 (2010) pp. 823–874.
- [18] S. Agostinelli et al., *GEANT4: A simulation toolkit*, Nucl. Instrum. Meth. **A506** (2003) pp. 250–303.

Chapter 4

Luminosity Measurement

4.1 Run I Luminosity

The ATLAS Run I data were recorded from 2011 to 2012, with a center-of-mass collision energy of $\sqrt{s} = 7\text{ TeV}$ in 2011 and $\sqrt{s} = 8\text{ TeV}$ during 2012. Integrated luminosities of $L = 5.46\text{ fb}^{-1}$ and 22.8 fb^{-1} were delivered by the LHC in the two years, of which 5.08 fb^{-1} and 21.3 fb^{-1} were recorded by the ATLAS detector. The recorded luminosity accounts for the data acquisition inefficiency, as well as the warm start period, an interval of several minutes after the LHC has declared stable beams during which the tracking detectors are ramped to high voltage and the pixel detector preamplifiers are turned on. After masking data recorded while one or more detector subsystems were not functioning properly, 4.57 fb^{-1} and 20.3 fb^{-1} of data are considered usable for physics analyses. The delivered, recorded, and physics-ready luminosity are shown as a function of time in figure 4.1a.

The LHC was typically operated with 1042 and 1368 colliding bunches in 2011 and 2012, respectively, with a bunch spacing of 50 ns. The peak instantaneous luminosity reached values as high as $\mathcal{L} \sim 8 \times 10^{33}\text{ cm}^{-2}\text{ s}^{-1}$, corresponding to a peak average pileup value of $\mu \sim 37$. The distribution of pileup values in 2011 and 2012 data are shown in figure 4.1b.

4.2 Measurement Overview

In terms of observed interaction rates, rather than beam parameters as in equation 3.1, the instantaneous luminosity at a pp collider is given by [1, 2]:

$$\mathcal{L} = \frac{R_{\text{inel}}}{\sigma_{\text{inel}}}, \quad (4.1)$$

where R_{inel} is the rate of inelastic pp collisions, and σ_{inel} is the pp inelastic cross section. For a storage ring with a revolution frequency f_r and n_b colliding bunch pairs, the instan-

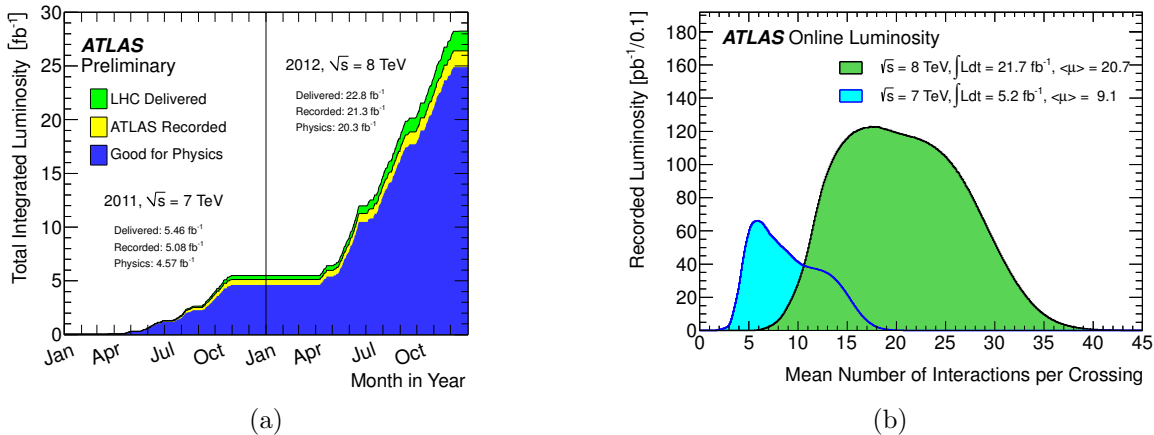


Figure 4.1: Left: The cumulative delivered, recorded, and physics-ready integrated luminosity versus time in 2011-2012. Right: Distribution of the number of interactions per bunch crossing in events recorded in 2011-2012.

taneous luminosity can be written in terms of the average number of inelastic pp collisions per bunch crossing, μ , as

$$\mathcal{L} = \frac{\mu f_r n_b}{\sigma_{\text{inel}}}. \quad (4.2)$$

The instantaneous luminosity is measured by ATLAS using several detectors and algorithms, which have some efficiency ϵ to detect a pp interaction and measure the *visible* number of interactions per bunch crossing, $\mu_{\text{vis}} = \epsilon \mu$. Defining the visible cross section to be $\sigma_{\text{vis}} \equiv \epsilon \sigma_{\text{vis}}$, the instantaneous luminosity as measured by a particular detector is:

$$\mathcal{L} = \frac{\mu_{\text{vis}} f_r n_b}{\sigma_{\text{vis}}}. \quad (4.3)$$

The luminosity is measured for each luminosity block, corresponding to time intervals of roughly 60 s (section 3.2.6). The visible cross section is a calibration constant for a particular detector, which is determined during dedicated calibration runs in which the luminosity is determined directly from the physical dimensions of the beams. The calibration procedure is described in section 4.4.

4.3 Luminosity Detectors

ATLAS performs many redundant luminosity measurements using several detectors. The detectors fall into two categories. *Event counting* detectors have a binary response, returning a 0 or 1 depending on whether a bunch crossing satisfies a set of criteria defined to detect an inelastic pp collision. Such detectors essentially measure $p(0; \mu)$, the probability that an

event falls in the zero bin of a Poisson distribution, from which the mean μ be calculated. *Hit counting* detectors, on the other hand, count some quantity proportional to the number of interactions in a given bunch crossing, such as the number of particles identified by a particular detector subsystem. A hit counting measurement typically yields more information about an event at the cost of additional systematic uncertainties.

Ideally, a luminosity detector exhibits the following features:

- The efficiency of the detector should be insensitive to pileup, or the variation of the efficiency with respect to pileup should be well understood. The visible cross sections are typically measured at $\mu \approx \mathcal{O}(1)$, while a typical data-taking run has a peak average pileup of up to $\mu \sim 40$; it is essential to understand the behavior of the visible cross section across this range of pileup values.
- The efficiency of the detector should be constant over long timescales.
- The response of the detector and the readout should fast enough to provide a bunch-by-bunch luminosity measurement. As the LHC bunches are not identical, with different numbers of protons and emittances, it is useful to measure luminosity for each colliding bunch pair, as often as once every 25 ns. The colliding bunch pairs are labeled by the bunch crossing identification number, or BCID, ranging from 1 to 2808; consecutive BCIDs are separated by 25 ns.
- The efficiency should be high enough to yield sufficient statistics. The data are used in increments as short as 20 s, so the statistics collected over this time scale should be high enough that the total uncertainty is dominated by systematic effects. On the other hand, for event counting detectors, the efficiency should not be so high that the detector is saturated; the uncertainty on μ is large if $p(0; \mu)$ is too close to 0 or 1.
- The backgrounds should be low and understandable. Detectors can be sensitive to a wide range of phenomena aside from pp collisions, which should not be counted as luminosity. For example, some detectors observe a phenomenon called *afterglow*, a small amount of activity in the BCIDs immediately following a collision likely due to photons from nuclear deexcitations in the detector material. The afterglow background is proportional to the luminosity in the colliding BCIDs, and decays away with several time constants. Collisions between a beam and residual gas in the beam pipe, called *beam-gas interactions*, can also contribute a low level of background, and is estimated by observing non-colliding bunches passing through the interaction region.

The central value of the luminosity measurement is determined by the *beam conditions monitor* (BCM) [3], which fulfills most of these desired criteria. The BCM consists of eight diamond-based particle detectors, four on each side of the interaction point at $|z| = 184$ cm and $|\eta| = 4.2$. The detectors have a physical cross section of approximately 1 cm^2 and are arranged in a cross pattern, with two independent readouts corresponding to the vertical and

horizontal pairs. The design purpose of the BCM is to monitor backgrounds and to trigger a beam dump if beam losses towards the inner detector become too high; accordingly, the detector has a very fast readout, and can provide a bunch-by-bunch luminosity measurement with a time resolution of ~ 0.7 ns. The luminosity is measured using event counting, and can be measured using any combination of the readouts. The configurations used require hits in either the vertical pair (BCMV) or the horizontal pair (BCM), and either coincident hits on both sides of the interaction point (AND) or a single hit on either side (OR). The small size of the active sensor leads to an efficiency of approximately 7% in the OR configuration, which allows for sufficient statistics without saturating the detector.

LUCID (LUminosity measurement using Cherenkov Integrating Detector) [4] provides a supplementary, bunch-by-bunch, event counting-based luminosity measurement. The detector consists of two sets of sixteen Cherenkov detectors surrounding the beampipe at $z = \pm 17$ m, occupying the pseudorapidity range $5.6 < |\eta| < 6.0$. As designed and initially constructed, the Cherenkov detectors are polished aluminum tubes filled with C_4F_{10} gas. The Cherenkov photons induced by charged particles traversing the gas are collected by photomultiplier tubes (PMTs) located at the far end of the tubes. Additional Cherenkov photons are produced in the quartz window separating the tube volume from the PMT. In this configuration, the typical single-particle yield is 60-70 photoelectrons due to photons created in the gas, and about 40 photoelectrons due to the quartz window. A hit is recorded if the PMT signal exceeds a preset threshold, corresponding to about 15 photoelectrons. However, the higher instantaneous luminosities due to the 50 ns bunch spacing led to saturation of the detectors, and hence on 30 July 2011, the gas was removed from the Cherenkov tubes to reduce the efficiency. The removal of the gas also improved the detector's stability and linearity with respect to pileup. Relative comparisons with other detectors were used to reestablish the detector calibration.

Several detector subsystems nominally designed for physics object reconstruction are also used for hit counting-based luminosity measurements. Algorithms using the tile calorimeter and the forward calorimeters (see section 3.2.4) determine the luminosity from detector currents proportional to the total particle flux in small regions of the calorimeters. The tile calorimeter algorithm monitors the PMT currents corresponding to a few selected cells near $|\eta| = 1.25$, where the highest sensitivity to changes in the luminosity is observed. Similarly, the forward calorimeter algorithm monitors the currents in the high voltage lines. In both cases, the detector is unable to provide a bunch-by-bunch measurement, and the current response is not sensitive to the low instantaneous luminosities during the dedicated calibration runs, requiring the calibration to be set using relative comparisons with LUCID or BCM. On the other hand, the detectors exhibit good linearity of response with pileup, and good short-term stability.

Finally, algorithms using the inner detector measure the luminosity by counting reconstructed tracks and vertices¹. The use of these higher-level objects confers certain benefits,

¹Pixel cluster counting, used by the CMS experiment, was also considered, but was not commissioned due to the difficulty of the subtraction of the background due to afterglow.

such as low background rates and good long-term stability, at the cost of increased computational requirements, which limit the data rate to $\mathcal{O}(100 \text{ Hz})$. Further, pileup effects can be significant; in particular, the efficiency of the vertex counting algorithm varies by as much as 30% up to pileup values of $\mu = 30$, limiting its utility to data with low pileup.

4.4 Luminosity Calibration: van der Meer Scans

The visible cross sections for the detectors and algorithms described in section 4.3 are calibrated during dedicated runs called van der Meer (vdM) scans [5]. The calibration procedure uses the definition of luminosity in terms of the beam parameters, given for a single colliding bunch by:

$$\mathcal{L} = f_r n_1 n_2 K \int \rho_1(x, y, z, t) \rho_2(x, y, z, t) dx dy dz dt, \quad (4.4)$$

where f_r is the revolution frequency, $n_{1,2}$ are the number of particles in the colliding bunches, and $\rho_{1,2}(x, y, z, t)$ are the time- and position-dependent particle density distribution, normalized so that $\int \rho_{1,2}(x, y, z, t) dx dy dz = 1$. K is a kinematic factor,

$$K = \sqrt{(\vec{v}_1 - \vec{v}_2)^2 - \frac{(\vec{v}_1 \times \vec{v}_2)^2}{c^2}}, \quad (4.5)$$

which, in the limit $|\vec{v}_{1,2}| \rightarrow c$, reduces to $2c \cos \alpha$, where α is the crossing angle between the beams. To simplify the current discussion, the crossing angle is assumed to be zero, and the bunch densities are assumed to be functions of x , y , and $z \pm ct$, i.e. that the transverse bunch profiles are constant over the duration of the collision². The luminosity can then be expressed as:

$$\mathcal{L} = f_r n_1 n_2 \int \hat{\rho}_1(x, y) \hat{\rho}_2(x, y) dx dy, \quad (4.6)$$

where $\hat{\rho}_{1,2}(x, y)$ are the transverse particle densities, normalized to unity. Under the further assumption that the transverse particle densities factorize in the horizontal and vertical directions, $\hat{\rho}(x, y) = \hat{\rho}_x(x) \hat{\rho}_y(y)$, where $\hat{\rho}_x(x)$ and $\hat{\rho}_y(y)$ are also normalized to unity, the luminosity can be written as:

$$\mathcal{L} = f_r n_1 n_2 \Omega_x(\hat{\rho}_{x1}, \hat{\rho}_{x2}) \Omega_y(\hat{\rho}_{y1}, \hat{\rho}_{y2}), \quad (4.7)$$

²In particular, the *hourglass effect* is neglected. The collisions occur in a drift space, where the beams are focused, or squeezed, onto the interaction point. The transverse size of the beam in direction i as a function of z is given by $\sigma_i^2(z) = \epsilon_i \beta_i^* \left(1 + \frac{(z-z_i^w)^2}{\beta_i^{*2}}\right)$, where ϵ_i is the transverse emittance, z_i^w is location of the optical waist, and β_i^* is the betatron function at $z = z_i^w$. The effect is significant when $\beta_i^* \lesssim \sigma_z$; during the vdM scans, $\sigma_z \approx 50 \text{ mm}$, while $\beta^* = 1.5 \text{ m-11 m}$, and hence the hourglass effect is neglected.

where $\Omega_x(\hat{\rho}_{x1}, \hat{\rho}_{x2}) = \int \hat{\rho}_{x1}(x)\hat{\rho}_{x2}(x)dx$, and similarly for the y direction³. As first proposed by van der Meer, the $\Omega_{x,y}$ parameters can be determined by measuring the interaction rate as a function of transverse beam displacement, $R_{x,y}(\delta)$. Without loss of generality, assume that beam 2 is displaced by δ in the x direction, while beam 1 is held fixed. Then, $R_x(\delta) = k \int \rho_{x1}(x)\rho_{x2}(x - \delta) dx$ for some constant k , and

$$\frac{R_x(0)}{\int R_x(\delta)d\delta} = \frac{k \int \rho_{x1}(x)\rho_{x2}(x) dx}{k \int \int \rho_{x1}(x)\rho_{x2}(x - \delta) dx d\delta} \quad (4.8)$$

$$= \int \rho_{x1}(x)\rho_{x2}(x) dx \quad (4.9)$$

$$= \Omega_x(\hat{\rho}_{x1}, \hat{\rho}_{x2}) \quad (4.10)$$

For convenience, define $\Sigma_{x,y}$ to be the characteristic widths of $R_{x,y}(\delta)$, given by:

$$\Sigma_{x,y} = \frac{1}{\sqrt{2\pi}} \frac{\int R_{x,y}(\delta) d\delta}{R_{x,y}(0)}. \quad (4.11)$$

For Gaussian beams, $\Sigma_{x,y}$ correspond to the Gaussian width of $R_{x,y}(\delta)$. Finally, the luminosity is given by

$$\mathcal{L} = \frac{f_r n_1 n_2}{2\pi \Sigma_x \Sigma_y}. \quad (4.12)$$

Equating this with the luminosity defined in equation 4.3, the visible cross section for a given detector and algorithm is given by

$$\sigma_{\text{vis}} = \mu_{\text{vis}}^{\text{MAX}} \frac{2\pi \Sigma_x \Sigma_y}{n_1 n_2}, \quad (4.13)$$

where $\mu_{\text{vis}}^{\text{MAX}}$ is the visible interaction rate per bunch crossing at the maximum of the scan curve, $R(\delta)$. The numbers of particles per bunch, $n_{1,2}$, are measured by the LHC Bunch Current Normalization Working Group using bunch current transformers (BCTs) [7–9].

4.4.1 2011 Luminosity Calibration

As an example, the 2011 pp calibration is derived from two pairs of scans in the x - and y -directions, performed during the same LHC fill on 15 May 2011 [2]. The beams had 14 colliding bunch pairs, $\sim 0.8 \times 10^{11}$ protons per bunch, $\beta^* = 1.5$ m, and a crossing angle of $\alpha = 240 \mu\text{rad}$. The resulting transverse beam size was approximately $\sigma_x \approx \sigma_y \approx 40 \mu\text{m}$, and the peak average number of interactions per crossing with head-on collisions was $\mu \approx 2.3$. The scan was performed in 25 equal steps over a displacement range of $\delta = \pm 233 \mu\text{m}$.

³The formalism can be generalized to the case where the beam profiles do not factorize in x and y ; see [6].

Figure 4.2 shows an example scan curve, with the specific visible interaction rate, $\mu_{\text{vis}}^{\text{sp}} \equiv \mu_{\text{vis}}/(n_1 n_2)$, plotted as a function of transverse beam separation for the BCMV_OR algorithm. Normalizing by the bunch current product, $n_1 n_2$, eliminates the dependence of the curve on the decreasing beam currents over the course of the scan. The vdM scan curve is fitted with a Gaussian plus a constant, which is used as $R_{x,y}(\delta)$ to calculate $\Sigma_{x,y}$ in equation 4.11. $\mu_{\text{vis}}^{\text{MAX}}$ is determined from the peak of the fitted function. The measured σ_{vis} values for both scans and all 14 colliding bunch pairs are shown in figure 4.3. The luminosity-weighted mean σ_{vis} is taken as the central value, while the scatter of the 28 measurements, which is not consistent with statistical variation, is taken as a systematic uncertainty on the reproducibility of the measurement.

The visible cross sections for several algorithms using during 2011 are shown in table 4.1, along with the efficiency assuming a total inelastic cross section of $\sigma_{\text{inel}} = (71.34 \pm 0.90) \text{ mb}$ [10].

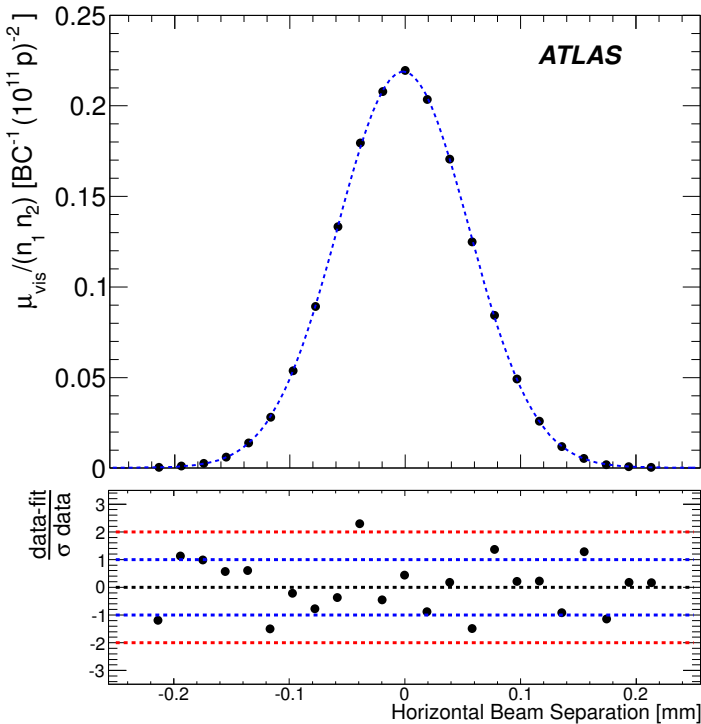


Figure 4.2: An example of a scan curve measured by BCMV_OR from the van der Meer scans on 15 May 2011. The specific visible interaction rate $\mu_{\text{vis}}^{\text{sp}} \equiv \mu_{\text{vis}}/(n_1 n_2)$ is shown as a function of transverse beam separation in the x direction for a single scan and BCID. The data are fitted with Gaussian plus constant. The bottom plot shows the residual deviation of the data from the fit, divided by the uncertainty on the data.

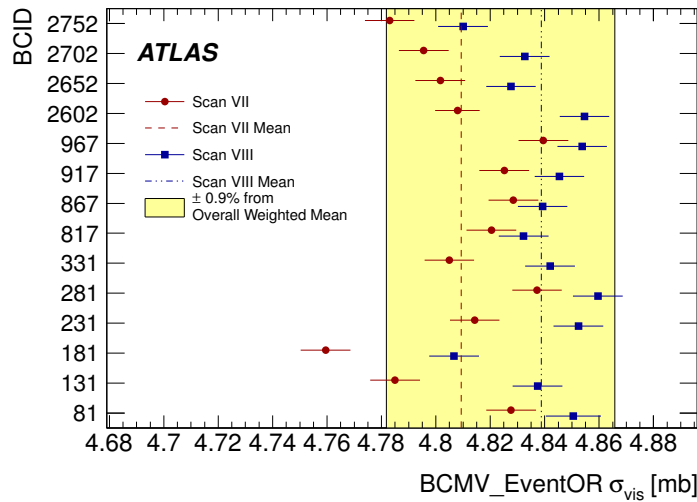


Figure 4.3: Measured σ_{vis} values from the vdM scans performed in May 2011. The error bars represent statistical uncertainties only. The vertical dashed lines indicate the weighted average over BCIDs from the two sets of scans. The yellow band shows a variation of $\pm 0.9\%$ from the total weighted average, equal to the systematic uncertainty due to the observed BCID-to-BCID and scan-to-scan variations.

Algorithm	$\sigma_{\text{vis}} \text{ (2011)}$	$\frac{\sigma_{\text{vis}}}{\sigma_{\text{inel}}}$
BCM_VOR	4.82 ± 0.07	0.068
BCM_HOR	4.78 ± 0.07	0.067
BCM_VAND	0.142 ± 0.002	0.002
BCM_HAND	0.140 ± 0.002	0.002
LUCID_OR	43.3 ± 0.7	0.607
LUCID_AND	13.7 ± 0.2	0.192

Table 4.1: Visible cross sections for pp luminosity measurement algorithms used in 2011. The corresponding efficiency of detecting an inelastic pp collision is also shown for $\sigma_{\text{inel}} = 71.34 \text{ mb}$.

4.5 Systematic Uncertainties

The systematic uncertainty on the 2011 and 2012 luminosity measurements are 1.8% and 2.8%⁴, respectively. No single source of uncertainty dominates the total; rather, the uncertainty is due to many sources, each contributing less than 1%. The sources of uncertainty on the 2011 luminosity measurement are shown in table 4.2, divided into uncertainties on the visible cross section measurement during vdm scans and uncertainties on the measurement performed over the course of data taking.

The combined uncertainty on the visible cross sections due to the vdm calibration procedure is 1.5%. The largest source of uncertainty is due to emittance growth and non-reproducibility, reflected in the scatter between BCIDs and between scans in figure 4.3. Other significant sources, each roughly 0.5%, include beam-beam effects, where the two colliding beams deflect each other away from the nominal transverse separation; transverse correlations which violate the assumption that the transverse particle densities factorize as $\rho(x, y) = \rho_x(x)\rho_y(y)$; pileup dependence; and the measurement of the number of protons per bunch, $n_{1,2}$.

Uncertainties on the luminosity measurement over the 2011 data-taking period total 0.9%. These uncertainties are dominated by variations in the detector efficiencies during 2011, quantified using relative comparisons between algorithms across the entire year, and pileup dependence, quantified using relative comparisons between algorithms at different pileup values. The relative comparisons are shown in figure 4.4.

The sources contributing to the 2.8% systematic uncertainty in 2012 are similar. The 1% increase from 2011 is largely due to long-term consistency: comparisons with tile and forward calorimeter measurements indicate that the BCMV_OR efficiency drifted with respect to the calorimeters by as much as 2% over the year. The full 2% is taken as a conservative systematic uncertainty.

4.6 Vertex-Based Luminosity Measurement

Primary vertices are points consistent with being the origin of a set of tracks reconstructed by the inner detector, nominally due to inelastic pp interactions. The reconstruction of tracks and vertices is described in section 5.1. Vertex counting [11] is an appealing luminosity measurement technique for a number of reasons. The backgrounds are very low, and can be controlled by requiring a minimum number of tracks per vertex, chosen here to be five tracks with $p_T > 400$ MeV. Further, the vertex reconstruction efficiency is expected to be stable throughout the data taking period. However, the technique has two significant drawbacks. First, the data is collected through the standard ATLAS data acquisition system, limiting the event rate during normal physics runs to $\mathcal{O}(100\text{ Hz})$. Depending on the trigger used, a correction for the trigger deadtime may also be necessary. Second, the efficiency of the vertex

⁴Preliminary uncertainty. The final uncertainty is expected to be around 2%.

Source	Uncertainty
Bunch population product ($n_1 n_2$)	0.5%
Beam centering	0.10%
Beam position jitter	0.30%
Emissittance growth/non-reproducibility	0.67% ⊕ 0.55%
Bunch-to-bunch σ_{vis} consistency	0.28%
Fit model	0.31%
Background subtraction	0.29%
Length scale calibration	0.30%
Absolute ID length scale	0.30%
Beam-beam effects	0.50%
Transverse correlations	0.50%
Pileup dependence	0.50%
Afterglow correction	0.2%
BCM Stability	0.2%
Long-term consistency	0.7%
Pileup dependence	0.5%
Total	1.8%

vdM calibration subtotal=1.5%
Uncertainties from a single
measurement of σ_{vis}

\mathcal{L} measurement subtotal=0.9%
Uncertainties evaluated from
all 2011 physics runs

Table 4.2: Systematic uncertainties on the integrated luminosity measured in 2011 using the BCM_VOR algorithm. The uncertainties are separated into uncertainties on the visible cross section (1.5%) and measurement uncertainties over the year (0.9%).

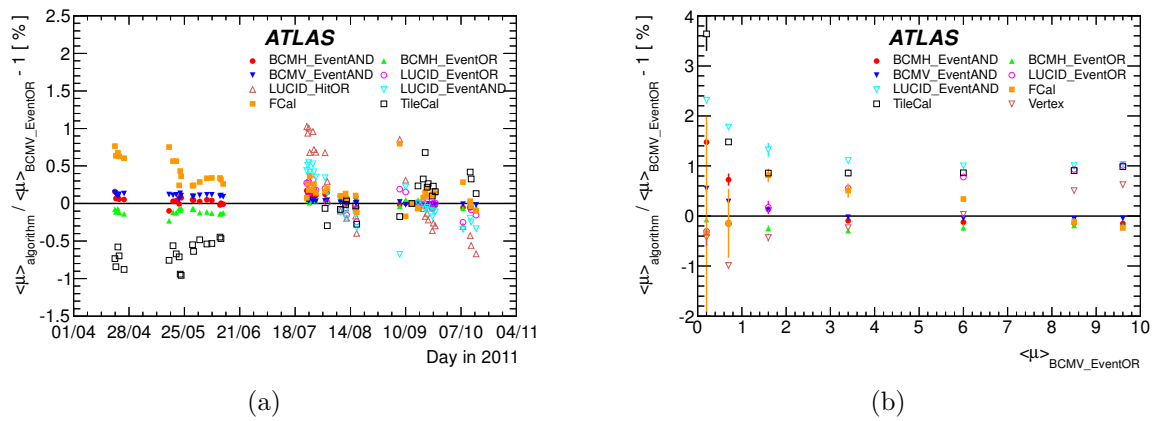


Figure 4.4: Left: Comparison of luminosities measured by different algorithms as a function of time in 2011. Right: Comparison of luminosities measured by different algorithms as a function of the average number of interactions per bunch cross, μ , as measured by BCM_VOR. The data were taken during a single run by separating the beams in the transverse direction, similar to a van der Meer scan.

reconstruction algorithm is significantly nonlinear with pileup, with the efficiency decreasing by $\sim 30\%$ between pileup values of $\mu = 1$ and $\mu = 30$.

4.6.1 Vertex Counting Method

The data for the inner detector-based luminosity measurements are collected through the standard ATLAS data acquisition system. Events are collected with either a random trigger or a trigger requiring hits in the minimum bias trigger scintillators (MBTS), two discs of scintillators mounted on the inner surfaces of the LAr end-cap cryostats ($2.12 < |\eta| < 3.85$). Both triggers can select a specific set of BCIDs, which is essential for special runs where a bunch-by-bunch measurement is necessary, e.g. the vdm scans. The random trigger records a fraction of all bunch crossings in a specific set of colliding BCIDs, enabling an unbiased measurement of μ_{vis} at the cost of lower statistics. The statistics collected worsen at low pileup values, where a large fraction of the triggered events do not contain a collision; hence, the random trigger is used mostly at high pileup. At lower pileup, the statistics can be recovered by using the MBTS trigger, which requires a small number of hits in the MBTS, usually at least two. Care must be taken to avoid bias due to the nontrivial trigger requirements: the trigger inefficiency, prescale, and deadtime must be taken into account. For vertices with at least five tracks, the inefficiency is negligible.

Vertices are reconstructed with two settings: the default reconstruction settings based on tracks with $p_T > 400 \text{ MeV}$, and tighter settings (“VtxLumi”) based on tracks with $p_T > 900 \text{ MeV}$ with stricter requirements on the track quality. The tighter settings were introduced in 2012 to reduce the computational requirements associated with collecting $\mathcal{O}(100 \text{ Hz})$ of inner detector data over the entire year. The studies described below are based on the 2011 data, where the vertex-based luminosity measurement is only performed on special runs, and use the default reconstruction settings.

The single-bunch instantaneous luminosity is calculated as follows. For the random trigger, the visible interaction rate is $\mu_{\text{vis}} = \frac{N_{\text{vtx}}}{N_{\text{evt}}}$, where N_{vtx} is the number of vertices recorded in N_{evt} triggered events. For the MBTS trigger, $\mu_{\text{vis}} = \frac{N_{\text{vtx}}}{f_r \Delta t}$, where N_{vtx} is the number of vertices recorded after correcting for the prescale and deadtime, $f_r = 11245.5 \text{ Hz}$ is the LHC revolution frequency, and Δt is the duration of the measurement. μ_{vis} is then corrected for pileup effects, described below in section 4.6.2, and finally the luminosity is given by equation 4.3.

4.6.2 Pileup Effects

The vertex reconstruction efficiency is strongly affected by three pileup-related phenomena:

- Vertex masking: a pp interaction fails to be reconstructed as a vertex because some or all of its tracks are used by an earlier vertex in the iterative reconstruction algorithm (see section 5.1. This is the dominant pileup effect, which causes a large drop in the reconstruction efficiency at high pileup.

- Fake vertices: a vertex passes the cut on the minimum number of tracks due to acquiring tracks from another nearby pp interaction. This is a subdominant but significant effect, which causes a small increase in the reconstruction efficiency at high pileup.
- Split vertices: a single interaction is reconstructed as two separate vertices. This is a significant effect when considering vertices with two or more tracks, but is negligible for vertices with at least five tracks.

Corrections are derived for vertex masking and fake vertices. The fake vertex correction is derived using truth matching in minimum bias Monte Carlo simulation. The simulation sample was generated using PYTHIA 8, with tune A2M [12, 13]. For a given cut on the minimum number of tracks per vertex, $n_{\text{trk,min}}$, a reconstructed vertex is labeled as fake if less than $n_{\text{trk,min}}$ of its tracks are matched to charged particles originating from the same generated pp interaction. The average number of reconstructed vertices labeled as fake by Monte Carlo truth matching is shown as a function of pileup in figure 4.5. The fake fractions show a significant dependence on μ and on the $n_{\text{trk,min}}$.

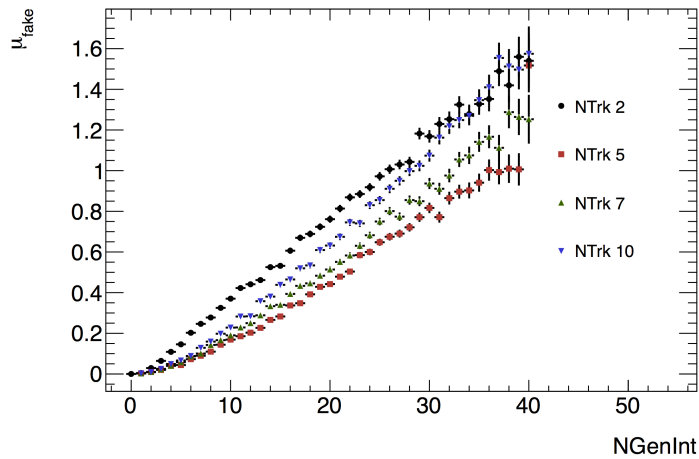


Figure 4.5: Average number of fake vertices per event as a function of the number of generated pp interactions.

A correction is derived for vertex masking using the distribution of longitudinal distances, Δz , between pairs of vertices in the same event. In the absence of masking, if the interaction region has a Gaussian longitudinal profile with width σ_z , then the Δz distribution would be a Gaussian with width $\sigma_z \times \sqrt{2}$. Masking manifests as an absence of reconstructed pairs near $\Delta z = 0$, as shown in figure 4.6.

The correction is derived in a data-driven way as follows.

1. In a data sample with exactly two interactions per event, the number of masked pairs is equal to the number of masked vertices. Using data taken at low pileup values and selecting events with exactly two reconstructed vertices, we calculate the 2-vertex

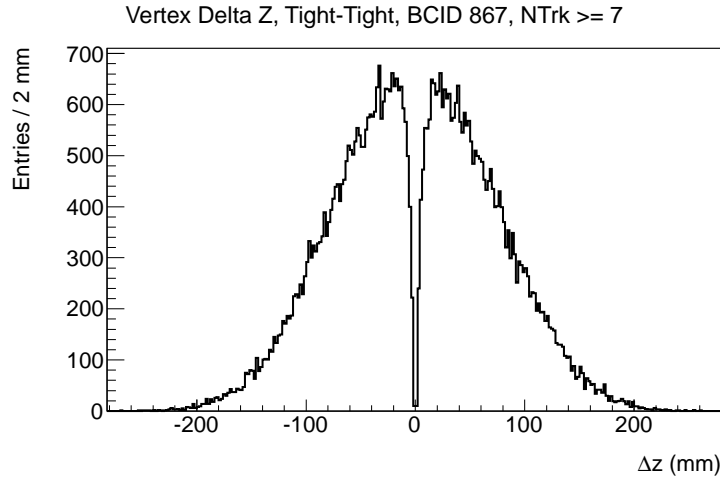


Figure 4.6: Δz distribution between pairs of vertices in the same event, with data from the May 2011 van der Meer scan.

masking probability $p_{\text{mask}}(\Delta z)$, i.e. the probability that only one of two vertices separated by Δz is reconstructed. This function is assumed to be a universal property of the vertexing algorithm, independent of μ .

Specifically, the expected Δz distribution in the absence of masking, $f_{\text{exp}}(\Delta z)$, is derived by randomly sampling pairs of points from the observed z -distribution of reconstructed vertices. Using $f_{\text{exp}}(\Delta z)$ as a template, the *observed* Δz distribution, $f_{\text{obs}}(\Delta z)$, is fitted in the range $30 \text{ mm} \leq |\Delta z| \leq 300 \text{ mm}$, where vertex masking is negligible. Finally, the masking probability is defined as:

$$p_{\text{mask}}(\Delta z) = \frac{f_{\text{exp}}(\Delta z) - f_{\text{obs}}(\Delta z)}{f_{\text{exp}}(\Delta z)} \quad (4.14)$$

The masking probability functions derived from minimum bias Monte Carlo and for low- μ data are shown in figures 4.7 and 4.8.

2. To derive a correction for a particular data sample at arbitrary μ , an *expected* Δz distribution, $f_{\text{exp}}(\Delta z)$, is again derived by randomly sample pairs of vertices from the observed primary vertex z -distribution. Then, the total probability p_{mask} that given any two tight vertices, only one is reconstructed can be computed:

$$p_{\text{mask}} = \int_{-\infty}^{\infty} p_{\text{mask}}(\Delta z) f_{\text{exp}}(\Delta z) d(\Delta z). \quad (4.15)$$

3. The total masking probability p_{mask} is used to generate a map between the number of reconstructible vertices per event, N_{vis} , and the average number of reconstructed vertices per event, μ_{rec} , as follows. Label the generated vertices v_i , $1 \leq i \leq N_{\text{gen}}$, in

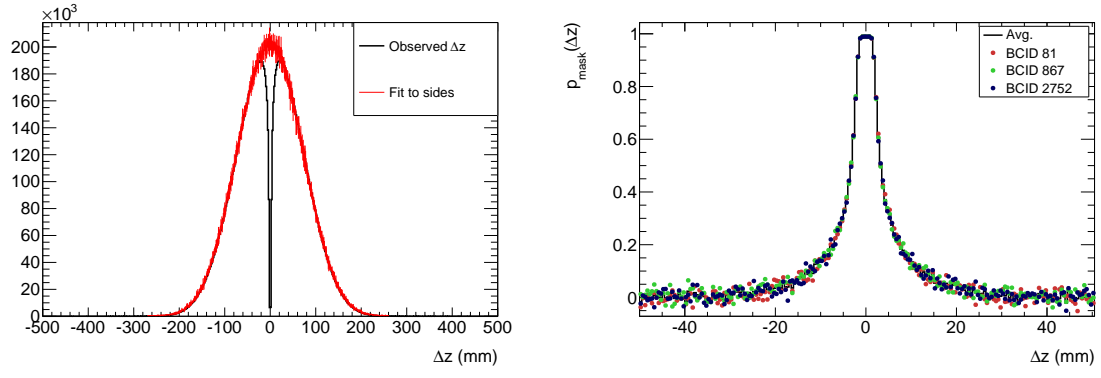


Figure 4.7: Calibration of the masking correction method on data, using run 182013. Left: Δz distributions and template fits using expected Δz distributions in the range $30 \text{ mm} \leq \Delta z \leq 300 \text{ mm}$. Right: pairwise vertex masking probability as a function of the longitudinal distance Δz between the vertices.

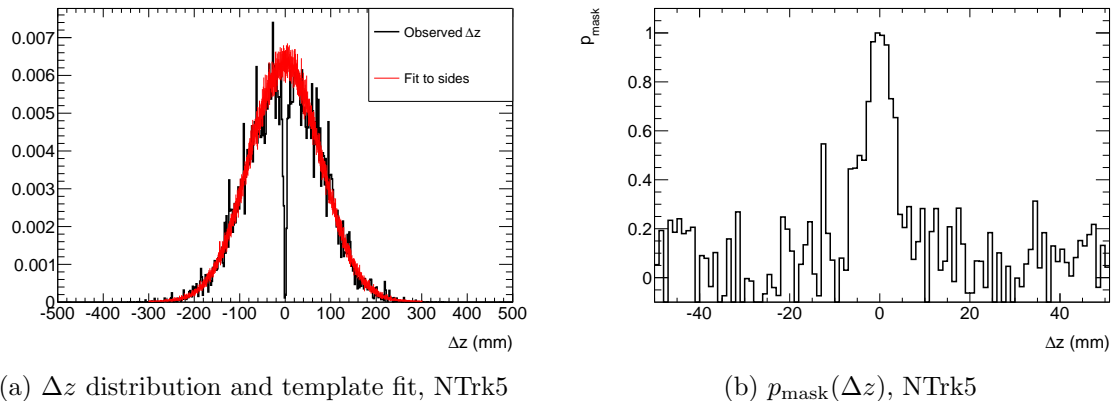


Figure 4.8: Calibration of the masking correction method on simulation, using 8 TeV minimum bias Monte Carlo (PYTHIA 8, tune A2M). Left: Δz distributions and template fits using expected Δz distributions in the range $30 \text{ mm} \leq \Delta z \leq 300 \text{ mm}$. Right: pairwise vertex masking probability as a function of the longitudinal distance Δz between the vertices.

the order in which the iterative vertexing algorithm reconstructs the vertices; similarly, let p_i , $1 \leq i \leq N_{\text{vis}}$, be the probability that vertex v_i is reconstructed. Proceeding vertex-by-vertex, the p_i follow a recursion relation:

$$p_1 = 1 \quad (4.16)$$

$$p_2 = p_1 \times (1 - p_{\text{mask}}) \quad (4.17)$$

$$\dots \quad (4.18)$$

$$p_k = \prod_{i=1}^{k-1} (p_i \times (1 - p_{\text{mask}}) + (1 - p_i) \times 1) \quad (4.19)$$

$$= \prod_{i=1}^{k-1} (1 - p_i p_{\text{mask}}) \quad (4.20)$$

$$= p_{n-1} \times (1 - p_{n-1} p_{\text{mask}}) \quad (4.21)$$

The average number of reconstructed vertices is then:

$$\langle N_{\text{rec}} \rangle = \sum_{i=1}^{N_{\text{vis}}} p_i. \quad (4.22)$$

4. Finally, a map is computed between the average number of reconstructible vertices, μ_{vis} , and the average number of reconstructed vertices, $\mu_{\text{rec}}(\mu_{\text{vis}})$, by convolving $\mu_{\text{rec}}(N_{\text{vis}})$ with a Poisson distribution:

$$\langle \mu_{\text{rec}} \rangle(\mu_{\text{vis}}) = \sum_{N_{\text{vis}}=0}^{\infty} P(N_{\text{vis}}; \mu_{\text{vis}}) \mu_{\text{rec}}(N_{\text{vis}}). \quad (4.23)$$

4.6.3 Vertex-Based Luminosity Measurements in 2011

Due to the low event rate available during physics runs, vertex counting was used to measure luminosity only in three special runs during 2011, where inner detector data were recorded by a special high-rate data stream. The data stream reads out events at $\mathcal{O}(10 \text{ kHz})$, recording only the inner detector from a small number of bunch crossings, typically less than four. The three runs are the vdM calibration run in May 2011, the pileup scan in September 2011 shown in figure 4.4b, and a high- β^* run with a single bunch used to measure the total pp cross section using the ALFA detector.

Van der Meer Scan

An example scan curve from the May 2011 vdM scan is shown in figure 4.9. The trigger used to collect the data required two hits in the MBTS, and selected 3 of the 14 colliding

bunch pairs. The peak interaction rate during the fill was $\mu \sim 2.3$. The data are corrected for vertex masking and fakes, with the correction factor reaching up to 3% at the peak of the scan curves. Following the protocol described in section 4.4, the visible cross section is determined to be (38.50 ± 0.12) mb, where the uncertainty reflects the RMS spread between the three bunch crossings and the two scans.

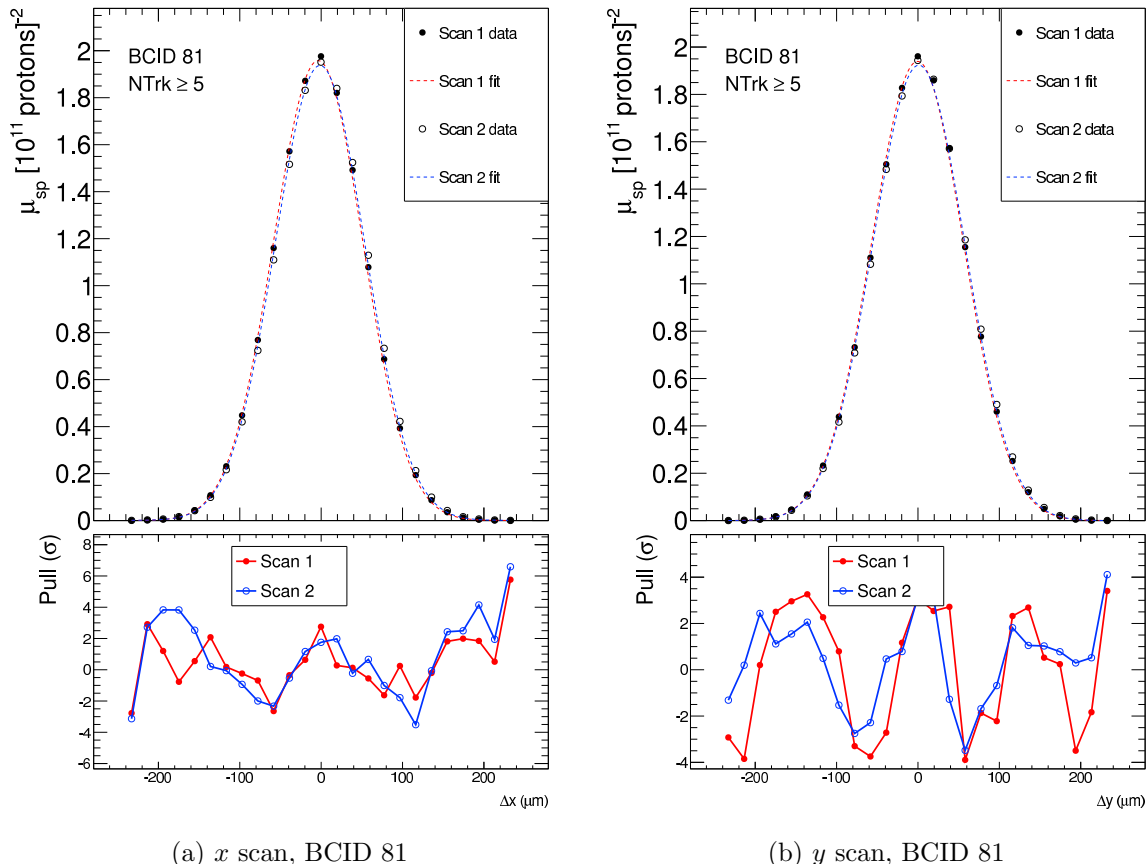


Figure 4.9: $\mu_{vis}^{(sp)}$ vs. beam separation, with single Gaussian plus constant fits, and pulls.

Pileup Scan

The September 2011 pileup scan is used to derive systematic uncertainties due to the non-linear response of algorithms with respect to the number of interactions per bunch crossing. The scan was performed at the end of a physics run, displacing the beams in the transverse direction to obtain a sample of data at over a pileup range of $0.02 \lesssim \mu \lesssim 10$ with otherwise identical conditions. The data was triggered by a random trigger selecting events from two

BCIDs, 200 and 999. The data are corrected for vertex masking and fakes, with the correction reaching up to 10% as shown in figure 4.10 with respect to BCM_VOR. A comparison of the luminosity measurements between vertex counting and BCM_VOR, shown in figure 4.11, exhibits a slope of about 0.1% per unit of μ .

ALFA Run

Finally, vertex counting provides a reliable luminosity measurement for the 2011 ALFA run, a special run used for a measurement of the total pp cross section [14]. The beams contained a single colliding bunch pair with $\beta^* = 90\text{ m}$ and $\mu \sim 0.03$, in order to measure the scattering angle of elastic pp collisions. A special luminosity analysis is required to address the very low instantaneous luminosity of $\mathcal{L} \sim 5 \times 10^{27}\text{ cm}^{-2}\text{ s}^{-1}$, about six orders of magnitude lower than a typical physics fill. The calorimeter methods are unusable due to a lack of sensitivity. For BCM and LUCID, the backgrounds at low instantaneous luminosity have a different composition: afterglow is negligible with a single colliding bunch, but beam-gas interactions can be significant, resulting in an extra 0.2% systematic uncertainty. The low-pileup conditions are ideal for vertex counting, eliminating the need to perform pileup corrections. The requirement of at least five tracks with $p_T > 400\text{ MeV}$ per vertex suppresses the beam-gas backgrounds. The data were recorded by a random trigger at approximately 1 kHz.

A comparison of luminosity measurements from BCM, LUCID, and vertex counting is shown in figure 4.12. To be consistent with the primary pp luminosity measurement, the central value is taken from BCM_VOR; vertex counting shows agreement with this value to within 0.5%.

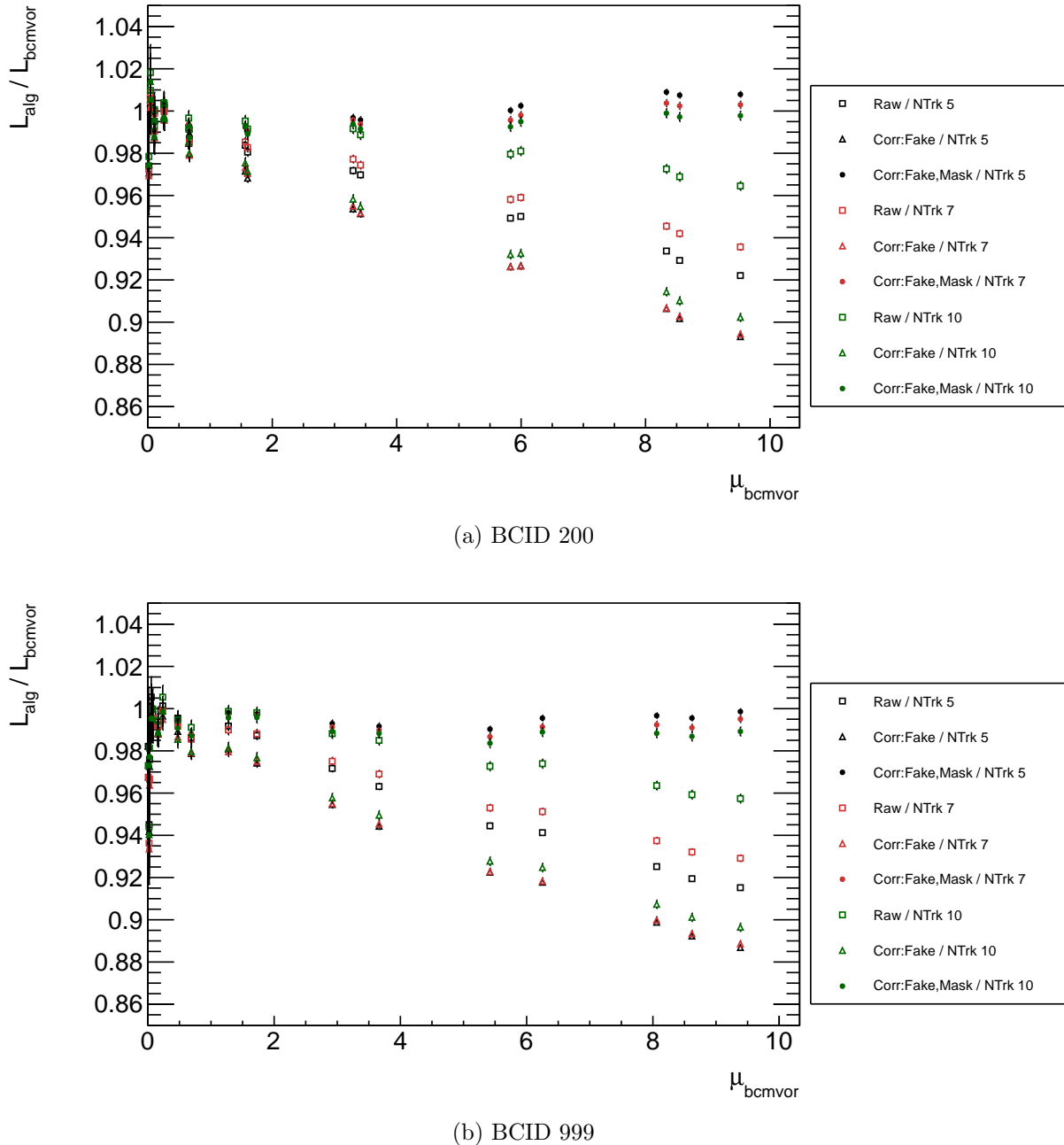


Figure 4.10: Ratio of luminosity values from vertexing to the reference value from BCM_VOR during the pileup scan in September 2011. The black points show the vertex-based luminosity with ≥ 5 tracks, the red with ≥ 7 tracks, and the green with ≥ 10 tracks. The different shapes show the application of each successive pileup correction: the hollow squares show the vertex-based luminosity with no pileup corrections applied, the hollow triangles are corrected for fake vertices, and the solid circles are corrected for both fake and masked vertices.

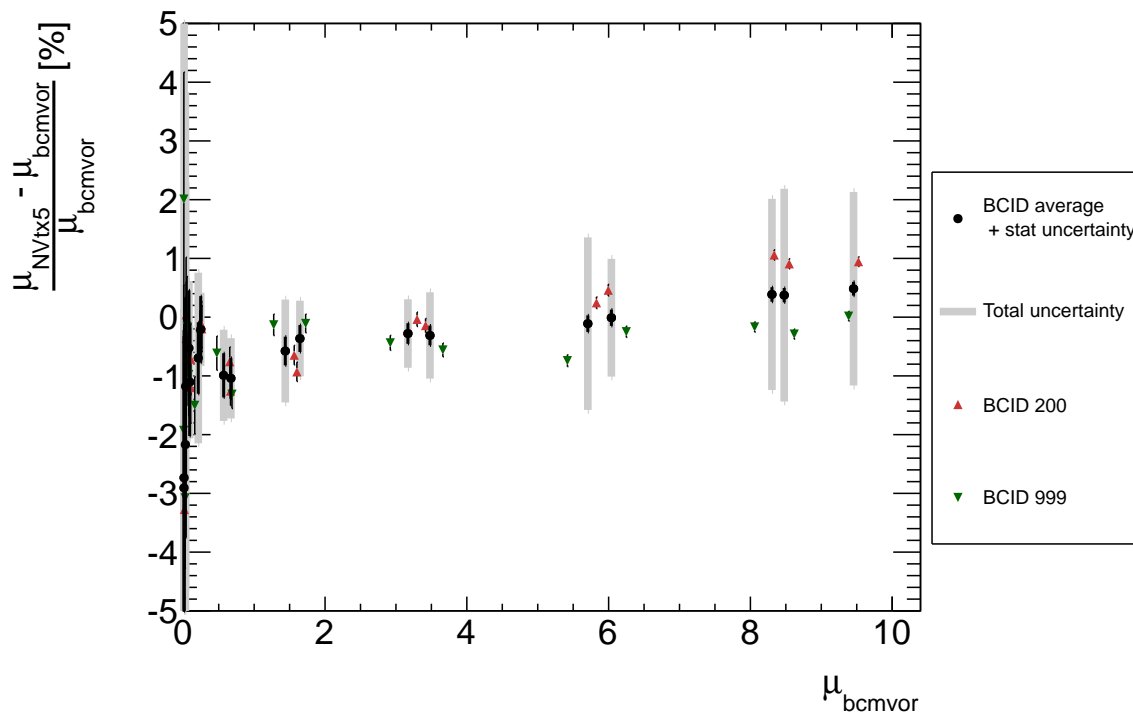


Figure 4.11: Percent difference between luminosities measured by vertex counting and BCM_VOR during the pileup scan in September 2011. Vertices are required to have at least five tracks. The black points show the central values, taken to be the average between the two colliding BCIDs. The gray bars show the spread between BCIDs and between different track cuts (≥ 5 , ≥ 7 , and ≥ 10), summed in quadrature.

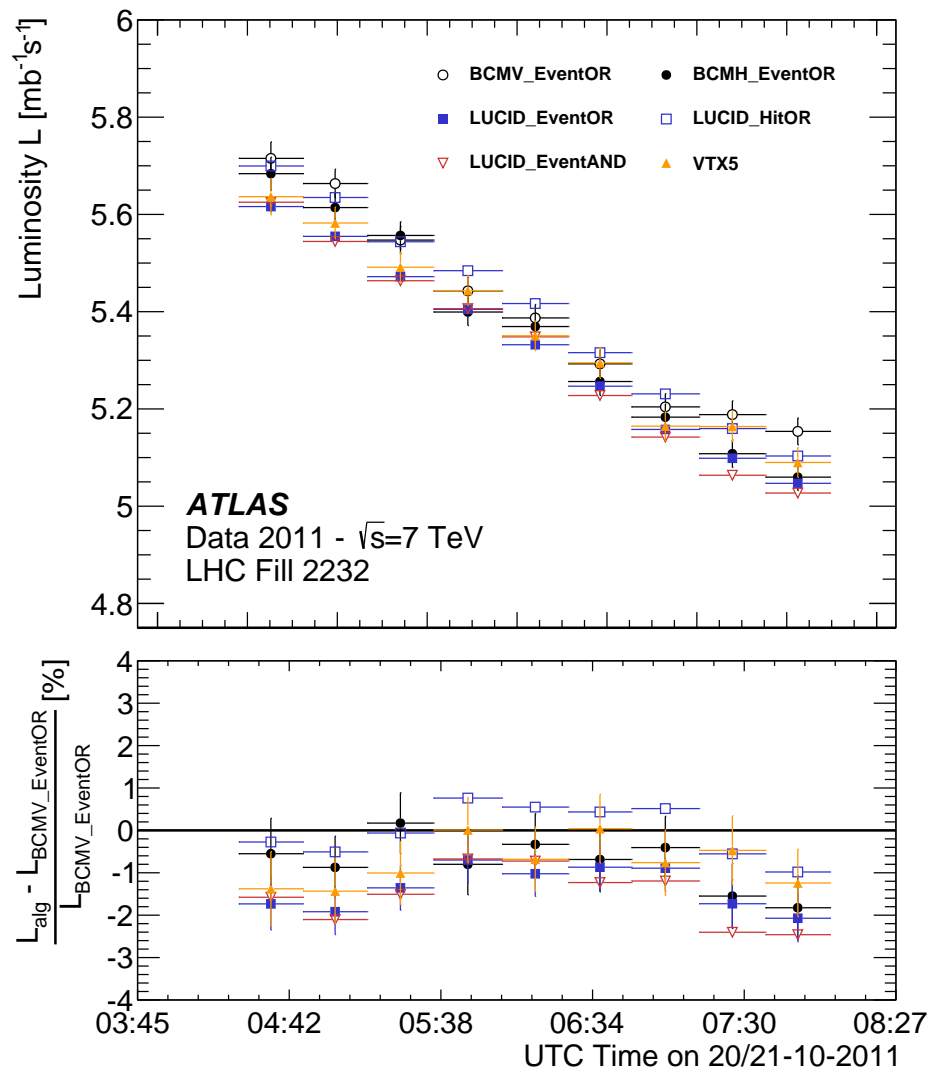


Figure 4.12: Luminosities measured by BCM, LUCID, and vertex counting during the $\beta^* = 90$ m ALFA run in October 2011.

Bibliography

- [1] P. Grafström and W. Kozanecki, *Luminosity determination at proton colliders*, Progress in Particle and Nuclear Physics (2015) pp. 1–52.
- [2] ATLAS Collaboration et al., *Improved luminosity determination in pp collisions at $\sqrt{s} = 7 \text{ TeV}$ using the ATLAS detector at the LHC*, arXiv **C73.8** (2013) p. 2518.
- [3] H. Frais-Kolbl, H. Frais-Koelbl, et al., *The ATLAS Beam Conditions Monitor*, JINST **3.02** (2008) P02004–P02004.
- [4] ATLAS Collaboration, *The ATLAS Experiment at the CERN Large Hadron Collider*, Journal of Instrumentation **3.08** (2008) S08003–438.
- [5] S. van der Meer, *Calibration of the Effective Beam Height in the ISR* (1968) pp. 1–4.
- [6] V. Balagura, *Notes on Van der Meer scan for absolute luminosity measurement*, Nuclear Inst. and Methods in Physics Research, A **654.1** (2011) pp. 634–638.
- [7] C. Barschel et al., *Results of the LHC DCCT Calibration Studies* (2012).
- [8] G. Anders et al., *Study of the Relative LHC Bunch Populations for Luminosity Calibration* (2012).
- [9] A. Alici et al., *Study of the LHC ghost charge and satellite bunches for luminosity calibration*. (2012).
- [10] ATLAS Collaboration, *Measurement of the total cross section from elastic scattering in pp collisions at $\sqrt{s} = 7 \text{ TeV}$ with the ATLAS detector*, Nuclear Physics B **889.C** (2014) pp. 486–548.
- [11] S. Pagan Griso, D. Yu, and B. Heinemann, *Luminosity Measurement in pp Collisions at $\sqrt{s} = 7 \text{ TeV}$ using Vertex Counting with the ATLAS Detector in 2011* (2013) pp. 1–59.
- [12] T. Sjöstrand, S. Mrenna, and P. Z. Skands, *A Brief Introduction to PYTHIA 8.1*, Comput. Phys. Commun. **178** (2008) pp. 852–867, arXiv: 0710.3820 [hep-ph].
- [13] ATLAS Collaboration, *Summary of ATLAS Pythia 8 tunes* (2012).
- [14] ATLAS Collaboration, *Measurement of the total cross section from elastic scattering in pp collisions at $\sqrt{s} = 7 \text{ TeV}$ with the ATLAS detector*, Nuclear Physics B **889.C** (2014) pp. 486–548.

Chapter 5

Event Reconstruction

Once recorded by the detector, events are reconstructed using a wide variety of algorithms designed to identify the products of collisions at the center of the detector. The algorithms transform the raw data read out from the detector – hits in the inner detector silicon layers and TRT straws, energy deposits in calorimeter cells, and hits in the muon stations – into a list of physics objects and their energies or momenta. This section describes the techniques used to identify the objects used in the analyses described in chapters 7 and 8. Section 5.1 describes the reconstruction of tracks and vertices. Sections 5.2, 5.3, and 5.4 detail the reconstruction and energy or momentum measurements of electrons, muons, and τ leptons. Sections 5.5 and 5.6 outline the reconstruction of jets and the total transverse momentum imbalance. Finally, section 5.7 lists the kinematic and quality requirements imposed on reconstructed objects.

5.1 Track and Vertex Reconstruction

Tracks, nominally due to charged particles traversing the inner detector, are reconstructed using a series of algorithms based on hits in the inner detector [1–3]. The primary “inside-out” algorithm begins by constructing three-dimensional space points associated with the hits in the pixel and SCT layers. Track seeds are formed from sets of three space points in the first four layers of the inner detector (three pixel layers and the innermost SCT layer), constrained to be consistent with a track originating from the interaction region. The track seeds are extended through the remaining SCT layers using a combinatorial Kalman filter. After screening the track candidates to reduce random coincidences and ambiguities from very close tracks, the tracks are extended through the TRT. Finally, the track is refitted using all of the associated hits.

A complementary “outside-in” algorithm identifies tracks with fewer or zero silicon hits, which can arise from hadron decays or photon conversions in the silicon layers, or from track seeds removed during the ambiguity resolution. The algorithm starts from TRT segments, and adds silicon hits proceeding inwards.

Vertices are points consistent with being the origin of a set of tracks. Primary vertices are vertices nominally due to pp collisions, while secondary vertices arise from other processes like hadron decays or photon conversions. The primary vertex reconstruction algorithm reconstructs vertices one by one, alternately finding a vertex seed and then fitting the corresponding tracks [3, 4]. For most applications, the tracks are required to have $p_T > 400$ MeV, no missing hits along the track in the pixel layers¹ (*holes*), and at most two holes in the SCT layers. The seed finding identifies the global maximum in the distribution of z coordinates of the tracks. The vertex position is then determined by an adaptive vertex fitting algorithm [5], a χ^2 -based fit which suppresses the contribution from outlier tracks. Tracks whose impact parameter is inconsistent by more than 7σ with the vertex position are then reused to seed a new vertex, until no further seeds can be found.

For most applications, the vertex reconstruction is performed twice. After reconstructing an initial set of primary vertices, the position and size of the interaction region, or *beam spot*, is determined from a fit to the spatial distribution of vertices. The vertices are then reconstructed a second time using the beam spot as a constraint for seed finding and track fitting².

5.2 Electrons

The signature of an electron is an energy deposit in the electromagnetic LAr calorimeter and a track pointing at the energy deposit [6, 7]. The electron reconstruction algorithm begins by searching for clusters of energy in the calorimeter, based on a grid of $N_\eta \times N_\phi = 200 \times 256$ towers of size $\Delta\eta \times \Delta\phi = 0.025 \times 0.025$. The tower energy is the sum of the cell energies in all longitudinal layers within the tower. Energy deposits with $E_T > 2.5$ GeV within a 3×5 window of towers form the seeds for both electrons and photons. Seed clusters are rejected if there is a large amount of energy in the adjacent two towers in η or in the hadronic calorimeter behind the cluster.

Next, the reconstruction algorithm searches for a track within a cone of radius $\Delta R = 0.3$ around the cluster barycenter. Two hypotheses are used for track pattern recognition and fitting: the standard pion hypothesis and an electron hypothesis that allows for larger energy losses due to bremsstrahlung. The cluster and track are required to satisfy one of the following two criteria:

- The barycenter of the cluster and the track extrapolation to the middle layer of the LAr calorimeter satisfy $\Delta\phi < 0.2$ in the direction of track bending or $\Delta\phi < 0.05$ in the other direction.
- The barycenter of the cluster and the track extrapolation to the middle layer of the LAr calorimeter, after rescaling the track momentum to the energy of the cluster, satisfy

¹Excluding missing hits due to an inactive detector element.

²For the luminosity measurement using vertices, the beam spot constraint is not applied in order to avoid biases due to changes in the size of the interaction region

$\Delta\phi < 0.1$ in the direction of track bending or $\Delta\phi < 0.05$ in the other direction. This recovers low-energy electrons that potentially lose a significant fraction of their energy before reaching the calorimeter.

For tracks with at least four silicon hits, the track and the cluster must also satisfy $|\Delta\eta| < 0.05$. Finally, the cluster and track are rebuilt using algorithms optimized for measurement of the electron properties. The cluster is rebuilt sequentially in all four layers, using an area of 3×7 layer-2 cells in the barrel or 5×5 layer-2 cells in the end-caps. The tracks of electron candidates are refit using an optimized electron track filter based on the Gaussian Sum Filter (GSF) algorithm [8]. The GSF track and the cluster must satisfy tighter spatial matching criteria: $\Delta\phi < 0.1$ in the direction of track bending, or $\Delta\phi < 0.05$ in the opposite direction. GSF tracks with less than four silicon hits are required to satisfy even tighter criteria: $|\Delta\eta| < 0.35$ or 0.2 in the TRT barrel or end-cap, and $\Delta\phi < 0.03$ in the direction of track bending or $\Delta\phi < 0.02$ in the other direction.

5.2.1 Identification

Further requirements can be imposed on electron candidates to suppress backgrounds from sources like misidentified hadronic jets, photon conversions, and electrons from hadron decays. Three increasingly stringent sets of cuts are defined, called `loose++`, `medium++`, and `tight++`³. The analyses described in chapters 7 and 8 use the `tight++` cuts to select signal electrons. The `medium++` and `loose++` cuts to derive data-driven background estimates. The `loose++` set of cuts impose requirements on the shower shape in the first and second calorimeter layers, the quality of the track, the fraction of energy in hadronic calorimeter cells behind the electromagnetic calorimeter cells, and the spatial match of the track and the calorimeter cluster. The `medium++` set of cuts contains more stringent versions of the `loose++` cuts, and additionally require a small track impact parameter with respect to the primary vertex, a minimum number of high-threshold TRT hits associated with the track, and a hit in the innermost pixel layer. The `tight++` set of cuts again contain more stringent versions of the `medium++` cuts, with an additional cut on the ratio of the cluster energy to the track momentum (E/p) and a veto of candidates associated to a photon conversion vertex.

5.2.2 Efficiency Measurements

The efficiency to detect an electron can be factorized into several components: seed cluster detection, reconstruction, and identification [7]. The efficiency to detect a cluster in the electromagnetic calorimeter is very high, above 99% for electrons with $E_T = 15$ GeV and 99.9% for $E_T = 45$ GeV. The reconstruction efficiency, covering the matching of a good-quality track to the cluster, and the identification efficiencies, covering the identification cuts with respect to reconstructed electrons, are measured using tag-and-probe techniques

³An alternative method of identification using a likelihood-based multivariate method has been developed, but is not used in this dissertation.

targeting $Z \rightarrow ee$ and $J/\Psi \rightarrow ee$ events. The combined reconstruction and identification efficiencies are shown in figure 5.1. The reconstruction efficiency accounts for 1–5% of the total efficiency loss for electrons with $E_T < 20$ GeV, and less than 1% for electrons with $E_T > 80$ GeV. The efficiencies are computed for both data and simulation, and the ratio between the two is used to correct the efficiency in simulation. The systematic uncertainty on the reconstruction efficiency is around 0.5% (0.5%–1.5%) for electrons with $p_T > 25$ GeV ($p_T < 25$ GeV), and 1%–2% (5%–6%) for the identification efficiency.

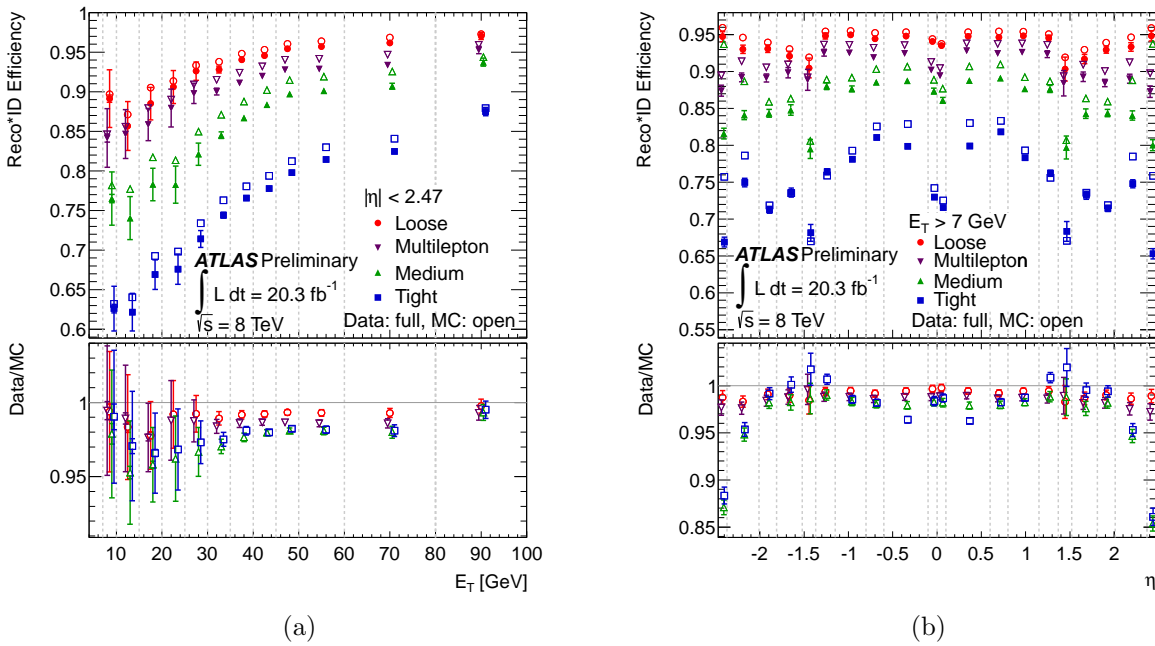


Figure 5.1: The combined reconstruction and identification efficiencies with respect to electrons detected as a cluster in the electromagnetic calorimeter, shown as a function of E_T (left) and η (right) [7]. The error bars show the statistical uncertainty (inner) and the statistical plus systematic uncertainty (outer). The *multilepton* identification cuts are optimized for low energy electrons in the $H \rightarrow ZZ^* \rightarrow 4\ell$ analysis, and are not used in this dissertation.

5.2.3 Energy and Momentum Measurement

For electron candidates with at least four silicon hits, the energy of the electron is taken from the calorimeter measurement, while the trajectory is taken from the GSF track. Candidates with fewer than four silicon hits are not used in this dissertation.

The energy measurement is calibrated using a multivariate algorithm trained on single-electron Monte Carlo (MC) simulation to determine the most probable electron energy. The method takes into account differences between data and simulation in the energy scales of each longitudinal layer and other detector effects not modeled in simulation.

After the initial simulation-based calibration, the electron energy scale and resolution are determined using $Z \rightarrow ee$ events. Corrections are applied to equalize the energy scale and resolution between data and simulation. The energy scales in data and simulation agree to within $\sim 1\%-2\%$ in the barrel and $\sim 4\%$ in the end-caps. The resolution corrections, parametrized as a Gaussian constant term, are approximately 0.8% in the barrel and 0.5%–2.5% in the end-caps. The systematic uncertainty on the energy scale ranges from 0.03%–0.22% for $E_T = 40\text{ GeV}$ and 0.27%–2.25% for $E_T = 200\text{ GeV}$, with larger uncertainties in the transition region between the barrel and the end-cap. The systematic uncertainty on the energy resolution is less than 10% for electrons with $E_T < 50\text{ GeV}$, and asymptotically approaches $\sim 40\%$ for high E_T . The energy resolution is shown as a function of E_T in figure 5.2.

5.3 Muons

Muons are reconstructed in several different ways, depending on the instrumentation available in the vicinity of the muon candidate [10]. The analyses described here use *combined* (CB) muons, consisting of matched tracks reconstructed independently in the inner detector and the muon spectrometer (MS). The tracks in the MS are local track segments reconstructed within each MDT or CSC layer. The muon momentum is determined from a statistical combination of the two track's parameters and their corresponding covariance matrices. Combined muons have the highest purity, but suffer from a loss of acceptance in the range $|\eta| < 0.1$, where the muon spectrometer has gaps to accommodate services for the inner detector and calorimeters, and $1.1 < \eta < 1.3$, where some trajectories only pass through one muon station due to incomplete installation. The remaining categories are *standalone* (SA) muons, consisting of a track only in the muon spectrometer; *segment-tagged* (ST) muons, consisting of an inner detector track and one or more track segments in the MDT or CSC chambers; and *calorimeter-tagged* (CaloTag) muons, consisting of an inner detector track matched to a calorimeter energy deposit consistent with the passage of a muon. These categories can recover efficiency in regions of the detector with less instrumentation at the cost of lower muon purity.

For all categories of muons, the inner detector track is required to have at least 1 pixel hit, at least 5 SCT hits, at most 2 pixel or SCT holes, and at least 9 TRT hits for $0.1 < |\eta| < 1.9$. Energy losses in the calorimeter due to ionization, bremsstrahlung, and electron pair production must also be taken into account.

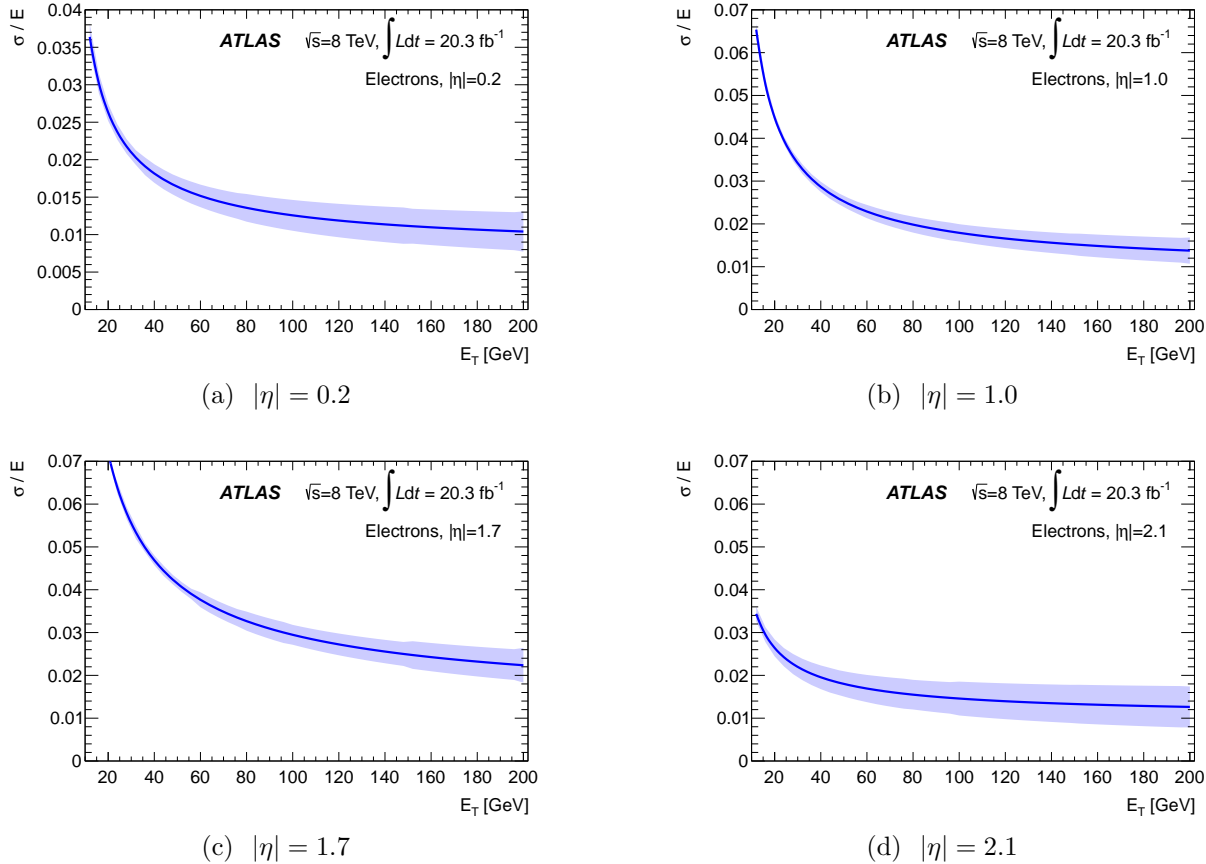


Figure 5.2: Electron energy resolution as a function of E_T for various values of $|\eta|$. The shaded band shows the uncertainty on the resolution [9].

5.3.1 Efficiency Measurements

The efficiency of the reconstructing CB muons is measured as:

$$\epsilon(\text{CB}) = \epsilon(\text{CB}|\text{ID})\epsilon(\text{ID}|\text{MS}), \quad (5.1)$$

where $\epsilon(\text{CB}|\text{ID})$ is the probability that a muon reconstructed as an inner detector track is also reconstructed as a CB muon, and $\epsilon(\text{ID}|\text{MS}) \approx \epsilon(\text{ID})$ is the probability that a muon with a track in the muon spectrometer, i.e. a CB or SA muon, is also reconstructed as an inner detector track. The latter approximation is made because $\epsilon(\text{ID})$ is not directly accessible in data.

The efficiencies are measured using tag-and-probe techniques similar to those described in section 5.2.2, targeting $Z \rightarrow \mu\mu$ and $J/\Psi \rightarrow \mu\mu$ events. The efficiencies for all types of muon are shown in figure 5.3. CB muons have an efficiency of greater than 97% in most of the pseudorapidity range, except for significant inefficiencies due to gaps in the muon

spectrometer in the ranges $|\eta| < 0.1$ and $1.1 < \eta < 1.3$. The measured efficiencies in data and simulation agree to within $\sim 2\%$, and the ratios in each pseudorapidity bin are used as scale factors to correct the efficiency in simulation. The systematic uncertainty on the scale factors is below 0.2% for most of the pseudorapidity range, rising to $\sim 0.3\%$ near $|\eta| \sim 2.5$ and $\sim 0.7\%$ near $|\eta| \sim 0$.

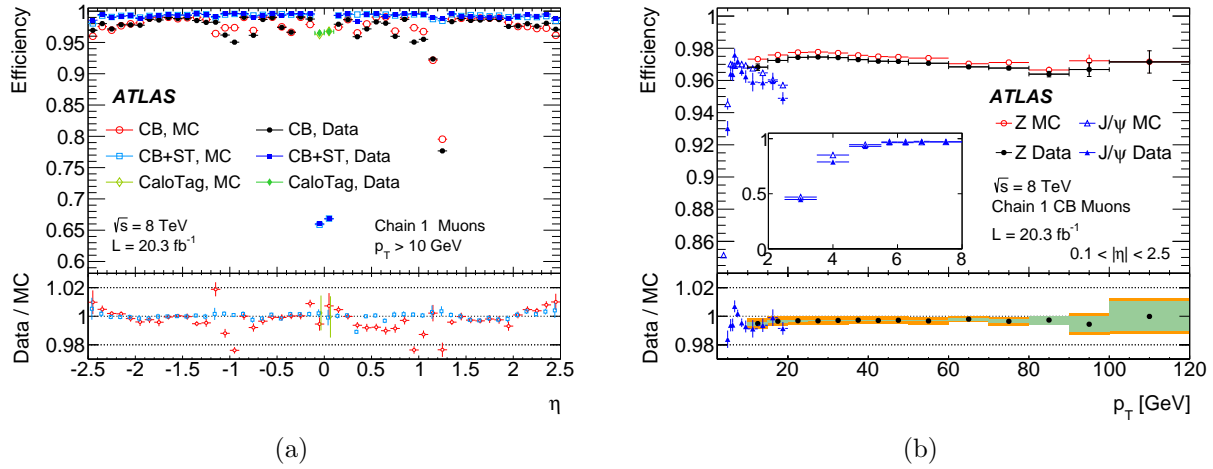


Figure 5.3: Muon reconstruction efficiencies as a function of η for muons with $p_T > 10$ GeV (left), and as a function of p_T for muons with $0.1 < |\eta| < 2.5$ (right) [10]. The uncertainty bars on the points indicate statistical uncertainties. The bottom plots show the ratio between the measured and simulated efficiencies, with the combination of statistical and systematic uncertainties indicated by the uncertainty bars.

5.3.2 Energy Scale and Resolution

The muon momenta in simulation are scaled and smeared to match the momentum scale and resolution in data. The discrepancies arise from mismodeling in various parts of the simulation, such as the muon energy loss before reaching the MS, the detector and its alignment, or the magnetic field. The corrections are derived from $J/\Psi \rightarrow \mu\mu$, $\Upsilon \rightarrow \mu\mu$, and $Z \rightarrow \mu\mu$ events using techniques similar to those described in section 5.2.3. The effect of the corrections on the invariant mass distribution of $Z \rightarrow \mu\mu$ events is shown in figure 5.4, along with the total systematic uncertainty. The muon resolution as measured in Z , Υ , and J/Ψ events is shown in figure 5.5.

5.4 τ Leptons

The signature of τ leptons is significantly more complex than electrons and muons due to the fact that they decay to a diverse set of final states. τ leptons have a proper decay length

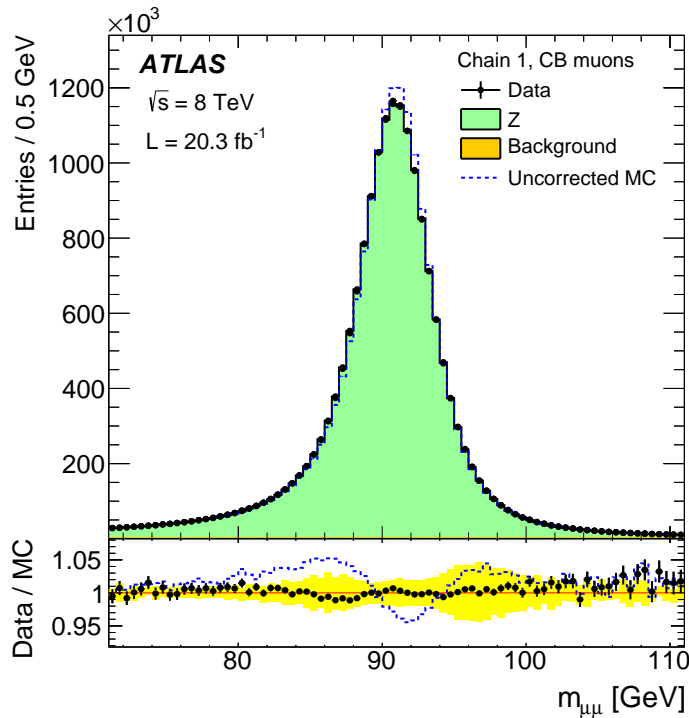


Figure 5.4: Dimuon invariant mass distribution of $Z \rightarrow \mu\mu$ events, using CB muons. The top panel shows the invariant mass distribution for data (black points), expected $Z \rightarrow \mu\mu$ signal from MC simulation (green), and expected background from MC simulation (yellow). The muon momentum corrections are applied to the MC simulation, and the total MC prediction is normalized to the data. The dashed histogram shows the background plus signal without muon momentum corrections. The bottom panel shows the ratio of the data to the normalized MC prediction, with the systematic uncertainty on the momentum corrections shown in the yellow band.

of $87\mu\text{m}$, and therefore typically decay before reaching the active layers of the detector. The leading decay modes are shown in table 5.1. The branching fractions to $e\bar{\nu}_e\nu_\tau$ or $\mu\bar{\nu}_\mu\nu_\tau$ are 17.83% and 17.41%, respectively [11]. The remaining 64.8% of decays are to hadrons plus a neutrino. The hadronic decay modes contain one charged pion in 72% of the decays, and three charged pions in 22% of the decays; the majority of the remainder contain one or more kaons. The hadronic decay modes also frequently contain neutral pions, with 78% containing at least one neutral pion.

In this dissertation, no effort is made to identify or reconstruct leptonic τ decays (τ_{lep}), regarding them only as electrons or muons plus missing transverse momentum (see section 5.6). Hadronic τ decays (τ_{had}) are identified using their visible decay products, namely the neutral and charged hadrons, which are collectively called $\tau_{\text{had-vis}}$. The signature consists of a narrow jet with one or three tracks, called one-prong or three-prong decays, respectively. Up to two $\pi^0 \rightarrow \gamma\gamma$ decays are also included. The reconstruction and identification proceeds as

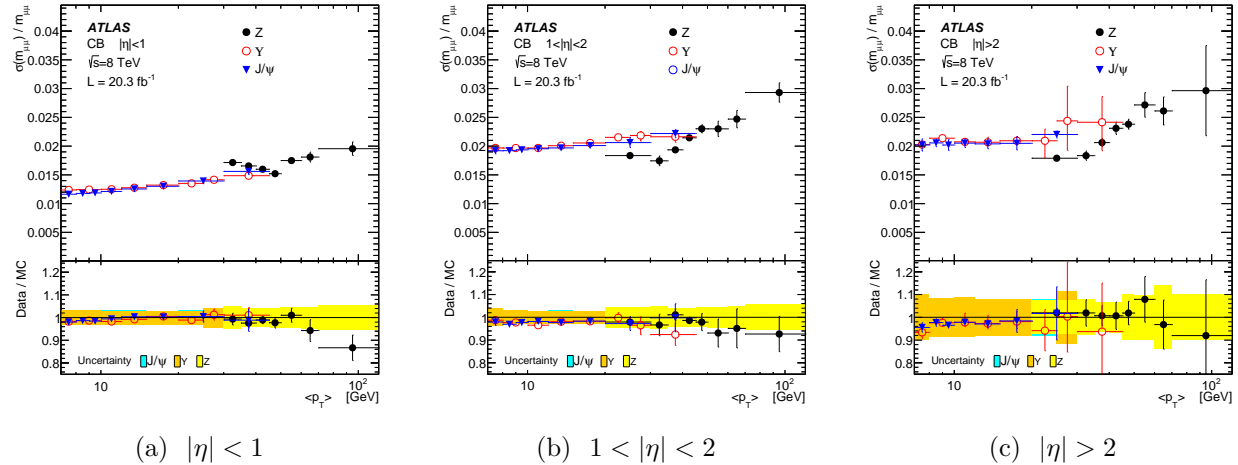


Figure 5.5: Dimuon invariant mass resolution for combined muons as a function of the average muon p_T in three pseudorapidity regions. The resolution is determined from $J/\Psi \rightarrow \mu\mu$, $\Upsilon \rightarrow \mu\mu$, and $Z \rightarrow \mu\mu$ events. Both muons are required to be in the same pseudorapidity region. The J/Ψ and Υ data are plotted as a function of $\bar{p}_T = \frac{p_{T1} + p_{T2}}{2}$, while Z data are plotted as a function of $p_T^* = m_Z \sqrt{\frac{\sin \theta_1 \sin \theta_2}{2(1 - \cos \alpha_{12})}}$, where $\theta_{1,2}$ are the polar angles of the two muons and α_{12} is the angle between the two muons, which removes the correlation between $m_{\mu\mu}$ and \bar{p}_T . The lower panels show the ratio between data and the corrected MC, with bands representing the uncertainty on the MC corrections for the three calibration samples.

Decay	Branching Fraction [%]
$e^- \bar{\nu}_e \nu_\tau$	17.83 ± 0.04
$\mu^- \bar{\nu}_\mu \nu_\tau$	17.41 ± 0.04
$\pi^- \nu_\tau$	10.83 ± 0.06
$\pi^- \pi^0 \nu_\tau$	25.52 ± 0.09
$\pi^- \pi^0 \pi^0 \nu_\tau$	9.30 ± 0.11
$\pi^- \pi^+ \pi^- \nu_\tau$	9.31 ± 0.06
$\pi^- \pi^+ \pi^- \pi^0 \nu_\tau$	4.62 ± 0.06

Table 5.1: Leading branching fractions of the τ lepton to final states with leptons or pions [11]. Most of the remaining decays are to final states with kaons.

follows [12]:

- Jets are reconstructed using the anti- k_t algorithm with a distance parameter of $R = 0.4$, built from TopoClusters calibrated with a local hadronic calibration. Jets with $p_T > 10 \text{ GeV}$ and $|\eta| < 2.5$ are used as seeds for τ lepton candidates.
- For each jet seed, the τ vertex is chosen to be the primary vertex with the greatest $\sum p_T$ of tracks in a cone of radius $\Delta R = 0.2$ around the jet seed. This vertex defines the $\tau_{\text{had-vis}}$ direction, i.e. is used to determine the η and ϕ of the τ candidate.
- π^0 candidates, consisting of a pair clusters within $\Delta R < 0.2$ of the τ candidate, are identified using a multivariate boosted decision tree (BDT) algorithm. The algorithm identifies up to two π^0 s.
- BDT-based identification algorithms are used to discriminate hadronic τ decays from the backgrounds, primarily due to jets with low track multiplicity. The BDTs use many input variables describing the energy cluster, the spatial arrangement and energy of the tracks, and the neutral pions. Separate BDTs are trained for one-prong and three-prong τ decays, using simulated $Z \rightarrow \tau\tau$, $W \rightarrow \tau\nu$, and $Z' \rightarrow \tau\tau$ decays for signal and collision data samples for the background. Three working points with different identification efficiencies are defined: **BDT-loose**, **BDT-medium**, and **BDT-tight**. The performance of the identification algorithms is shown in figure 5.6. The correction factors applied to simulated samples to equalize the efficiencies in simulation and real data are shown in figure 5.7. The correction factors are derived by measuring the efficiencies in data and simulation, using a tag-and-probe method targeting $Z \rightarrow \tau_{\text{lep}}\tau_{\text{had}}$ events. For the **BDTTight** working point, the corrections range from 94%–96%, and carry uncertainties between 2.0%–2.2%.
- An additional BDT-based algorithm rejects one-prong τ candidates consistent with an electron. The most powerful discriminating variables are the ratio of high- to low-threshold TRT hits on the track and the ratio of energies deposited in the electromagnetic and hadronic calorimeters. The electron rejection power versus the τ efficiency, derived from simulated $Z \rightarrow ee$ events, is shown in figure 5.8.

5.4.1 Energy Scale and Resolution

The hadronic τ reconstruction and identification are based on calorimeter cells calibrated at the local hadronic scale. Several corrections are applied to correct the energy to a τ -specific energy scale (TES). First, corrections are derived using simulated $Z \rightarrow \tau\tau$, $W \rightarrow \tau\nu$, and $Z' \rightarrow \tau\tau$ events, generated with PYTHIA8. These corrections are determined as a function of the reconstructed $\tau_{\text{had-vis}}$ energy and pseudorapidity based on the medium identification working point. A small pseudorapidity correction, reaching up to $|\Delta\eta| = 0.01$, corrects a bias

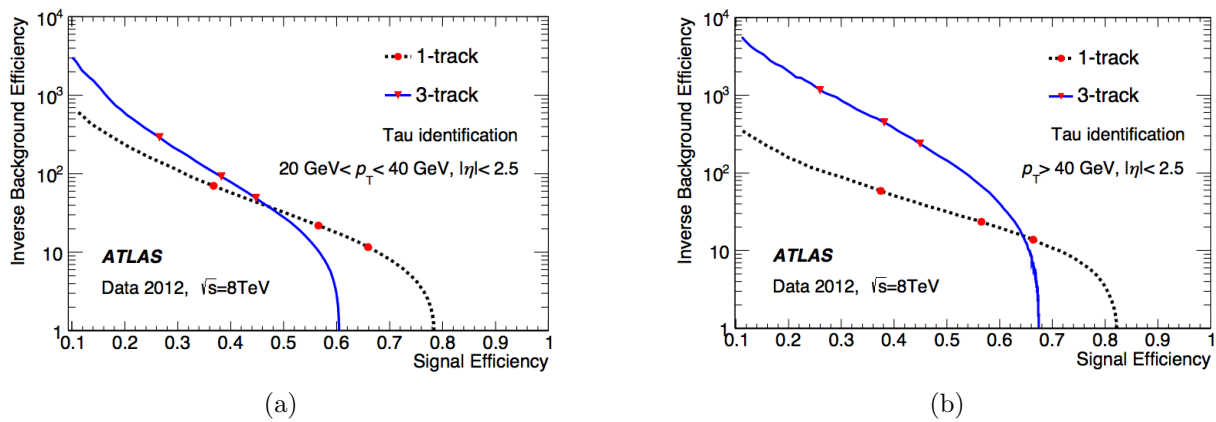


Figure 5.6: Inverse background efficiency (rejection power) versus signal efficiency for the BDT-based offline τ identification algorithm [12]. (a) shows the efficiency for τ leptons with $20 \text{ GeV} < p_T < 40 \text{ GeV}$, and (b) shows the efficiency for τ leptons with $p_T > 40 \text{ GeV}$. The three points on each curve correspond to the BDT-tight, BDT-medium, and BDT-loose working points, in order of increasing signal efficiency and decreasing background rejection power. The background consists of simulated multijet events, while the signal consists of simulated Z , W , and Z' events decaying to τ leptons.

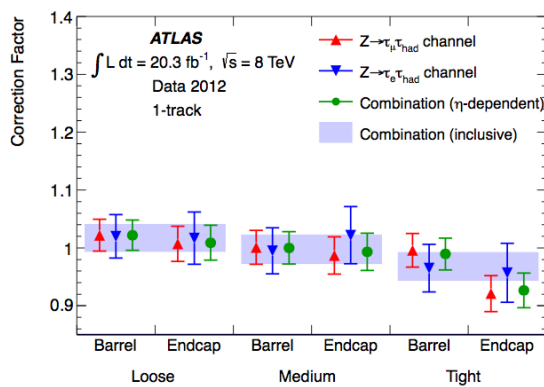


Figure 5.7: Correction factors applied to simulation to equalize the efficiency to that measured in data, as measured in Z tag-and-probe data [12]. The error bars show the combined statistical and systematic uncertainty.

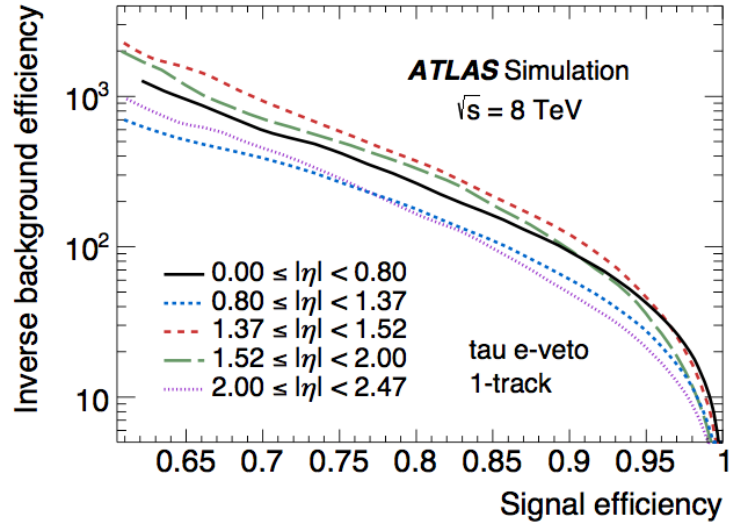


Figure 5.8: Electron rejection power versus 1-track τ_{had} efficiency for the electron rejection BDT [12].

due to underestimated cluster energies in poorly-instrumented regions of the calorimeter. To account for pileup, 90 MeV – 420 MeV per additional reconstructed vertex is subtracted from the reconstructed $\tau_{\text{had-vis}}$ energy, depending on η . The simulated $\tau_{\text{had-vis}}$ energy resolution after these corrections is shown in figure 5.9, and ranges between about 20% at very low energy to about 5% above a few hundred GeV.

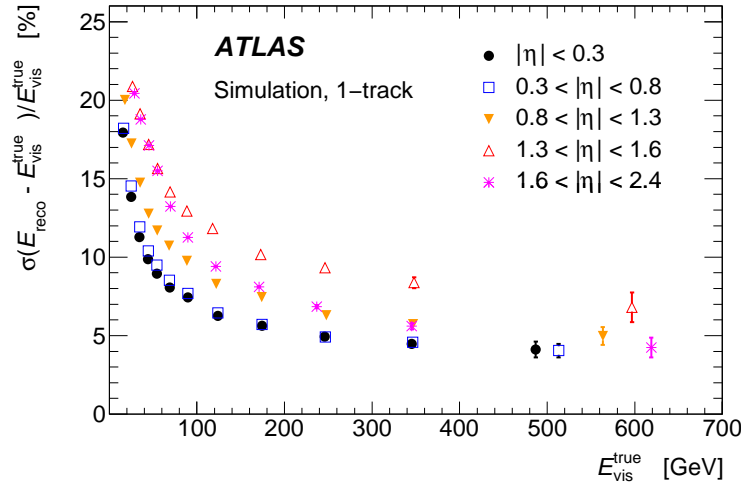


Figure 5.9: Energy resolution for hadronically decaying τ leptons with one associated track in various pseudorapidity regions [12]. The resolution is the standard deviation of a Gaussian fit to the distribution of $\frac{E_{\text{reco}} - E_{\text{true-vis}}}{E_{\text{true-vis}}}$ in bins of $E_{\text{true-vis}}$ and $|\eta_{\text{true-vis}}|$.

Finally, data-driven corrections and systematic uncertainties on the τ energy scale are derived using a *deconvolution* method [13]. The method combines the systematic uncertainties on the single-particle response of the calorimeters based on the well-known branching fractions of hadronically decaying τ leptons. A TES correction of about 1% is determined. Including additional systematic uncertainties covering the detector modeling, pileup, non-closure of the calibration method, and the hadronic shower model, the total TES uncertainty is 2%–3% for one-prong decays and 2%–4% for three-prong decays.

5.5 Jets

Jets play an important complementary role to leptons in the analyses described in the following chapters. The new physics scenarios considered often produce jets in addition to the three required leptons. If the new particles are colored, as in strongly produced supersymmetry, then high- p_T jets can be produced in cascade decays. Alternatively, if the new particles decay via the weak interaction, then the decays will often contain hadronically decaying weak bosons. From the background point of view, due to the colored initial state in pp collisions, jets are produced copiously at the LHC. Despite the stringent lepton identification cuts, jets misidentified as leptons or containing semileptonic decays can constitute a significant source of backgrounds to trilepton final states.

The reconstruction of jets in the calorimeter is based on topological clusters of energy [13, 14]. The reconstruction steps are shown in figure 5.10. Clusters are formed by grouping together calorimeter cells based on their signal-to-noise ratio, S/N , where the N includes electronic noise and contributions from pileup interactions. Cells with $S/N > 4$ form the cluster seeds, which are then expanded to include all connected cells with $S/N > 2$. Finally, cells along the perimeter with $S/N > 0$ are added to the cluster. The cluster energies are then calibrated according to one of two scales: the electromagnetic (EM) scale assumes that the cell energy is due to an electromagnetic shower, while the local cell signal weighting (LCW) method classifies energy deposits as electromagnetic or hadronic in origin. The jets used in this dissertation are constructed from cells calibrated at the LCW scale.

Next, the jet finding algorithms group the calibrated clusters into collections of jets. The algorithm used in this dissertation is the anti- k_t algorithm with a distance parameter of $R = 0.4$, implemented in FASTJET [15, 16]. A distance measure between objects, $d_{i,j}$, and between objects and the beam, $d_{i,B}$, is defined as

$$d_{i,j} = \min(k_{t,i}^{2p}, k_{t,j}^{2p}) \frac{\Delta_{ij}^2}{R^2}, \quad (5.2)$$

$$d_{i,B} = k_{t,i}^{2p}, \quad (5.3)$$

where $k_{t,i}$ is the transverse momentum of object i , $\Delta_{ij} = \sqrt{(y_i - y_j)^2 + (\phi_i - \phi_j)^2}$ is the geometrical distance in rapidity ($y_{i,j}$) and azimuthal angle ($\phi_{i,j}$), and p is a parameter that controls the relative importance of energy versus geometrical (Δ_{ij}) scales, taken to be $p = -1$

Jet reconstruction

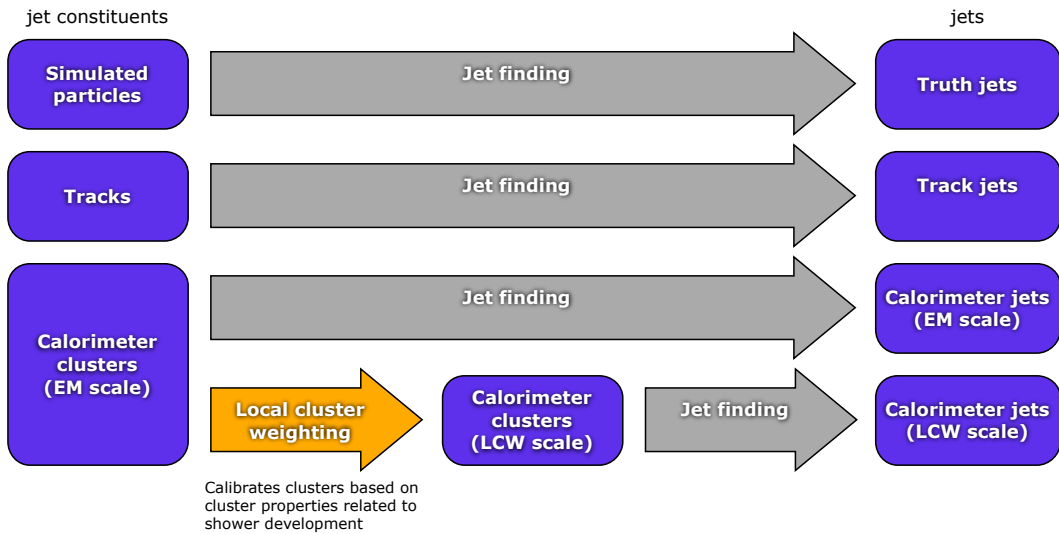


Figure 5.10: Overview of the jet reconstruction, showing the inputs to and outputs from the jet finding algorithms [14]. The bottom two rows show the reconstruction of calorimeter jets, while the top two rows show jets built from truth particles in simulation and from tracks.

for the anti- k_t algorithm. The algorithm combines objects sequentially by considering the smallest distance in the event. If the smallest distance is between two objects i and j , then the objects are combined. If the smallest distance is between object i and the beam B , then i is classified as a jet and removed from the object list. The algorithm continues until there are no objects left.

Loose quality cuts are applied to reject events with jets due to non-collision sources, such beam-gas collisions between protons in one beam and the residual gas in the beam pipe, beam-halo events due to collisions with upstream collimators, muons from cosmic rays, and calorimeter noise. The cuts have an efficiency of above 99.8% for retaining real jets.

5.5.1 Energy Scale and Resolution

The jet energy is calibrated in several steps, as shown in figure 5.11. First, pileup and origin corrections are applied. Energy contributions from pileup interactions in the same or nearby bunch crossings are subtracted based on simulation, with the correction determined in bins of jet p_T and η as a function of the number of reconstructed vertices in the event and the average number of interactions per crossing expected from the instantaneous luminosity. The geometry of the jet is corrected to point from the primary event vertex, rather than the nominal center of the ATLAS detector.

The energy and pseudorapidity of the jet are initially calibrated based on the relationship between jets reconstructed from calorimeter clusters and jets reconstructed from truth par-

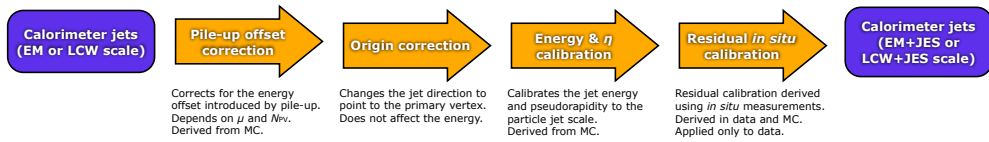


Figure 5.11: Overview of the jet calibration scheme [14].

ticles in simulation. Then, *in situ* corrections are applied to the calibrated jets to correct for effects not described by the initial simulation-based calibration. The corrections are based on balancing the transverse momenta of jets against other well-calibrated objects. Jets in the central region, with detector rapidity $|\eta_{\text{det}}| < 1.2$, are calibrated against photons and leptonically decaying Z bosons. Jets with high transverse momentum, $p_{\text{T}} > 210 \text{ GeV}$, are also calibrated using multijet events, balancing the high- p_{T} jet against several low- p_{T} jets. Jets with $1.2 < |\eta_{\text{det}}| < 2.8$ are calibrated against central jets with $|\eta_{\text{det}}| < 0.8$; due to a lack of statistics with which to derive the calibration, more forward jets, with $\pm 2.8 < \eta_{\text{det}} < 4.5$, are assigned the same calibration as jets with $\eta_{\text{det}} = \pm 2.8$. The *in situ* calibrations shift the jet energy by about 2% for $p_{\text{T}} < 100 \text{ GeV}$, and decreasing to about 1% for $p_{\text{T}} > 200 \text{ GeV}$.

A large number of systematic uncertainties are assigned to the *in situ* calibration procedure, related to the modeling of the detector and physics processes in simulation and to the *in situ* methods themselves. The uncertainties are summarized in figure 5.12. Additionally, systematic uncertainties related to the pileup correction, high- p_{T} jets, jet flavor, and differences simulation settings are assigned where appropriate.

5.5.2 Pileup Suppression

Jets due to pileup interactions can be suppressed using the track information, at the cost of introducing some pileup-dependence to the jet reconstruction inefficiency [17]. For a given jet and primary vertex, the *jet vertex fraction* (JVF) is defined as the ratio of the $\sum p_{\text{T}}$ of tracks associated with the jet and matched to the primary vertex to the $\sum p_{\text{T}}$ of all tracks associated to the jet, shown schematically in figure 5.13. Specifically, letting \mathcal{T} be the set of tracks associated to the jet, the JVF is defined as:

$$\text{JVF} = \frac{\sum_{i \in \mathcal{T}} p_{\text{T},i} \Theta_V(i)}{\sum_{i \in \text{jet}} p_{\text{T},i}}, \quad (5.4)$$

where $\Theta_V(i) = 1$ if the track i is matched to the primary vertex and 0 otherwise. If \mathcal{T} is empty, then $\text{JVF} \equiv -1$. In this dissertation, the primary vertex is chosen as the vertex with the highest $\sum p_{\text{T}}^2$ of tracks, and $\text{JVF} > 0.5$ is required for jets with $20 \text{ GeV} < p_{\text{T}} < 50 \text{ GeV}$.

5.5.3 b -tagging

The model-independent trilepton analysis (chapter 7) also makes use of the tagging of jets due to b quarks. Jets containing b quarks have several features which distinguish them from

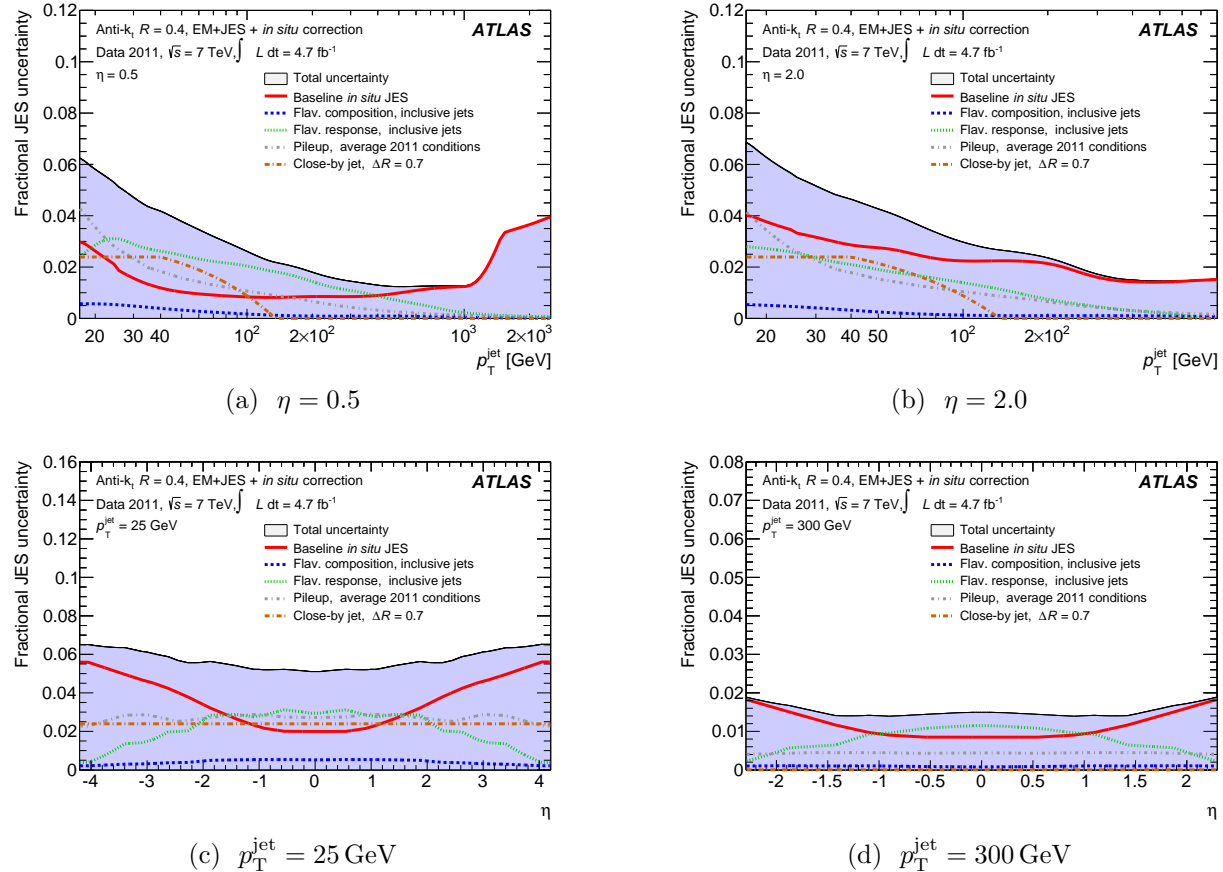


Figure 5.12: Sample-dependent fractional jet energy scale (JES) systematic uncertainty as a function of p_T^{jet} (top) and η (bottom), at fixed values of η or p_T^{jet} , respectively [14]. The jets are reconstruction using the anti- k_T algorithm with a radius parameter of $R = 0.4$ from clusters at the LCW scale, and are calibrated as described in the text. The shaded area shows the total systematic uncertainty, while the colored lines show the contribution of various individual sources of uncertainty.

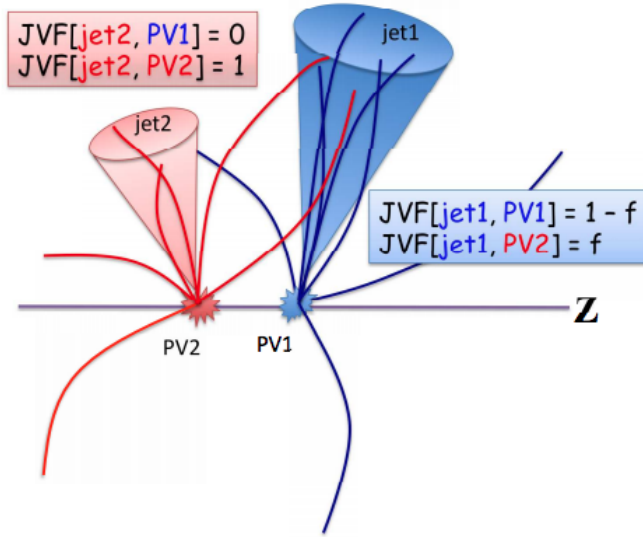


Figure 5.13: Schematic representation of the jet vertex fractions in the case of two jets and two primary vertices [17]. f is the fraction of track p_T in jet 1 due to tracks associated with vertex PV2.

jets due to light quarks or gluons. B hadrons have proper decay lengths of approximate 0.5 mm, long enough to be observed in the form of tracks or vertices reconstructed away from the primary interaction point. They also have large masses compared to other hadrons, leading to wider jets with more particles.

The algorithm used to tag b -jets is an artificial neural network called the MV1 algorithm [18]. The neural network uses three simpler likelihood-based algorithms as inputs [19, 20]:

- **IP3D:** Uses the transverse and longitudinal impact parameters of the tracks associated with a jet.
- **SV1:** Attempts to reconstruct a secondary vertex from the tracks associated with a jet. The most sensitive variable is the decay length significance between the secondary vertex and the primary event vertex. Additionally, the algorithm uses the invariant mass of tracks associated with the secondary vertex, the ratio of the energy of tracks assigned to the vertex to the energy of all tracks within the jet, and the number of two-track vertex candidates within the jet.
- **JetFitter:** Constructs a line connecting the primary vertex with one or more points associated with b - or c -hadron decays using a Kalman filter. The algorithm makes use of variables similar to the SV1 algorithm, along with the flight length significance between decays. Note that the algorithm does not require secondary vertices, allowing for the identification of decays with only one track.

The MV1 algorithm is trained on simulated data, using b -jets as signal and light quark jets as background, and returns a tag weight for each jet. The tag weight is used to establish working points with a given signal efficiency and background rejection power, as shown in figure 5.14a. The model-independent trilepton analysis uses the working point with 80% signal efficiency, with a corresponding light-flavor rejection power of about 25. The performance of the algorithm as a function of transverse momentum is shown in figure 5.14b.

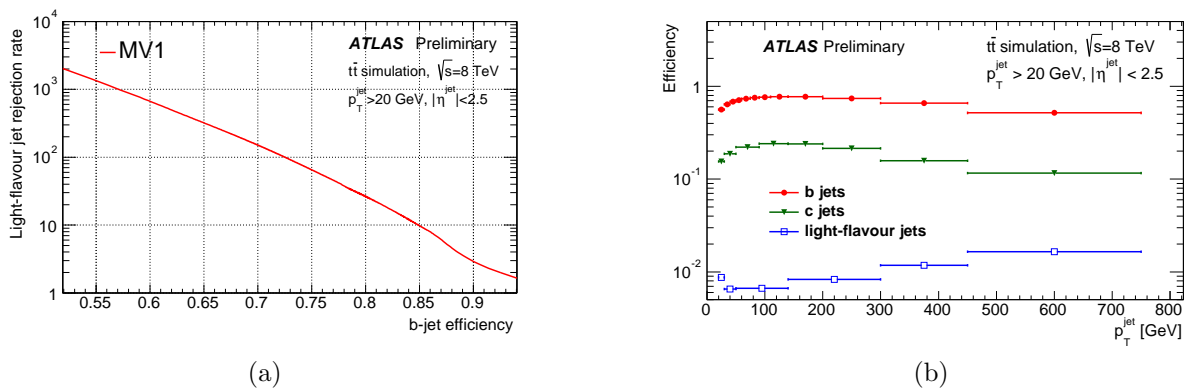


Figure 5.14: Performance of the MV1 b -tagging algorithm. The inclusive signal efficiency versus background rejection is shown at left. The signal and background efficiencies at the 70% working point are shown as a function of p_T at right.

5.6 Invisible Particles

Neutrinos interact only via the weak interaction, and hence escape the detector without interacting with any of the detector components. The same is true for any new stable, neutral, and colorless particles, such as the lightest supersymmetric particle in R parity-conserving scenarios or sterile neutrinos. The presence of such particles can only be inferred through the overall imbalance of the transverse momentum⁴ of the other visible collision products, $\mathbf{E}_T^{\text{miss}} = (E_x^{\text{miss}}, E_y^{\text{miss}})$.

The missing transverse momentum is defined as the negative vector sum of the visible objects in the event [21, 22]. The energies are mostly determined from calorimeter measurements, except for muons. To avoid using calorimeter energy deposits multiple times, the algorithm assigns energy to deposits to a single object according to a strict order: electrons are identified first, followed by photons, hadronically decaying τ leptons, jets, and muons. Depending on the analysis requirements, the energy of a given physics object can be determined using the full reconstruction algorithm, or the energy deposits can be calibrated to the EM or LCW scales. Finally, topological clusters and tracks not assigned to physics

⁴The longitudinal momentum imbalance, E_z^{miss} , is not useful in pp collisions due to the unknown longitudinal momenta of the initial colliding partons.

objects are included in $\mathbf{E}_T^{\text{miss}}$ calculation as the so-called soft term. The missing transverse energy is given by:

$$E_{x(y)}^{\text{miss}} = - \left(E_{x(y)}^e + E_{x(y)}^\gamma + E_{x(y)}^\tau + E_{x(y)}^{\text{jets}} + E_{x(y)}^\mu + E_{x(y)}^{\text{soft}} \right), \quad (5.5)$$

where each term on the right represents the total momentum of the reconstructed objects in the x or y directions.

The measured $\mathbf{E}_T^{\text{miss}}$ receives contributions from sources besides invisible particles, including calorimeter noise, particles falling in insensitive regions of the detector, energy mismeasurements, and pileup interactions. These effects are mitigable to varying degrees. Particles falling outside the detector acceptance contribute irreducibly to the $\mathbf{E}_T^{\text{miss}}$ resolution. For physics objects like electrons or jets, the noise and pileup contributions are suppressed by the reconstruction algorithms and identification cuts. To reduce the noise and pileup contributions to the soft term, the cells are grouped into topological clusters. Rejecting events where the $\mathbf{E}_T^{\text{miss}}$ is parallel or antiparallel to the physics objects can mitigate the impact of energy mismeasurements.

5.7 Object Selection

The analyses described in this dissertation search for energetic leptons and jets produced in the decays of new heavy particles. The leptons and jets typically have large transverse momenta and are well-separated from other objects in the event, due to the large difference in the mass scale between the final decay products (leptons or hadrons with mass $m \lesssim 10$ GeV) and the parents (W/Z bosons or the new particles themselves, with mass $m \gtrsim 80$ GeV). The new particles typically have short lifetimes, and hence the leptons and jets are produced promptly at the location of the initial proton-proton interaction, consistent with originating from the selected primary vertex. These properties can be used to suppress backgrounds due to Standard Model processes and detector effects, described in chapter 6.

5.7.1 Leptons

The events used in this dissertation are required to have at least three reconstructed electrons, muons, or hadronically decaying τ leptons. A summary of the lepton selections is shown in tables 5.2 and 5.3. Leptons are required to satisfy the following requirements:

- **Transverse momentum:** Electrons and muons must have $p_T > 15$ GeV, while hadronically decaying τ leptons must have $p_T > 20$ GeV. The transverse momentum cut is driven by the availability of triggers with which to perform data-driven estimates of backgrounds due to sources like semileptonically decays in jets or misidentified jets (see section 6.2.2).

- **Geometrical acceptance:** Electrons are required to have $|\eta| < 2.47$, excluding the transition region $1.37 < |\eta| < 1.52$ between the barrel and end-cap calorimeters. Muons and τ leptons are required to have $|\eta| < 2.5$.
- **Particle identification:** To suppress the reducible backgrounds, the leptons must satisfy strict requirements related to particle identification. Electrons candidates must satisfy the `tight++` set of identification cuts. Electrons are neglected if they fall in a region affected by the presence of a dead front end board in the first or second sampling layer, a dead high voltage supply, or a masked cell in the core. Muons are required to be *combined*, with associated hits in the inner detector and muon spectrometer. Specifically, associated inner detector track must have:
 - A B-layer hit, unless the muon passes through a deactivated region of the B-layer.
 - ≥ 1 pixel hit and ≥ 5 SCT hits, including any deactivated sensors along the trajectory.
 - ≤ 2 total missing hits in the pixel and SCT, excluding deactivated sensors along the trajectory.
 - A successful extension into the TRT, with ≥ 6 TRT hits, of which $< 90\%$ are classified as outlier hits.

Finally, τ leptons must satisfy the `BDT-tight` selection criteria.

- **Impact parameter:** The inner detector track associated with electrons and muons must be consistent with originating from the event primary vertex. The transverse impact parameter significance, defined as the transverse impact parameter d_0 divided by its uncertainty σ_{d_0} , is required to satisfy $\frac{d_0}{\sigma_{d_0}} < 3$. Similarly, the longitudinal impact parameter z_0 is required to satisfy $z_0 \sin \theta < 0.5$ mm. These requirements suppress leptons from semileptonic heavy flavor decays.
- **Isolation:** To further reduce the impact of non-prompt and misidentified leptons, the leptons are required to be isolated from other activity in the event. The cuts on electrons and muons are similar, and limit the amount of nearby activity as measured by inner detector tracks and calorimeter energy deposits:
 - For both electrons and muons, a cut is applied on `ptcone30`, the sum of transverse momenta of tracks associated to the same primary vertex as the lepton within a cone of radius $\Delta R = 0.3$.
 - For muons, a cut is applied on `Etcone30`, the scalar sum of transverse energies of calorimeter cells within $\Delta R < 3.0$ of the muon track.
 - For electrons, a cut is applied on `TopoEtcone30`, the sum of topological calorimeter clusters within a cone of $\Delta R < 3.0$. The use of topological clusters reduces the impact of pileup and out-of-cone leakage.

In this dissertation, the electron and muon isolation variables are required to be less than 10% of the lepton transverse momentum for leptons with $p_T < 100 \text{ GeV}$, and less than $10 \text{ GeV} + 0.01 \times p_T$ for leptons with $p_T \geq 100 \text{ GeV}$.

Isolation requirements are also applied at the trigger level. For the lowest- p_T unprescaled electron and muon triggers, `ptcone20`, the sum of transverse momenta of all tracks within a cone of radius $\Delta R = 0.2$, is required to satisfy $\text{ptcone20}/p_T < 0.1$.

Cut	Electrons	Muons
Object ID	<code>Tight++</code>	Combined Tight
Leading (trigger) E_T/p_T	$E_T > 26 \text{ GeV}$	$p_T > 26 \text{ GeV}$
Subleading E_T/p_T	$E_T > 15 \text{ GeV}$	$p_T > 15 \text{ GeV}$
Trigger Acceptance	$(\eta < 2.47) \&\& !(1.37 < \eta < 1.52)$	$ \eta < 2.4$
Acceptance	$(\eta < 2.47) \&\& !(1.37 < \eta < 1.52)$	$ \eta < 2.5$
Calo. Isolation ($E_T, p_T < 100 \text{ GeV}$)	$\text{TopoEtcone30} < 0.1 \times E_T$	$\text{Etcone30} < 0.1 \times p_T$
Calo. Isolation ($E_T, p_T > 100 \text{ GeV}$)	$\text{TopoEtcone30} < 10 \text{ GeV} + 0.01 \times E_T$	$\text{Etcone30} < 10 \text{ GeV} + 0.01 \times p_T$
Track Isolation ($E_T, p_T < 100 \text{ GeV}$)	$\text{ptcone30} < 0.1 \times E_T$	$\text{ptcone30} < 0.1 \times p_T$
Track Isolation ($E_T, p_T > 100 \text{ GeV}$)	$\text{ptcone30} < 10 \text{ GeV} + 0.01 \times E_T$	$\text{ptcone30} < 10 \text{ GeV} + 0.01 \times p_T$
Track d_0	$\frac{d_0}{\sigma_{d_0}} < 3$	$\frac{d_0}{\sigma_{d_0}} < 3$
Track z_0	$z_0 \sin \theta < 0.5 \text{ mm}$	$z_0 \sin \theta < 0.5 \text{ mm}$

Table 5.2: Electron and muon selection criteria.

Cut	τ leptons
Object ID	BDT Tight
p_T	$p_T > 26 \text{ GeV}$
Acceptance	$ \eta < 2.5$

Table 5.3: τ lepton selection criteria.

5.7.2 Jets and Missing Transverse Energy

Jets are required to have $p_T > 30 \text{ GeV}$, in order to limit the presence of pileup jets. For the geometrical acceptance, jets must lie in the range $|\eta| < 4.5$, so that the jet falls within instrumented regions of the detector. Pileup jets are additionally suppressed with a cut on the JVF (section 5.5.2): for jets with $p_T < 50 \text{ GeV}$, the JVF must be at least 0.5.

Jets consistent with originating from the decay of a b -hadron are identified using the MV1 algorithm [18], with an efficiency of 80%.

For the missing transverse momentum calculation, calorimeter cells associated with electrons or photons with $p_T > 10 \text{ GeV}$ are calibrated specifically to the corresponding object. Cells associated with τ leptons are calibrated as jets, rather than as hadronically decaying τ leptons, due to the ambiguity between jets and τ leptons when using BDT-loose τ leptons in the data-driven reducible background estimate, described in section 6.2.5.

5.7.3 Overlap Removal

Objects are frequently reconstructed as multiple objects; for example, a muon with a hard bremsstrahlung emission might be reconstructed as a muon, an electron, and a jet. In order to resolve ambiguities, the following overlap removal procedure is applied:

- If $\Delta R(e, e) < 0.1$, remove the lower p_T electron, to avoid “a potential bias in the simulation of the reconstruction efficiency for two real, close-by same-flavor leptons” [23].
- If $\Delta R(e, \text{jet}) < 0.2$, remove the jet. This addresses the ambiguity between electrons and jets.
- If $0.2 < \Delta R(\text{jet}, e) < 0.4$ and $p_T(\text{jet}) > 30 \text{ GeV} + 0.05 * p_T(e)$, remove the electron. This suppresses the reducible electron background.
- If $\Delta R(\mu, e) < 0.1$, remove the electron. This addresses cases where a muon radiates a hard photon, which is then reconstructed as an electron.
- If $\Delta R(\mu, \text{jet}) < 0.1$, and:

$$\begin{aligned} p_T^{\text{jet}} < 0.5 p_T^\mu & : p_T^\mu < 200 \text{ GeV}, \text{ or} \\ p_T^{\text{jet}} < 100 \text{ GeV} & : p_T^\mu \geq 200 \text{ GeV}, \end{aligned} \quad (5.6)$$

remove the jet. This is intended to reduce efficiency loss due to the next step from jets induced by muons at high muon p_T .

- If $\Delta R(\text{jet}, \mu) < 0.3$, remove the muon. This requirement suppresses the reducible muon backgrounds.

Bibliography

- [1] T. Cornelissen et al.,
Concepts, Design and Implementation of the ATLAS New Tracking (NEWT) (2007).
- [2] ATLAS Collaboration, *Performance of the ATLAS Silicon Pattern Recognition Algorithm in Data and Simulation at $\sqrt{s} = 7$ TeV* (2010) pp. 1–14.
- [3] ATLAS Collaboration, *Performance of the ATLAS Inner Detector Track and Vertex Reconstruction in the High Pile-Up LHC Environment* (2012) pp. 1–20.
- [4] ATLAS Collaboration, *Performance of primary vertex reconstruction in proton-proton collisions at $\sqrt{s} = 7$ TeV in the ATLAS experiment* (2010) pp. 1–10.
- [5] W. Waltenberger, R. Frühwirth, and P. Vanlaer, *Adaptive vertex fitting*, Journal of Physics G: Nuclear and Particle Physics **34**.12 (2007) N343–N356.
- [6] ATLAS Collaboration,
Electron reconstruction and identification efficiency measurements with the ATLAS detector using the 2011 LHC proton–proton collision data, The European Physical Journal C **74**.7 (2014) pp. 2941–38.
- [7] ATLAS Collaboration, *Electron efficiency measurements with the ATLAS detector using the 2012 LHC proton–proton collision data* (2014) pp. 1–50.
- [8] ATLAS Collaboration, *Improved electron reconstruction in ATLAS using the Gaussian Sum Filter-based model for bremsstrahlung* (2012) pp. 1–22.
- [9] ATLAS Collaboration, *Electron and photon energy calibration with the ATLAS detector using LHC Run 1 data*, The European Physical Journal C **74**.10 (2014) pp. 3071–48.
- [10] ATLAS Collaboration, *Measurement of the muon reconstruction performance of the ATLAS detector using 2011 and 2012 LHC proton–proton collision data*, The European Physical Journal C **74**.11 (2014) pp. 3130–34.
- [11] K. Olive et al., *Review of Particle Physics*, Chin.Phys. **C38** (2014) p. 090001.
- [12] ATLAS Collaboration, *Identification and energy calibration of hadronically decaying tau leptons with the ATLAS experiment in pp collisions at $\sqrt{s} = 8$*

$$\sqrt{s} = 8$$

$s = 8$

TeV

TeV , The European Physical Journal C **75**.7 (2015) pp. 303–33, ISSN: 1434-6052.

- [13] ATLAS Collaboration, *Jet energy measurement with the ATLAS detector in proton-proton collisions at $\sqrt{s} = 7$ TeV*, arXiv.org 3 (2011) pp. 2304–118, arXiv: 1112.6426 [hep-ex].
- [14] ATLAS Collaboration, *Jet energy measurement and its systematic uncertainty in proton–proton collisions at $\sqrt{s} = 7$ TeV with the ATLAS detector*, The European Physical Journal C **75**.1 (2015) pp. 17–101.
- [15] M. Cacciari, G. P. Salam, and G. Soyez, *The anti- k_t jet clustering algorithm*, arXiv **0804**.04 (2008) pp. 063–063.
- [16] M. Cacciari, G. P. Salam, and G. Soyez, *FastJet User Manual*, arXiv **C72** (2012) p. 1896.
- [17] ATLAS Collaboration, *Pile-up subtraction and suppression for jets in ATLAS* (2013) pp. 1–42.
- [18] ATLAS Collaboration, *Calibration of the performance of b-tagging for c and light-flavour jets in the 2012 ATLAS data* (2014) pp. 1–19.
- [19] ATLAS Collaboration, *Expected Performance of the ATLAS Experiment, Detector, Trigger and Physics* (2009) pp. 1–1852.
- [20] ATLAS Collaboration, *Commissioning of the ATLAS high-performance b-tagging algorithms in the 7 TeV collision data* (2011) pp. 1–22.
- [21] ATLAS Collaboration, *Performance of missing transverse momentum reconstruction in proton-proton collisions at $\sqrt{s} = 7$ TeV with ATLAS*, The European Physical Journal C **72**.1 (2012) pp. 1844–35.
- [22] ATLAS Collaboration, *Performance of Missing Transverse Momentum Reconstruction in ATLAS studied in Proton-Proton Collisions recorded in 2012 at 8 TeV* (2013) pp. 1–41.
- [23] D. L. Adams et al., *Recommendations of the Physics Objects and Analysis Harmonisation Study Groups 2014* (2014) pp. 1–41.

Chapter 6

Background Estimation

The relevant Standard Model processes contributing to multilepton final states are diboson production (WZ , ZZ), production of a top quark pair in association with a weak gauge boson ($t\bar{t} + V$), and triboson production ($VVV^{(*)}$, where $V = W$ or Z). Examples tree-level Feynman diagrams of these processes are shown in figure 6.1. These backgrounds, called *prompt* backgrounds, are estimated using Monte Carlo (MC) simulation, as described in section 6.1. Significant backgrounds also arise from processes where at least one reconstructed lepton is due to the semileptonic decay of a hadron, the misidentification of a jet, or the asymmetric conversion of a photon in the detector; such backgrounds are called *reducible* backgrounds. These backgrounds are estimated using either MC simulation or a data-driven technique called the *fake factor* method, and are described in section 6.2.

6.1 Prompt Backgrounds

The prompt backgrounds are estimated using MC simulation. The hard-scattering processes are modeled by dedicated event generators, possibly including the emission of additional partons. Additional QCD radiation is modeled using a parton shower. The detector response is simulated with the ATLAS simulation framework [1] using the GEANT4 toolkit [2]. Pileup is included by overlaying simulated minimum-bias interactions from PYTHIA [3] on the hard scattering event. Simulated events are assigned weights to reproduce the observed pileup distributions in data, and also to account for small differences in the trigger, reconstruction, and identification efficiencies between simulation and data.

The details of the modeling of each sample are described below. The generator, parton shower, PDF set, and underlying event tune for the samples are summarized in table 6.1, and the cross sections, next-to-leading-order (NLO) K -factors, equivalent sample luminosities, and number of events are shown in table 6.2.

- SHERPA [4] is used to model WW , WZ , and ZZ production. Both bosons in the events decay leptonically. Up to three additional parton emissions are included in the matrix element. An important feature of SHERPA is that it accurately models the $W + \gamma^*$

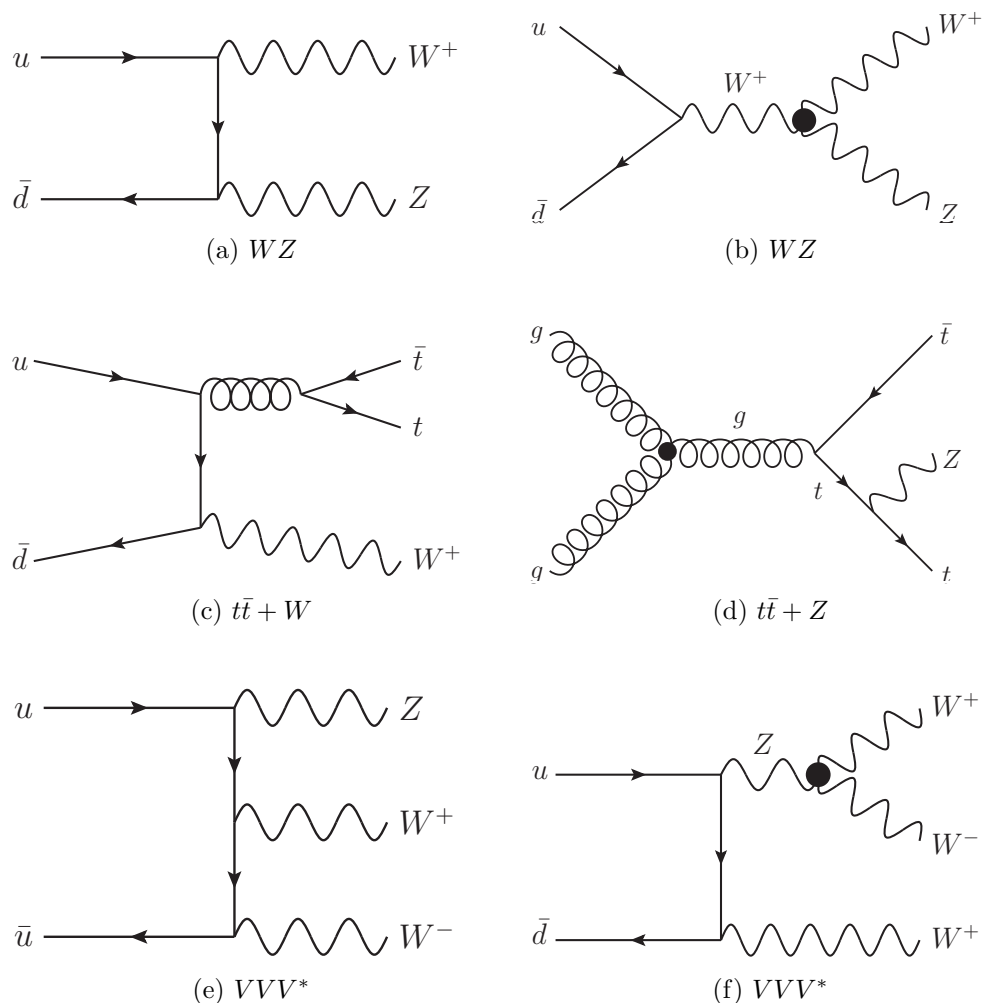


Figure 6.1: Example tree-level Feynman diagrams of Standard Model processes leading to trilepton final states.

Process	Generator	Parton shower and hadr.	PDF set	UE tune
WZ	SHERPA 1.4.3	SHERPA	CT10 [6]	SHERPA
ZZ	SHERPA 1.4.5	SHERPA	CT10	SHERPA
$t\bar{t} + W/Z$	MADGRAPH 5.1.3.33	PYTHIA 6.426	CTEQ6L1 [7]	AUET2B [8]
$VVV^{(*)}$	MADGRAPH 5.1.3.33	PYTHIA 6.426	CTEQ6L1	AUET2B
$Z + \gamma$	SHERPA	SHERPA	CT10	SHERPA

Table 6.1: Configurations of the background MC samples used in this dissertation. The generator, parton shower and hadronization, PDF, and underlying event tune are shown for each sample.

and $Z + \gamma^*$ contributions down to very low γ^* masses; for electron decays, a cut of $m(ee) > 100$ MeV is applied, while for muon and τ decays, SHERPA naturally cuts off the divergence. To increase the statistics in the phase space relevant for this analysis, the WZ samples requires at least two leptons to have $p_T > 5$ GeV. Finally, the WZ sample also treats the b and c quarks as massive, which improves the modeling of heavy flavor jets at the cost of increased computation time.

- $t\bar{t} + V$ production is modeled with MADGRAPH [5], with PYTHIA for the parton shower.
- $WWW^{(*)}$, $ZWW^{(*)}$, and $ZZZ^{(*)}$ are modeled using MADGRAPH, with PYTHIA for the parton shower. Their contributions to all the signal regions are negligible.

Process	$\sigma \times \epsilon_{\text{filter}}$ [pb]	K-factor	$\int \mathcal{L} dt$ [fb $^{-1}$]	Events Simulated
WZ (3 $e\mu$)	2.67	1	2,244	5,998,980
ZZ (4 $e\mu$)	8.6551	1.1	367	3,497,893
WWW (3 $l3\nu$)	5.10×10^{-3}	—	9,800	50,000
ZWW (4 $l2\nu$)	1.55×10^{-3}	—	32,260	50,000
ZZZ (4 $l2\nu$)	0.33×10^{-3}	—	151,500	50,000
$t\bar{t} + W$	0.104100	1.17	3,284	399,997
$t\bar{t} + Wj$	0.093317	1.17	3,663	399,896
$t\bar{t} + Z$	0.067690	1.35	4,377	399,996
$t\bar{t} + Zj$	0.087339	1.35	3,392	399,895
$t\bar{t} + WW$	0.000920	1.00	10,870	10,000
$ee + \gamma$	32.26	—	274	8,849,673
$\mu\mu + \gamma$	32.32	—	278	8,978,579

Table 6.2: Cross section times filter efficiencies, NLO K-factors (if used), equivalent integrated luminosities, and number of events simulated for the background MC samples used in this dissertation. The filter efficiencies account for filters applied to the samples to remove events outside the phase space relevant for the analyses, e.g. imposing cuts on lepton p_T .

6.2 Reducible Backgrounds

The reducible backgrounds encompass a variety of processes in which one or more reconstructed lepton arises due to a non-prompt process or a misidentification of a jet. Such leptons are referred to here as *fake*¹. Sources of such leptons include semileptonic hadron decays, misidentified jets, particles penetrating the calorimeter and leaving hits in the muon spectrometers, and asymmetric photon conversions in the detector. The backgrounds are estimated using simulation or a data-driven technique, depending on the source. The contribution from $Z + \gamma$, where the photon converts asymmetrically and is reconstructed as an electron, is estimated using simulation, as described in section 6.2.1. Other reducible contributions are estimated using a data-driven technique called the *fake factor* method, which is described in section 6.2.2.

6.2.1 $Z + \gamma$ Background

Backgrounds due to $Z + \gamma$, where the Z boson decays leptonically and the photon converts asymmetrically in the detector and is reconstructed as a single electron, are estimated with SHERPA, as shown in table 6.1. The rate of photons being reconstructed as electrons is observed to be overestimated in MC, especially for denominator electrons. The net effect of this mismodeling is a *deficit* in the background prediction, due to its larger effect on the subtraction of prompt contamination in the fake factor method than on the prompt background estimation itself. Scale factors are derived to account for the mismodeling of the conversion rate.

The principle of the method is the same as that used to estimate the electron “charge flip” mismeasurement rate. Charge flips and conversions occur through similar processes: charge flips occur through trident processes in which an electron emits a photon, which then converts asymmetrically and is reconstructed as an electron of the wrong charge. The method determines the charge flip rate in data and MC using events with same-sign electrons with invariant mass close to m_Z ; such events are dominant $Z \rightarrow e^+e^-$ events, where one electron has undergone a charge flip. The charge flip rates are determined in both data and MC using a likelihood minimization. The ratio of the two rates gives the scale factors, shown in table 6.3. The scale factor is applied to each $Z + \gamma$ event based on the classification of the reconstructed lepton closest to the truth photon (within $\Delta R < 0.2$). A 30% systematic uncertainty is assigned on the scale factors, mostly due to variations in the scale factors obtained from different MC generators.

6.2.2 Fake Factor Method

The fake factor method estimates the reducible backgrounds in each signal region by characterizing the fake leptons in terms of quantities sensitive to the non-prompt or fake process,

¹Note that real leptons from, e.g., semileptonic heavy flavor decays are included in the fake leptons.

	$ \eta < 2.2$	$2.2 < \eta < 2.37$	$2.37 < \eta < 2.47$
Numerators	1.02	0.95	0.95
Denominators	0.82	0.66	0.40

Table 6.3: Data-to-MC scale factors for photon conversions.

such as isolation, impact parameter, or particle identification cuts. Two orthogonal sets of reconstructed leptons are defined: *numerator* leptons (N) satisfy the nominal signal lepton selection criteria, while *denominator* leptons (D) satisfy most of the nominal selection criteria, except with inverted requirements on quantities sensitive to the reducible process. The reducible background is estimated in a data-driven way from a control region consisting of events with a mix of numerator and denominator leptons, together with a parametrization of the relationship between numerators and denominators.

The relationship between numerator and denominator objects is called the *fake factor*, f , defined as the ratio of the number of fake leptons satisfying the numerator criteria to those satisfying the denominator criteria. The fake factor is measured in a control region enriched in fake leptons. The success of the method depends largely on the extrapolation of the f from the measurement control region to the signal regions. To capture the dependence on the event kinematics, f can be measured as a function of various lepton or event variables; in this dissertation, the fake factors are all measured in bins of lepton p_T and η .

Once f has been measured, the reducible background is determined as follows. In signal events with three or more leptons, any subset of the leptons could be real or fake. For example, an event might contain two real leptons from a Drell-Yan process plus a non-prompt third lepton from a semileptonic heavy flavor decay. Label such an event $\ell_1^R \ell_2^R \ell_3^F$, indicating the classification of the three leptons at truth level as either real (R) or fake (F). The ordering of the letters corresponds to some canonical ordering of the leptons, such as p_T ordering. If an event contains one lepton from a W decay plus two non-prompt or fake leptons, the event would be labeled $\ell_1^R \ell_2^F \ell_3^F$ (or $\ell_1^F \ell_2^R \ell_3^F$ or $\ell_1^F \ell_2^F \ell_3^R$).

The quantity we desire to determine is the number of events containing three real leptons, $n_{\ell_1^R \ell_2^R \ell_3^R}$. The quantity actually measured in a signal region is the number of events containing three numerator objects, $n_{\ell_1^N \ell_2^N \ell_3^N}$. Any of these numerator objects could be real or fake, so the sample can be decomposed as:

$$n_{\ell_1^N \ell_2^N \ell_3^N} = n_{\ell_1^R \ell_2^R \ell_3^R} + n_{\ell_1^R \ell_2^R \ell_3^F} + n_{\ell_1^R \ell_2^F \ell_3^R} + n_{\ell_1^R \ell_2^F \ell_3^F} + \quad (6.1)$$

$$+ n_{\ell_1^F \ell_2^R \ell_3^R} + n_{\ell_1^F \ell_2^R \ell_3^F} + n_{\ell_1^F \ell_2^F \ell_3^R} + n_{\ell_1^F \ell_2^F \ell_3^F} \quad (6.2)$$

The reducible background prediction is $n_{\ell_1^N \ell_2^N \ell_3^N} - n_{\ell_1^R \ell_2^R \ell_3^R}$, the number of signal events where at least one lepton is fake. To determine the other terms, we use events with one or more denominator leptons. For example, consider $\ell_1^D \ell_2^N \ell_3^N$ events, where the first lepton is a denominator and the remaining leptons are numerators. Assuming that the denominator lepton is always a fake lepton, the number of $\ell_1^D \ell_2^N \ell_3^N$ events, each weighted by the fake factor

f corresponding to the denominator lepton (represented schematically by $n_{\ell_1^D \ell_2^N \ell_3^N} f_1$), equals the number of $\ell_1^N \ell_2^N \ell_3^N$ events where the first lepton is fake:

$$n_{\ell_1^D \ell_2^N \ell_3^N} f_1 = n_{\ell_1^F \ell_2^R \ell_3^R} + n_{\ell_1^F \ell_2^R \ell_3^F} + n_{\ell_1^F \ell_2^F \ell_3^R} + n_{\ell_1^F \ell_2^F \ell_3^F}. \quad (6.3)$$

Similarly, the remaining permutations of numerators and denominators yield:

$$n_{\ell_1^N \ell_2^D \ell_3^N} f_2 = n_{\ell_1^R \ell_2^F \ell_3^R} + n_{\ell_1^R \ell_2^F \ell_3^F} + n_{\ell_1^F \ell_2^R \ell_3^R} + n_{\ell_1^F \ell_2^R \ell_3^F} \quad (6.4)$$

$$n_{\ell_1^N \ell_2^N \ell_3^D} f_3 = n_{\ell_1^R \ell_2^R \ell_3^F} + n_{\ell_1^R \ell_2^F \ell_3^F} + n_{\ell_1^F \ell_2^R \ell_3^F} + n_{\ell_1^F \ell_2^F \ell_3^F} \quad (6.5)$$

$$n_{\ell_1^D \ell_2^D \ell_3^N} f_1 f_2 = n_{\ell_1^F \ell_2^F \ell_3^R} + n_{\ell_1^F \ell_2^F \ell_3^F} \quad (6.6)$$

$$n_{\ell_1^D \ell_2^N \ell_3^D} f_1 f_3 = n_{\ell_1^F \ell_2^R \ell_3^F} + n_{\ell_1^F \ell_2^F \ell_3^F} \quad (6.7)$$

$$n_{\ell_1^N \ell_2^D \ell_3^D} f_2 f_3 = n_{\ell_1^R \ell_2^F \ell_3^F} + n_{\ell_1^F \ell_2^F \ell_3^F} \quad (6.8)$$

$$n_{\ell_1^D \ell_2^D \ell_3^D} f_1 f_2 f_3 = n_{\ell_1^F \ell_2^F \ell_3^F} \quad (6.9)$$

These equations contain eight equations and eight unknowns, so the system can be solved for the reducible background prediction:

$$\ell_1^N \ell_2^N \ell_3^N - \ell_1^R \ell_2^R \ell_3^R = (\ell_1^N \ell_2^N \ell_3^D f_3 + \ell_1^N \ell_2^D \ell_3^N f_2 + \ell_1^D \ell_2^N \ell_3^N f_1) \quad (6.10)$$

$$- (\ell_1^N \ell_2^D \ell_3^D f_2 f_3 + \ell_1^D \ell_2^N \ell_3^D f_1 f_3 + \ell_1^D \ell_2^D \ell_3^N f_1 f_2) \quad (6.11)$$

$$+ \ell_1^D \ell_2^D \ell_3^D f_1 f_2 f_3 \quad (6.12)$$

Note that throughout this method, we have assumed that the leptons used for the measurement of f and the denominator leptons in trilepton events are always reducible leptons. In practice, real leptons contaminate both of these samples. The contribution from real denominator leptons is accounted for using simulation, where the lepton can be classified as real or fake using the truth record of the event.

The remainder of this chapter presents the measurement of the fake factors f for electrons, muons, and τ leptons.

6.2.3 Electron Fake Factors

The background estimation for reducible electrons targets the reducible contribution from two sources: semileptonic heavy flavor decays and misidentified light hadrons. The electron denominator objects are required to pass all of the nominal signal electron requirements except for either failing the `medium++` requirements and passing the `loose++` requirements, or having a larger transverse impact parameter, $3 < \frac{d_0}{\sigma_{d_0}} < 10$, as shown in table 6.4. The two inverted requirements are combined in an exclusive OR. The parameter space between `medium++` and `loose++`, rather than between `tight++` and `medium++`, is used for two reasons. First, for the model-independent trilepton analysis (chapter 7), electrons passing `medium++`

and failing `loose++` are used to define a validation region to test the fake factor method. Second, requiring the electrons to fail `medium++` reduces the prompt contamination in the denominator sample.

Besides passing all of the remaining cuts listed in table 5.2, denominator electrons with $p_T < 24 \text{ GeV}$ must pass an additional cut designed to mitigate an observed inefficiency for loose offline electrons with respect to the loose electron triggers used in the measurement of the fake factors. The inefficiency is likely due to the lack of Gaussian sum filter (GSF) tracking [9] at the trigger level. In order to remove electrons with large amounts of bremsstrahlung whose tracks may not be reconstructed by the non-GSF tracking algorithm in the trigger, denominator electrons are required to satisfy the `tight++` requirements on the matching between the track and the calorimeter cluster in $\Delta\eta$ and $\Delta\phi$. The cut is not applied to electrons with $p_T > 24 \text{ GeV}$, as photon triggers with no track requirement are used in this range.

Criteria	Numerator	Denominator
IsEM ID	<code>tight++</code>	<code>!medium++ && loose++</code>
Impact Parameter Significance	$\frac{ d_0 }{\sigma_{d_0}} < 3$	$3 < \frac{ d_0 }{\sigma_{d_0}} < 10$

Table 6.4: Electron denominator definitions. The denominators are taken to be an exclusive OR combination of the two selection inversions. Additionally, denominator objects must pass the tight requirement on the $\Delta\eta$ and $\Delta\phi$ between the track and the cluster.

The fake factors are measured in a control sample of single-electron events, using the entire 20.3 fb^{-1} 2012 dataset. The triggers used to collect events are listed in table 6.5; photon triggers are used where available ($p_T > 24 \text{ GeV}$), and loose electron triggers are used otherwise ($15 \text{ GeV} < p_T < 24 \text{ GeV}$).

Events are required to have $m_T < 40 \text{ GeV}$ and $E_T^{\text{miss}} < 40 \text{ GeV}$ to suppress contamination from single- W production, where m_T is the transverse mass of the electron and missing transverse energy in the event. Events with two or more electrons, whether numerators or denominators, are rejected in order to suppress prompt contamination from $Z \rightarrow \ell\ell$ events. The electrons are required to be trigger-matched to the trigger used to collect the event in the relevant p_T range. The residual prompt contamination, comprised mostly of W and Z events with smaller contributions from Drell-Yan, $t\bar{t}$ and single- t , is subtracted using simulation. The numerator and denominator event yields, as well as the predicted prompt contamination, are shown in figure 6.2. The prompt contamination consists primarily of W and Z events. The relative size of the prompt contamination is quite large for numerator objects, increasing from 20% to $\sim 60\%$ from $p_T = 20 \text{ GeV}$ to $p_T = 50 \text{ GeV}$, despite the cuts intended to reduce the W and Z contributions. The fake factors are binned two-dimensionally in p_T and η , shown in figure 6.3. The p_T dependence of the fake factors is shown in figure 6.4, for the inclusive sample (left) and for various $|\eta|$ ranges (right).

To help clarify the origin of the structure in η observed at low p_T , the numerator and denominator counts are also shown versus η for $p_T < 24 \text{ GeV}$ in figure 6.5. The numerator

p_T range [GeV]	Trigger Name	Average 2012 Prescale
15–17	EF_e5_loose0	56080.5
17–24	EF_e15vh_loose0	1549.7
24–45	EF_g20_loose	4412.6
45–65	EF_g40_loose	348.3
65–85	EF_g60_loose	80.9
85–105	EF_g80_loose	28.5
105–125	EF_g100_loose	13.0
125–210	EF_g120_loose	1.0
>210	EF_g200_etcut	1.0

Table 6.5: Triggers used to collect electron numerator and denominator objects in various p_T ranges, along with the average trigger prescale in 2012. Electron triggers are denoted by `EF_e`, and photon triggers by `EF_g`. The number indicates the E_T cut in GeV. Triggers labeled `loose` or `loose0` impose shower shape requirements similar to the offline `loose++` electron identification criteria. The trigger labeled `etcut` only imposes the E_T cut, with no shower shape requirement.

counts are relative flat versus η in the central region, and approximately double for $|\eta| \gtrsim 2$. The denominator counts exhibit a significant increase near the barrel/end-cap overlap region and for $|\eta| \gtrsim 2$, nearly tripling the counts compared to the central region.

The following sources of systematic uncertainty are considered:

- **Prompt subtraction:** The presence of real, prompt leptons from Standard Model processes in the sample used to measure the fake factors is accounted for using MC simulation. Uncertainties on the simulated samples include luminosity; cross section uncertainties; and reconstruction, trigger, and identification efficiency scale factors. These lead to a maximum uncertainty of about 20% on the fake factors where the prompt subtraction is largest.
- **Trigger efficiency correction:** As mentioned previously, an inefficiency is observed in the loose electron triggers for offline `loose++` electrons. This is due to the lack of GSF tracking in the trigger. For the fake factor derivation, this affects electrons in the range $15 \text{ GeV} < p_T < 24 \text{ GeV}$, where photon triggers are not available. Imposing the `tight++` cut on the track-cluster matching (the $\Delta\eta$ and $\Delta\phi$ between the electron track and calorimeter cluster) mitigates most, but not all, of the inefficiency, by cutting out electrons with large amounts of bremsstrahlung whose track are not reconstructed in the trigger. Based on a comparison of loose electron and photon triggers in the range $24 \text{ GeV} < p_T < 85 \text{ GeV}$, a correction of about 8% is applied to loose electron-triggered events, and the same value is taken as systematic uncertainty.
- **Extrapolation to signal region:** Two systematic uncertainties are assigned to account for bias due to the extrapolation of fake factors from the control region to the

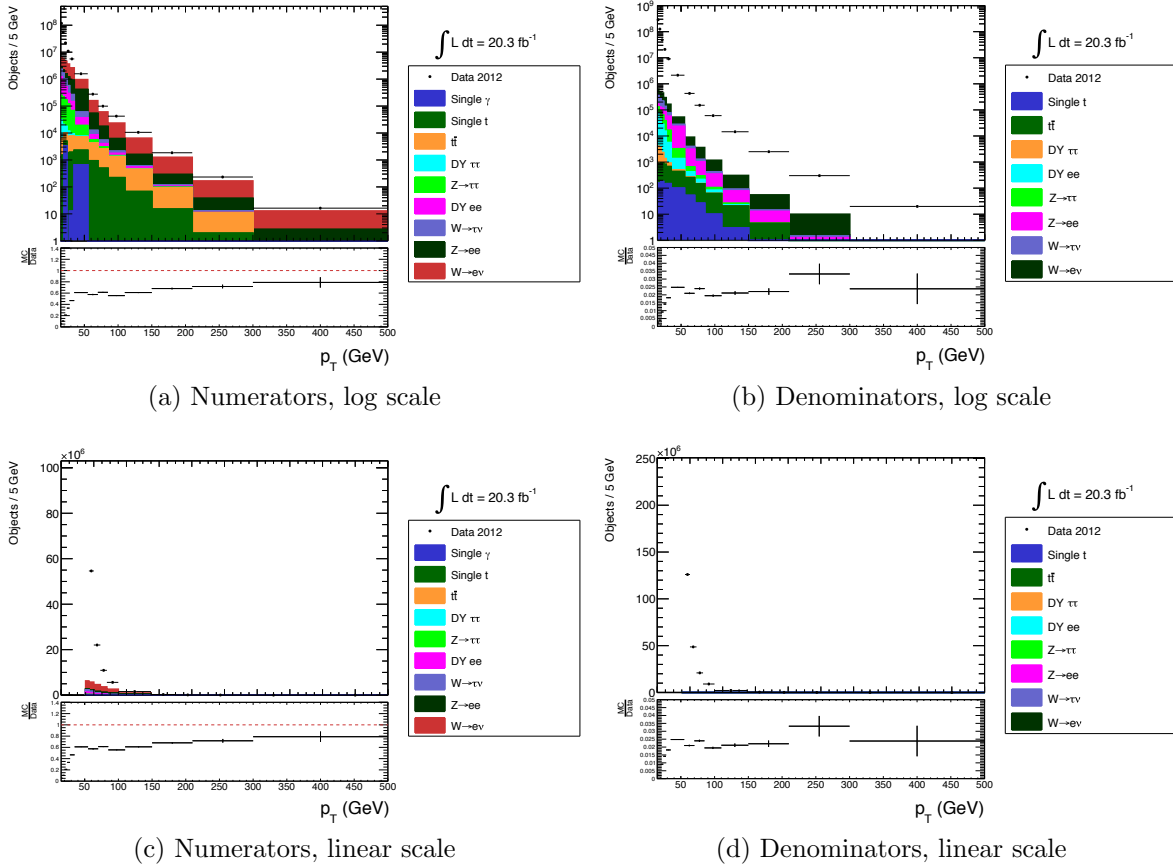
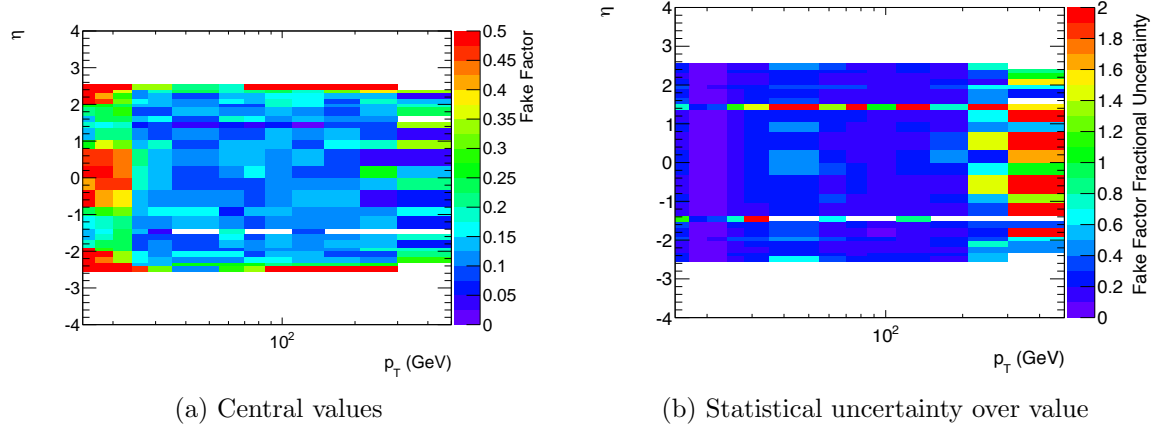
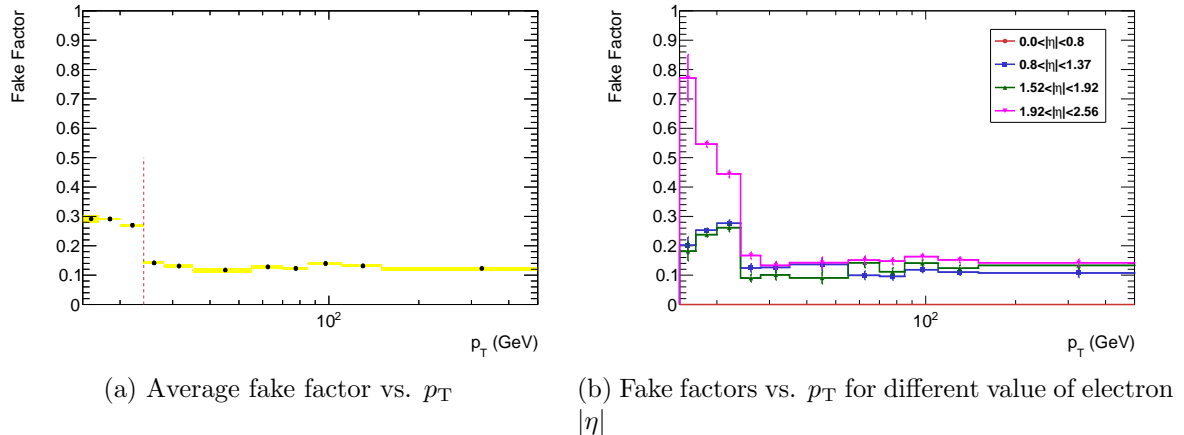


Figure 6.2: Numerator and denominator electron object counts. The data sample consists of all single-electron events in the 2012 dataset, with cuts to reduce prompt contamination as described in the text. The markers represent object counts from 2012 data, and the colored histograms indicate the prompt subtractions estimated from MC.

signal region. First, the cuts on m_T and E_T^{miss} are varied from $< 40 \text{ GeV}$ to $< 25 \text{ GeV}$ and $< 55 \text{ GeV}$. A p_T -dependent systematic uncertainty of up to 15% is assigned.

Second, MC-based truth studies indicate that the fake factor values are quite different for fake electrons due to heavy- and light-flavor jets, so a difference in the heavy flavor fractions between the control and signal regions will bias the fake factors. The effect of this is estimated using a $t\bar{t}$ MC sample, where fake factors are derived separately for fake electrons arising from heavy- and light-flavor jets. The heavy flavor fractions in the control and signal regions are estimated using the d_0 distributions, using the difference in d_0 distributions between heavy- and light-flavor fakes in the $t\bar{t}$ sample. The largest variation in the fake factors from accounting for the different heavy flavor fractions is 20%, which is assigned as a uniform systematic uncertainty independent of p_T and η .

Figure 6.3: Electron fake factors parametrized in p_T and η .Figure 6.4: Electron fake factors projected in p_T . The discontinuity at 24 GeV is due to a change in the the denominator requirements; below 24 GeV, where electron triggers are used, additional requirements are imposed on the track-cluster matching, which cause a drop in the denominator counts, and an increase in the fake factor values.

The systematic and total uncertainties on the fake factors are shown as a function of p_T in figure 6.6.

6.2.4 Muon Fake Factors

The muon fake factor method is similar to that used in the ATLAS same-sign dilepton search on the 7 TeV dataset [10]. The method targets non-prompt muons from semileptonic heavy flavor decays, punch-through, and decays-in-flight of long-lived mesons by inverting the isolation requirements. Specifically, the denominator muons are defined as follows:

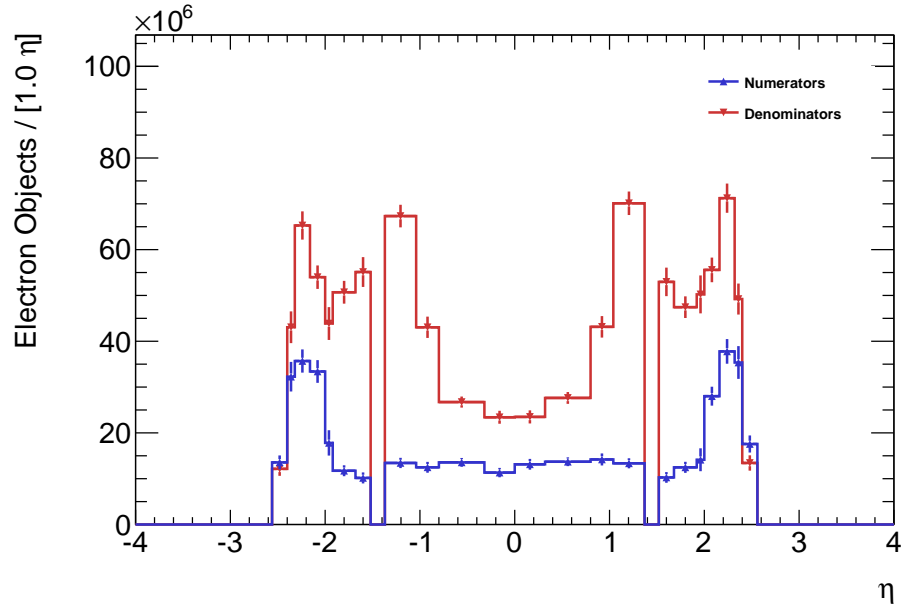


Figure 6.5: Electron numerator and denominator object counts versus η for $p_T < 24 \text{ GeV}$.

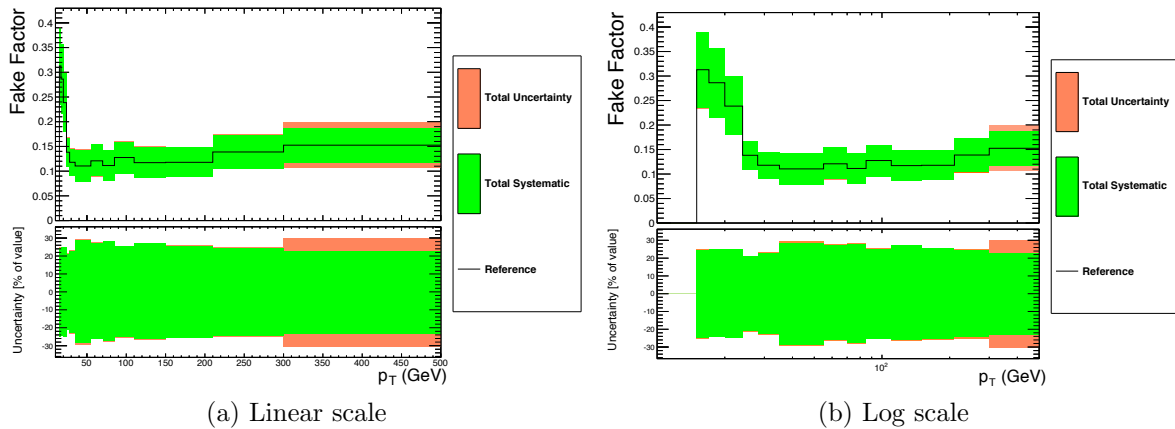


Figure 6.6: Electron fake factors vs. p_T , with systematic and total uncertainties. The statistical uncertainty includes both the data and prompt subtraction Monte Carlo statistics. The total uncertainty is the sum in quadrature of the statistical and systematic uncertainty.

- Pass all numerator muon requirements in table 5.2, except the requirements on $E_{\text{T}}^{\text{cone},30}$, $p_{\text{T}}^{\text{cone},30}$, and $\frac{d_0}{\sigma_{d_0}}$.
- Pass a looser impact parameter cut:

$$\left| \frac{d_0}{\sigma_{d_0}} \right| < 10 \quad (6.13)$$

- Invert isolation:

$$E_T^{\text{cone},30}, p_T^{\text{cone},30} > \begin{cases} 0.15p_T & : p_T < 100 \text{ GeV} \\ 15 + 0.01p_T \text{ GeV} & : p_T > 100 \text{ GeV} \end{cases} \quad (6.14)$$

$$\frac{E_T^{\text{cone},30}}{p_T} < 2.0 \quad (6.15)$$

$$\frac{p_T^{\text{cone},30}}{p_T} < 2.0 \quad (6.16)$$

$$(6.17)$$

- If $p_T < 40 \text{ GeV}$, apply the same overlap requirement as the signal regions, removing the muon if $\Delta R(\mu, \text{jet}) < 0.3$. This overlap requirement is not applied for muons with $p_T > 40 \text{ GeV}$, which increases the statistical precision at the expense of additional systematic uncertainty. This is denoted by “dR” or “non-dR” below, for example in figure 6.9.

The muon fake factors are measured in a same-sign dimuon sample. The trigger used to collect the events requires two muons with $p_T > 13 \text{ GeV}$. The use of same-sign muons suppresses the prompt contamination from Z/γ^* events. The measurement uses only muons with large track impact parameter significance, $|\frac{d_0}{\sigma_{d_0}}| > 3$, to obtain a sample enriched in non-prompt muons (if both muons satisfy this requirement, then both are counted in the measurement). An extrapolation factor is derived from Monte Carlo to account for the fact that the signal region requires $|\frac{d_0}{\sigma_{d_0}}| < 3$, as detailed below.

Two sets of fake factors are measured, depending on the jet activity in the event. In the following, jets are required to have $p_T > 30 \text{ GeV}$, and be separated from muons with $\Delta R(\mu, \text{jet}) > 0.3$.

- **Inclusive:** Applied to events with zero jets. The measurement uses the entire same-sign dimuon sample.
- **Two-Jet:** Applied to events with one or more jet. The measurement uses same-sign dimuon events with at least two jets with $p_T > 30 \text{ GeV}$.

Fake muons from the two-jet sample are expected to come primarily from $W + \text{jets}$ and $t\bar{t}$ processes, while the inclusive sample also includes contributions from $b\bar{b}$. Figure 6.7 shows the p_T distributions of numerator and denominator muons in the measurement sample along with the expected prompt contributions.

The extrapolation factor from the measurement control region, with $|\frac{d_0}{\sigma_{d_0}}| > 3$, to the signal region, with $|\frac{d_0}{\sigma_{d_0}}| < 3$, is derived from various Monte Carlo samples. The extrapolation factor is simply the ratio of fake factors derived in Monte Carlo using the control region cut ($|\frac{d_0}{\sigma_{d_0}}| > 3$) to those using the signal region cut ($|\frac{d_0}{\sigma_{d_0}}| < 3$). The central value is taken from the POWHEG $t\bar{t}$ sample, using all truth-level non-prompt muons, as shown in figure 6.8.

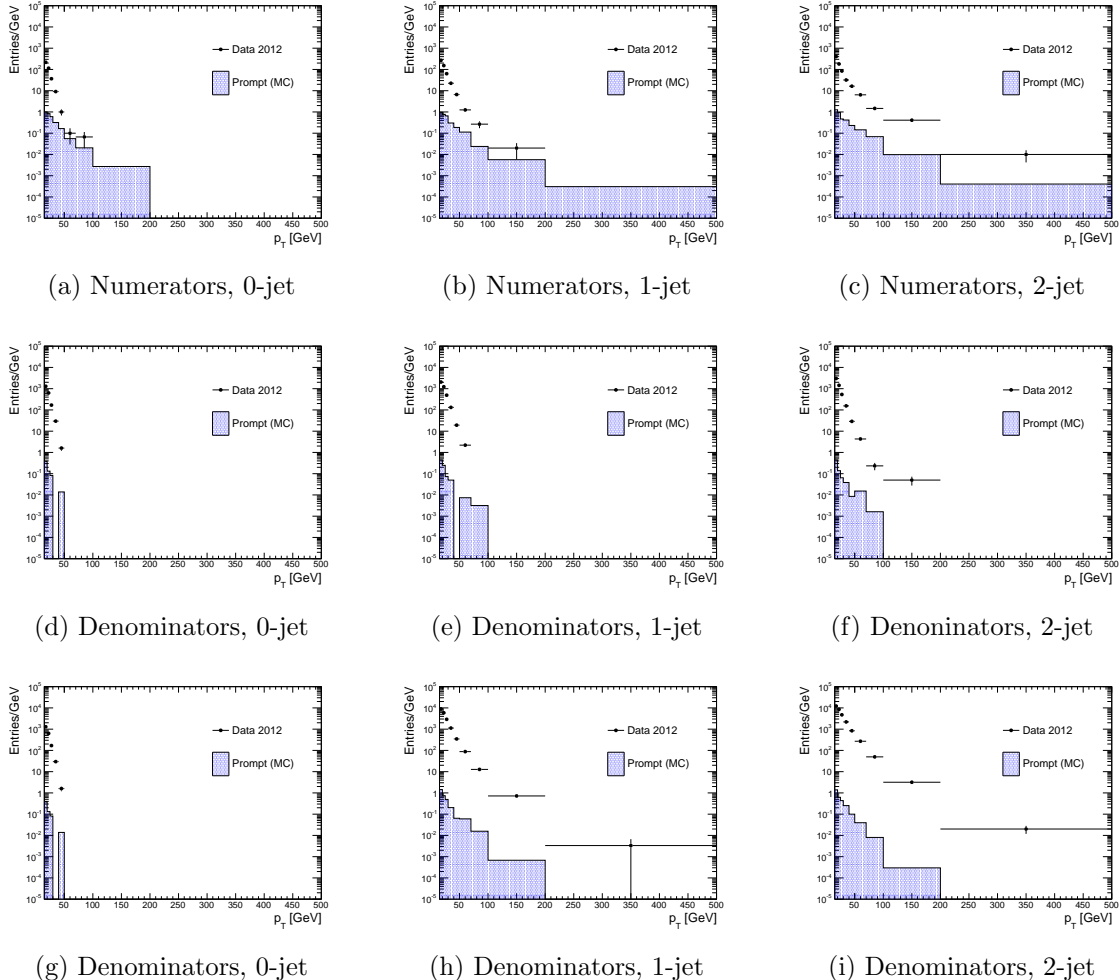


Figure 6.7: p_T spectrum of muons used in fake factor measurement. The left plots show events with zero jets, the middle plots show events with one jet, and the right plots show events with two or more jets. All numerator events require both numerator and denominator be separated from a jet by $\Delta R > 0.3$; the same requirement is applied to denominators in the second row of plots, while the third row shows denominators that are not required to be isolated from nearby jets.

A systematic uncertainty is assigned by comparing with other samples (MC@NLO $t\bar{t}$ and PYTHIA8 $b\bar{b}$ and $c\bar{c}$), and using only same-sign dimuon events in these samples.

The fake factors are parametrized one-dimensionally in p_T and η , as there are insufficient statistics to do a full two-dimensional parametrization. The fake factor is computed as:

$$f(p_T, \eta) = \frac{f(p_T) \times f(\eta)}{\langle f \rangle} \quad (6.18)$$

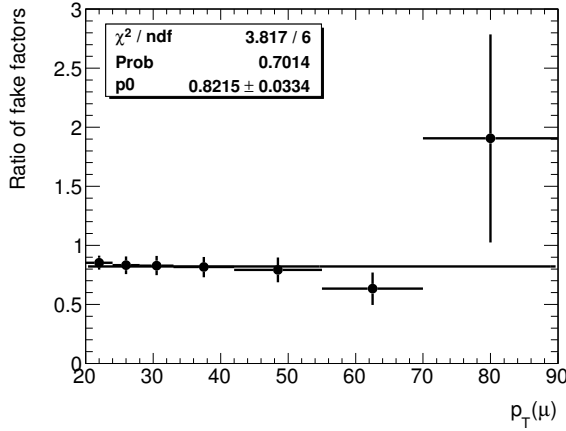


Figure 6.8: Ratio between the fake factors for muons with $|d_0|/\sigma(d_0) > 3$ compared to fake factors with nominal numerator and denominator definitions. These fake factors are derived from a POWHEG $t\bar{t}$ sample.

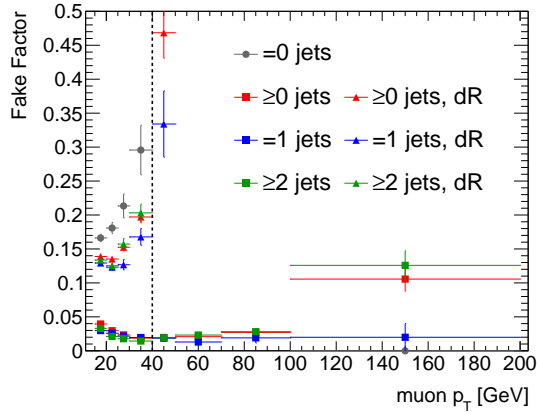


Figure 6.9: Muon fake factors as a function of p_T . Two sets of fake factors are plotted, with and without the “dR” requirement. The vertical dashed line at 40 GeV indicates the point at which the fake factors switch from the “dR” points, where the denominators are required to be separated from nearby jets, to the lower, non-“dR” points where the jet-isolation requirement is dropped to improve the statistics.

where $\langle f \rangle$ is the total average fake factor. The measured fake factors are shown in figures 6.9 and 6.10.

The sources of systematic uncertainty considered are listed below, and the fractional systematic uncertainty is shown in figure 6.11.

- **Prompt subtraction:** The normalization of the simulated prompt subtraction samples is varied by $\pm 10\%$, leading to a systematic uncertainty of 1%–6%.

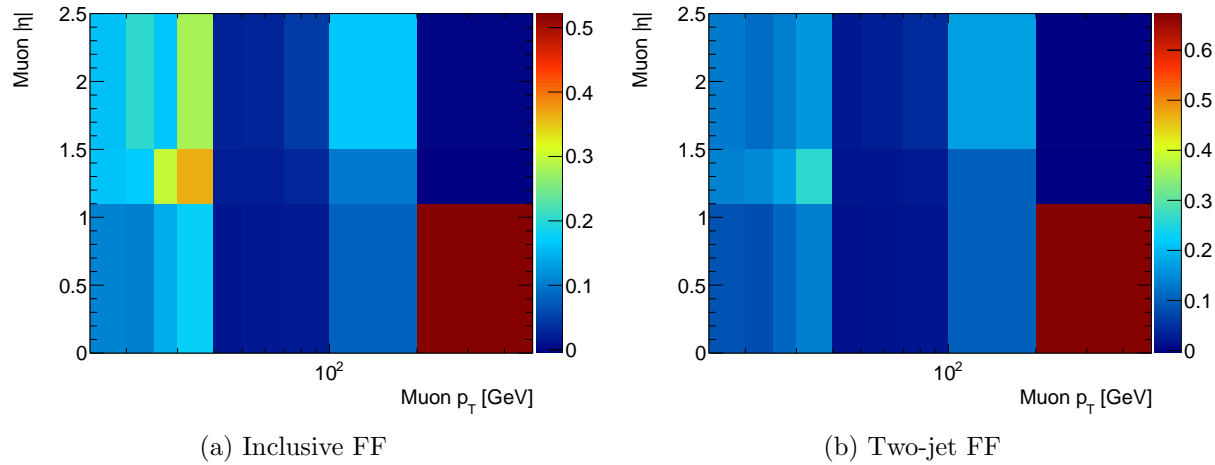


Figure 6.10: Muon fake factors as functions of p_T and $|\eta|$. The left plot shows fake factors measured in the inclusive control sample and applied to events with zero jets. The right plot shows fake factors measured in events with two jets, and applied to events with at least one jet.

- **Topological dependence:** The difference between the inclusive and two-jet fake factors is taken as a systematic uncertainty. The uncertainty is symmetrized, using the full difference as both upward and downward uncertainty, and ranges from 3% to 36%.
 - **Dependence on d_0 significance:** As mentioned previously, the extrapolation factor is derived in a number of different Monte Carlo samples. The largest deviation of 24% is taken as a systematic uncertainty.
 - **Light flavor fraction:** As with the electron fake factors, the fake factor values are quite different for muons originating from light flavor (LF) sources (π/K decay or punch-through) versus heavy flavor (HF) decays. The systematic uncertainty is derived using the difference in momenta measured by the inner detector and muon spectrometer as a discriminant between HF and LF fakes. The difference in HF/LF fraction between the control and signal regions is estimated, and the HF and LF fake factors measured in Monte Carlo are used to estimate the effect of the discrepancy in HF/LF fraction. A systematic uncertainty of 2% to 21% is assigned.

6.2.5 Tau Lepton Fakes

The detector signature of hadronically decaying τ leptons, consisting of a jet with one or more associated tracks, is not as distinctive as the signature of electrons and muons. Differentiating between jets, which are copiously produced in proton-proton collisions, and hadronically

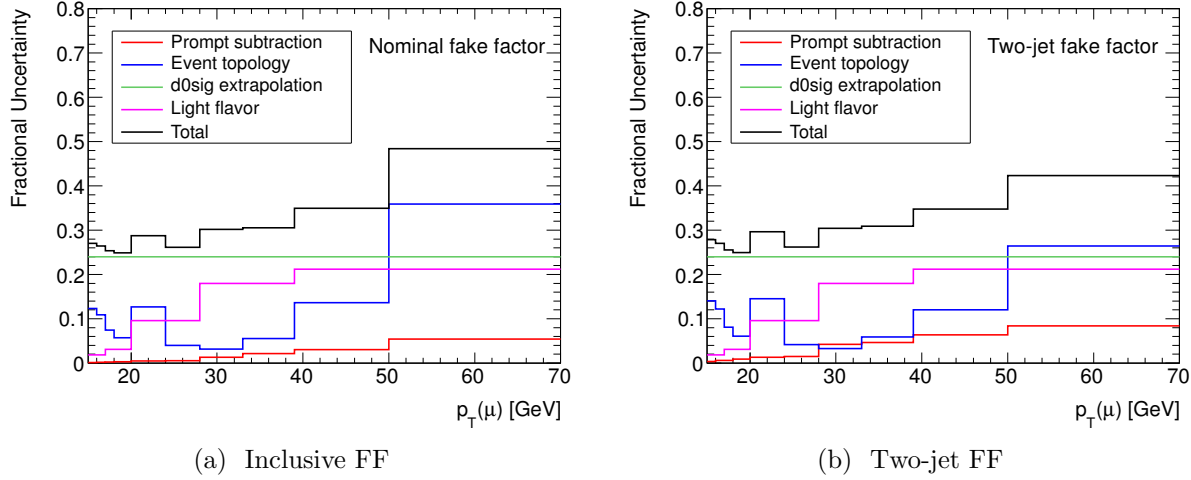


Figure 6.11: Systematic uncertainties on muon fake factor as a function of $p_T(\mu)$. The left plot shows the uncertainties for the inclusive fake factor, while the right shows the uncertainty for the two-jet fake factor.

decaying τ leptons is difficult, and accordingly the reducible backgrounds in events containing a hadronically decaying τ lepton is much larger.

The τ identification algorithm (section 5.4) employs a multivariate discriminant based on calorimeter shower shapes and tracking information. The fake rate is strongly dependent on the jet fragmentation, in particular whether the parton initiating the jet is a gluon, light quark, or heavy quark. In constructing the denominator definition, a tighter efficiency working point reduces the dependence on the initial parton, thereby improving the extrapolation of the fake factors to the signal regions; on the other hand, the working point must be loose enough to collect sufficient statistics. The denominator definition requires τ candidates to have a `BDTScore` which fails the `BDT-Medium` selection threshold, but exceeds 0.9 times the p_T -dependent `BDT-Loose` threshold. In simulation, this definition is seen to be relatively insensitive to the type of parton initiating the jet. The fake factors are measured two-dimensionally in bins of p_T and $|\eta|$, and a correction is applied as a function of the highest MV1 b -tag weight of all jets in the event.

Fake Factor Measurement

The τ lepton fake factors are measured using a tag-and-probe method in a sample targeting $W+jets$ events. Events are required to have a muon satisfying the numerator criteria (tag) plus a hadronically decaying τ candidate (probe). To avoid biasing the fake factors, no other requirements are imposed to reject the prompt contamination (for example, requiring the muon and $\tau_{\text{had-vis}}$ to have the same sign biases the sample towards gluon-initiated jets). The prompt contamination, dominantly from $Z+jets$ and $t\bar{t}$ production, is subtracted using

simulation.

The muon- $\tau_{\text{had-vis}}$ invariant mass and $\tau_{\text{had-vis}} p_T$ spectra for numerators and denominators are shown in figure 6.12, along with the prompt contribution estimated from simulation. Figure 6.13 shows the resulting fake factors.

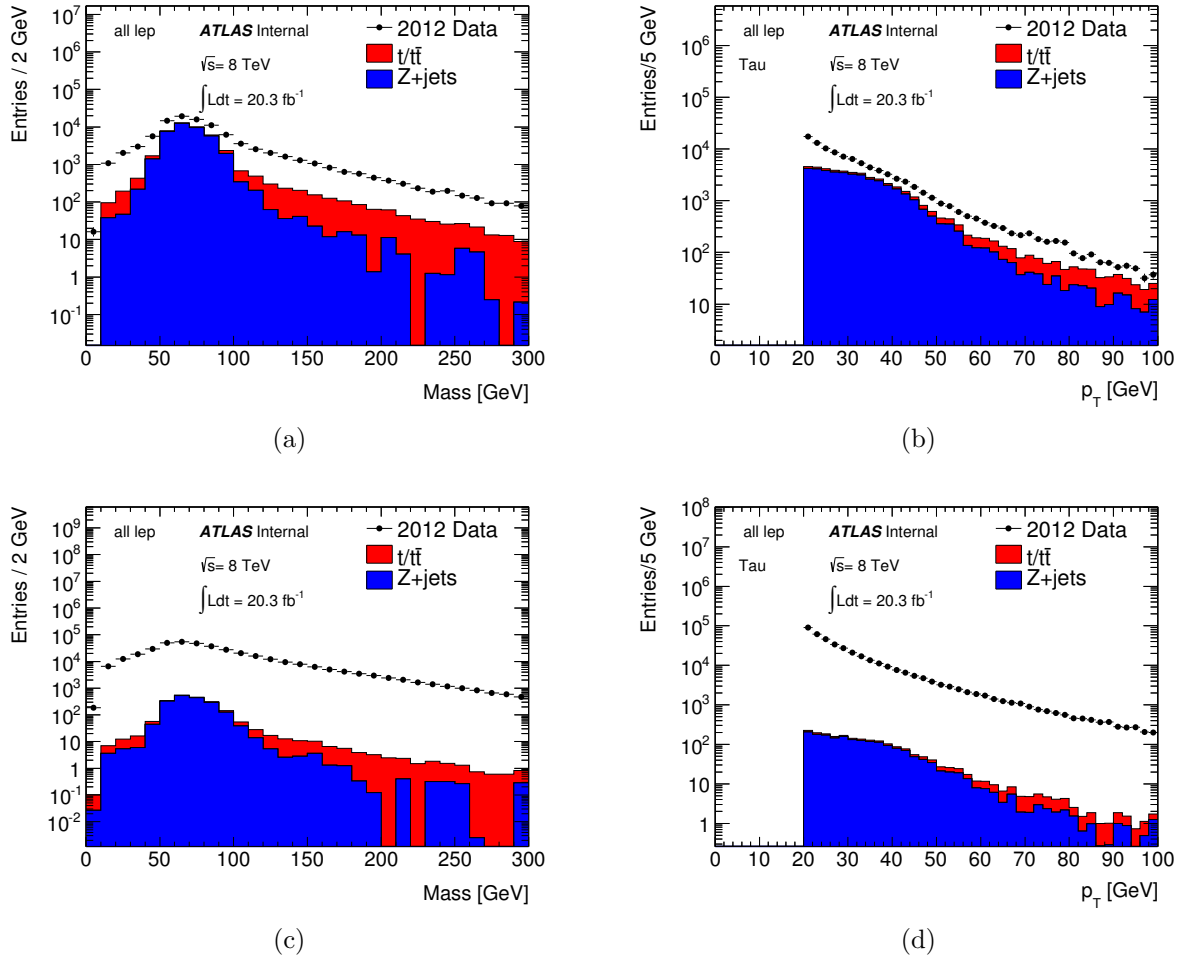


Figure 6.12: Invariant mass of the muon and $\tau_{\text{had-vis}}$ pair (left) and p_T of the τ candidate (right). The top plots show the distributions for numerator $\tau_{\text{had-vis}}$ candidates, while the bottom plots show the distributions for denominator $\tau_{\text{had-vis}}$ candidates. The filled histograms show the prompt contamination estimated from simulation.

Systematic Uncertainties

The following sources of systematics uncertainties on the τ fake factors are considered:

- Uncertainties on the simulation-based estimates of the prompt contamination.

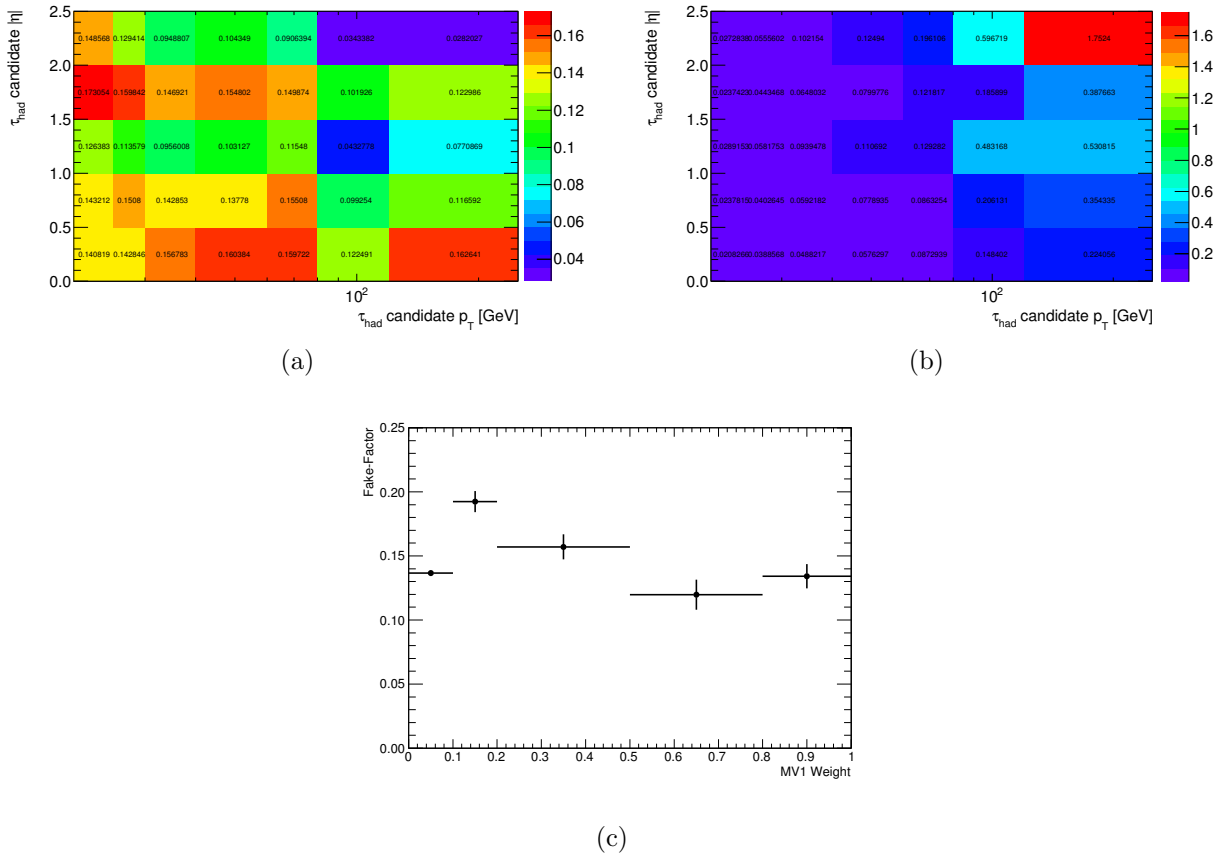


Figure 6.13: τ lepton fake factors binned in p_T and $|\eta|$ (left), and the corresponding statistical uncertainty (right). The correction for the maximum MV1 b -tag weight of all jets in the event is also shown (bottom). The fake factors are derived from $W + \text{jets}$ events.

- Uncertainties associated with the binning choice.
- Dependence of the fake factors on the flavor of the initiating parton.

The uncertainty due to the prompt contamination estimation is derived by fluctuating the normalizations of the Monte Carlo samples by their theoretical uncertainties. The resulting variations in the fake factors are between 5%-17%, and are largest for $30 \text{ GeV} \lesssim p_T \lesssim 40 \text{ GeV}$, where the contribution from $Z \rightarrow \tau_\mu \tau_{\text{had}}$ is greatest.

To estimate the effect of the binning, the fake factors are reapplied to the same sample they were derived from. The results are shown in figure 6.14. An uncertainty of 5% is assigned.

Finally, to estimate the effect of differences in flavor composition between the measurement sample and the signal regions, the fake factors are applied to a $t\bar{t}$ validation region. In simulation, this validation region is observed to have a substantially different flavor compo-

sition from the $W+jets$ measurement sample. A systematic uncertainty of 25% covers the observed differences between the fake background estimate and the data.

In total, the systematic uncertainties are in the range 25%-30%, and are largest around $30 \text{ GeV} \lesssim p_T \lesssim 40 \text{ GeV}$.

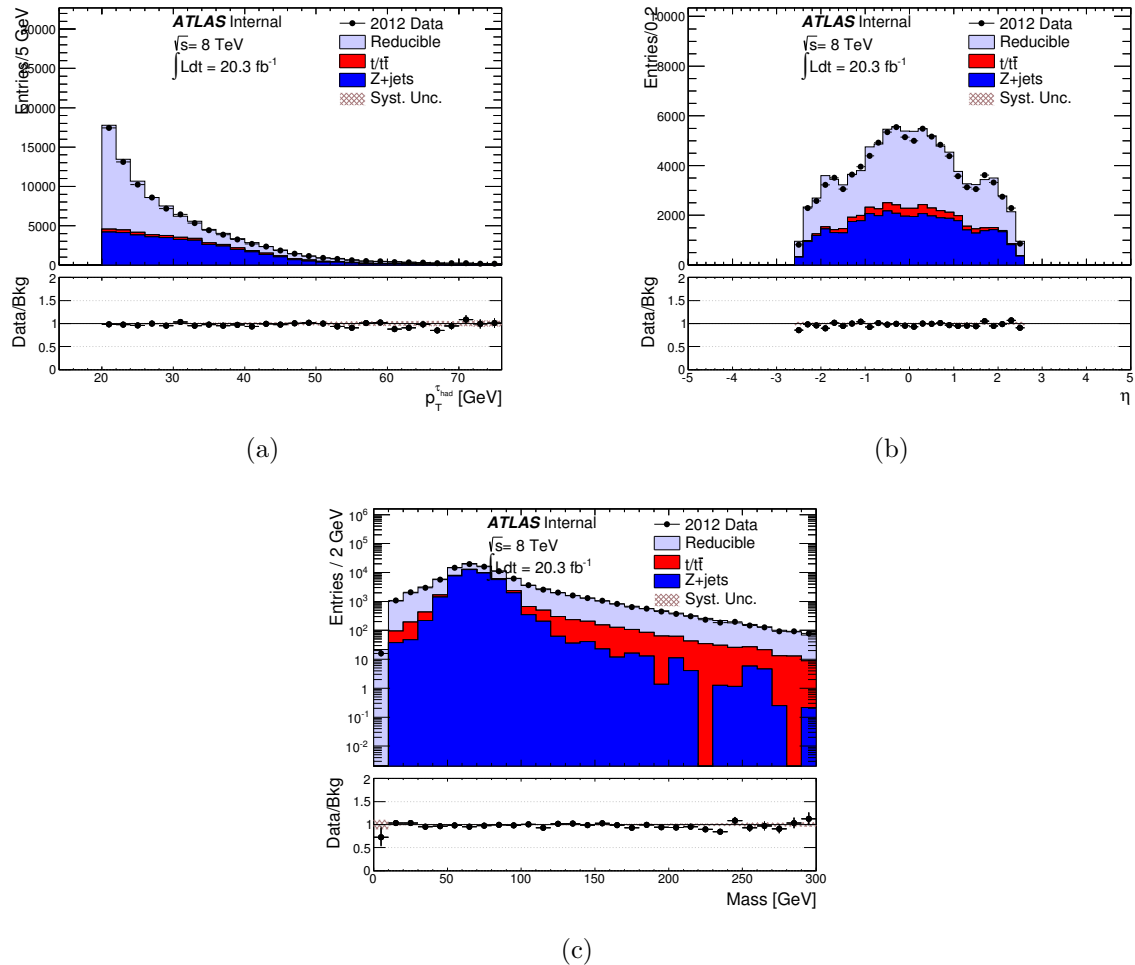


Figure 6.14: Results of the closure test, comparing the data to the fake factor-based background estimate in a $t\bar{t}$ validation region. The $\tau_{\text{had-vis}} p_T$ (left), $|\eta|$ (right), and the dilepton invariant mass (bottom) are shown.

Bibliography

- [1] ATLAS Collaboration, *The ATLAS Simulation Infrastructure*, The European Physical Journal C **70**.3 (2010) pp. 823–874.
- [2] S. Agostinelli et al., *GEANT4: A simulation toolkit*, Nucl. Instrum. Meth. **A506** (2003) pp. 250–303.
- [3] T. Sjöstrand, S. Mrenna, and P. Z. Skands, *PYTHIA 6.4 Physics and Manual*, JHEP **0605** (2006) p. 026, arXiv: hep-ph/0603175.
- [4] T. Gleisberg et al., *Event generation with SHERPA 1.1*, JHEP **0902** (2009) p. 007, arXiv: 0811.4622 [hep-ph].
- [5] J. Alwall et al., *The automated computation of tree-level and next-to-leading order differential cross sections, and their matching to parton shower simulations*, JHEP **1407** (2014) p. 079, arXiv: 1405.0301 [hep-ph].
- [6] H.-L. Lai et al., *New parton distributions for collider physics*, Phys. Rev. **D 82** (2010) p. 074024, arXiv: 1007.2241 [hep-ph].
- [7] P. M. Nadolsky et al., *Implications of CTEQ global analysis for collider observables*, Phys. Rev. **D78** (2008) p. 013004, arXiv: 0802.0007 [hep-ph].
- [8] ATLAS Collaboration, *Further ATLAS tunes of PYTHIA6 and Pythia 8*, ATL-PHYS-PUB-2011-014 (2011).
- [9] ATLAS Collaboration, *Improved electron reconstruction in ATLAS using the Gaussian Sum Filter-based model for bremsstrahlung* (2012) pp. 1–22.
- [10] ATLAS Collaboration, *Search for anomalous production of prompt like-sign lepton pairs at $\sqrt{s} = 7$ TeV with the ATLAS detector*, JHEP **1212** (2012) p. 007, arXiv: 1210.4538 [hep-ex].

Chapter 7

Model-Independent Trilepton Search

Events containing three or more leptons are useful probes of phenomena beyond the Standard Model. The production of three or more leptons is predicted by many models of phenomena beyond the Standard Model, as described in section 2.2. The expected Standard Model backgrounds are typically small; depending on the flavor and charge of the three leptons, such events primarily arise from diboson production (WZ , ZZ), or from single boson (W , Z/γ^*) or $t\bar{t}$ production along with one or more leptons from misidentified or semileptonically decaying jets.

This chapter presents a search for physics beyond the Standard Model using events containing three or more leptons [1]. Many signal regions are defined based on the properties of the leptons, jets, and overall momentum imbalance of the event, with the goal of being broadly sensitive to the nonresonant production of trilepton final states by phenomena beyond the Standard Model. The results are first presented in a model-independent fashion, establishing upper limits on the production of events with three or more charged leptons from non-Standard Model sources. The limits are then used to confront a model predicting new doubly charged scalar particles.

7.1 Event Selection

This section describes the selection of events containing at least three leptons in the pp collision data and Monte Carlo simulation samples.

7.1.1 Triggering

Collisions events for this analysis are triggered using the unprescaled single-electron or single-muon triggers with the lowest transverse momentum thresholds. The triggers require at least one of the following criteria to be satisfied:

- One electron with $p_T > 24 \text{ GeV}$. The electron must satisfy cuts similar to the `medium++`

identification criteria at the trigger level, an isolation requirement of $\frac{p_T^{\text{cone}20}}{p_T} < 0.1$, and cuts on the leakage into the hadronic calorimeter.

- One electron with $p_T > 60 \text{ GeV}$. The electron must also satisfy the medium identification cuts, but the isolation and leakage requirements are removed.
- One muon with $p_T > 24 \text{ GeV}$, satisfying an isolation requirement of $\frac{p_T^{\text{cone}20}}{p_T} < 0.12$.
- One muon with $p_T > 36 \text{ GeV}$, with no isolation requirement.

The triggers with higher transverse momentum thresholds remove the isolation requirements in order to improve the efficiency at higher p_T . Triggered events are required to have an offline lepton matched to the trigger object within $\Delta R = \sqrt{(\Delta\eta)^2 + (\Delta\phi)^2} < 0.1$. To avoid trigger turn-on effects near the p_T threshold, the offline lepton must have $p_T > 26 \text{ GeV}$. Additionally, trigger-matched muons must have $|\eta| < 2.4$ to avoid uninstrumented regions of the detector.

7.1.2 Trilepton Event Selection

After successful triggering and overlap removal, events are required to have at least three selected leptons, with at most one hadronically decaying τ lepton. The primary event vertex, chosen as the reconstructed vertex with the highest $\sum p_T^2$ of tracks, must have at least three tracks. Finally, events are rejected if they contain “bad jets” not associated to real energy deposits in the calorimeters due to pp collisions, i.e. from electronics problems or cosmic rays [2].

7.2 Analysis Strategy

The analysis defines a large number of nonexclusive signal regions, designed to target new physics models and to compartmentalize the expected backgrounds. First, the events are divided into six categories as follows. First, the events are divided into three categories based on the properties of any opposite-sign, same-flavor (OSSF) lepton pairs in the event:

- **on- Z :** events containing an OSSF lepton pair consistent with the decay of a Z boson, with invariant mass within 20 GeV of m_Z ;
- **off- Z , OSSF:** events containing an OSSF pair that do not fall in the on- Z category; and
- **off- Z , mixed:** events containing no OSSF pairs.

The on- Z category also includes events containing three leptons (two of which form an OSSF pair) with invariant mass within 20 GeV of m_Z , to include events containing a Z boson where a photon from final state radiation converts and is reconstructed as a prompt electron.

Next, the events are further divided into two categories based on the number of electron or muon candidates in the event:

- **3L**: events containing at least three electrons or muons, and
- **2L+ τ_{had}** : events containing exactly two electrons or muons and a hadronically decaying τ lepton.

After dividing the events into these six exclusive categories, many signal regions are defined based on the lower bound in various kinematic variables. An ordering is imposed on the leptons for the sake of disambiguation: in the 3L category, the leptons are ordered by p_T , while in the 2L category, the electrons or muons are ordered by p_T , and the τ_{had} is the third lepton. The variables used to define the signal regions are:

- H_T^{leptons} : the scalar sum of the transverse momenta of the leading three leptons. Events containing new particles with masses significantly greater than m_W or m_Z will typically have larger H_T^{leptons} than the Standard Model backgrounds.
- Minimum p_T^ℓ : the p_T of the softest of the leading three leptons. As with H_T^{leptons} , the p_T of leptons produced in the decays of heavy particles will tend to be larger than those from the expected Standard Model backgrounds.
- H_T^{jets} : the scalar sum of the transverse momenta of all selected jets in the event. This variable is sensitive to strongly produced new particles, where leptons are produced in the decays of heavy colored particles, such as squarks, the superpartners of quarks in supersymmetry. Such events often contain hard jets in addition to the three leptons. Conversely, the Standard Model WZ and ZZ backgrounds are weakly produced, and have softer H_T^{jets} distributions.
- E_T^{miss} : the magnitude of the missing transverse momentum in the event. In models of new physics, leptons can be produced in association with new invisible particles, such as stable neutralinos in R -parity conserving supersymmetry, or with neutrinos if the new particles decay via W bosons. Requiring large E_T^{miss} can distinguish such signals from the Standard Model backgrounds, where the E_T^{miss} is primarily due to neutrinos from W or τ decays. Requiring large E_T^{miss} also suppresses backgrounds due to $Z+\text{jets}$, where the jet decays semileptonically or is misidentified as a lepton.
- m_{eff} : the scalar sum of H_T^{jets} , E_T^{miss} , and the p_T of all identified leptons in the event. As with H_T^{leptons} by itself, multilepton production due to the decays of heavy particles will typically have a harder m_{eff} distribution than the Standard Model backgrounds.
- m_T^W : for events in the on- Z categories, the transverse mass of the missing transverse momentum, \vec{p}_T^{miss} , and the highest- p_T lepton not associated with a Z boson candidate, defined as:

$$m_T^W = \sqrt{2|\vec{p}_T^\ell| |\vec{p}_T^{\text{miss}}| (1 - \cos(\Delta\phi))}, \quad (7.1)$$

Variable	Meaning					
H_T^{jets}	Σp_T of all jets in the event					
m_T^W	Transverse mass of W -boson candidate (on- Z events only)					
Variable	Meaning	Lower Bounds [GeV]				Additional Requirements
H_T^{leptons}	Σp_T of leading three leptons	0	200	500	800	
Min. p_T^ℓ	p_T of softest (third) lepton	0	50	100	150	
E_T^{miss}	Missing transverse momentum	0	100	200	300	$H_T^{\text{jets}} < 150 \text{ GeV}$
E_T^{miss}		0	100	200	300	$H_T^{\text{jets}} \geq 150 \text{ GeV}$
m_{eff}		0	600	1000	1500	
m_{eff}	All transverse activity	0	600	1200		$E_T^{\text{miss}} \geq 100 \text{ GeV}$
m_{eff}		0	600	1200		$m_T^W \geq 100 \text{ GeV, on-}Z$
Variable	Meaning	Lower Bounds				
b -tags	Number of b -tagged jets	1	2			

Table 7.1: Kinematic signal regions defined in the analysis.

where $\Delta\phi$ is the azimuthal angle between the transverse momentum of the lepton, \vec{p}_T^ℓ , and the missing transverse momentum, \vec{p}_T^{miss} .

- $N_{b\text{-tags}}$, the number of b -tagged jets. New physics scenarios related to the hierarchy problem (section 2.2) often couple preferentially to the third generation, due to the dominant effect of the top quark in the running of the Higgs mass.

The signal regions are defined in table 7.1. The signal regions use one of H_T^{leptons} , the minimum p_T^ℓ , E_T^{miss} , m_{eff} , and n_b as binning variables. H_T^{jets} , E_T^{miss} , and m_T^W are used to impose additional requirements on the signal regions. In total, 138 signal regions are defined.

7.3 Systematic Uncertainties

Systematic uncertainties are assigned to the signal and background predictions to account for possible modeling inaccuracies. The sources of uncertainty considered are:

- Uncertainties on the reducible background estimates from the data-driven estimation method, as described in section 6.2.2. The uncertainties ranges between 20% to 30% for the electron fake factors, 25% to 50% for the muon fake factors, and 25% to 30% for the τ lepton fake factors.

Sample	Uncertainty
$t\bar{t} + V$	30% [3, 4]
ZZ	4.3%
WZ	7.6%

Table 7.2: Systematic uncertainties on the normalizations of the background contributions estimated with simulation.

- Simulated Monte Carlo samples, whether signal or background, must be normalized to the integrated luminosity of the data. The weight assigned to each event is:

$$w = \frac{\mathcal{L}\sigma_{\text{process}}}{N_{\text{sim}}}, \quad (7.2)$$

where \mathcal{L} is the integrated luminosity of the data, σ_{process} is the cross section of the simulated process, and N_{sim} is the number of simulated events. The integrated luminosity carries an uncertainty of 2.8%, as described in section 4.5. The cross sections are taken from calculations with uncertainties due to various sources, including the fixed order of the calculation, the choice of renormalization and factorization scales, and the PDFs. For the dominant WZ and ZZ backgrounds, the predictions from SHERPA are compared to those from the next-to-leading-order generator VBFNLO. The generators show good agreement, and the systematic uncertainty on the cross section is determined from VBFNLO by varying the factorization and renormalization scales up and down by factors of two. The uncertainties are shown in table 7.2.

No systematic uncertainty is assigned to the normalization of the $Z + \gamma$ sample. Rather, a large uncertainty of 30% is assigned due to the reweighting procedure described in section 6.2.1. The $VVV^{(*)}$ sample is also not assigned an uncertainty due to its small contribution to the signal regions.

- Events are also weighted to account for differences between data and Monte Carlo simulation in the lepton trigger, reconstruction, and identification efficiencies. The scale factors and associated uncertainties are provided by the relevant ATLAS combined performance groups. The electron (section 5.2.2) and muon (section 5.3.1) scale factors are close to unity, with uncertainties in the range 1–5%. The scale factors for the τ lepton identification efficiency range from 94–96% for the **BDTTight** working point, and carry uncertainties between 2.0–2.2% (section 5.4).
- The lepton energy scales carry uncertainty which has a small effect on the signal regions due to leptons or events near E_T or p_T thresholds, as described in sections 5.2.3, 5.3.2, and 5.4.1.

- The jet energies are scaled and smeared as described in section 5.5.1. The uncertainty affects the H_T^{jets} and m_{eff} distributions, and also the lepton-jet overlap removal procedure.
- The lepton and jet energy uncertainties are also propagated to the missing transverse energy, E_T^{miss} .
- The efficiencies of the b -tagging algorithm carry uncertainties which are parameterized based on matching the identified b -jets to truth b -jets.
- Finally, the Monte Carlo samples carry statistical uncertainty due to simulating a finite number of events.

The dominant sources of uncertainty depend on the signal region, but are generally due to Monte Carlo statistical uncertainties, the fake factor uncertainties, and theoretical cross section uncertainties.

7.4 Background Validation

The background estimates are verified in several dedicated validation regions, which are orthogonal to the signal regions. Events containing two leptons are used to test the selection of prompt leptons and their corresponding scale factors and energy corrections. The reducible backgrounds are tested in $t\bar{t}$ validation regions, where the events are required to have two same-sign leptons to target semileptonic decays where one lepton arises from a reducible process. Finally, the fake factor method is validated in events with modified, intermediate lepton selections, where the signal leptons are between the numerator and denominator definitions used in the nominal reducible background estimate.

7.4.1 Dilepton Validation Regions

Three dilepton validation regions target the three flavors of leptons: ee , $\mu\mu$, and $\mu\tau_{\text{had}}$. The ee and $\mu\mu$ regions require an opposite-sign lepton pair of the appropriate flavor. The invariant mass distributions of the dilepton system in these regions are shown in figure 7.1. Some disagreement is observed in the ee invariant mass distribution; this discrepancy is covered by the electron energy scale systematic uncertainties.

The ee and $\mu\mu$ validation regions are also used to generate scale factors to account for efficiency differences between simulation and data when applying cuts on lepton isolation or impact parameter. The scale factors are computed from events with a dilepton pair with invariant mass within 10 GeV of m_Z , and are shown in figure 7.2. The efficiencies between data and simulation are mostly consistent to within 0.5%, except for cuts on isolation on low- p_T leptons, where the efficiencies deviate by up to 2%.

The $\mu\tau_{\text{had}}$ region applies addition cuts to reduce the large contribution from fake τ leptons in $W+\text{jets}$ events:

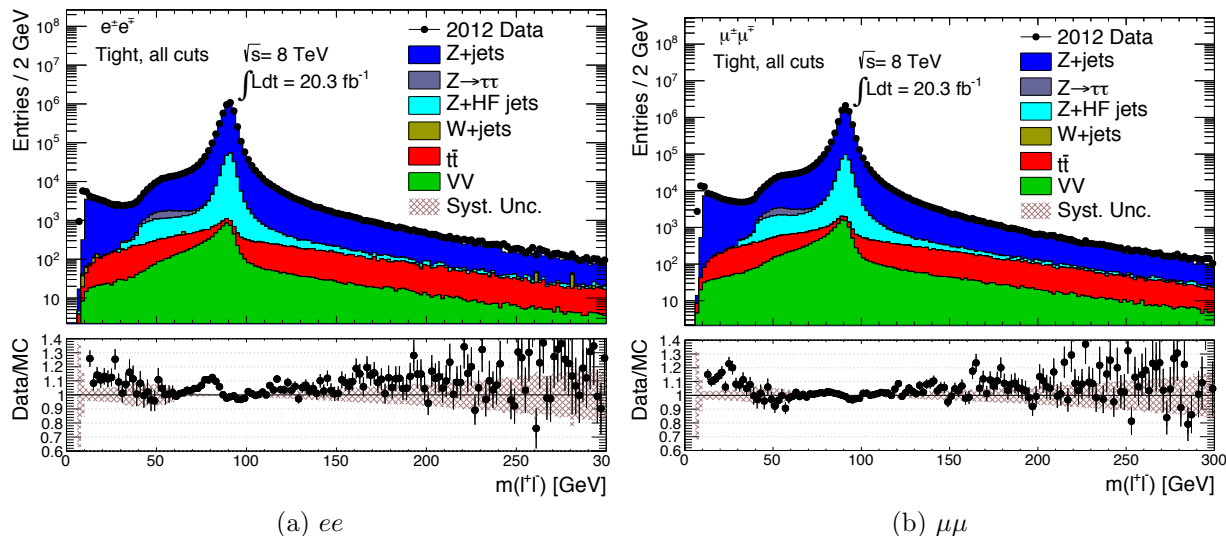


Figure 7.1: Dilepton invariant mass distributions for the ee (left) and $\mu\mu$ (right) validation regions. The shaded bands on the ratio plots show the systematic uncertainty on the background estimate due to the MC sample statistical uncertainties and normalizations. The disagreement between data and simulation in the ee mass distribution is covered by the electron energy scale uncertainties, not shown in the plot.

- $\cos \Delta\phi(\mu, E_T^{\text{miss}}) + \cos \Delta\phi(\tau, E_T^{\text{miss}}) > -0.15$,
 - $\Delta\phi(\mu, \tau_{had}) > 2.4$,
 - $m_T^\mu < 50 \text{ GeV}$,
 - $42 < m_Z^{vis.} < 82 \text{ GeV}$, and
 - $p_T^\mu < 40 \text{ GeV}$.

The p_T distribution of the $\tau_{\text{had-vis}}$ is shown in figure 7.3. The data agree well with the background estimate.

7.4.2 $t\bar{t}$ Validation Regions

In signal regions that veto Z bosons and require large H_T^{jets} or E_T^{miss} , a large reducible background component is expected from $t\bar{t}$ events, where both W bosons decay leptonically and a third lepton arises from a misidentified jet or semileptonic heavy flavor decay. This process is tested in the $t\bar{t}$ validation regions, which require at least one b -tagged jet with $p_T > 30 \text{ GeV}$, exactly two electrons or muons with the same charge, and $H_T^{\text{jets}} < 500 \text{ GeV}$. The requirement that the leptons have the same sign vetoes dilepton $t\bar{t}$ events with two prompt leptons from W decays, while the H_T^{jets} requirement reduces the potential contamination

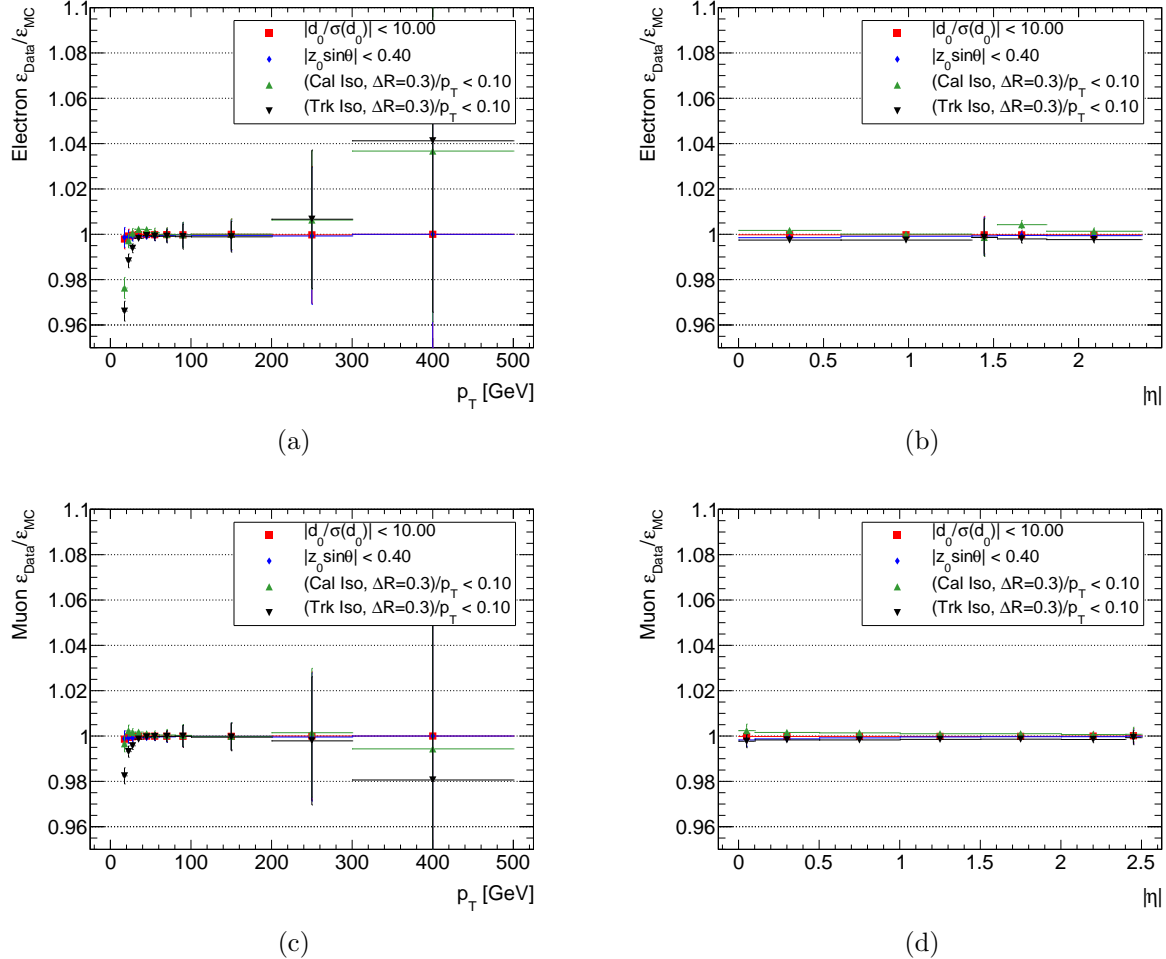


Figure 7.2: Ratios of efficiencies between data and simulation for electrons (top) and muons (bottom) as functions of p_T (left) and $|\eta|$ (right).

from new BSM phenomena. Note that events containing hadronically decaying τ leptons are used to derive a systematic uncertainty on the τ fake factors due to the flavor composition of the events (section 6.2.5), and so are not used as a validation region.

The E_T^{miss} distribution of events in the $t\bar{t}$ validation region is shown in figure 7.4. The data agree well with the background estimate.

7.4.3 Intermediate Fake Factor Validation Regions

The fake factor method is further validated in regions containing events with two signal (numerator) leptons and one “intermediate” lepton, which fulfills selection criteria looser than the numerator criteria but tighter than the denominator criteria. Separate fake factors are derived for intermediate leptons; these are defined schematically as $\langle \text{intermediate} \rangle / \langle \text{denominator} \rangle$,

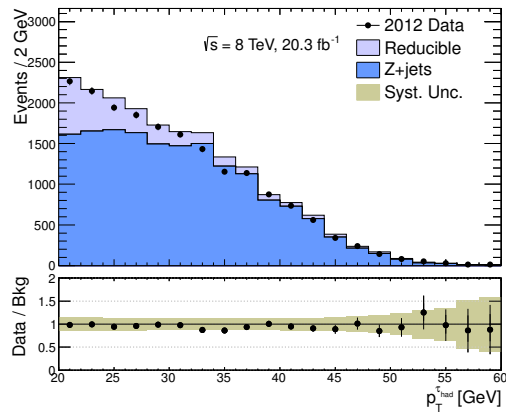


Figure 7.3: p_T distribution of the $\tau_{\text{had-vis}}$ candidates in the $\mu\tau_{\text{had}}$ validation region. The shaded band on the ratio plot shows the total systematic uncertainty on the background estimate.

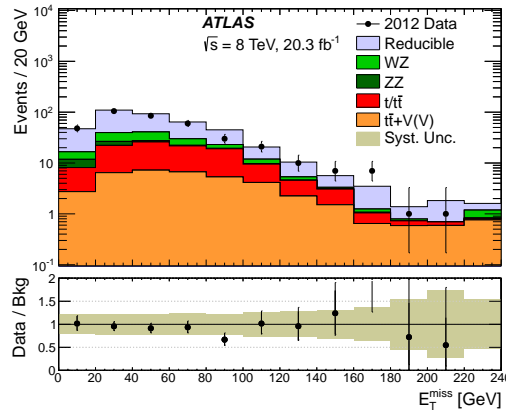


Figure 7.4: $t\bar{t}$ validation regions for all flavor (e, μ) combinations. The shaded band on the ratio plot shows the total systematic uncertainty on the background estimate.

rather than $\langle \text{numerator} \rangle / \langle \text{denominator} \rangle$. Specifically, the intermediate leptons satisfy most of the numerator criteria except for:

- **Electrons:** the electron must pass the `medium++` cuts, but fail the `tight++` cuts.
- **Muons:** the muon must fail one of the isolation cuts, satisfying either $0.10 < \frac{p_T^{\text{cone},30}}{p_T} < 0.15$ or $0.10 < \frac{E_T^{\text{cone},30}}{p_T} < 0.15$.
- **Taus:** the τ lepton must pass the `Medium-BDT` identification requirement, but fail the `tight-BDT` identification requirement.

The first two regions, targeting reducible electrons and muons, require an OSSF pair of electrons or muons, plus a third intermediate electron or muon of the opposite flavor. The events are largely due to $Z \rightarrow ee$ or $Z \rightarrow \mu\mu$ events, with an additional lepton that is either prompt and fails the signal lepton criteria, or is due to a reducible process. The p_T and η distributions of the intermediate electrons and muons are shown in figure 7.5.

The events containing an intermediate τ_{had} are much more abundant than intermediate electrons or muons, so three τ_{had} validation regions are defined, mirroring the signal region categories. Events are required to contain two electrons or muons plus an intermediate τ_{had} , and are separated into on- Z , off- Z /OSSF, and off- Z /mixed categories, depending on the two electrons or muons. The p_T and η of the intermediate τ_{had} is shown for each category in figure 7.6.

7.5 Results and Limits

The results of the search are organized as follows. For each category, the distributions of the various kinematic variables (H_T^{leptons} , H_T^{jets} , m_{eff} , E_T^{miss} , m_T^W , N_{jets} , $N_{b-\text{tags}}$, and the p_T of the third lepton) are produced, where applicable. Then, in each of the 138 signal regions, the number of observed and expected events are compared, and, absent any significant deviations, 95% confidence level (CL) upper limits are derived on the number of events from new physics, N_{95} . The corresponding upper limit on the *visible cross section*, σ_{95}^{vis} , is defined as

$$\sigma_{95}^{\text{vis}} = \frac{N_{95}}{\mathcal{L}}, \quad (7.3)$$

where $\mathcal{L} = 20.3 \text{ fb}^{-1}$ is the integrated luminosity of the data. The limits are calculated using a modified frequentist CL_s prescription [5], described in more detail in appendix C.

The results for the H_T^{leptons} signal regions are shown here for demonstrative purposes. The H_T^{leptons} distributions are shown in figure 7.7. The backgrounds are dominated by the reducible contributions in the 3L, off- Z , no-OSSF channel and in all three 2L+ τ_{had} channels. In the other two channels, the WZ and ZZ contributions are dominant. The expected signal

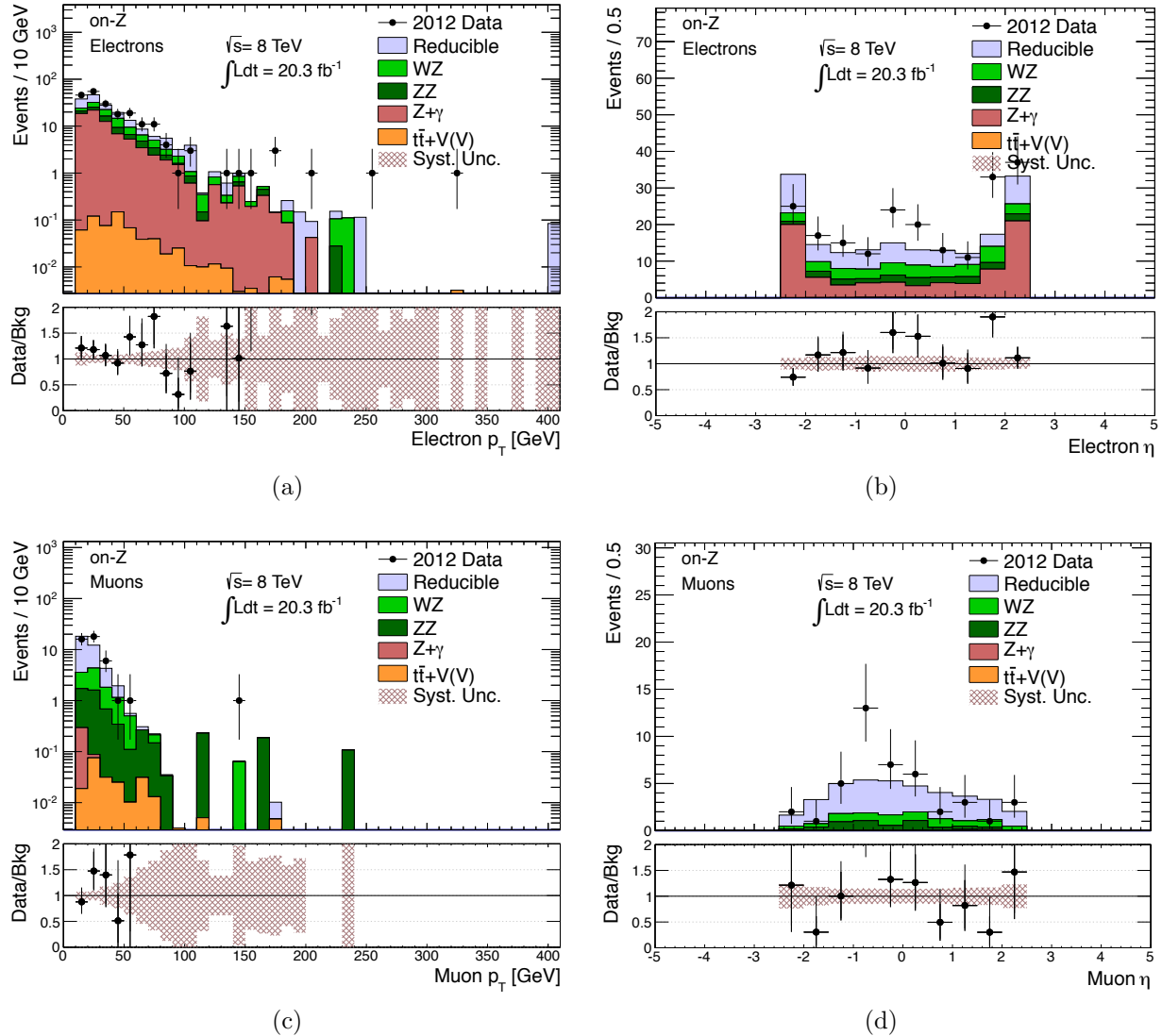


Figure 7.5: p_T (left) and η (right) distributions of the off- Z electron (top) or muon (bottom) satisfying the intermediate selection criteria. The other two leptons in the event are required to satisfy the numerator selection criteria and form an opposite-sign, same-flavor pair, with different flavor from the intermediate lepton. The shaded bands on the ratio plots show the systematic uncertainty on the background estimate due to the MC sample statistical uncertainties and normalizations.

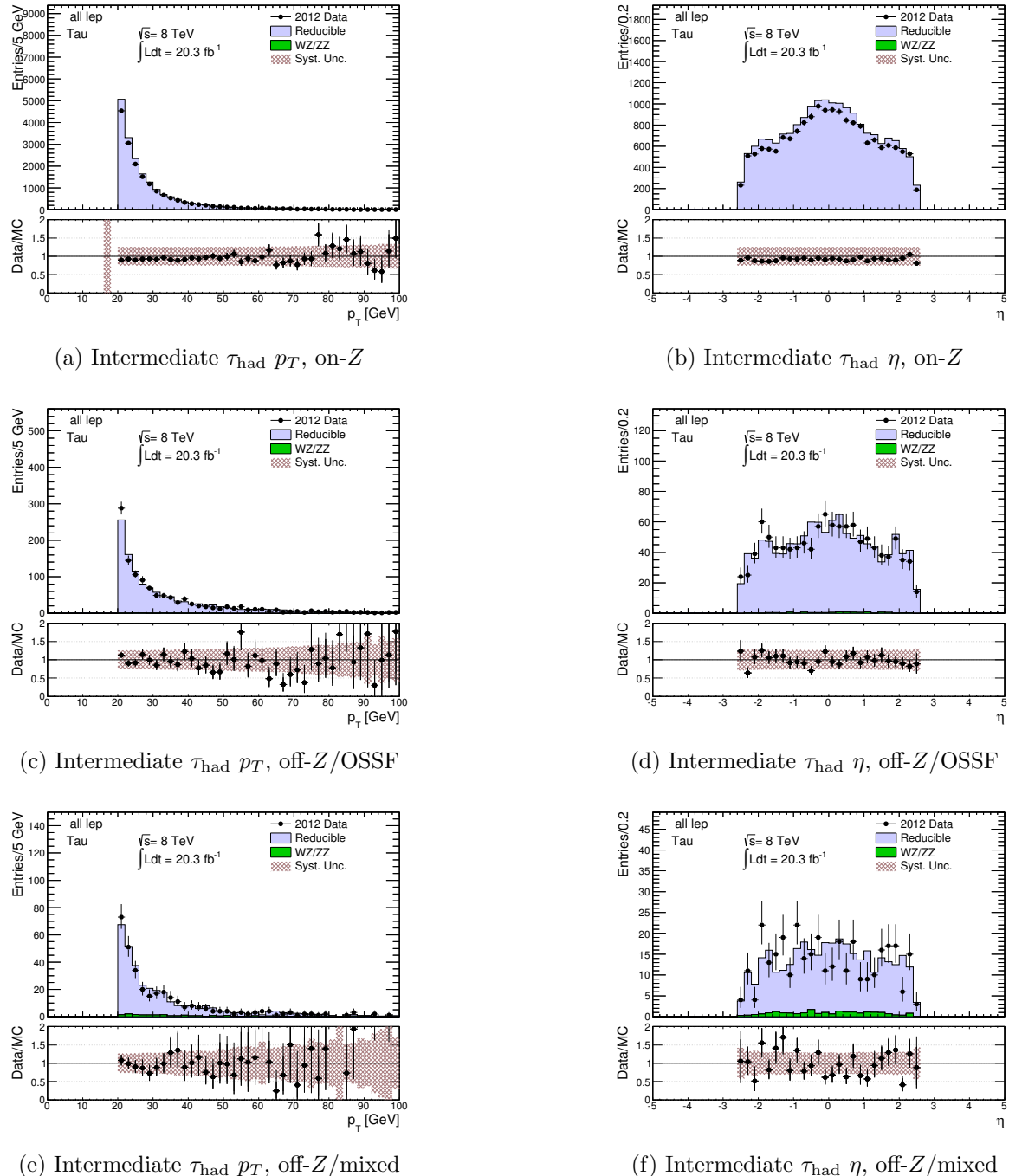


Figure 7.6: p_T and η distributions of the intermediate τ_{had} in the on- Z , off- Z /OSSF, and off- Z /mixed intermediate validation regions.

from an excited τ neutrino [6] with mass $m(\nu_\tau^*) = 0.5$ TeV is also shown; the excited neutrinos are pair produced via contact interactions, and decay to $Z\nu_\tau$ or $W^\pm\tau^\mp$. The observed and expected event counts in the three corresponding signal regions ($H_T^{\text{leptons}} > 200$ GeV, $H_T^{\text{leptons}} > 500$ GeV, and $H_T^{\text{leptons}} > 800$ GeV) are shown in table 7.3.

Finally, the upper limits on the visible cross section, σ_{95}^{vis} , in each of the 138 signal regions are shown in figure 7.8. The deviations between the observed and expected in all 138 signal regions are shown in figure 7.9, in units of the total uncertainty on the background expectation. The agreement between the data and the background prediction is quantified in terms of the p_0 -value, the probability to observe at least as many events as observed in the present measurement assuming the background-only hypothesis. The most significant excess corresponds to a p_0 -value of 0.05, or a 1.7σ deviation, in the $m_{\text{eff}} > 1000$ GeV signal region in the 2L+ τ_{had} , on- Z channel.

$H_T^{\text{leptons}} \geq$	$t\bar{t} + V(V)$	$VV(V)$	Reducible	Total	Observed
$\geq 3e/\mu, \text{ off-}Z, \text{ no-OSSF}$					
200 GeV	2.0 ± 0.6	1.6 ± 0.4	2.1 ± 1.1	5.7 ± 1.4	6
500 GeV	0.13 ± 0.06	0.09 ± 0.03	0 ± 0.7	0.22 ± 0.70	1
800 GeV	0.06 ± 0.04	0 ± 0.03	0 ± 0.7	0.06 ± 0.70	0
$2e/\mu + \geq 1\tau, \text{ off-}Z, \text{ no-OSSF}$					
200 GeV	1.2 ± 0.4	2.3 ± 0.5	19 ± 6	22 ± 6	14
500 GeV	0.01 ± 0.01	0.03 ± 0.01	0.32 ± 0.73	0.36 ± 0.73	0
800 GeV	0 ± 0.003	0.01 ± 0.01	0.11 ± 0.71	0.12 ± 0.71	0
$\geq 3e/\mu, \text{ off-}Z, \text{ OSSF}$					
200 GeV	7.5 ± 2.3	63 ± 8	9 ± 4	78 ± 9	56
500 GeV	0.34 ± 0.12	3.3 ± 0.5	0 ± 0.7	3.7 ± 0.9	1
800 GeV	0.01 ± 0.01	0.54 ± 0.12	0 ± 0.7	0.5 ± 0.7	0
$2e/\mu + \geq 1\tau, \text{ off-}Z, \text{ OSSF}$					
200 GeV	0.64 ± 0.21	4.4 ± 0.6	68 ± 20	73 ± 20	67
500 GeV	0.06 ± 0.03	0.17 ± 0.04	1.1 ± 0.9	1.3 ± 0.9	0
800 GeV	0 ± 0.003	0 ± 0.03	0 ± 0.7	0 ± 0.7	0
$\geq 3e/\mu, \text{ on-}Z$					
200 GeV	23 ± 7	410 ± 50	18 ± 8	450 ± 50	387
500 GeV	0.82 ± 0.25	10.9 ± 2.3	0.6 ± 0.8	12.3 ± 2.4	12
800 GeV	0.05 ± 0.03	0.92 ± 0.23	0.10 ± 0.70	1.1 ± 0.7	3
$2e/\mu + \geq 1\tau, \text{ on-}Z$					
200 GeV	1.1 ± 0.4	20.7 ± 2.7	160 ± 50	180 ± 50	148
500 GeV	0.02 ± 0.01	0.82 ± 0.23	1.2 ± 0.9	2.0 ± 1.0	3
800 GeV	0 ± 0.003	0.04 ± 0.02	0 ± 0.71	0.04 ± 0.71	0

Table 7.3: Expected and observed event yields for the H_T^{leptons} signal regions.

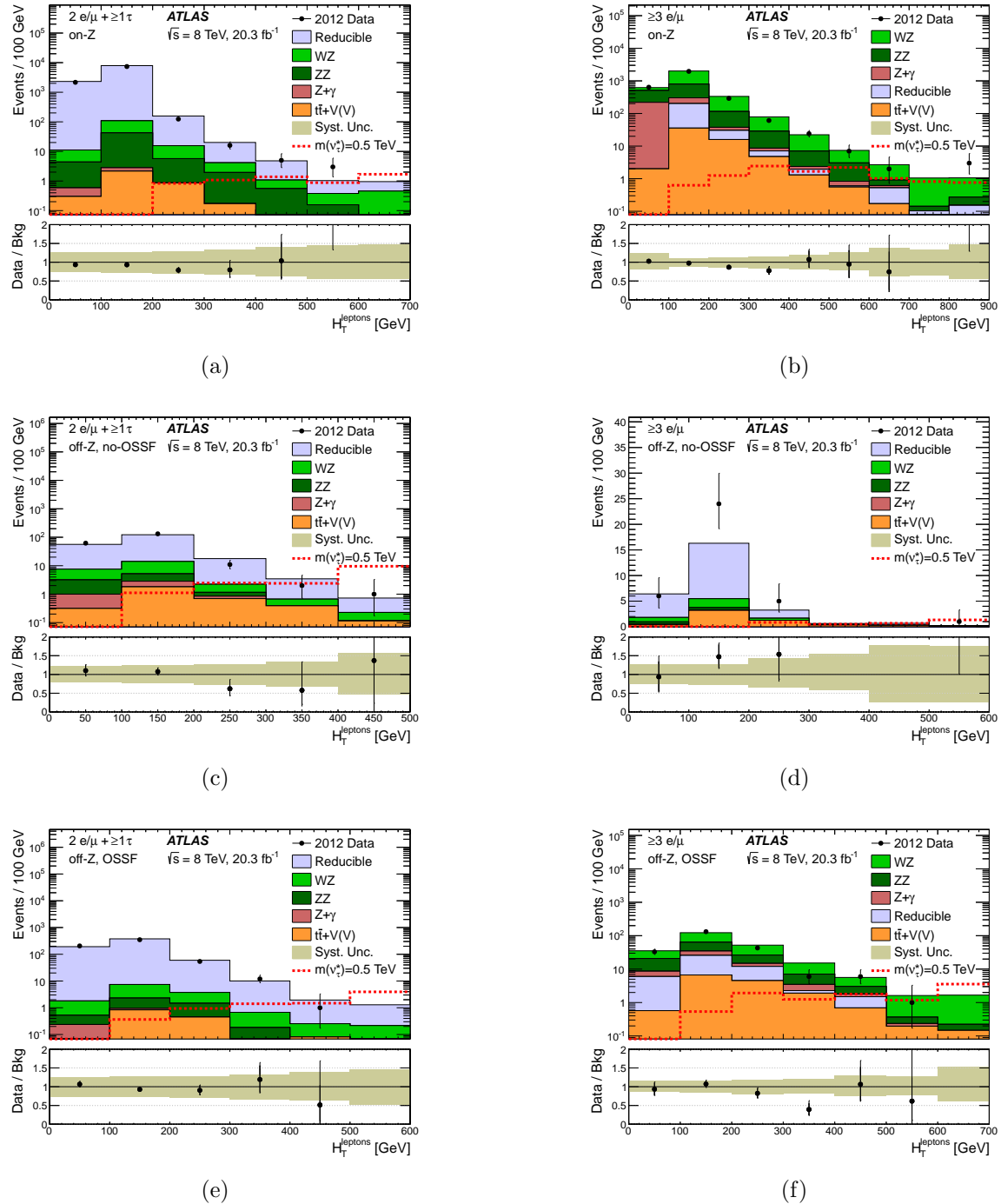


Figure 7.7: $H_T^{leptons}$ distributions in the six categories: (a) $2e/\mu + \geq 1\tau_{had}$, on- Z , (b) $\geq 3e/\mu$, on- Z , (c) $2e/\mu + \geq 1\tau_{had}$, off- Z , no-OSSF, (d) $\geq 3e/\mu$, off- Z , no-OSSF, (e) $2e/\mu + \geq 1\tau_{had}$, off- Z , OSSF, and (f) $\geq 3e/\mu$, off- Z , OSSF. The expected signal from an excited τ neutrino with mass $m(\nu_\tau^*) = 0.5$ TeV is shown to illustrate the sensitivity of the different signal regions. The lower panel shows the ratio of the observed data to the background prediction.

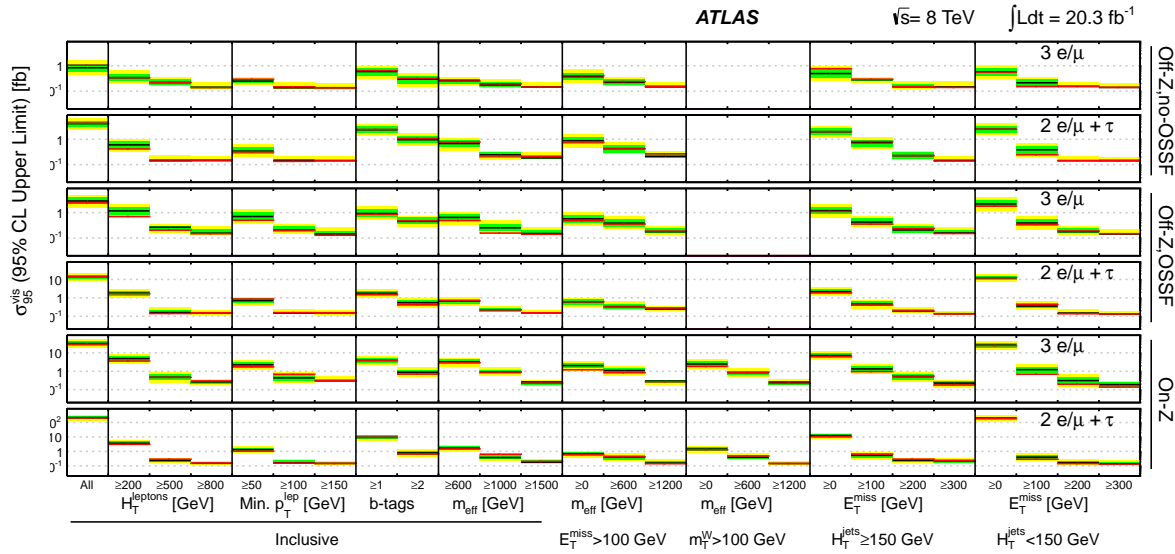


Figure 7.8: 95% CL upper limits on the visible cross section of trilepton event production from new physics, σ_{95}^{vis} , in each signal region.

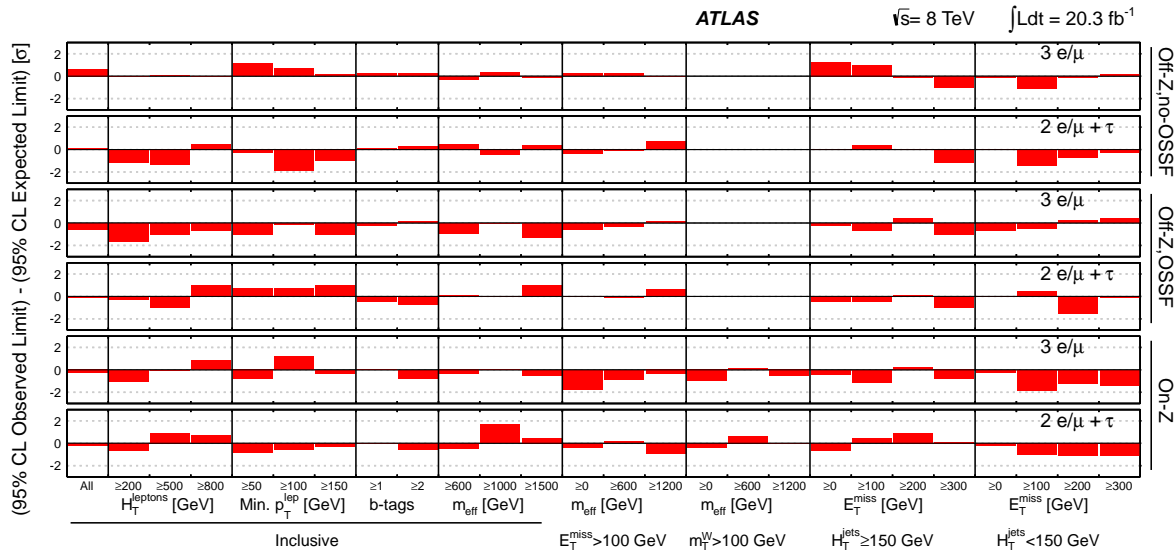


Figure 7.9: Deviations between the observed event counts and the background expectations in each signal region divided by the total uncertainty on the background prediction.

7.6 Model Testing

The 95% CL upper limits on trilepton event production from new physics derived in section 7.5 provide a useful tool with which to confront models of new physics producing trilepton final states. To facilitate the comparison of the model-independent limits with the predictions of a model (i.e. a set of simulated events from an event generator), per-lepton fiducial efficiencies are provided to quantify approximately the efficiency of triggering, reconstructing and selecting fiducial leptons at truth level. The definition of fiducial truth leptons is as follows:

- **Transverse momentum:** Electrons and muons are required to have $p_T > 10 \text{ GeV}$, while τ leptons are required to have $p_T > 15 \text{ GeV}$.
- **Pseudorapidity:** The same pseudorapidity cuts as the reconstructed signal leptons are applied. Electrons must have $|\eta| < 2.47$, excluding the region $1.37 < |\eta| < 1.52$, and muons and τ leptons must have $|\eta| < 2.5$.
- **Isolation:** For electrons and muons, the sum of the transverse momenta of all charged particles with $p_T > 1 \text{ GeV}$ within a cone of radius $\Delta R = 0.3$ of the lepton, denoted $p_{T,\text{cone},30,\text{truth}}$, must satisfy $p_{T,\text{cone},30,\text{truth}}/p_T < 0.15$. Similarly, the $E_{T,\text{cone},30,\text{truth}}$, defined as the sum of all stable, visible particles within a cone of radius $\Delta R = 0.3$, is required to satisfy $E_{T,\text{cone},30,\text{truth}}/p_T < 0.15$.
- **Origin and Decay:** Leptons must originate from the hard scattering interaction (as opposed to the interaction with the detector as simulated by GEANT4), and not arise from the decay of a hadron. Electrons and muons are also required to be stable; τ leptons are required to decay hadronically.

The per-lepton fiducial efficiencies are measured in a sample of simulated WZ events. The efficiencies are determined separately for electrons, muons, hadronically decaying τ leptons, electrons from τ decays, and muons from τ decays. Fiducial leptons are matched to reconstructed leptons satisfying the selection criteria (section 5.7.1), within a cone of $\Delta R = 0.1$ for electrons and muons and $\Delta R = 0.2$ for hadronically decaying τ leptons and electrons and muons from τ decays. The efficiency, ϵ_ℓ , is the ratio of the number of matched reconstructed leptons to the number of fiducial leptons within the geometrical acceptance. For electrons, hadronically decaying τ leptons, and electrons from τ decays, the efficiency is measured separately in bins of p_T and $|\eta|$, with the efficiency of a given lepton taken to be $\epsilon_\ell(p_T, \eta) \equiv \epsilon_\ell(p_T) \cdot \epsilon_\ell(|\eta|)/\langle \epsilon_\ell \rangle$, where $\langle \epsilon_\ell \rangle$ is the average efficiency of the inclusive sample. For muons, the efficiency is measured in bins of p_T for $|\eta| < 0.1$ and $|\eta| > 0.1$.

The efficiencies are shown in tables 7.4 and 7.5. Given a model of new physics, they can be used to compute the number of events expected in each of the signal regions; for example, an event with three leptons ℓ_1 , ℓ_2 , and ℓ_3 has an efficiency $\epsilon = \epsilon_{\ell_1} \epsilon_{\ell_2} \epsilon_{\ell_3}$ to be reconstructed and selected.

p_T [GeV]	Prompt e		Prompt μ		$\tau \rightarrow e$		$\tau \rightarrow \mu$		τ_{had}
	$ \eta > 0.1$	$ \eta < 0.1$	$ \eta > 0.1$	$ \eta < 0.1$	$ \eta > 0.1$	$ \eta < 0.1$	$ \eta > 0.1$	$ \eta < 0.1$	
10–15	0.045±0.001	0.021±0.001	0.003±0.002	0.027±0.002	0.013±0.001	0.005±0.003	-	-	
15–20	0.484±0.003	0.704±0.003	0.37±0.01	0.384±0.005	0.539±0.005	0.29±0.02	0.071±0.003	-	
20–25	0.571±0.003	0.808±0.002	0.42±0.01	0.47±0.01	0.62±0.01	0.35±0.03	0.25±0.01	-	
25–30	0.628±0.002	0.855±0.002	0.45±0.01	0.52±0.01	0.68±0.01	0.39±0.03	0.31±0.01	-	
30–40	0.681±0.002	0.896±0.001	0.50±0.01	0.57±0.01	0.71±0.01	0.42±0.03	0.31±0.01	-	
40–50	0.713±0.002	0.920±0.001	0.52±0.01	0.60±0.01	0.75±0.01	0.42±0.04	0.31±0.01	-	
50–60	0.746±0.002	0.932±0.001	0.52±0.01	0.64±0.01	0.76±0.01	0.42±0.03	0.31±0.01	-	
60–80	0.767±0.002	0.940±0.001	0.52±0.01	0.67±0.01	0.78±0.01	0.42±0.03	0.32±0.01	-	
80–100	0.800±0.003	0.940±0.002	0.52±0.01	0.68±0.02	0.79±0.02	0.42±0.04	0.32±0.02	-	
100–200	0.820±0.003	0.940±0.002	0.52±0.01	0.70±0.03	0.81±0.02	0.42±0.05	0.32±0.02	-	
200–400	0.83±0.01	0.94±0.01	0.52±0.05	0.72±0.08	0.91±0.06	-	-	-	0.29±0.05
400–600	0.83±0.04	0.93±0.02	0.50±0.20	-	-	-	-	-	-
≥ 600	0.83±0.05	0.92±0.08	-	-	-	-	-	-	-

Table 7.4: The fiducial efficiency for electrons, muons, and τ leptons in different p_T ranges ($\epsilon_{fid}(p_T)$). For electrons and muons from τ decays, the p_T is that of the electron or muon, not the τ . The uncertainties shown reflect the statistical uncertainties of the simulated samples only.

$ \eta $	Prompt e	$\tau \rightarrow e$	τ_{had}
0.0–0.1	0.640±0.003	0.37±0.01	0.24±0.01
0.1–0.5	0.699±0.001	0.41±0.01	0.31±0.01
0.5–1.0	0.702±0.001	0.41±0.01	0.28±0.01
1.0–1.5	0.660±0.002	0.37±0.01	0.21±0.01
1.5–2.0	0.605±0.002	0.36±0.01	0.25±0.01
2.0–2.5	0.602±0.002	0.38±0.01	0.25±0.01

Table 7.5: The fiducial efficiency for electrons and τ leptons in different η ranges ($\epsilon_{fid}(\eta)$). For electrons from τ decays, the η is that of the electron, not the τ . The uncertainties shown reflect the statistical uncertainties of the simulated samples only.

7.6.1 Example: Doubly Charged Scalar Particles

An example of confronting models of new physics with the model-independent limits in section 7.5, limits are established on a model of predicting doubly charged scalar particles within the context of left-right symmetry [7–10]. The model contains several scalar particles of charge 0, ± 1 , and ± 2 , the neutral component of which generates neutrino mass via the seesaw mechanism (section 2.2.3). Only pair production of the doubly charged particles, $H_{L,R}^{\pm\pm}$, is considered here, where L denotes coupling to $SU(2)_L$ or $SU(2)_R$. The phenomenology of the particles is similar, differing in their couplings to left- and right-handed fermions and in their pair production cross sections due to different gauge couplings.

The $H_{L,R}^{\pm\pm}$ decay to two charged leptons, and in general do not conserve lepton flavor. In scenarios where the $H_{L,R}^{\pm\pm}$ decay to electrons or muons, the strongest limits are derived from same-sign dilepton signatures. An ATLAS search at $\sqrt{s} = 8$ TeV excluded $H_L^{\pm\pm}$ masses below 465 GeV – 550 GeV and $H_R^{\pm\pm}$ masses below 370 GeV – 435 GeV, depending on the flavor of the lepton pair ($e^\pm e^\pm$, $e^\pm \mu^\pm$, or $\mu^\pm \mu^\pm$) [11]. If the $H_{L,R}^{\pm\pm}$ decay to $e^\pm \tau^\pm$ or $\mu^\pm \tau^\pm$, however, then competitive limits can be established using model-independent trilepton limits.

The model is confronted against the model-independent limits in the off- Z , OSSF categories, using the H_T^{leptons} signal regions and combining the **3L** and **2L+ τ_{had}** categories. Events are simulated using PYTHIA8 using the MSTW2008 leading order PDF set, with mass hypotheses in 50 GeV increments between 50 GeV – 600 GeV, plus an additional point at a mass of 1 TeV. The $H_T^{\text{leptons}} > 200$ GeV signal regions are used for $H^{\pm\pm}$ mass hypotheses below 200 GeV, while the $H_T^{\text{leptons}} > 500$ GeV signal regions are used for larger mass hypotheses. The resulting observed and expected limits are shown in figure 7.10. For left-handed doubly charged particles, masses below 400 GeV (400 GeV) are excluded for 100% branching fraction to $e^\pm \tau^\pm$ ($\mu^\pm \tau^\pm$), compared to expected limits of 350 ± 50 GeV (370 ± 20 GeV). The corresponding limits from a CMS search at $\sqrt{s} = 7$ TeV are 293 GeV (300 GeV) for 100% branching fraction to $e^\pm \tau^\pm$ ($\mu^\pm \tau^\pm$) [12].

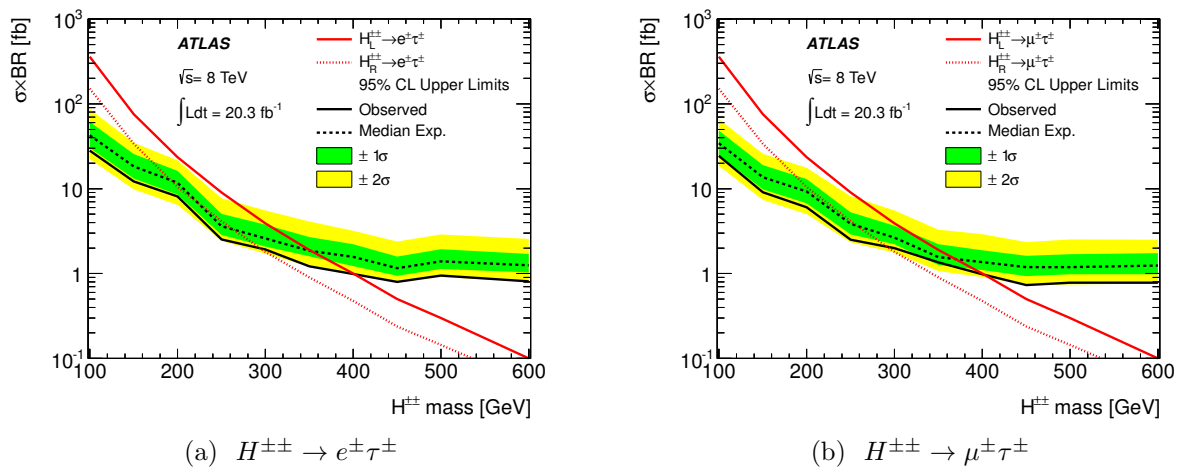


Figure 7.10: Observed and expected 95% CL limits on the cross section times branching ratio for $H^{\pm\pm}$ decaying to $e^\pm \tau^\pm$ (left) and $\mu^\pm \tau^\pm$ (right). The solid and dashed red lines show the expected cross section times branching ratio for left- and right-handed $H^{\pm\pm}$, respectively.

Bibliography

- [1] ATLAS Collaboration, *Search for new phenomena in events with three or more charged leptons in pp collisions at $\sqrt{s} = 8$ TeV with the ATLAS detector*, Accepted by JHEP (2014), arXiv: 1411.2921v2 [hep-ex].
- [2] ATLAS Collaboration, *Jet energy measurement and its systematic uncertainty in proton–proton collisions at $\sqrt{s} = 7$ TeV with the ATLAS detector*, The European Physical Journal C **75**.1 (2015) pp. 17–101.
- [3] M. V. Garzelli et al., *Z^0 -boson production in association with a $t\bar{t}$ pair at next-to-leading order accuracy with parton shower effects*, Physical Review D **85**.7 (2012) pp. 074022–6.
- [4] J. M. Campbell and R. K. Ellis, *$t\bar{t}W^\pm$ production and decay at NLO*, JHEP **2012**.7 (2012) pp. 52–12.
- [5] A. L. Read, *Presentation of search results: The $CL(s)$ technique*, J.Phys. **G28** (2002) pp. 2693–2704.
- [6] U. Baur, M. Spira, and P. M. Zerwas, *Excited-quark and-lepton production at hadron colliders*, Physical Review D **42**.3 (1990) p. 815.
- [7] J. C. Pati and A. Salam, *Lepton Number as the Fourth Color*, Phys.Rev. **D10** (1974) pp. 275–289.
- [8] R. N. Mohapatra and J. C. Pati, *Left-Right Gauge Symmetry and an Isoconjugate Model of CP Violation*, Phys.Rev. **D11**.3 (1975) pp. 566–571.
- [9] G. Senjanovic and R. N. Mohapatra, *Exact Left-Right Symmetry and Spontaneous Violation of Parity*, Phys.Rev. **D12**.5 (1975) pp. 1502–1505.
- [10] T. G. Rizzo, *Doubly Charged Higgs Bosons and Lepton Number Violating Processes*, Phys.Rev. **D25** (1982) pp. 1355–1364.
- [11] ATLAS Collaboration, *Search for anomalous production of prompt same-sign lepton pairs and pair-produced doubly charged Higgs bosons with $\sqrt{s} = 8$ TeV pp collisions using the ATLAS detector*, JHEP **2015**.3, 41 (2015).

- [12] CMS Collaboration,
A search for a doubly-charged Higgs boson in pp collisions at $\sqrt{s} = 7$ TeV,
The European Physical Journal C **72** (2012) p. 2189, arXiv: 1207.2666 [hep-ex].

Chapter 8

Trilepton Resonance Search

The sensitivity of a search using events with many electrons or muons can be enhanced significantly if the leptons are produced resonantly, allowing the use of a mass constraint. Searches for resonant dilepton production have a rich history, including the discoveries of the J/ψ [1, 2], the Υ [3], and the Z boson [4]. At the LHC, the resonant four-lepton channel proved instrumental in the recent discovery of the Higgs boson [5, 6]. Resonant dilepton searches have also placed strong constraints on a variety of new physics scenarios, such as new gauge bosons [7, 8] and doubly-charged scalar particles [9].

This chapter presents a search for the resonant production of three leptons using 20.3 fb^{-1} of pp collision data at $\sqrt{s} = 8 \text{ TeV}$ [10]. Trilepton resonances have been used previously at lower energies to place constraints on lepton flavor violation in muon and τ lepton decays [11, 12]. This analysis targets high-mass heavy leptons, L^\pm , decaying to three leptons via an intermediate on-shell Z boson, $L^\pm \rightarrow Z + \ell \rightarrow \ell\ell\ell$, where $\ell = e$ or μ . The final state is fully reconstructible, giving both a trilepton and a Z mass constraint with which to discriminate the signal from the background.

The chapter is organized as follows. Section 8.1 describes the models of new physics used to motivate the analysis. Section 8.2 describes the search strategy, including the event selection and the identification of trilepton resonance candidates. Section 8.3 lists the sources of systematic uncertainty on the signal and background estimates. The background estimates are validated in section 8.4. Finally, the results and interpretations are shown in sections 8.6 and 8.7.

8.1 Signal Models

The search is motivated by two models of phenomena beyond the Standard Model: the type III neutrino seesaw model [13] and extra generations of vector-like leptons [14], discussed earlier in sections 2.2.3 and 2.2.3. Both models propose heavy, charged, and colorless fermions which are made unstable by mixing with Standard Model leptons. The type III seesaw model

also includes a neutral heavy lepton, N^0 , with the same mass as the L^\pm ¹.

The new particles are pair produced via gauge interactions, $q\bar{q} \rightarrow L^\pm L^\mp$ or $q\bar{q}' \rightarrow L^\pm N^0$, as shown in figure 8.1. The production cross sections depend on how the new particles couple to $SU(2)_L \times U(1)_Y$: the type III seesaw fermions transform in the adjoint representation of $SU(2)_L$ and have zero hypercharge, $(\mathbf{3}, 0)$, while the heavy lepton in the generic vector-like lepton model inherits its gauge couplings from its $SU(5)$ multiplet, $(1, -1)$. The different gauge couplings, plus the various production modes, lead to significant differences in production rates. The production cross sections of the two models are shown in figure 8.2.

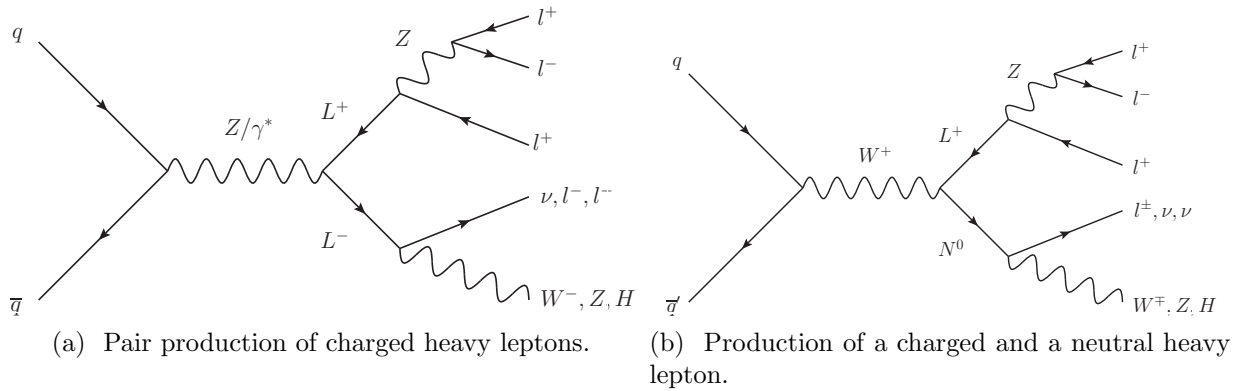


Figure 8.1: Production and decay of new heavy leptons to final states with a trilepton resonance.

The heavy leptons are made unstable by introducing mixing terms with the Standard Model leptons. For example, consider a single extra generation of fermions transforming in the adjoint representation of $SU(2)_L$, as in the type III seesaw model:

$$\Sigma \equiv \begin{pmatrix} N^0/\sqrt{2} & L^+ \\ L^- & -N^0/\sqrt{2} \end{pmatrix}. \quad (8.1)$$

The Lagrangian contains Yukawa terms mixing the heavy leptons with Standard Model leptons, $\ell = e, \mu, \tau$:

$$-\mathcal{L} \ni \sum_{\ell=e, \mu, \tau} \sqrt{2}\phi^0 \bar{\Psi} Y_{L\ell} \psi_\ell + \text{h.c.}, \quad (8.2)$$

where $\Psi \equiv L_R^{+c} + L_R^-$ is a Dirac spinor representing the four charged degrees of freedom, ψ_ℓ are Dirac spinors corresponding to the Standard Model leptons, $\phi \equiv (\phi^+, \phi^0)^T \equiv (\phi^+, (v + H + i\eta)/\sqrt{2})^T$ is the Higgs doublet, and $Y_{L\ell}$ are Yukawa couplings. After electroweak symmetry

¹The masses are equal at tree level due to $SU(2)$ symmetry. Radiative corrections introduce a small mass splitting of $\sim 250 \text{ MeV} - 350 \text{ MeV}$, which is inconsequential for this analysis [15].

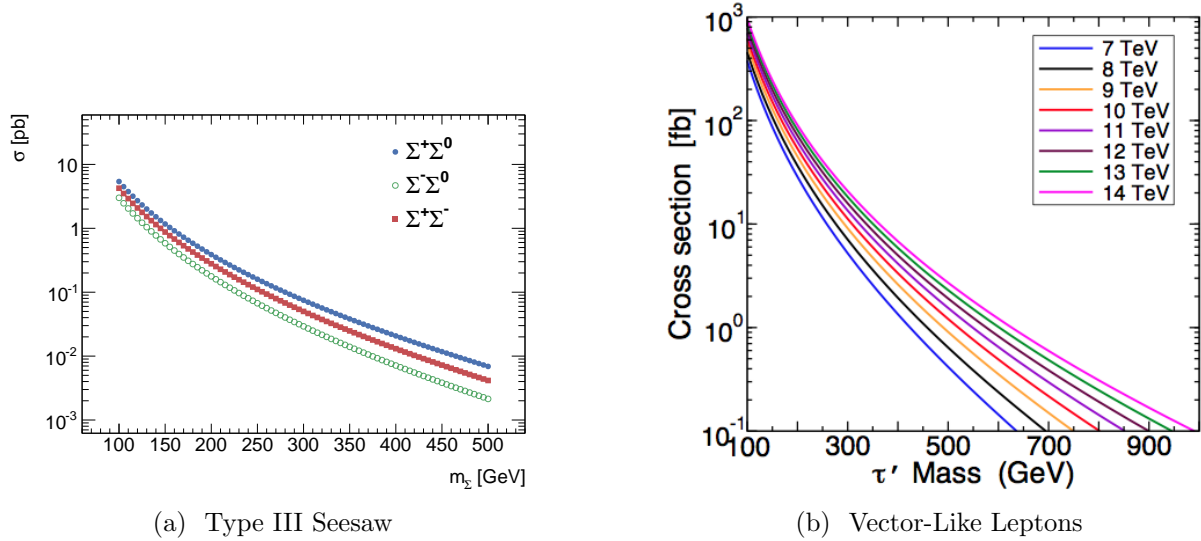


Figure 8.2: Production cross sections at $\sqrt{s} = 8$ TeV for heavy lepton pair production for the type III seesaw model (left) and the vector-like leptons model (right).

breaking, the mass matrices take the form

$$-\mathcal{L} \ni \sum_{\ell=e,\mu,\tau} (\bar{\psi}_{\ell,R} \quad \bar{\Psi}_R) \begin{pmatrix} m_\ell & 0 \\ Y_{L\ell}v & M_{L^\pm} \end{pmatrix} \begin{pmatrix} \psi_{\ell,L} \\ \Psi_L \end{pmatrix} + (\bar{\psi}_{\ell,L} \quad \bar{\Psi}_L) \begin{pmatrix} m_\ell & Y_{L\ell}^\dagger v \\ 0 & M_{L^\pm} \end{pmatrix} \begin{pmatrix} \psi_{\ell,R} \\ \Psi_r \end{pmatrix}. \quad (8.3)$$

Diagonalizing the mass matrices leads to off-diagonal terms in the gauge interactions, with couplings proportional to the mixing parameters $V_{L\ell} = \frac{v}{\sqrt{2}} M_{L^\pm}^{-1} Y_{L\ell}$. These couplings enable the decay of the heavy leptons to a boson (W , Z , or H) plus a Standard Model lepton or neutrino, with partial widths given by²:

²Note that for the type III seesaw model, the small mass splitting between the charged and neutral states also allows the decay $L^\pm \rightarrow N^0 \pi^\pm$. For mixing angles large enough that the L^\pm decay promptly, this decay mode is negligible [15].

$$\Gamma(N^0 \rightarrow \ell^- W^+) = \Gamma(N^0 \rightarrow \ell^+ W^-) = \frac{g^2}{64\pi} |V_{L\ell}|^2 \frac{M_{L^\pm}^3}{M_W^2} \left(1 - \frac{M_W^2}{M_{L^\pm}^2}\right)^2 \left(1 + 2\frac{M_W^2}{M_{L^\pm}^2}\right), \quad (8.4)$$

$$\sum_\ell \Gamma(N^0 \rightarrow \nu_\ell Z) = \frac{g^2}{64\pi c_W^2} \sum_\ell |V_{L\ell}|^2 \frac{M_{L^\pm}^3}{M_Z^2} \left(1 - \frac{M_Z^2}{M_{L^\pm}^2}\right)^2 \left(1 + 2\frac{M_Z^2}{M_{L^\pm}^2}\right), \quad (8.5)$$

$$\sum_\ell \Gamma(N^0 \rightarrow \nu_\ell H) = \frac{g^2}{64\pi} \sum_\ell |V_{L\ell}|^2 \frac{M_{L^\pm}^3}{M_W^2} \left(1 - \frac{M_H^2}{M_{L^\pm}^2}\right)^2, \quad (8.6)$$

$$\sum_\ell \Gamma(L^+ \rightarrow \nu_\ell W^+) = \frac{g^2}{32\pi} \sum_\ell |V_{L\ell}|^2 \frac{M_{L^\pm}^3}{M_W^2} \left(1 - \frac{M_W^2}{M_{L^\pm}^2}\right)^2 \left(1 + 2\frac{M_W^2}{M_{L^\pm}^2}\right), \quad (8.7)$$

$$\Gamma(L^+ \rightarrow \ell^+ Z) = \frac{g^2}{64\pi c_W^2} |V_{L\ell}|^2 \frac{M_{L^\pm}^3}{M_Z^2} \left(1 - \frac{M_Z^2}{M_{L^\pm}^2}\right)^2 \left(1 + 2\frac{M_Z^2}{M_{L^\pm}^2}\right), \quad (8.8)$$

$$\Gamma(L^+ \rightarrow \ell^+ H) = \frac{g^2}{64\pi} |V_{L\ell}|^2 \frac{M_{L^\pm}^3}{M_W^2} \left(1 - \frac{M_H^2}{M_{L^\pm}^2}\right)^2. \quad (8.9)$$

The branching fractions of the charged and neutrino heavy leptons are shown as function of m_{L^\pm} in figure 8.3. Note that these branching fractions are common to all the models considered in this analysis.

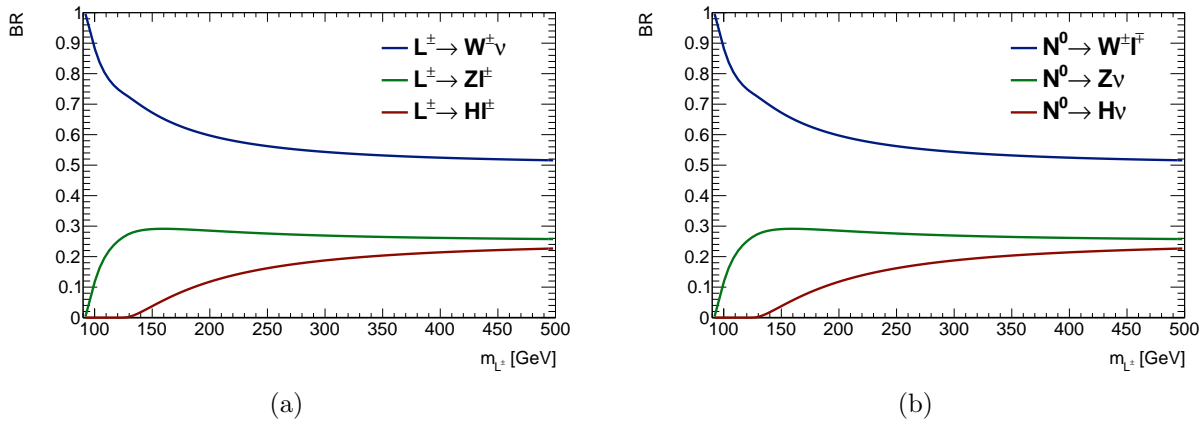


Figure 8.3: Branching ratios of a L^\pm (left) or N^0 (right) decaying via mixing with Standard Model leptons.

Constraints on the mixing parameters $V_{L\ell}$ can be derived from precision measurements of the Z width, and constraints on products of the mixing parameters from flavor violation

experiments like $\mu \rightarrow e\gamma$ [16–19]. These are shown in equations 8.10–8.15. Note that the L^\pm decays are prompt if the mixing angles are larger than $\sim 10^{-4}$ [20]. In this analysis, only mixings with electrons and muons are considered, as heavy leptons decaying to $Z + \tau$ do not produce a narrow trilepton mass peak.

$$|V_{Le}| < 5.5 \times 10^{-2} \quad (8.10)$$

$$|V_{L\mu}| < 6.3 \times 10^{-2} \quad (8.11)$$

$$|V_{L\tau}| < 6.3 \times 10^{-2} \quad (8.12)$$

$$|V_{Le}V_{L\mu}| < 1.7 \times 10^{-7} \quad (8.13)$$

$$|V_{Le}V_{L\tau}| < 4.2 \times 10^{-4} \quad (8.14)$$

$$|V_{L\mu}V_{L\tau}| < 4.9 \times 10^{-4}. \quad (8.15)$$

8.1.1 Signal Monte Carlo Samples

Signal events are generated using Monte Carlo simulation, with eleven mass hypotheses in the range $100 \text{ GeV} \leq m_{L^\pm} \leq 400 \text{ GeV}$ for the vector-like leptons model and ten mass hypothesis in the range $100 \text{ GeV} \leq m_{L^\pm, N^0} \leq 500 \text{ GeV}$ for the type III seesaw model. The samples are summarized in table 8.1. The events are generated with MADGRAPH 4.5.2 and 5.2.2.1 [21], for the vector-like leptons and type III seesaw models, respectively, using the CTEQ6L1 [22] PDF set and the AU2 underlying event tune [23]. Showering is performed with PYTHIA 8 [24]. Decays of the heavy leptons in the vector-like leptons model are performed using BRIDGE [25], while decays in the type III seesaw samples are performed by MADGRAPH. The cross sections for both samples are calculated at leading order (LO) in QCD, and are shown in table 8.1.

For the type III seesaw model, the charged and neutral heavy leptons are generated with identical masses. The simulated decay modes are listed in table 8.2. The mixing parameters are chosen to be $V_{Le} = 0.055$, $V_{L\mu} = 0.063$, and $V_{L\tau} = 0$, yielding a mix of ee , $e\mu$, and $\mu\mu$ decays. For the vector-like leptons model, one heavy lepton is required to decay via $L^\pm \rightarrow Z(\ell\ell)\ell$, where $\ell = e, \mu, \tau$. The two heavy leptons are constrained to decay to the same flavor of Standard Model lepton, which is chosen with equal probability to be an electron, muon, or τ . For both models, the events are reweighted to correspond to electron-only or muon-only mixing scenarios.

8.2 Search Strategy

8.2.1 Event Selection and Heavy Lepton Reconstruction

The event selection is very similar to that used in the model-independent analysis, described in section 7.1. In particular, the same definitions are used for leptons and jets, in order to

Mass [GeV]	Cross Section [pb]	Equivalent L [fb^{-1}]
Type III Seesaw		
100	1.273	7.7×10^2
120	2.138	2.9×10^2
160	0.853	6.5×10^2
200	0.346	1.4×10^3
250	0.135	3.5×10^3
300	0.0604	3.8×10^3
350	0.02969	7.2×10^3
400	0.01566	1.3×10^4
450	0.008733	2.3×10^4
450	0.00504	4.0×10^4
Vector-Like Leptons		
100	0.378	1.1×10^4
110	0.264	9.2×10^3
120	0.193	1.0×10^4
130	0.142	1.3×10^4
140	0.106	1.7×10^4
160	0.0645	2.7×10^4
180	0.0407	4.3×10^4
200	0.0265	6.7×10^4
250	0.0104	1.8×10^5
300	0.00457	4.1×10^5
400	0.00115	1.7×10^6

Table 8.1: Mass values, production cross sections, and equivalent luminosities of the signal Monte Carlo samples.

Production Mode	Decay 1	Decay 2
$pp \rightarrow N^0 L^+$	$N^0 \rightarrow \ell^+ W^-$	$L^+ \rightarrow \ell^+ Z$
$pp \rightarrow N^0 L^+$	$N^0 \rightarrow \ell^- W^+$	$L^+ \rightarrow \ell^+ Z$
$pp \rightarrow N^0 L^+$	$N^0 \rightarrow \nu_\ell Z$	$L^+ \rightarrow \ell^+ Z$
$pp \rightarrow N^0 L^+$	$N^0 \rightarrow \nu_\ell H$	$L^+ \rightarrow \ell^+ Z$
$pp \rightarrow N^0 L^-$	$N^0 \rightarrow \ell^- W^+$	$L^- \rightarrow \ell^- Z$
$pp \rightarrow N^0 L^-$	$N^0 \rightarrow \ell^+ W^-$	$L^- \rightarrow \ell^- Z$
$pp \rightarrow N^0 L^-$	$N^0 \rightarrow \nu_\ell Z$	$L^- \rightarrow \ell^- Z$
$pp \rightarrow N^0 L^-$	$N^0 \rightarrow \nu_\ell H$	$L^- \rightarrow \ell^- Z$
$pp \rightarrow L^- L^+$	$L^- \rightarrow \ell^- Z$	$L^+ \rightarrow \ell^+ Z$
$pp \rightarrow L^- L^+$	$L^- \rightarrow \nu_l W^-$	$L^+ \rightarrow \ell^+ Z$
$pp \rightarrow L^- L^+$	$L^- \rightarrow \ell^- H$	$L^+ \rightarrow \ell^+ Z$
$pp \rightarrow L^- L^+$	$L^- \rightarrow \ell^- Z$	$L^+ \rightarrow \nu_l W^+$
$pp \rightarrow L^- L^+$	$L^- \rightarrow \ell^- Z$	$L^+ \rightarrow \ell^+ H$

Table 8.2: Production modes and decays of the two heavy leptons simulated for the type III seesaw signal samples.

make use of the same fake factor method to estimate the reducible backgrounds. Events containing a heavy lepton candidate are selected as follows.

- The triggers and vertex requirements are the same as those used for the model-independent analysis, as described in section 7.1.
- Events are required to have at least three electrons or muons (eee , $ee\mu$, $\mu\mu e$, $\mu\mu\mu$) satisfying the lepton selection criteria (table 5.2).
- Events must have one Z candidate, consisting of a opposite-sign, same-flavor (OSSF) pair of leptons with $|m_{l^+l^-} - m_Z| < 10$ GeV. The Z mass is taken to be $m_Z = 91.1876$ GeV [26].
- Four-lepton events with two leptonic Z candidates with $|m_{\ell\ell} - m_Z| < 10$ GeV are rejected to suppress the Standard Model ZZ background. The efficiency loss for signal events is less than $\sim 4\%$.
- If an event contains more than three leptons, a unique trilepton candidate in each event is chosen as follows:
 - Choose the OSSF pair with invariant mass closest to m_Z .
 - Choose the third (“off- Z ”) lepton to be the closest in ΔR to the reconstructed Z four-momentum.
- For low heavy lepton mass hypotheses, $m_{L^\pm} \lesssim 200$ GeV, the Z and the third lepton tend to be collimated. The expected background and signal ΔR distributions for selected trilepton candidate are shown in figure 8.4. Imposing a cut on the $\Delta R(Z, \ell_3)$ of the trilepton candidates improves the signal significance, and also provides a useful control region defined by inverting the cut.

The value is chosen based on a study of the expected sensitivity of the analysis at different values of the cut. The expected sensitivity is determined using a simple cut-and-count framework using narrow mass windows. The half-width of the mass windows is taken from a linear fit to the full-width half-maxima of the signal peaks as determined from the signal fits (section B.0.2). The expected 95% CL exclusion on the signal cross section is then determined from the number of signal and background events inside the mass window predicted from Monte Carlo simulation, using the CL_s method implemented in the `mclimits` framework [27].

The expected exclusions for several cut values are shown in figure 8.5. The same cut is applied to all signal categories; no significant gain is observed by optimizing each category individually. Smaller values of the cut ($\Delta R(Z, \ell_3) \lesssim 2.0$) perform similarly to more stringent cuts at low signal mass hypotheses but worse at higher mass hypotheses. Cuts above $\Delta R(Z, \ell_3) \lesssim 3.0$ perform approximately equally. For simplicity, a flat cut value $\Delta R(Z, \ell_3) < 3.0$ is chosen, independent of the mass hypothesis.

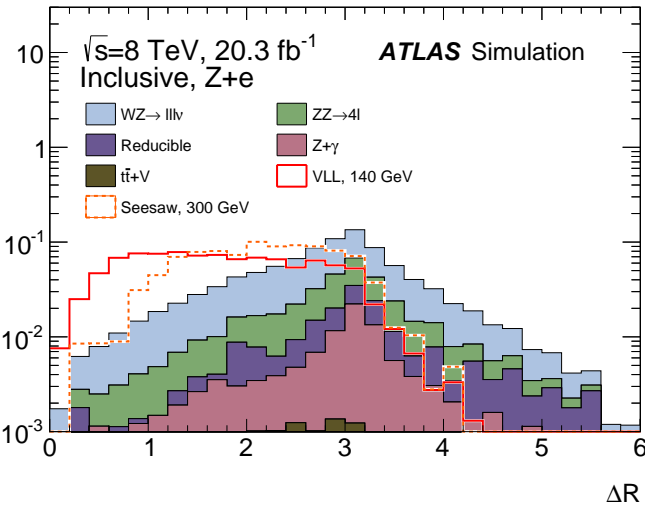


Figure 8.4: Expected $\Delta R(Z, \ell_3)$ distributions for background and signal for events containing a Z candidate plus an electron.

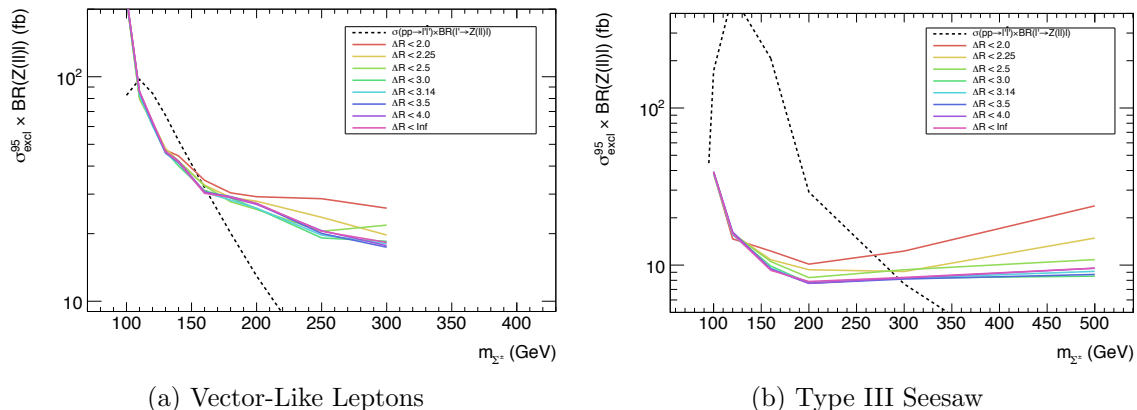


Figure 8.5: Expected upper limits on the heavy lepton production cross section times branching ratio to final states with least one $Z(\ell\ell) + \ell$ decay for different cuts on the maximum value of $\Delta R(Z, \ell_3)$.

- The variable used to apply the trilepton mass constraint is $\Delta m \equiv m_{3\ell} - m_{\ell^+\ell^-}$, where the invariant mass of the two leptons associated with a Z boson decay is subtracted by the trilepton mass. This method reduces the impact of the lepton energy or momentum resolutions on the width of the resonance peak, at the cost of introducing some width due to the intrinsic width of the Z , $\Gamma_Z = 2.4952 \pm 0.0023$ GeV [26]. Over most of the mass range, this variable reduces the width of the signal peaks, as shown in table 8.3.

m_{L^\pm} [GeV]	$Z + e$		$Z + \mu$	
	FWHM ($m_{3\ell}$) [GeV]	FWHM (Δm) [GeV]	FWHM ($m_{3\ell}$) [GeV]	FWHM (Δm) [GeV]
100	6.57	5.99	4.73	6.82
110	6.43	4.98	5.96	4.90
120	5.58	5.89	5.29	5.21
130	6.31	5.84	5.58	5.65
140	6.62	6.44	6.30	6.25
160	7.77	7.53	7.82	7.71
180	8.77	8.22	9.06	8.67
200	9.55	8.68	11.30	10.88
300	13.68	12.03	21.65	20.31
400	17.73	15.56	33.68	31.78

Table 8.3: Comparison of the full-width, half-maxima of the signal peaks between the Δm and $m_{3\ell}$ variables. The signal peaks are modeled using a Voigtian function, a convolution of a Gaussian and a Lorentzian, fit to the Monte Carlo simulation. The fit is described in section 8.5.1. The full-width, half-maximum of a Voigtian is given approximately by $\text{FWHM} \approx 0.5346f_L + \sqrt{0.02166f_L^2 + f_G^2}$, where $f_L = 2\gamma$ is the FWHM of the Lorentzian and $f_G = 2\sigma\sqrt{2\log 2}$ is the FWHM of the Gaussian.

After identifying the trilepton candidates, six mutually exclusive signal regions are defined. First, to target the flavor structure of the heavy lepton mixing, events are divided into two flavor channels, $Z + e$ and $Z + \mu$, depending on the flavor the off- Z lepton. Second, as the heavy leptons are pair produced, signal events contain additional activity due to the decay of the second heavy lepton. Events are divided into three exclusive categories based on other activity in the event:

- 4ℓ : events containing a fourth lepton, either an electron or a muon, passing the normal lepton criteria.
- $3\ell + jj$: events containing exactly three leptons and a jet pair with $60.385 \text{ GeV} < m_{jj} < 150.9 \text{ GeV}$.
- 3ℓ -only: all other events, i.e. events with three leptons and no jet pair satisfying the invariant mass requirement.

The choice of these three categories is motivated in figure 8.6, which shows the fraction of events with various activity from the decay of the other heavy lepton. The additional activity includes extra leptons, neutrinos, and jets from W , Z , and H boson decays. Assuming that the mixing with τ leptons is zero ($V_{\tau L} = 0$), the requirements of a fourth lepton or a hadronically decaying boson are very efficient on signal events. If the second heavy fermion is charged, then the only decay mode that fails both requirements is $L^\pm \rightarrow W^\pm(\tau^\pm\nu)\nu$, where the τ lepton decays hadronically. If the second heavy fermion is neutral, then only the $N^0 \rightarrow Z(\nu\nu)\nu$ and a small fraction of $N^0 \rightarrow H\nu$ decay modes fail both requirements.

Categorization targeting neutrinos is less effective at separating signal from the large WZ background (see figures B.5-B.8).

In some cases, it is useful to consider the events without dividing into these three categories, distinguishing events only by the flavor of the off- Z lepton. This is referred to as the “Inclusive” signal region below.

The performance of the selection procedure is shown in tables 8.4 and 8.5 in terms of the efficiency on fiducial events³. The fiducial events are required to have three truth-level leptons satisfying $p_T > 15$ GeV and $|\eta| < 2.5$, where two of the leptons form a Z candidate with $|m_{\ell^+\ell^-} - m_Z| < 10$ GeV, the third lepton is of the correct flavor, and the trilepton mass satisfies $|m_{3\ell} - m_{L^\pm}| < 5$ GeV. The efficiency of the event selection for the $Z + e$ ($Z + \mu$) decay channel ranges from 20% (36%) at $m_{L^\pm} = 100$ GeV to 35% (38%) at $m_{L^\pm} = 400$ GeV. The selection efficiency is discussed in more detail in section 8.7.1.

In all six signal regions, the backgrounds are dominated by diboson production, ZZ in the 4ℓ category and WZ in the remaining categories. Reducible processes, $t\bar{t} + V$ production, and, for the $Z + e$ signal regions, $Z + \gamma$ make up a smaller part of the total background. The contribution from triboson production is negligible.

Process	Preselection	Bachelor e	$ m_{\ell^+\ell^-} - m_Z < 10$ GeV	Veto $2Z$	$\Delta R < 3.0$	4ℓ	$3\ell + jj$	3ℓ -only
VLL, 100 GeV	34.8 ± 0.8	31.8 ± 0.8	30.6 ± 0.8	30.3 ± 0.8	29.8 ± 0.8	5.4 ± 0.4	9.6 ± 0.5	14.7 ± 0.6
VLL, 110 GeV	47.8 ± 0.6	43.5 ± 0.6	42.1 ± 0.6	41.7 ± 0.6	40.1 ± 0.6	7.6 ± 0.3	11.0 ± 0.4	21.5 ± 0.5
VLL, 120 GeV	53.5 ± 0.6	49.1 ± 0.6	46.7 ± 0.6	45.7 ± 0.6	42.4 ± 0.6	10.4 ± 0.4	11.7 ± 0.4	20.4 ± 0.5
VLL, 130 GeV	60.4 ± 0.6	53.9 ± 0.6	50.9 ± 0.6	49.4 ± 0.6	44.5 ± 0.6	12.5 ± 0.4	12.7 ± 0.4	19.4 ± 0.5
VLL, 140 GeV	64.3 ± 0.6	57.8 ± 0.6	55.9 ± 0.6	53.8 ± 0.6	49.1 ± 0.6	15.3 ± 0.4	16.4 ± 0.4	17.4 ± 0.5
VLL, 160 GeV	66.3 ± 0.6	59.3 ± 0.6	57.2 ± 0.6	55.2 ± 0.6	49.9 ± 0.6	17.5 ± 0.5	14.8 ± 0.4	17.6 ± 0.5
VLL, 180 GeV	69.8 ± 0.6	62.0 ± 0.6	59.4 ± 0.6	57.3 ± 0.7	50.5 ± 0.7	19.7 ± 0.5	16.3 ± 0.5	14.4 ± 0.5
VLL, 200 GeV	70.7 ± 0.6	62.4 ± 0.7	59.6 ± 0.7	57.7 ± 0.7	52.0 ± 0.7	20.9 ± 0.6	16.7 ± 0.5	14.5 ± 0.5
VLL, 250 GeV	75.1 ± 0.7	65.4 ± 0.7	62.6 ± 0.7	61.5 ± 0.7	54.8 ± 0.8	24.5 ± 0.7	15.2 ± 0.5	15.1 ± 0.5
VLL, 300 GeV	77.1 ± 0.7	66.2 ± 0.8	63.0 ± 0.8	62.5 ± 0.8	54.7 ± 0.8	25.8 ± 0.7	16.9 ± 0.6	12.1 ± 0.5
VLL, 400 GeV	77.6 ± 0.7	66.9 ± 0.8	64.2 ± 0.8	64.1 ± 0.8	56.2 ± 0.8	27.7 ± 0.7	18.1 ± 0.6	10.3 ± 0.5
Seesaw, 100 GeV	38.1 ± 0.6	35.1 ± 0.5	33.6 ± 0.5	33.4 ± 0.5	30.8 ± 0.5	8.0 ± 0.3	9.6 ± 0.3	13.1 ± 0.4
Seesaw, 120 GeV	51.7 ± 0.4	47.4 ± 0.4	45.0 ± 0.4	44.0 ± 0.4	40.3 ± 0.4	12.8 ± 0.3	12.8 ± 0.3	14.8 ± 0.3
Seesaw, 160 GeV	61.1 ± 0.5	54.8 ± 0.5	53.2 ± 0.5	51.6 ± 0.5	46.4 ± 0.5	16.7 ± 0.4	14.1 ± 0.3	15.7 ± 0.3
Seesaw, 200 GeV	65.7 ± 0.5	59.1 ± 0.5	57.4 ± 0.5	55.9 ± 0.5	5 ± 0.5	20.3 ± 0.4	14.6 ± 0.3	15.2 ± 0.4
Seesaw, 250 GeV	67.1 ± 0.7	60.5 ± 0.7	59.2 ± 0.7	58.2 ± 0.7	50.5 ± 0.7	22.1 ± 0.6	14.0 ± 0.5	14.4 ± 0.5
Seesaw, 300 GeV	72.9 ± 0.7	64.9 ± 0.7	63.3 ± 0.7	62.6 ± 0.7	54.1 ± 0.8	23.0 ± 0.6	16.7 ± 0.6	14.4 ± 0.5
Seesaw, 350 GeV	72.0 ± 0.7	65.1 ± 0.8	63.8 ± 0.8	63.5 ± 0.8	55.3 ± 0.8	25.1 ± 0.7	15.7 ± 0.6	14.6 ± 0.6
Seesaw, 400 GeV	71.7 ± 0.7	64.1 ± 0.8	62.7 ± 0.8	62.3 ± 0.8	52.9 ± 0.8	24.3 ± 0.7	15.0 ± 0.6	13.6 ± 0.5
Seesaw, 450 GeV	76.2 ± 0.8	67.0 ± 0.9	66.0 ± 0.9	65.7 ± 0.9	55.4 ± 0.9	26.7 ± 0.8	18.4 ± 0.7	10.3 ± 0.6
Seesaw, 500 GeV	72.0 ± 0.7	63.6 ± 0.8	61.1 ± 0.8	60.8 ± 0.8	52.5 ± 0.8	24.0 ± 0.7	15.1 ± 0.6	13.4 ± 0.5

Table 8.4: Percent of fiducial events remaining at various stages in the cutflow for the $Z + e$ signal regions.⁰ Only statistical uncertainties due to finite Monte Carlo statistics are shown. The preselection cut requires three selected leptons, with one OSSF pair, as well as the general event selection cuts listed above.

³Note that cut imposing a flavor requirement on the reconstructed off- Z lepton has a different efficiency between the vector-like lepton sample and the seesaw sample. This is a consequence of the flavor content of the samples used to compute the efficiencies: the vector-like lepton samples are divided into two samples with 100% branching fraction to either $Z + e$ or $Z + \mu$, while the seesaw samples contain both $Z + e$ and $Z + \mu$ decays.

Process	Preselection	Bachelor μ	$ m_{l+l-} - m_Z < 10$ GeV	Veto $2Z$	$\Delta R < 3.0$	$4l$	$3l + jj$	Else
VLL, 100 GeV	52.0 ± 0.7	50.8 ± 0.7	47.2 ± 0.7	46.1 ± 0.7	45.6 ± 0.7	6.4 ± 0.4	14.0 ± 0.5	25.2 ± 0.6
VLL, 110 GeV	61.0 ± 0.4	59.3 ± 0.4	56.8 ± 0.4	55.4 ± 0.4	53.6 ± 0.4	11.9 ± 0.3	14.2 ± 0.3	27.5 ± 0.4
VLL, 120 GeV	67.0 ± 0.3	64.8 ± 0.4	61.7 ± 0.4	59.6 ± 0.4	56.1 ± 0.4	14.9 ± 0.3	13.9 ± 0.3	27.3 ± 0.3
VLL, 130 GeV	70.2 ± 0.3	67.6 ± 0.3	64.2 ± 0.3	61.4 ± 0.3	56.9 ± 0.3	16.3 ± 0.3	14.3 ± 0.2	26.3 ± 0.3
VLL, 140 GeV	72.3 ± 0.3	70.1 ± 0.3	66.7 ± 0.3	63.4 ± 0.3	58.5 ± 0.3	17.3 ± 0.3	15.6 ± 0.2	25.6 ± 0.3
VLL, 160 GeV	75.2 ± 0.3	72.7 ± 0.3	68.5 ± 0.3	65.0 ± 0.3	59.2 ± 0.3	21.2 ± 0.3	15.6 ± 0.2	22.3 ± 0.3
VLL, 180 GeV	77.0 ± 0.3	74.6 ± 0.3	69.0 ± 0.3	65.9 ± 0.3	59.3 ± 0.3	22.7 ± 0.3	16.1 ± 0.2	20.5 ± 0.3
VLL, 200 GeV	77.9 ± 0.3	75.1 ± 0.3	69.0 ± 0.3	66.0 ± 0.3	58.4 ± 0.3	23.9 ± 0.3	16.1 ± 0.2	18.4 ± 0.2
VLL, 250 GeV	78.6 ± 0.3	75.2 ± 0.3	67.6 ± 0.3	65.7 ± 0.3	57.9 ± 0.3	26.8 ± 0.3	16.2 ± 0.2	14.9 ± 0.2
VLL, 300 GeV	78.9 ± 0.2	76.0 ± 0.3	68.0 ± 0.3	66.7 ± 0.3	57.8 ± 0.3	28.8 ± 0.3	16.3 ± 0.2	12.7 ± 0.2
VLL, 400 GeV	78.7 ± 0.2	75.3 ± 0.3	66.5 ± 0.3	65.6 ± 0.3	56.3 ± 0.3	29.2 ± 0.3	16.6 ± 0.2	10.6 ± 0.2
Seesaw, 100 GeV	53.5 ± 0.6	52.1 ± 0.6	48.4 ± 0.6	47.1 ± 0.6	46.0 ± 0.6	19.2 ± 0.5	12.1 ± 0.4	14.7 ± 0.4
Seesaw, 120 GeV	67.7 ± 0.4	66.0 ± 0.4	61.3 ± 0.4	58.9 ± 0.4	54.6 ± 0.4	21.2 ± 0.4	11.9 ± 0.3	21.5 ± 0.4
Seesaw, 160 GeV	74.5 ± 0.4	72.3 ± 0.4	68.5 ± 0.4	65.8 ± 0.4	59.5 ± 0.5	25.2 ± 0.4	14.0 ± 0.3	20.2 ± 0.4
Seesaw, 200 GeV	74.3 ± 0.4	71.7 ± 0.5	66.8 ± 0.5	65.1 ± 0.5	58.8 ± 0.5	26.3 ± 0.4	15.2 ± 0.4	17.3 ± 0.4
Seesaw, 250 GeV	76.1 ± 0.6	73.5 ± 0.6	67.3 ± 0.7	66.2 ± 0.7	58.5 ± 0.7	28.4 ± 0.6	14.4 ± 0.5	15.7 ± 0.5
Seesaw, 300 GeV	78.5 ± 0.6	76.4 ± 0.6	69.5 ± 0.7	68.8 ± 0.7	60.1 ± 0.7	29.5 ± 0.7	17.1 ± 0.6	13.5 ± 0.5
Seesaw, 350 GeV	78.0 ± 0.6	75.7 ± 0.7	68.8 ± 0.7	68.1 ± 0.7	59.0 ± 0.8	29.4 ± 0.7	15.5 ± 0.6	14.1 ± 0.5
Seesaw, 400 GeV	75.3 ± 0.7	72.7 ± 0.7	64.2 ± 0.8	63.4 ± 0.8	54.4 ± 0.8	27.7 ± 0.7	15.0 ± 0.6	11.8 ± 0.5
Seesaw, 450 GeV	76.2 ± 0.8	73.2 ± 0.8	65.8 ± 0.8	65.3 ± 0.9	55.5 ± 0.9	28.5 ± 0.8	15.2 ± 0.6	11.9 ± 0.6
Seesaw, 500 GeV	75.5 ± 0.7	72.9 ± 0.7	65.4 ± 0.8	65.0 ± 0.8	55.1 ± 0.8	27.5 ± 0.7	15.5 ± 0.6	12.2 ± 0.5

Table 8.5: Percent of fiducial events remaining at various stages in the cutflow for the $Z + \mu$ signal regions. Only statistical uncertainties due to finite Monte Carlo statistics are shown. The preselection cut requires three selected leptons, with one OSSF pair, as well as the general event selection cuts listed above.

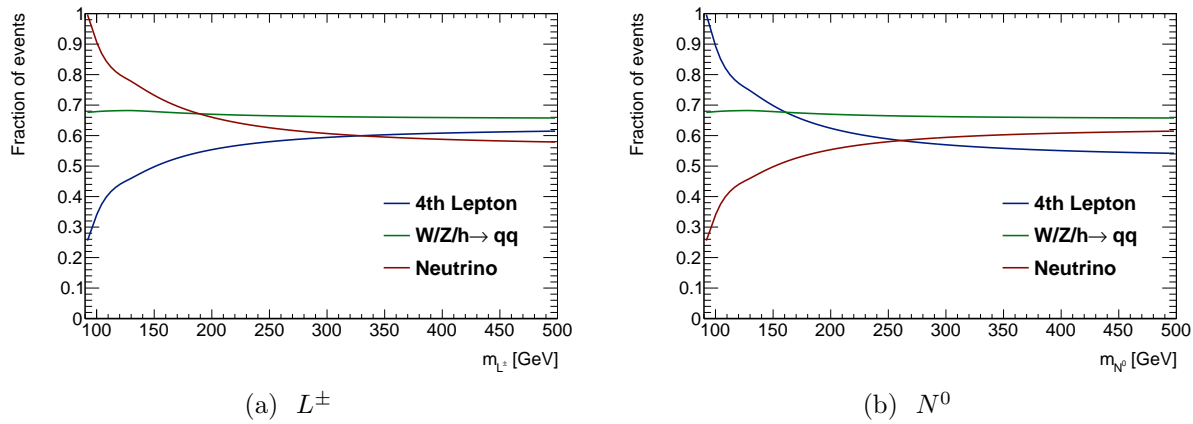


Figure 8.6: Fraction of events with various activity on the opposite side of the event, for $L^\pm L^\mp$ events at left, and $L^\pm N^0$ events at right. The left plot, showing the opposite side activity for a $L^\pm L^\mp$ final state, is identical for the type III seesaw and vector-like lepton models.

8.3 Systematic Uncertainties

The signal predictions and background estimates are assigned systematic uncertainties from several sources. In approximate order of significance, these are:

- **Diboson shape uncertainty:** A systematic uncertainty is assigned to the modeling of the diboson Δm spectra by comparing SHERPA to POWHEG. SHERPA is used as a central value, with uncertainty given by the symmetric difference between SHERPA and POWHEG. As shown below in section 8.5.2, the shapes of the 4ℓ and 3ℓ -only signal regions are consistent with the inclusive signal region, so the shape uncertainty is taken from the inclusive signal region. The comparison for the WZ background is shown in figure 8.7.

In the case of the ZZ background, the procedure is complicated by the fact that the POWHEG sample is filtered to remove events with OSSF lepton pairs with $m_{l^+l^-} < 4$ GeV (`m114`). In order to compare the samples in a common phase space, the `m114` filter is emulated on the SHERPA sample by rejecting events that contain a OSSF pair of truth leptons with $m_{l^+l^-} < 4$ GeV. The events from the POWHEG sample are weighted using the ratio of SHERPA to SHERPA with `m114` filter. The comparison of SHERPA to the scaled POWHEG events is shown in figure 8.8.

- **Monte Carlo statistics:** The Monte Carlo samples carry statistical uncertainty due to containing a finite number of events.
- **Monte Carlo sample normalizations:** As discussed in section 7.3, the signal and background Monte Carlo samples are normalized to the measured luminosity of the data using theoretical cross sections. The uncertainty on the measured luminosity is 2.8%, while the uncertainties on the WZ , ZZ , and $t\bar{t} + V$ backgrounds are 7.6%, 4.3%, and 22%, respectively. A cross section uncertainty is not assigned to the $Z + \gamma$ backgrounds; instead, as described next, a large uncertainty is assigned due to applying scale factors to correct the simulated rate of photon conversions. Similarly, an uncertainty is not assigned for the $VVV^{(*)}$ cross section, due to its small contribution to the signal regions.
- **Charge flip scale factors:** The rate of trilepton events due to $Z + \gamma$, where the photon converts asymmetrically and is reconstructed as an electron, is observed to be overestimated in Monte Carlo. As detailed in section 6.2.1, the events are reweighted to correct this overestimation, with a corresponding uncertainty of 30%.
- **Fake factor method:** The systematic uncertainty on the fake factors is described in sections 6.2.3 and 6.2.4. They range from 20–30% for electrons and 25–50% for muons.
- **Lepton efficiencies:** To equalize the lepton trigger, reconstruction, and identification efficiencies between data and simulation, events in simulation are weighted by the

ratio of efficiencies in data to simulation (see sections 5.2.2 and 5.3.1). The ratio of efficiencies is typically close to unity, and the corresponding uncertainty ranges from 1–5%.

- **Lepton energy scale and resolution** (LES/LER): To improve agreement between data and simulation, the electron energy is scaled in data, and the electron energy and muon momenta are smeared in Monte Carlo (see sections 5.2.3 and 5.3.2). The corrections carry small systematic uncertainties that primarily affect the analysis due to leptons migrating between passing and failing the selection, or lepton pairs moving in or out of the Z mass window.
- **Jet energy scale and resolution** (JES/JER): Like the leptons, systematic uncertainties are assigned to the jet energy scale and resolution (see section 5.5.1). The jet energy uncertainties have a small impact on this analysis, only affecting the normalization of the $3\ell + jj$ signal regions when the dijet mass is pushed in or out of the window $60.385 \text{ GeV} < m_{jj} < 150.9 \text{ GeV}$.

Figures 8.9 and 8.10 show the fractional uncertainty due to each source of uncertainty in 20 GeV bins for each signal region, as well as the total systematic uncertainty and expected statistical uncertainty. Note that the uncertainties shown are bin-by-bin uncertainties from the Monte Carlo and fake factor predictions, and do not directly reflect the final uncertainties incorporated in the fit-based limit setting; this is discussed in section 8.5.

The impact of each uncertainty in each signal region, in terms of fractional uncertainty on the total normalization, is shown for the total background prediction in table 8.6, and some example signal points in tables 8.7–8.9. The total uncertainty on the background prediction ranges from 6.0% to 8.7% depending on the signal region, while the total uncertainty on the signal predictions range from approximately 4% to 7%.

	$Z + e$				$Z + \mu$			
	Total	4ℓ SR	$3\ell + jj$ SR	3ℓ -only SR	Total	4ℓ SR	$3\ell + jj$ SR	3ℓ -only SR
σ_{ZZ}	0.9	3.9	0.9	0.8	0.7	3.8	0.4	0.6
σ_{WZ}	4.9	0.1	4.6	5.1	5.3	—	4.9	5.6
$\sigma_{t\bar{t}V}$	0.4	1.5	2.9	0.1	0.4	0.9	2.9	0.1
Luminosity	2.6	2.8	2.7	2.6	2.5	2.6	2.4	2.5
γ conv. SFs	2.0	—	1.2	2.1	—	—	—	—
ℓ efficiency	1.6	1.8	1.6	1.6	0.9	0.9	1.0	0.9
e reducible SFs	1.7	—	0.5	1.9	0.1	0.9	0.1	0.1
μ reducible SFs	0.3	—	0.3	0.3	3.4	0.6	4.3	3.5
JES/JER	0.1	$^{+0.2}_{-0.0}$	3.3	0.4	0.1	0.2	3.2	0.5
LES/LER	0.6	$^{+1.0}_{-0.3}$	$^{+0.3}_{-1.2}$	$^{+0.7}_{-0.4}$	0.1	0.1	0.2	0.1
MC Statistics	2.4	5.0	4.3	2.6	1.2	3.5	2.8	1.2
Total	6.9	7.4	8.4	7.1	7.0	6.0	8.7	7.2

Table 8.6: The impact of different sources of uncertainty on the background prediction in each signal region, in terms of percent of the total background normalization.

	$Z + e$				$Z + \mu$			
	Incl SR	4ℓ SR	$3\ell + jj$ SR	3ℓ -only SR	Incl SR	4ℓ SR	$3\ell + jj$ SR	3ℓ -only SR
Luminosity	2.8	2.8	2.8	2.8	2.8	2.8	2.8	2.8
l scale factors	1.7	1.7	1.7	1.6	1.1	1.1	1.1	1.0
MC Statistics	2.1	4.5	3.7	3.0	1.4	2.7	2.7	2.2
JES/JER	0.0	0.2	3.6	3.0	0.2	0.3	3.0	2.2
LES/LER	0.1	0.4	0.1	0.1	0.1	0.2	0.2	0.2
Total	3.9	5.6	6.1	5.3	3.3	4.0	5.1	4.3

Table 8.7: The impact of different sources of systematic uncertainty on the signal prediction for the type III seesaw model with $m_{L^\pm} = 160$ GeV, in terms of percent of the total signal normalization.

	$Z + e$				$Z + \mu$			
	Incl SR	4ℓ SR	$3\ell + jj$ SR	3ℓ -only SR	Incl SR	4ℓ SR	$3\ell + jj$ SR	3ℓ -only SR
Luminosity	2.8	2.8	2.8	2.8	2.8	2.8	2.8	2.8
l scale factors	1.8	1.7	1.8	1.9	1.2	1.2	1.2	1.2
MC Statistics	3.0	5.7	4.9	4.7	2.2	3.7	3.8	3.6
JES/JER	0.1	—	1.6	1.7	0.2	0.3	2.0	2.3
LES/LER	0.4	0.1	1.0	0.4	0.3	0.0	0.9	0.3
Total	4.5	6.5	6.2	6.0	3.8	4.8	5.3	5.3

Table 8.8: The impact of different sources of systematic uncertainty on the signal prediction for the type III seesaw model with $m_{L^\pm} = 300$ GeV, in terms of percent of the total signal normalization.

	$Z + e$				$Z + \mu$			
	Incl SR	4ℓ SR	$3\ell + jj$ SR	3ℓ -only SR	Incl SR	4ℓ SR	$3\ell + jj$ SR	3ℓ -only SR
Luminosity	2.8	2.8	2.8	2.8	2.8	2.8	2.8	2.8
l scale factors	1.8	1.8	1.8	2.0	1.3	1.4	1.3	1.3
MC Statistics	3.0	5.5	4.8	4.8	2.4	4.0	3.9	4.1
JES/JER	—	—	1.7	1.9	0.3	0.5	1.8	2.5
LES/LER	0.4	0.5	2.1	1.7	0.4	1.6	2.8	2.2
Total	4.5	6.4	6.4	6.4	3.9	5.4	6.0	6.1

Table 8.9: The impact of different sources of systematic uncertainty on the signal prediction for the type III seesaw model with $m_{L^\pm} = 500$ GeV, in terms of percent of the total signal normalization.

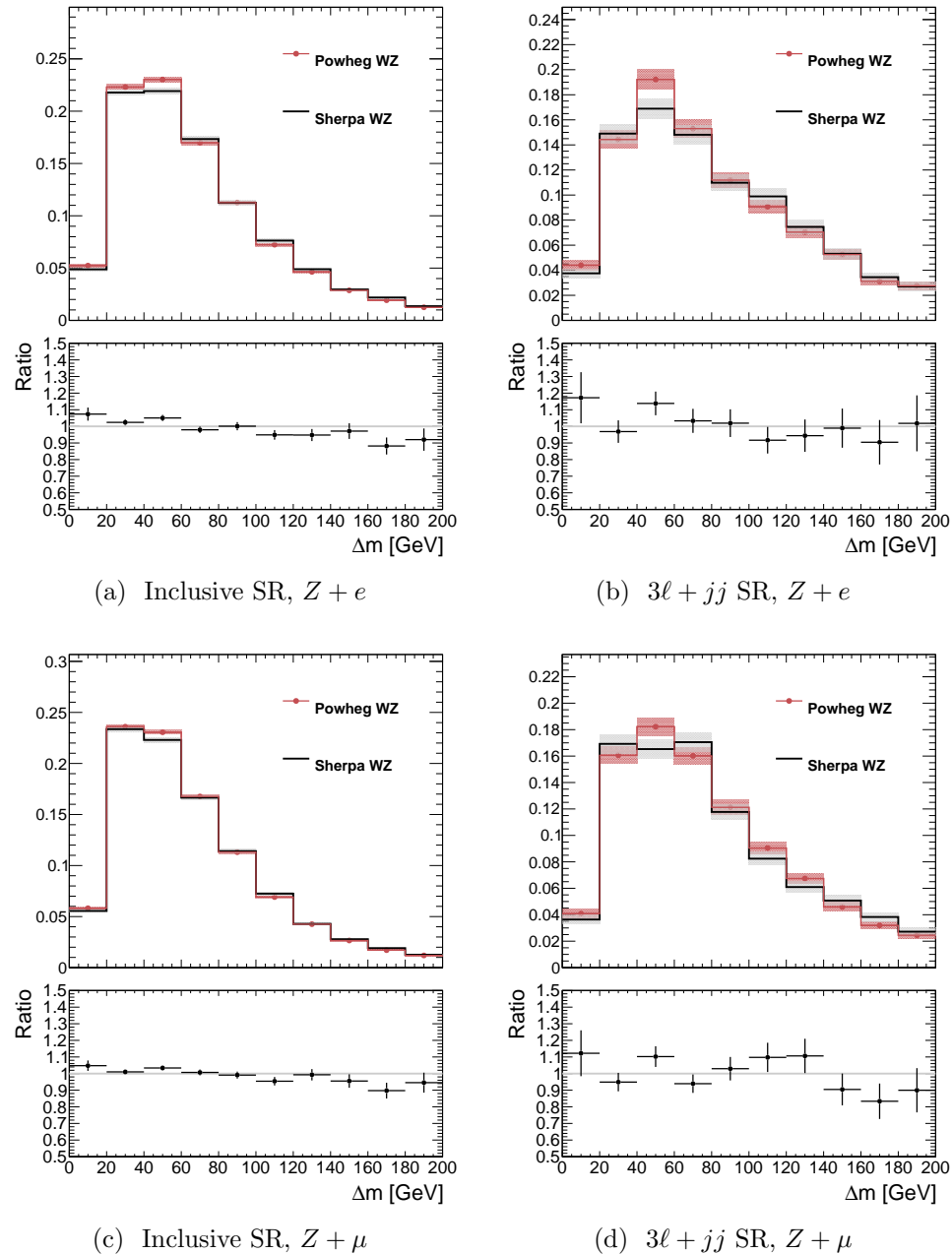


Figure 8.7: Comparison of the Δm distributions between POWHEG and SHERPA for the WZ backgrounds. The top panels show the Δm distributions, normalized to unity, and the bottom panels show the ratio of POWHEG to SHERPA. The shaded bands and error bars represent the statistical uncertainties. The 4ℓ signal region is omitted due to the negligible number of WZ events with four leptons.

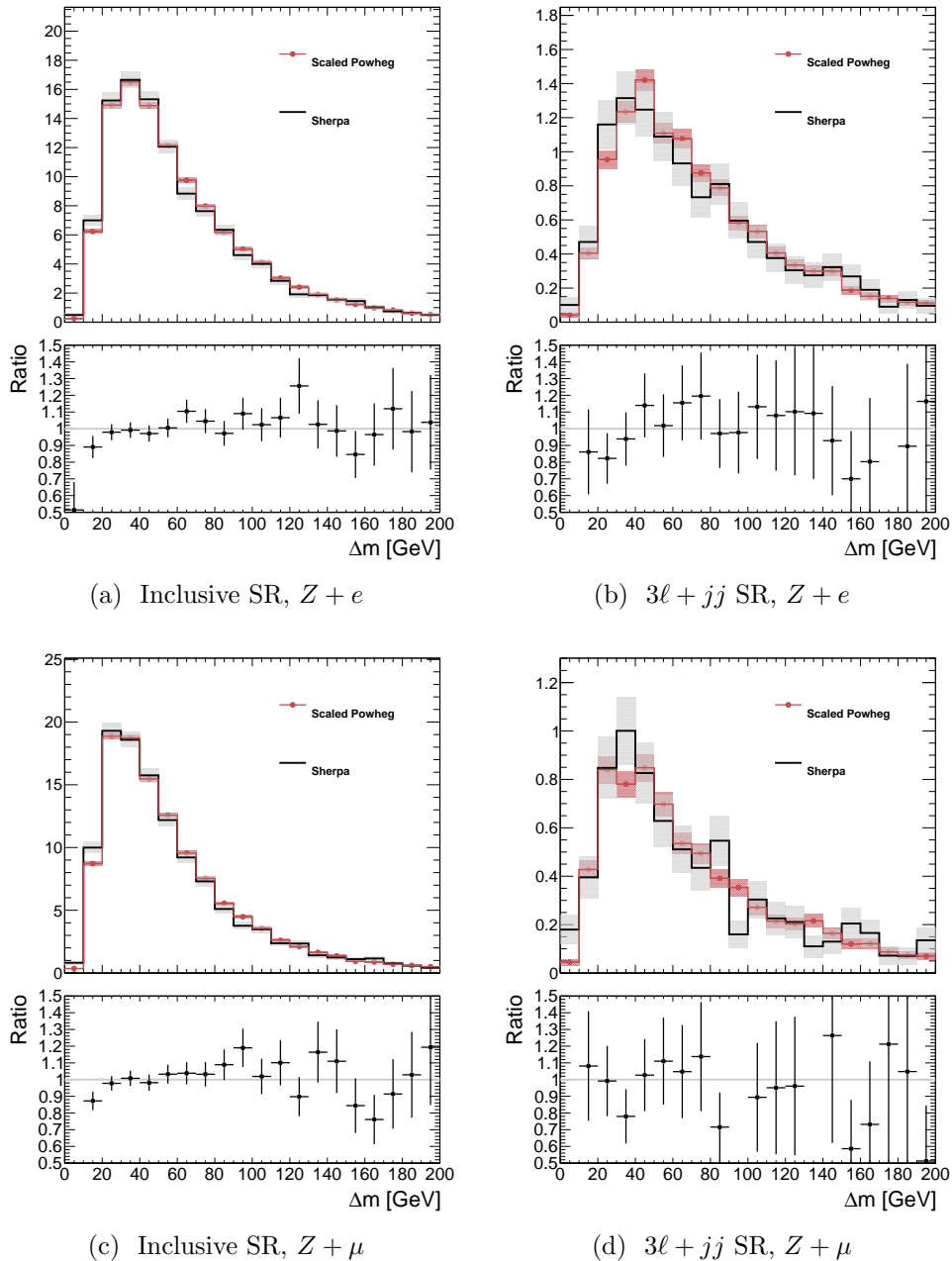


Figure 8.8: Comparison of the Δm distributions between POWHEG and SHERPA for the ZZ backgrounds. The top panels show the Δm distributions, normalized to unity, and the bottom panels show the ratio of POWHEG to SHERPA. The shaded bands and error bars represent the statistical uncertainties. The POWHEG events are weighted to account for the `mll4` filter.

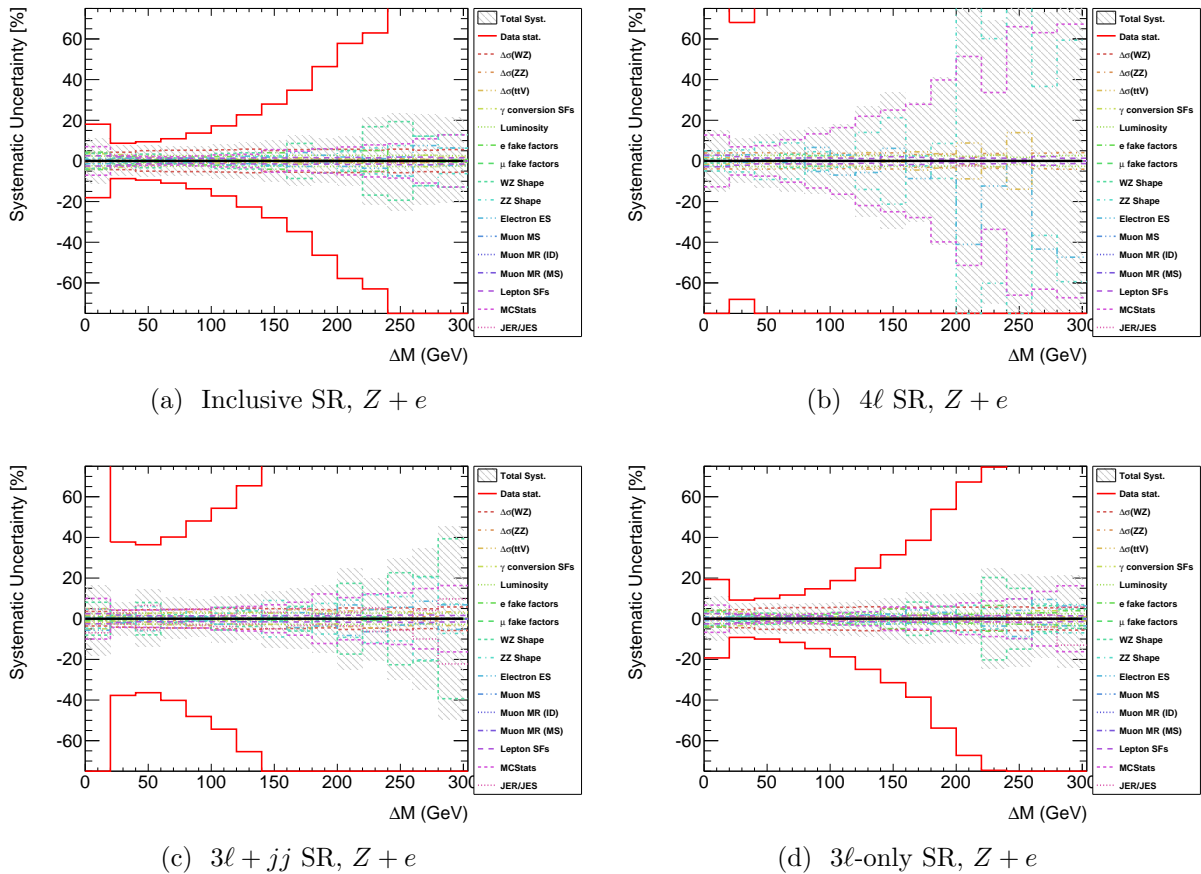


Figure 8.9: Systematics summary plots for each signal region in the $Z + e$ flavor channel. The contribution from each source of systematic uncertainty is shown in 20 GeV bins, along with the total systematic uncertainty and the expected statistical uncertainty. Note that these uncertainties reflect bin-by-bin uncertainties on the Monte Carlo predictions, and do not necessarily correspond to the final uncertainty after fitting the background shapes.

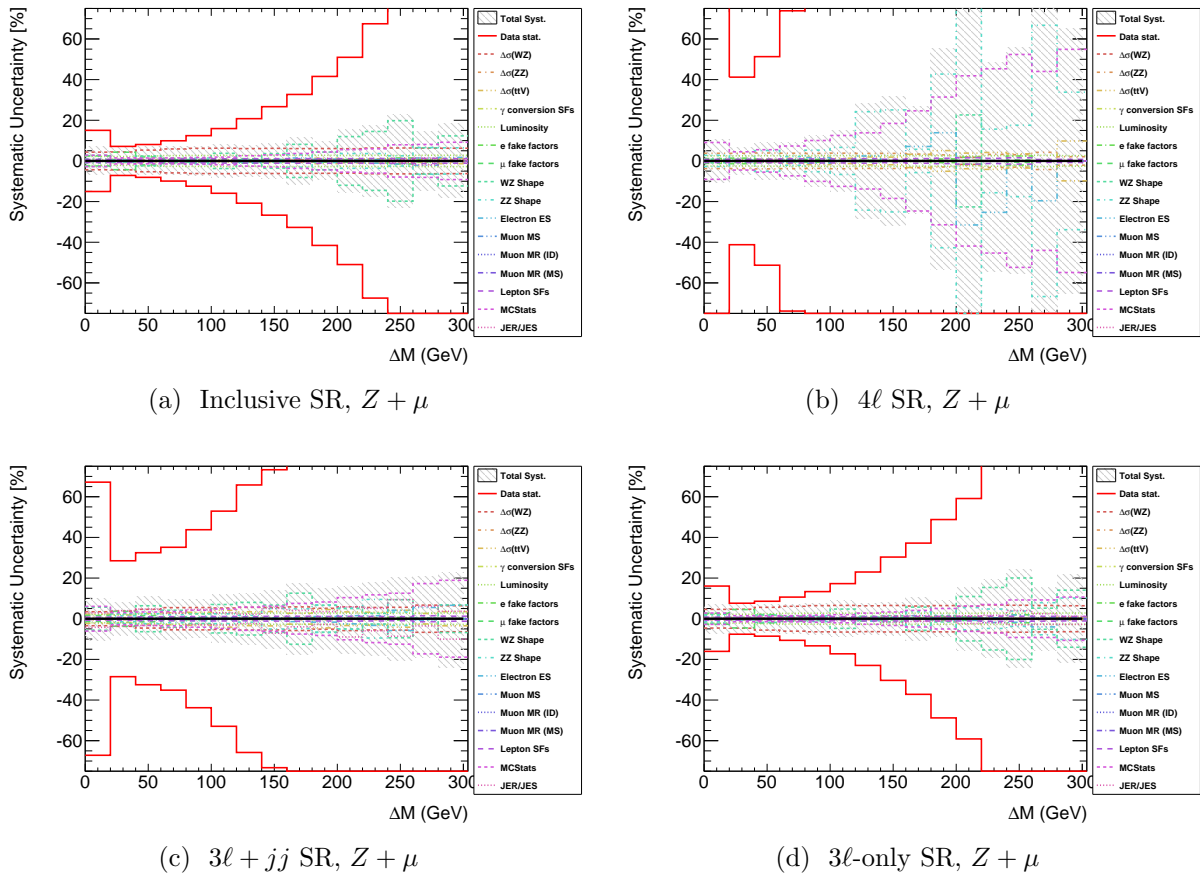


Figure 8.10: Systematics summary plots for each signal region in the $Z + \mu$ flavor channel. The contribution from each source of systematic uncertainty is shown in 20 GeV bins, along with the total systematic uncertainty and the expected statistical uncertainty. Note that these uncertainties reflect bin-by-bin uncertainties on the Monte Carlo predictions, and do not necessarily correspond to the final uncertainty after fitting the background shapes.

8.4 Background Validation

For each flavor channel, four validation regions are defined to test the background predictions from the Monte Carlo simulation samples and the fake factor procedure. Each region starts from the set of events with three selected electrons or muons, two of which form an OSSF pair of leptons.

The **high ΔR** region contains events with large separation between the Z candidate momentum and the off- Z lepton momentum, $\Delta R(Z, \ell_3) > 3$. Events are also required to have exactly three leptons, and to satisfy $\Delta m < 200 \text{ GeV} - m_Z$, to limit signal contamination from hypotheses with larger m_{L^\pm} where the Z and the off- Z lepton are less collimated. The region has a similar background composition to the signal regions with three leptons, and tests the WZ , ZZ , and reducible background predictions.

The **ZZ** region contains events with two OSSF lepton pairs with invariant mass within 10 GeV of m_Z . The region tests the ZZ background prediction.

The **off-Z** region contains events with exactly three leptons, with an OSSF pair within 50 GeV of m_Z , but no OSSF pairs with invariant mass within 20 GeV of m_Z . As the event does not contain a Z candidate, the trilepton selection is modified: the highest mass OSSF pair is selected, and the third lepton is chosen to be the remaining lepton. In the $Z + e$ flavor channel, this region tests the $Z + \gamma$ background prediction. In the $Z + \mu$ channel, the region is dominated by ZZ , where one lepton is not selected, and the other two leptons originate from an off-shell Z^*/γ^* .

The **WZ** region contains events with exactly three leptons, two of which form an OSSF pair within 10 GeV of m_Z , and the third of which satisfies $40 \text{ GeV} < m_T^W < 90 \text{ GeV}$. Additionally, the validation region requires $40 \text{ GeV} < E_T^{\text{miss}} < 100 \text{ GeV}$ and zero jets, which suppresses signal contamination.

The definition of each validation region and the backgrounds tested are summarized in table 8.10. The total number of observed and predicted events in each region is shown in table 8.11, and the corresponding Δm distributions are shown in figures 8.11-8.14. Good agreement is seen in most validation regions, with the observed and predicted normalizations agreeing to better than 1.5σ . A deficit of data with respect to the background prediction is seen in the off- Z , $Z + \mu$ validation region, corresponding to 2.3σ . The region is dominated by contributions from ZZ , where only three leptons pass the selection requirements and no OSSF lepton pair is reconstructed with invariant mass within 20 GeV of m_Z .

Control Region	Definition	Background Tested
High ΔR	$\Delta R(Z, \ell_3) > 3.0$ $\Delta m < 200 \text{ GeV} - m_Z$	WZ , ZZ , and reducible
Off Z	Reject events with $ m_u - m_Z < 20 \text{ GeV}$	$Z + \gamma$ ($Z + e$ events) and ZZ ($Z + \mu$ events)
Two Z	Require 2 Z candidates ($ m_u - m_Z < 10 \text{ GeV}$)	ZZ
WZ	3 leptons, 0 jets, $40 \text{ GeV} < m_T^W < 90 \text{ GeV}$, $40 \text{ GeV} < E_T^{\text{miss}} < 100 \text{ GeV}$	WZ

Table 8.10: Definitions and targeted backgrounds of the four validation regions.

Channel	Validation Region	Data	Background Prediction	$\frac{\text{Data}-\text{Bkgd}}{\sigma_{\text{bkgd}}}$
$Z + e$	High- ΔR	239	239 ± 14	0.0
$Z + e$	Off-Z	360	349 ± 44	+0.2
$Z + e$	ZZ	39	37 ± 2	+0.3
$Z + e$	WZ	140	133 ± 10	+0.4
$Z + \mu$	High- ΔR	302	301 ± 12	+0.1
$Z + \mu$	Off-Z	163	200 ± 8	-2.3
$Z + \mu$	ZZ	74	63 ± 3	+1.2
$Z + \mu$	WZ	222	193 ± 14	+1.5

Table 8.11: Summary of the number of events observed and predicted for each validation region. The uncertainty on the background prediction is the total systematic uncertainty. The difference between the observed and predicted number of events divided by the combined statistical and systematic uncertainty on the prediction is also shown.

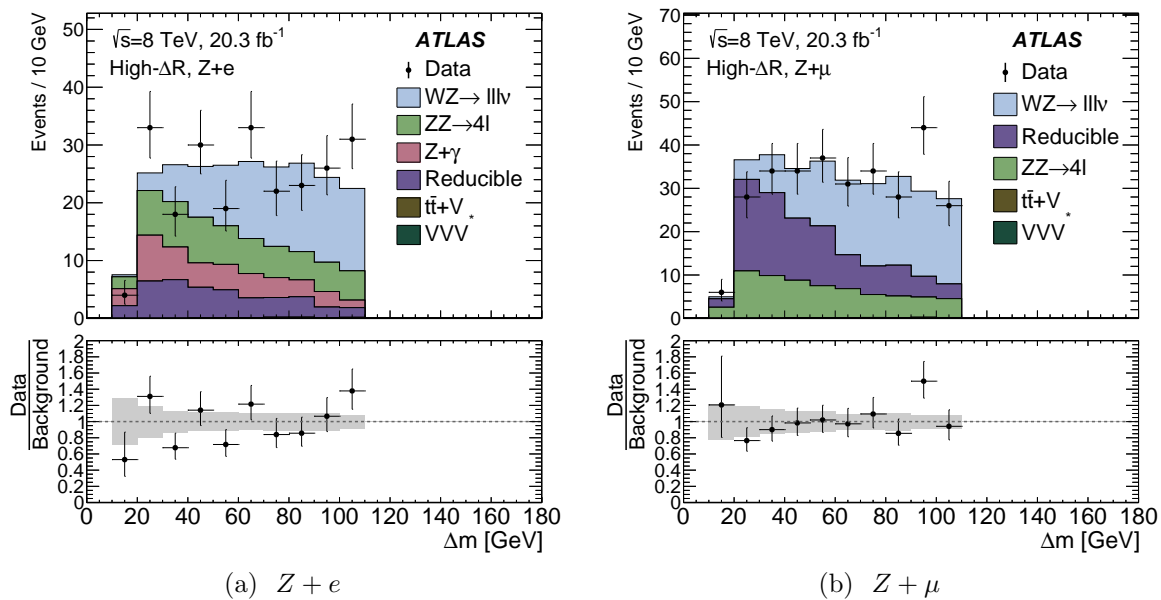


Figure 8.11: Δm distributions for the high ΔR validation regions.

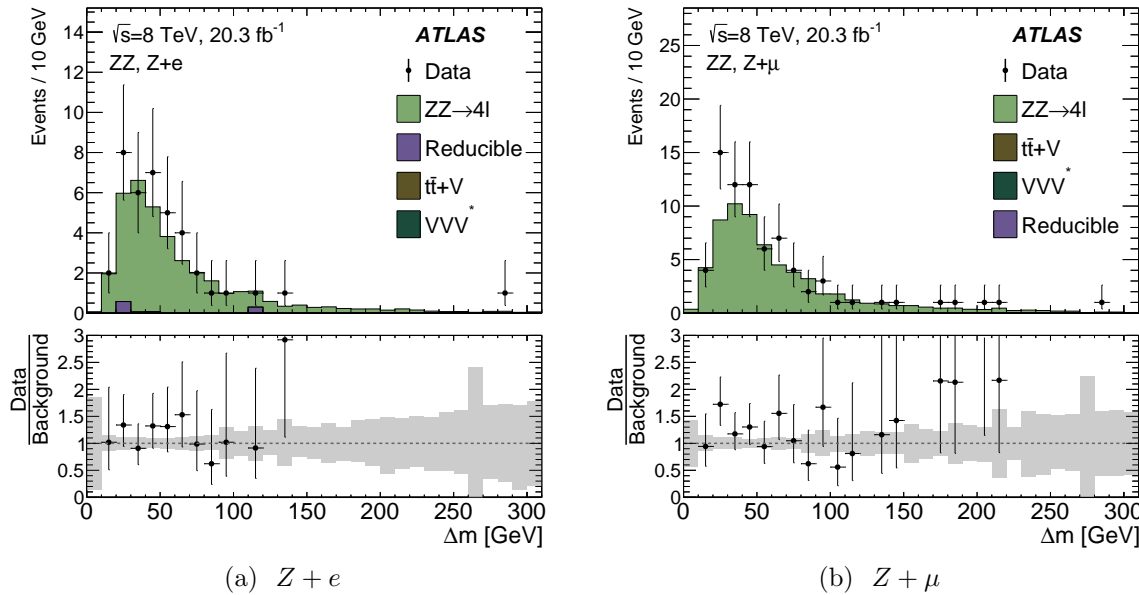


Figure 8.12: Δm distributions for the ZZ validation regions.

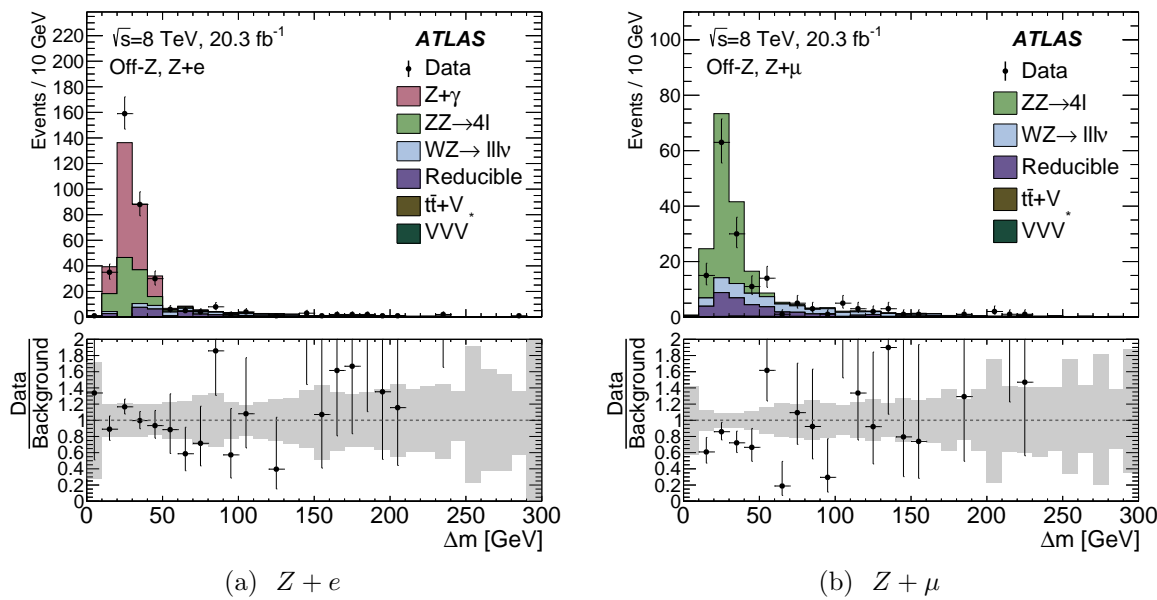
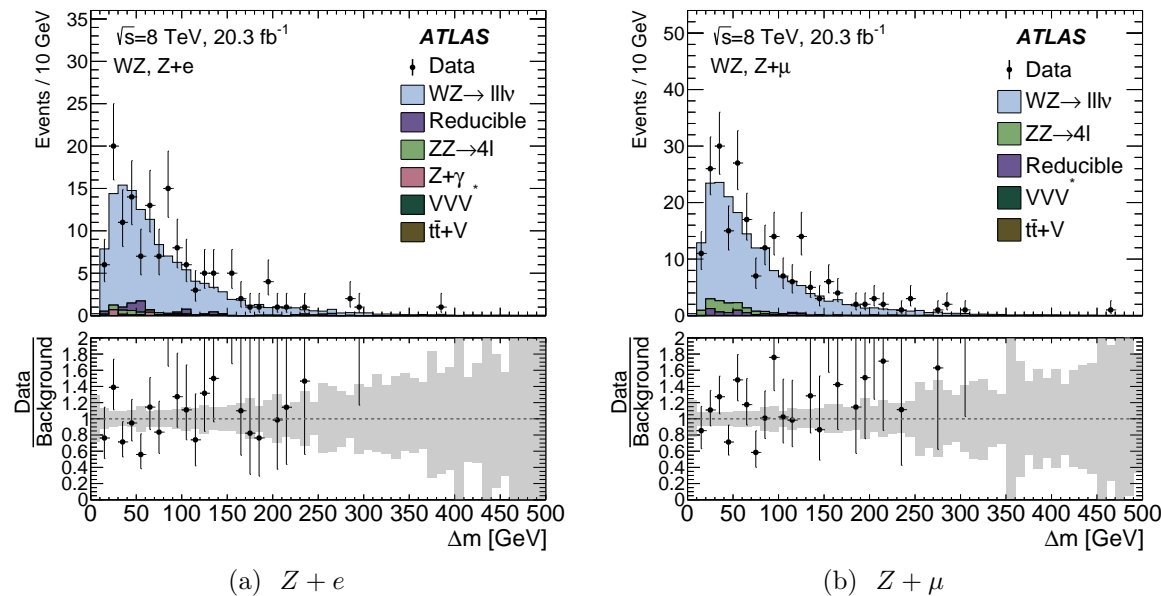


Figure 8.13: Δm distributions for the off- Z validation regions.

Figure 8.14: Δm distributions for the WZ validation regions.

8.5 Signal and Background Fit Model

The numbers of signal and background candidate events in data are determined from an unbinned maximum-likelihood fit of a combination of signal and background models to the Δm distributions in each signal region. The signal and background processes are modeled with analytical probability density functions (p.d.f.s). The parameters of the p.d.f.s are determined from fits to the Δm distributions predicted by simulation or the fake factor procedure. Then, in each flavor channel, the data is fitted with the combined signal and background model, performed simultaneously on the three categories. In each signal region, the normalization of the dominant background (ZZ or WZ) is a free parameter in the fit. The normalizations of all other backgrounds are constrained to fluctuate according to Gaussian probability distributions with mean and width values equal to the estimates and the total uncertainties before fitting. The resulting uncertainties on the fit parameters are incorporated in the limit setting as Gaussian-distributed nuisance parameters. Similarly, the shape uncertainty between the Δm distributions predicted by SHERPA and POWHEG is incorporated as a Gaussian-distributed nuisance parameter multiplying a template given by the difference between the two p.d.f.s.

8.5.1 Signal Modeling

The Δm distributions for the type III seesaw and vector-like leptons scenarios contain two distinct pieces: a peak associated with the correct identification of the three leptons due to the heavy lepton decay, and a broader component due to cases where the trilepton candidate does not originate from a heavy lepton decay. Accordingly, the distributions are modeled using the sum of two functions: a Voigtian⁴ for the peak and a Landau function for the combinatorial component. The signal parametrization is given by the following expression:

$$\mathcal{S}(m_L^\pm) = f_V F_V(\Delta m; \gamma_V, m_V, \sigma_V) + (1 - f_V) F_L(\Delta m; \sigma_L, m_L), \quad (8.16)$$

$$(8.17)$$

where F_V and F_L are the Voigtian and Landau functions, respectively; f_V denotes the fraction of events in the Voigtian; γ_V , m_V and σ_V are the Lorentzian width, mean and Gaussian width of the Voigtian; and σ_L and m_L are the width and mean of the Landau distribution.

The Δm distributions at each simulated mass point for both the type III seesaw and the vector-like leptons models are fitted with $\mathcal{S}(m_L^\pm)$, separately for each flavor channel and category. An example fit from the 300 GeV mass hypothesis of the vector-like leptons model is shown in figure 8.15. The full fit results from the inclusive categories are shown in tables B.1–B.4. f_V roughly corresponds to how often the correct three leptons from the resonant decay are reconstructed and selected, and ranges from $\sim 60\%$ ($\sim 70\%$) at $m_{L^\pm} = 120$ GeV to 58% (55%) at $m_{L^\pm} = 400$ GeV for the type III seesaw (vector-like leptons) model. As mentioned

⁴A convolution of a Lorentzian and a Gaussian.

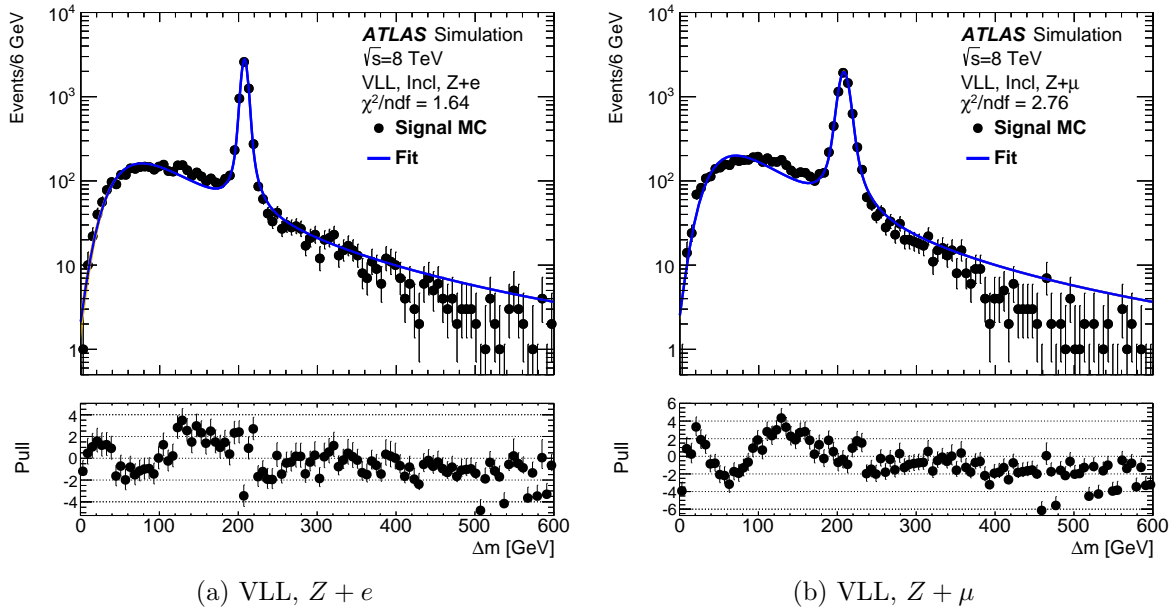


Figure 8.15: Fit of a Landau and a Voigtian to the inclusive distribution of the Δm at 300 GeV for the vector-like leptons model for $Z + e$ final states (a) and $Z + \mu$ final states (b).

in section 8.1.1, the type III seesaw samples were simulated without intrinsic Z width, and hence the width parameters determined from the vector-like leptons samples are used instead.

Signal hypotheses at intermediate mass points between the simulated values are obtained by linearly interpolating the fit parameters determined at the nearest simulated points above and below. To validate the linear interpolation between the mass points, a closure test was performed comparing the fit parameters determined at a simulated mass point with the values obtained from a linear interpolation between the adjacent simulated points. The resulting fit parameters for the 120 GeV and 160 GeV mass points are shown in table 8.12.

Signal	m_L	σ_L	m_V	σ_V	γ_V	f_V
120 GeV, fitted	32.89 ± 1.5	10.224 ± 0.66	28.4355 ± 0.02	2.4767 ± 0.2	0.73 ± 0.12	0.75
120 GeV, interpolated	31.96 ± 0.47	9.511 ± 0.71	28.49 ± 0.02	2.13 ± 0.02	0.98 ± 0.21	0.73
160 GeV, fitted	35.43 ± 0.46	11.018 ± 0.21	68.2511 ± 0.03	2.85 ± 0.14	1.59 ± 0.08	0.70
160 GeV, interpolated	36.97 ± 0.5	11.68 ± 0.24	68.22 ± 0.03	2.65 ± 0.13	1.641 ± 0.07	0.69

Table 8.12: Comparison of the interpolated and directly fitted parameters of the signal fits. The comparison is shown for the 120 GeV and 160 GeV mass points of the vector-like lepton model.

8.5.2 Background Fits

The dominant diboson backgrounds are modeled using a Bukin function, a 5-parameter function designed to model asymmetric peaks:

$$\mathcal{P}(x; x_p, \sigma_p, \xi, \rho) = A_p \exp \left[\frac{\xi \sqrt{\xi^2 + 1} (x - x_1) \sqrt{2 \log 2}}{\sigma_p (\sqrt{\xi^2 + 1} - \xi)^2 \log(\sqrt{\xi^2 + 1} + \xi)} + \rho \left(\frac{x - x_i}{p_p - x_i} \right)^2 - \log 2 \right], \quad (8.18)$$

where $\rho = \rho_1$ and $x = x_i$ for $x < x_1$, and $\rho = \rho_2$ and $x_i = x_2$ for $x \leq x_2$. The function describes the diboson Δm distribution well, in particular successfully modeling the turn-on region at low values of Δm . However, the fit parameters are strongly correlated, with some pairs exceeding 99% correlation. To reduce the number of free parameters, two parameters, σ_p and ξ_p , are constrained to be linear functions of x_p using pseudoexperiments. 100 toy datasets are generated from the fitted 5-parameter Bukin function, and the Bukin function fit is repeated on each toy dataset. The scatter plots of σ_p versus x_p and ξ_p versus x_p are shown in figures 8.16 and 8.17, along with the linear least squares fits used to constrain σ_p and ξ_p .

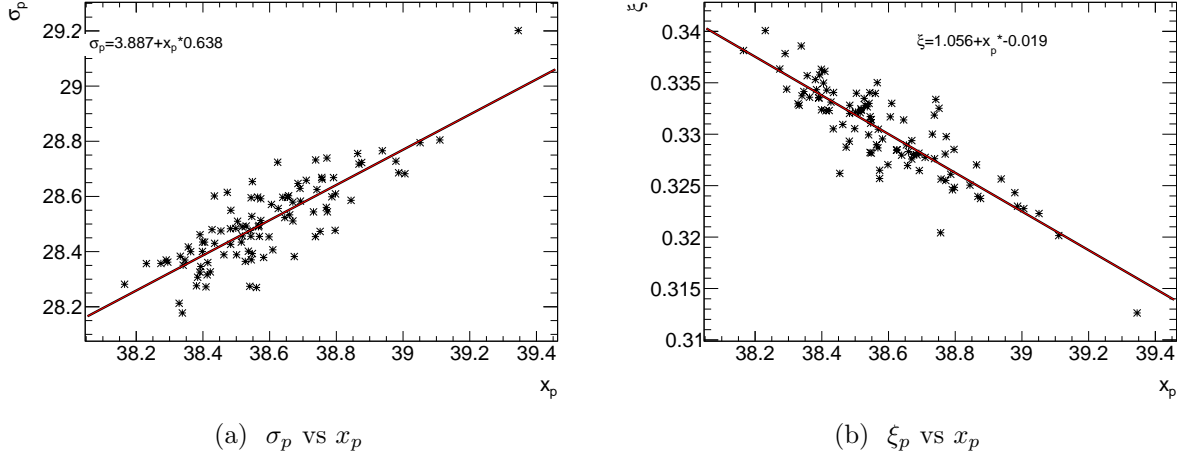


Figure 8.16: Scatter plot showing the correlation between σ_p and x_p (left) and ξ_p and x_p (right), determined from 100 toy experiments on the WZ background sample in the inclusive signal region. The line shows the linear least squares fit used to constrain the parameter on the y -axis.

The shapes of the diboson Δm distributions in the categorized signal regions are compared to the inclusive signal regions using unbinned Kolmogorov-Smirnov tests, shown in figures 8.18 and 8.19 and tables 8.13 and 8.14. The shapes of the Δm distributions in the 4ℓ and 3ℓ -only signal regions are consistent with the inclusive regions; therefore, to take advantage of the larger statistics in the inclusive signal region, the shape from the inclusive

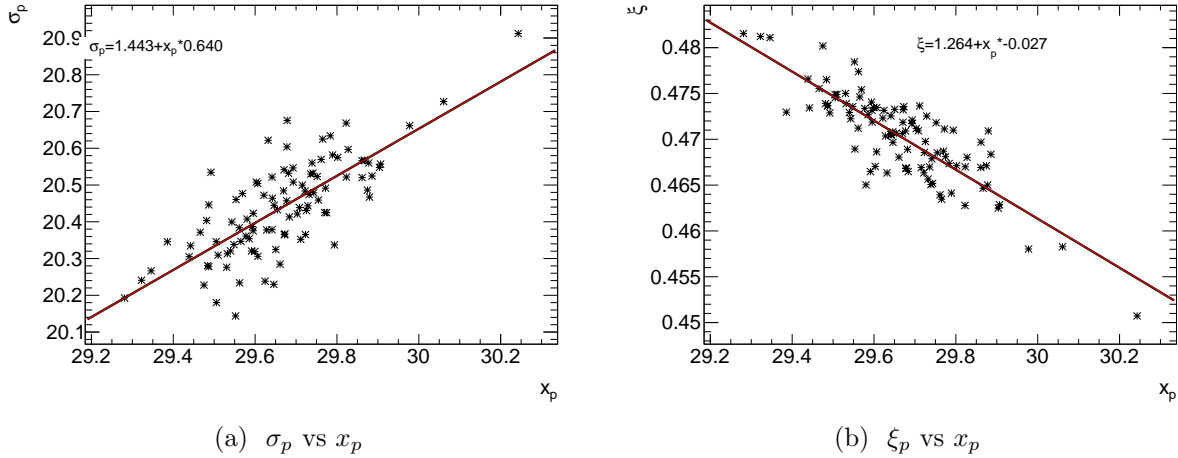


Figure 8.17: Scatter plot showing the correlation between σ_p and x_p (left) and ξ_p and x_p (right), determined from 100 toy experiments on the ZZ background sample in the inclusive signal region. The line shows the linear least squares fit used to constrain the parameter on the y -axis.

signal region is used to model the 4ℓ and 3ℓ -only signal regions. The fits for the inclusive and $3\ell + jj$ signal regions are shown in figures 8.20 and 8.21.

Signal Region	KS probability	D
$4\ell, Z + e$	0.4109	0.060
$3\ell + jj, Z + e$	0.001	0.122
3ℓ -only, $Z + e$	0.782	0.019
$4\ell, Z + \mu$	0.520	0.043
$3\ell + jj, Z + \mu$	0.130	0.098
3ℓ -only, $Z + \mu$	0.946	0.016

Table 8.13: Results of Kolmogorov-Smirnov tests comparing the ZZ Δm shapes between the categorized signal regions and the inclusive signal regions. The Kolmogorov-Smirnov probability and test statistic are shown.

The most important remaining backgrounds are due to reducible processes and $Z(l\bar{l}) + \gamma$. The $Z(l\bar{l}) + \gamma$ background is only significant in the $Z + e$ signal regions. Due to the limited statistics from the fake factor estimate, the individual categories are combined into a single inclusive distribution for electron and muons. The reducible backgrounds are fitted with Landau distributions, shown in figure 8.22. The individual regions are then normalized to the expectations from the individual categories ⁵.

⁵In categories where the fake factor method predicts overall normalization that is negative but consistent

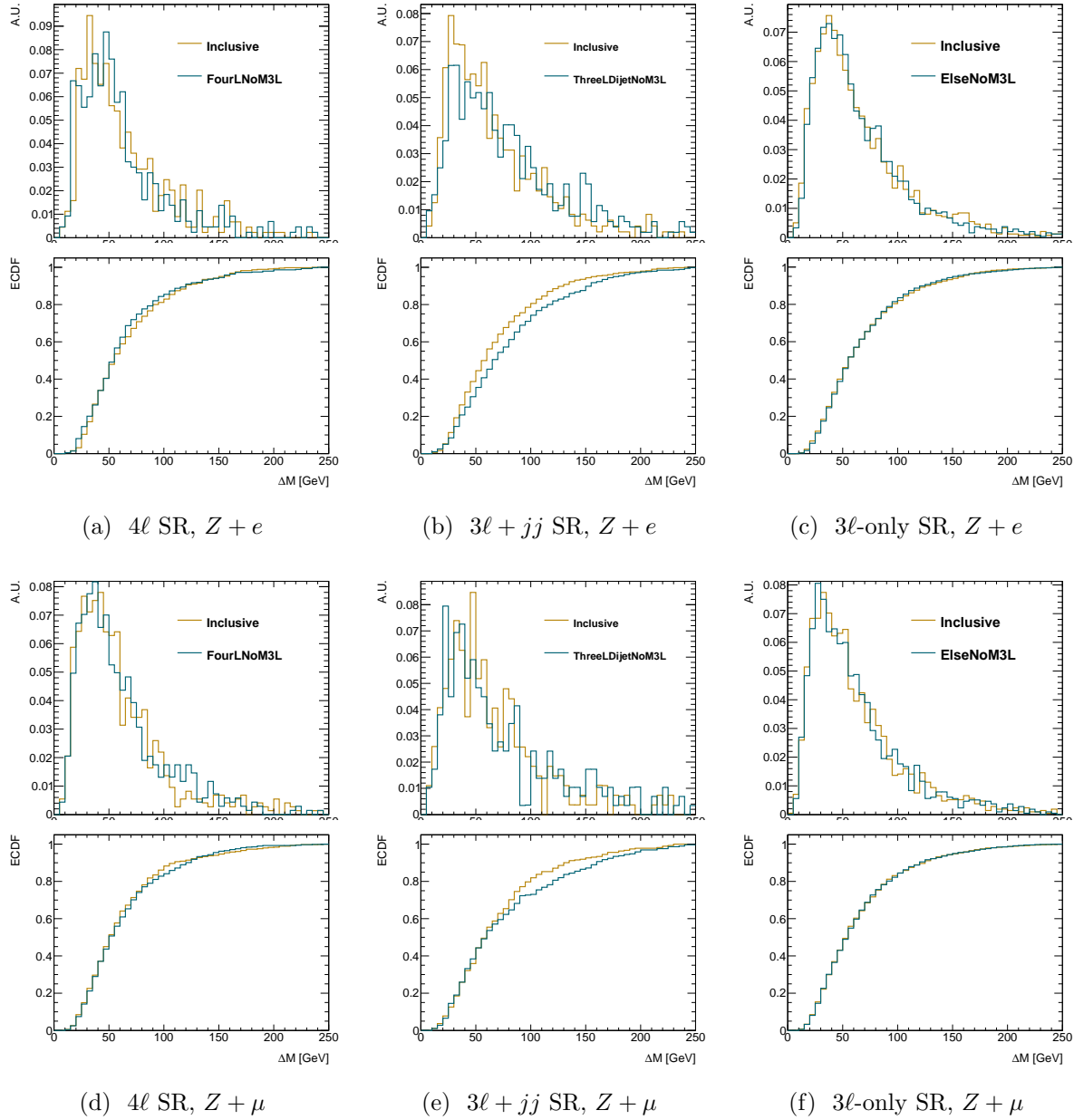


Figure 8.18: Comparison of $ZZ \Delta m$ shapes between the inclusive signal region and the categorized signal regions, with empirical distribution functions.

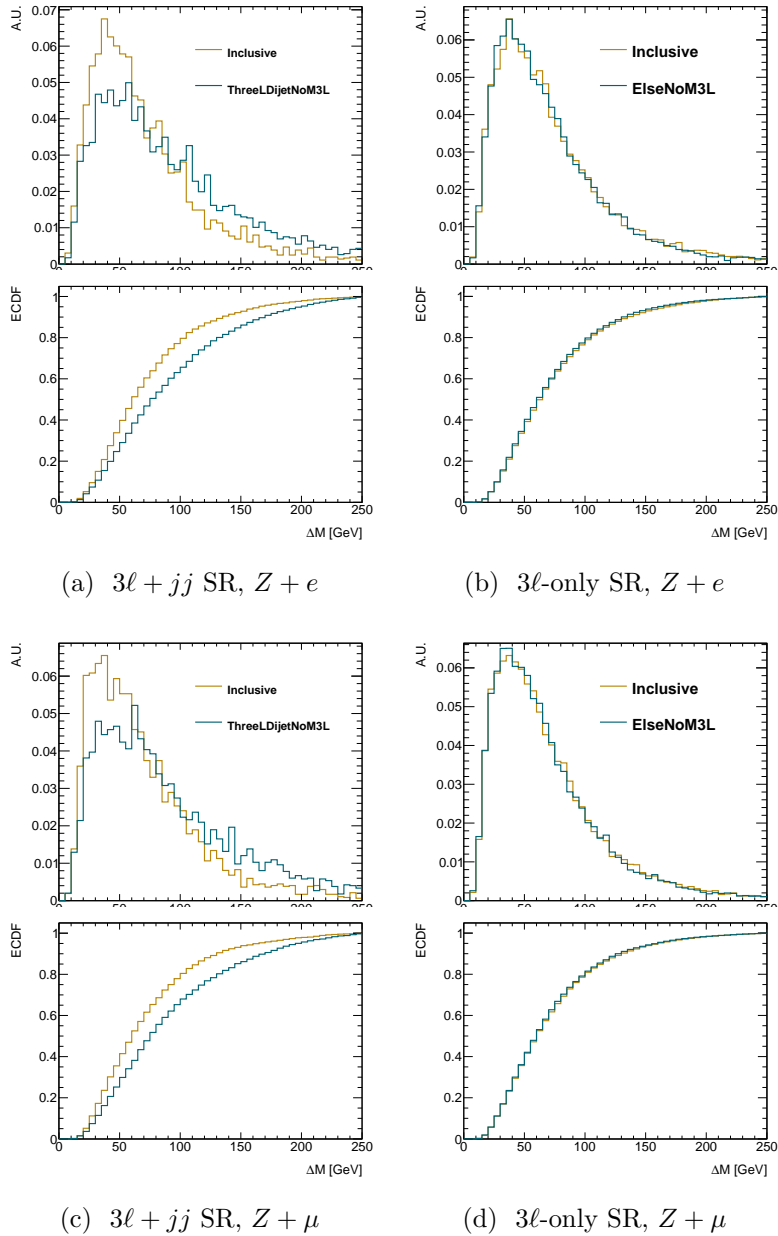


Figure 8.19: Comparison of WZ Δm shapes between the inclusive signal region and the categorized signal regions, with empirical distribution functions. The 4ℓ signal regions are not shown due to the lack of WZ events with four leptons.

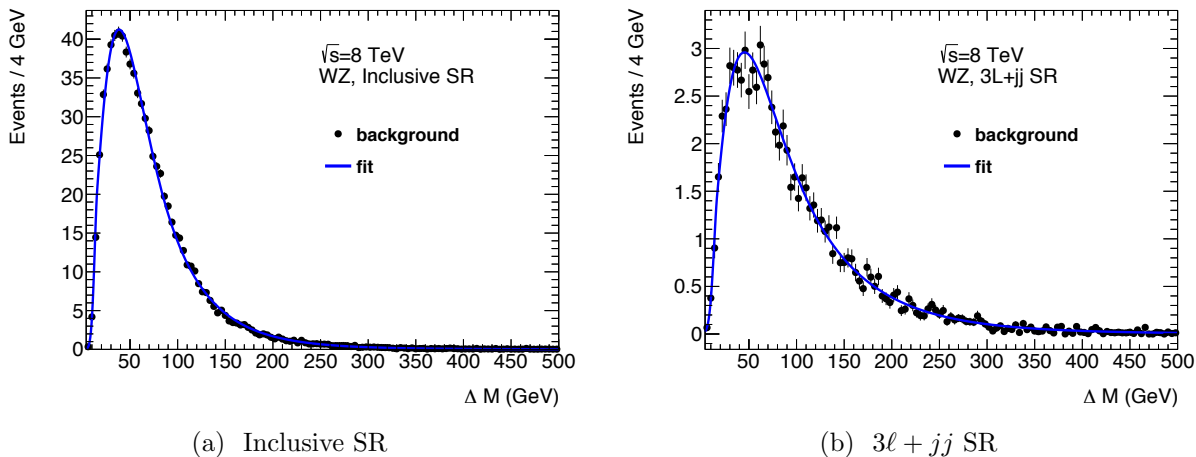


Figure 8.20: Δm distributions from Monte Carlo and BUKIN function fits for the WZ background. The $Z + e$ and $Z + \mu$ events are combined. The inclusive (left) and $3\ell + jj$ (right) signal regions are shown.

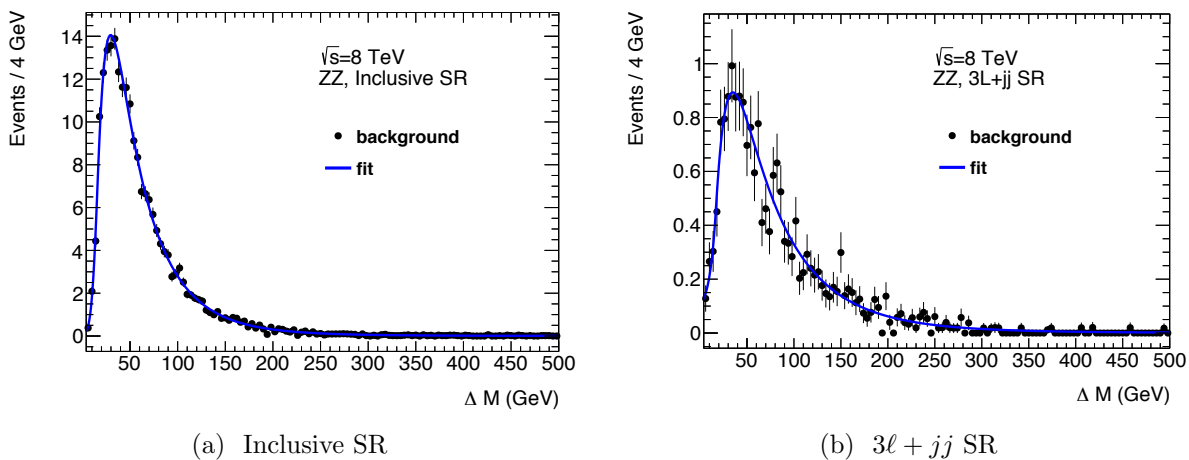


Figure 8.21: Δm distributions from Monte Carlo and Bukiin function fits for the ZZ background. The $Z + e$ and $Z + \mu$ events are combined. The inclusive (left) and $3\ell + jj$ (right) signal regions are shown.

Signal Region	KS probability	D
$3\ell + jj, Z + e$	0.0	0.165
$3\ell\text{-only}, Z + e$	0.012	0.016
$3\ell + jj, Z + \mu$	0.0	0.152
$3\ell\text{-only}, Z + \mu$	0.0349	0.012

Table 8.14: Results of Kolmogorov-Smirnov tests comparing the $WZ \Delta m$ shapes between the categorized signal regions and the inclusive signal regions. The Kolmogorov-Smirnov probability and test statistic are shown.

The $Z(l\bar{l}) + \gamma$ background is only significant in the $3\ell\text{-only}, Z + e$ signal region. This background is modeled with the sum of a Landau and a Gaussian, shown in figure 8.23a. The remaining small contributions from $t\bar{t} + V$ and triboson processes are modeled together with a Landau function, shown in figure 8.23b.

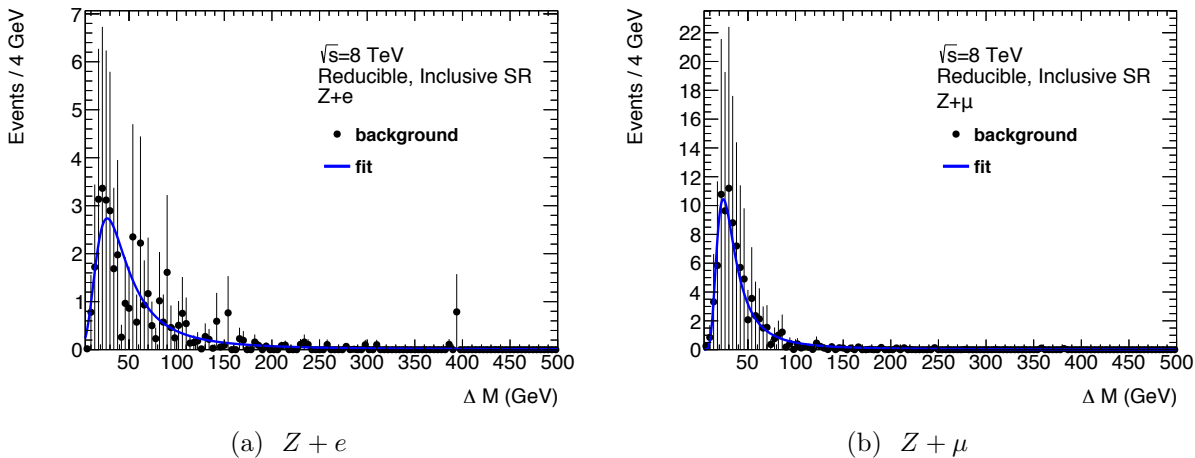


Figure 8.22: Δm distributions from Monte Carlo and Landau function fits for the reducible backgrounds in the inclusive signal region, for $Z + e$ (left) and $Z + \mu$ (right) events.

with zero within statistical uncertainties, which can occur due to the prompt subtraction, the normalization is set to zero.

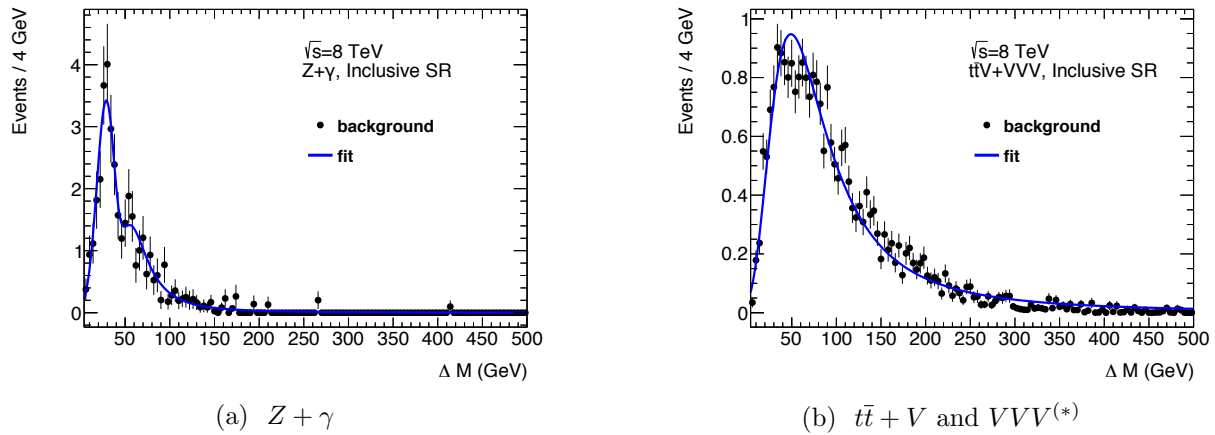


Figure 8.23: Δm distributions from Monte Carlo and Landau function fits for the $Z + \gamma$ (left) and $t\bar{t} + V$ plus $VVV^{(*)}$ (right) backgrounds. For the $Z + \gamma$ background, the inclusive, $Z + e$ signal region is shown; the background is negligible in the $Z + \mu$ signal regions. For the $t\bar{t} + V$ plus $VVV^{(*)}$ backgrounds, the inclusive signal region is shown, with the $Z + e$ and $Z + \mu$ channels combined.

8.6 Results

The total number of observed events each signal region is shown in table 8.15. The predicted backgrounds before and after performing the unbinned maximum-likelihood fit in the background-only hypothesis are also shown. The Δm distributions for the pre-fit background estimates and the data are shown in figure 8.24, with examples signals from the vector-like leptons model with $m_{L^\pm} = 140$ GeV and the type III seesaw model with $m_{L^\pm} = 300$ GeV also shown. The data agree with the background expectation in all cases, and no clear peak indicating resonant trilepton production is seen in any of the signal regions.

Process	$Z + e$			$Z + \mu$		
	4l SR	$3\ell + jj$ SR	3 ℓ -only SR	4 ℓ SR	$3\ell + jj$ SR	3 ℓ -only SR
Before combined background-only fit						
ZZ	10.9 ± 0.6	11.7 ± 0.8	91 ± 5	21.4 ± 1.1	7.5 ± 0.6	90 ± 5
WZ	0.08 ± 0.01	35.3 ± 3.1	337 ± 28	—	46 ± 4	480 ± 40
$Z + \gamma$	—	2.3 ± 0.8	35 ± 11	—	—	—
Reducible	—	1.6 ± 0.5	38 ± 14	1.5 ± 0.3	8.8 ± 3.0	79 ± 22
$t\bar{t} + V, VVV^{(*)}$	1.2 ± 0.2	7.8 ± 1.7	2.3 ± 0.4	1.5 ± 0.2	9.5 ± 2.1	3.3 ± 0.5
Total Background	12.2 ± 0.7	59 ± 4	504 ± 34	24.4 ± 1.2	72 ± 6	650 ± 50
After combined background-only fit						
ZZ	15 ± 4	13.4 ± 2.3	107 ± 9	22 ± 5	10.1 ± 1.6	88 ± 8
WZ	0.08 ± 0.03	39 ± 6	393 ± 28	0.02 ± 0.02	56 ± 9	460 ± 40
$Z + \gamma$	—	2.2 ± 0.8	34 ± 11	—	—	—
Reducible	—	1.8 ± 1.2	37 ± 13	1.8 ± 0.9	10.2 ± 2.8	92 ± 24
$t\bar{t} + V, VVV^{(*)}$	1.1 ± 0.3	7.5 ± 1.7	2.5 ± 0.6	1.5 ± 0.4	9.1 ± 2.1	3.3 ± 0.8
Total Background	16 ± 4	64 ± 7	574 ± 34	25 ± 5	85 ± 10	640 ± 40
Data	16	64	573	25	86	651

Table 8.15: Observed and expected number of events in the six signal regions, before and after the combined unbinned maximum-likelihood fit. The pre-fit uncertainties represent the total systematic uncertainties on the background estimates. The post-fit uncertainties are determined by the maximum-likelihood fit.

Good agreement is seen between the pre-fit and post-fit normalizations for the 4ℓ and $3\ell + jj$ categories in the $Z + \mu$ flavor channel. The largest change in normalization due to the fit is in the 4ℓ category for the $Z + e$ flavor channel, where the fitted ZZ normalization exceeds the prediction by 35%. The WZ and ZZ normalizations increase by roughly 15% in the $3\ell + jj$ and 3ℓ -only categories in the $Z + e$ flavor channel, and 30% in the $3\ell + jj$ category in the $Z + \mu$ flavor channel. The projections of the fit results in the background-only

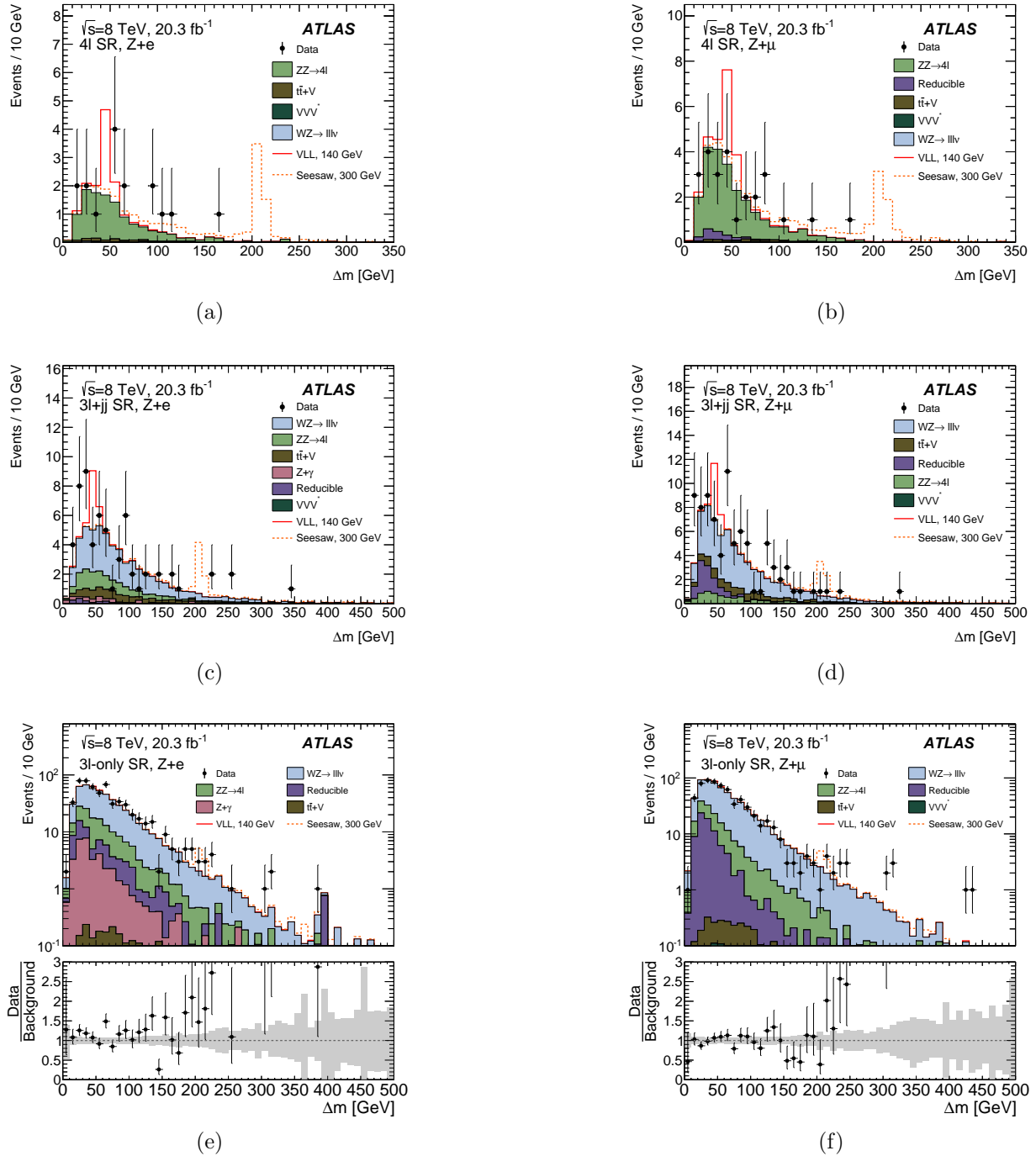


Figure 8.24: The Δm distributions for the 4ℓ (top), $3\ell + jj$ (middle), and 3ℓ -only (bottom) categories, divided into the $Z+e$ (left) and $Z+\mu$ (right) flavor channels. The data are shown as black points, while the pre-fit background expectations are shown in the solid histograms. Signal contributions from a 140 GeV L^\pm in the VLL model and a 300 GeV L^\pm in the seesaw model are also shown. The error bars on the points represent statistical uncertainties, and the shaded bands represent the systematic uncertainties on the background predictions.

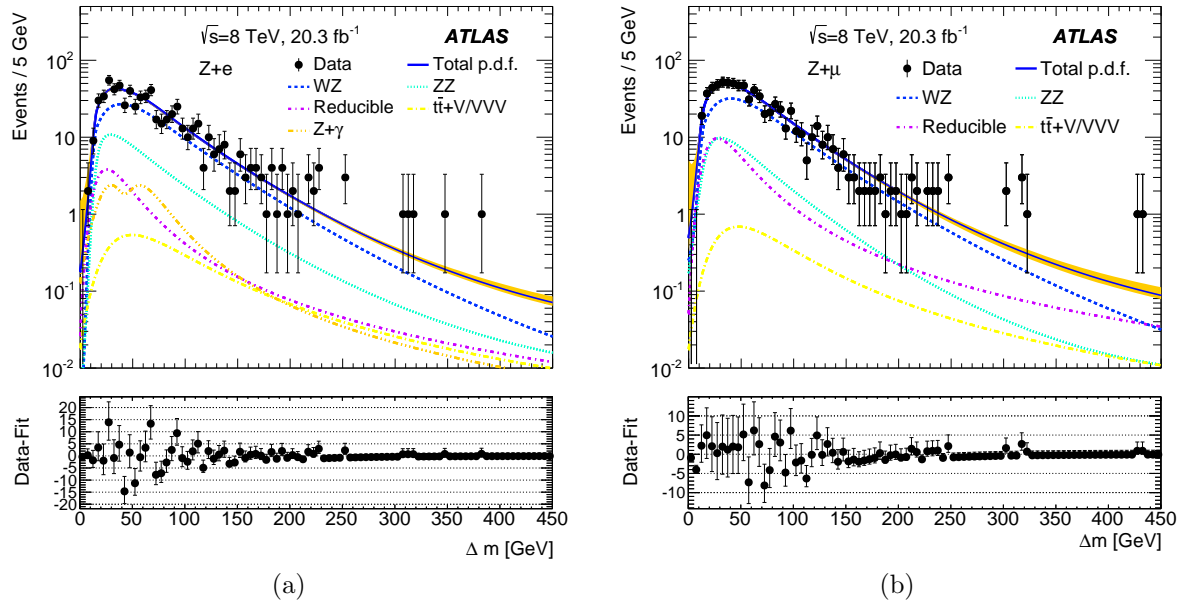


Figure 8.25: Projections onto the Δm variable of the background-only unbinned maximum-likelihood fits, shown superimposed on the data with the three categories in each flavor channel added together. The $Z + e$ flavor channel is shown in (a), and the $Z + \mu$ channel is shown in (b). The contributions of the separate background components to the total background-only fit are also shown. The error bars on the data points represent statistical uncertainties. Good agreement is observed between the background model and the data.

hypothesis are shown in figure 8.25 for the combination of the three categories in each flavor channel.

8.7 Interpretation

The data are well described by the combined fit to the three categories in each flavor channel. The consistency of the data with the background-only hypothesis is expressed in terms of the p_0 -value, the probability that, assuming the background-only hypothesis is true, an experiment would yield at least as many events as observed in the current measurement (see appendix C). The local p_0 -value for the Δm distribution is scanned in 3 GeV intervals for signal mass hypotheses in the range 100 GeV – 400 GeV for the vector-like leptons model, and 100 GeV – 500 GeV for the seesaw model, using the unbinned maximum-likelihood fit described in section 8.5 with the signal strength set to zero. The p_0 -values are calculated using the frequentist hypothesis test based on the profile likelihood ratio test statistic and approximated with asymptotic formulae [28]. The results are shown in figure 8.26. The minimum p_0 -value is $p_0 = 0.02$ at a mass of 183 GeV for the $Z + e$ flavor channel, and

$p_0 = 0.05$ at a mass of 109 GeV for the $Z + \mu$ flavor channel.

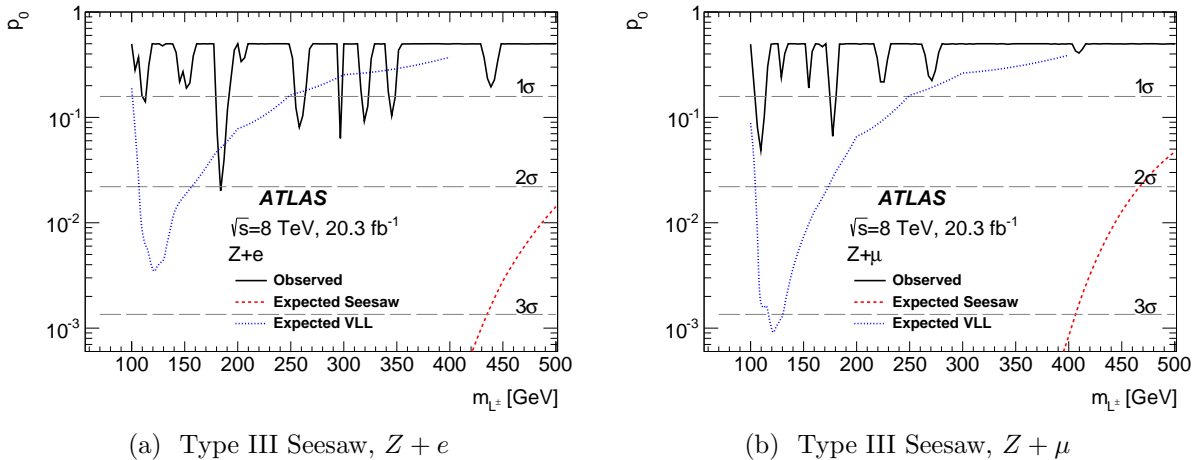


Figure 8.26: p_0 -values for the background-only hypothesis as a function of the heavy lepton mass and the corresponding expected p_0 -values for the vector-like lepton model (blue) and the type-III seesaw model.

8.7.1 Limits on Models

Since no significant excess above the background expectation is observed, the fit model is used to derive 95% confidence level (CL) exclusion limits on the heavy lepton pair-production cross section, σ , using the CL_s method [29]. The heavy leptons are assumed to mix with a single flavor of Standard Model lepton, either electron or muon. The limits are shown for the vector-like leptons model in figure 8.27 and for the type III seesaw model in figure 8.28, evaluated in the same 3 GeV intervals as the p_0 -values. The vector-like leptons model is excluded for electron-only mixing in the heavy lepton mass ranges 129 GeV – 144 GeV and 163 GeV – 176 GeV, with an expected exclusion in the range 109 GeV – 152 GeV. The corresponding observed (expected) exclusion for the muon-only mixing scenario is 114 GeV – 153 GeV and 160 GeV – 168 GeV (105 GeV – 167 GeV). The significantly higher production cross sections for the type III seesaw model lead to an observed (expected) exclusion in the electron-only mixing scenario in the heavy lepton mass range 100 GeV – 430 GeV (100 GeV – 436 GeV). For the muon-only mixing scenario, the observed exclusion is in the ranges 100 GeV – 401 GeV and 419 GeV – 468 GeV, while the expected exclusion is 100 GeV – 419 GeV.

Model-Independent Limits

The constraints shown in figures 8.27 and 8.28 are relevant to the specific VLL and type III seesaw models considered, and are not necessarily applicable to other scenarios predicting trilepton resonances with an intermediate Z boson. A more model-independent observable

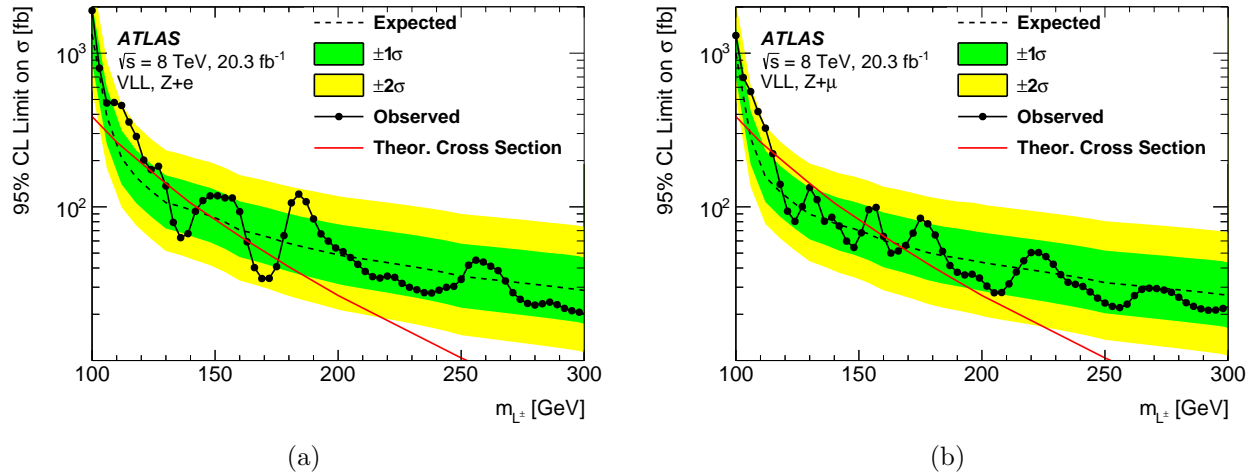


Figure 8.27: 95% CL upper limits on the vector-like lepton cross section. The left (right) plot shows the limits assuming 100% branching fraction to e/ν_e (μ/ν_μ). The solid line shows the observed limit. The dashed line shows the median expected limit for a background-only hypothesis, with green and yellow bands indicating the expected fluctuations at the $\pm 1\sigma$ and $\pm 2\sigma$ levels. The limit is evaluated in 3 GeV intervals.

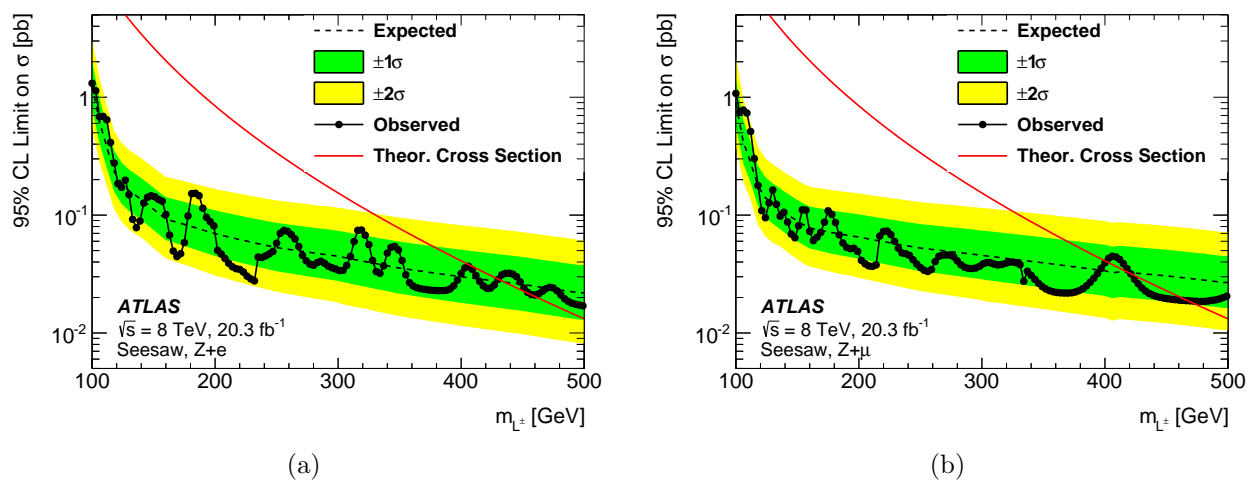


Figure 8.28: 95% CL upper limits on the type III seesaw production cross section. The left (right) plot shows the limits assuming 100% branching fraction to e/ν_e (μ/ν_μ). The solid line shows the observed limit. The dashed line shows the median expected limit for a background-only hypothesis dataset, with green and yellow bands indicating the expected fluctuations at the $\pm 1\sigma$ and $\pm 2\sigma$ levels. The limit is evaluated in 3 GeV intervals.

is the *visible cross section*, σ_{vis} , defined as the number of observed events with $Z + \ell$ -induced trilepton resonances for a given resonance mass divided by the integrated luminosity of the data sample, 20.3 fb^{-1} . The 95% CL upper limits on σ_{vis} , denoted σ_{95}^{vis} , are derived from a fit to each flavor channel with $f_V = 1$, i.e. using only the peak component of the signal. The results for the two flavor channels, derived from the inclusive event selection without dividing the events into the three categories, are shown in figure 8.29.

The limits on σ_{vis} can be used to test specific models after taking into account the model's acceptance with respect to a fiducial volume, \mathcal{A} , and reconstruction and selection efficiency of events within the fiducial volume, ϵ_{fid} . The 95% CL upper limit on the cross section for the model is given by:

$$\sigma_{95} = \frac{\sigma_{95}^{\text{vis}}}{\mathcal{A} \times \epsilon_{\text{fid}}}. \quad (8.19)$$

The acceptance \mathcal{A} is defined as the probability for generated signal events to lie within a fiducial volume defined by the kinematics of the generated leptons. The leptons are considered at *particle level*, i.e. after parton shower and hadronization and with lifetimes longer than 10^{-11} s , and are *dressed*, including the contributions from radiated photons within a cone of $\Delta R = 0.1$. The fiducial volume requires that events contain an L^\pm decaying to a prompt electron or muon and a Z boson that then decays to electrons or muons. The three leptons from the L^\pm decay are required to have $p_T > 15 \text{ GeV}$ and lie within $|\eta| < 2.5$, with at least one lepton satisfying $p_T > 26 \text{ GeV}$. Two of the leptons must form a OSSF pair with a mass within 10 GeV of m_Z , and the Z boson and the off- Z lepton must be separated by $\Delta R < 3$. The events are divided into flavor channels according to the flavor of the off- Z lepton. For the VLL and type III seesaw models used in this analysis, the acceptance of events containing an $L^\pm \rightarrow Z(\ell\ell)\ell$ decay to fall within the fiducial volume is in the range 60–65% for most of the mass range, decreasing at higher masses due to the cut on the ΔR between the Z boson and the off- Z lepton. The acceptance decreases at low masses due to the lepton p_T requirement, reaching 30–35% at $m_{L^\pm} = 100 \text{ GeV}$.

For type III seesaw and VLL events within the fiducial volume, ϵ_{fid} ranges from 20% to 49% if the other heavy lepton decays to a neutrino and a W , Z , or H boson. If the other heavy lepton decays to an electron or a muon, the efficiency is 10–20% lower, due to the increased probability of incorrectly selecting the off- Z lepton. The event selection efficiencies for the type III seesaw model in scenarios where the second heavy lepton decays to a W boson are shown in figure 8.30 as a function of m_{L^\pm} ; the efficiencies for scenarios where the second heavy lepton decays to a Z or H boson and for the vector-like leptons model are consistent with these efficiencies within the statistical uncertainties.

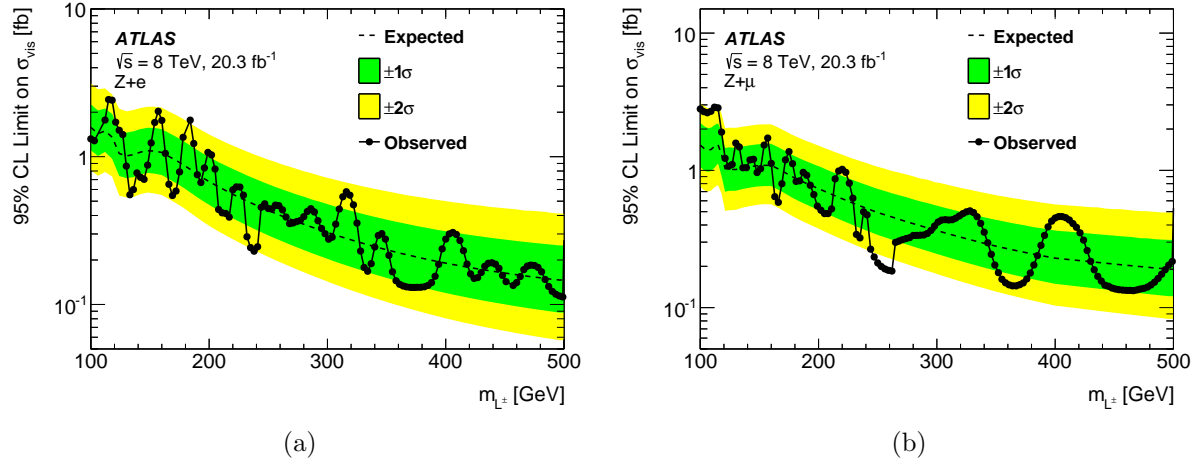


Figure 8.29: Upper limits at 95% CL on σ_{vis} for the $Z + e$ (left) and $Z + \mu$ (right) flavor channels, derived without dividing events into the three categories. The limits are evaluated in 3 GeV intervals.

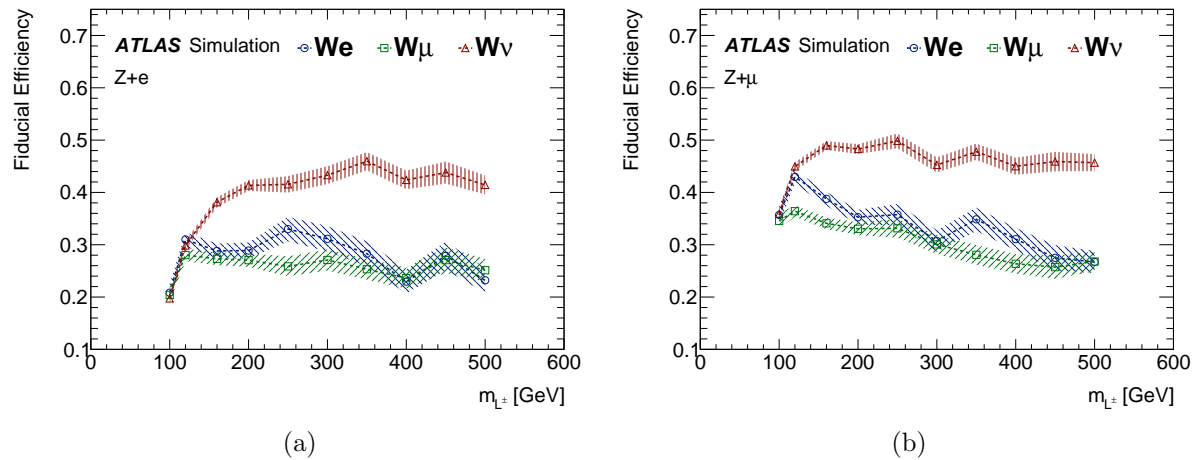


Figure 8.30: Efficiencies for reconstructing and correctly identifying the $L^\pm \rightarrow Z(\ell\ell)\ell^\pm$ decay in events within the fiducial volume for the type III seesaw model. The left (right) plot shows the efficiencies for events containing a $L^\pm \rightarrow Z(\ell\ell)e$ ($L^\pm \rightarrow Z(\ell\ell)\mu$) decay. The decay of the second heavy lepton is specified in the legend. The shaded bands show the statistical uncertainty.

Bibliography

- [1] J. E. Augustin et al., *Discovery of a Narrow Resonance in e^+e^- Annihilation*, Phys. Rev. Lett. **33** (1974) p. 1406.
- [2] J. J. Aubert et al., *Experimental Observation of a Heavy Particle J* , Phys. Rev. Lett. **33** (1974) p. 1404.
- [3] S. W. Herb et al., *Observation of a Dimuon Resonance at 9.5 GeV in 400-GeV Proton-Nucleus Collisions*, Phys. Rev. Lett. **39** (1977) p. 252.
- [4] UA1 Collaboration, G. Arnison et al., *Experimental observation of lepton pairs of invariant mass around 95 GeV/c^2 at the CERN SPS collider*, Physics Letters B **126** (1983) p. 398.
- [5] ATLAS Collaboration, *Observation of a new particle in the search for the Standard Model Higgs boson with the ATLAS detector at the LHC*, Physics Letters B **716.1** (2012) pp. 1–29.
- [6] The CMS Collaboration, *Observation of a new boson at a mass of 125 GeV with the CMS experiment at the LHC*, Physics Letters B **716.1** (2012) pp. 30–61.
- [7] ATLAS Collaboration, *Search for high-mass dilepton resonances in pp collisions at $\sqrt{s} = 8$ TeV with the ATLAS detector*, Physical Review D **90.5** (2014), arXiv: 1405.4123 [hep-ex].
- [8] The CMS Collaboration, *Search for physics beyond the standard model in dilepton mass spectra in proton-proton collisions at $\sqrt{s} = 8$ TeV*, JHEP **2015.4** (2015) pp. 25–49.
- [9] ATLAS Collaboration, *Search for anomalous production of prompt same-sign lepton pairs and pair-produced doubly charged Higgs bosons with $\sqrt{s} = 8$ TeV pp collisions using the ATLAS detector*, JHEP **2015.3**, 41 (2015).
- [10] ATLAS Collaboration, *Search for heavy lepton resonances decaying to a Z boson and a lepton in pp collisions at $\sqrt{s} = 8$ TeV with the ATLAS detector* (2015), arXiv: 1506.01291 [hep-ex].
- [11] U. Bellgardt et al., *Search for the Decay $\mu^+ \rightarrow e^+e^+e^-$* , Nucl.Phys. **B299** (1988) p. 1.

- [12] LHCb Collaboration, *Searches for violation of lepton flavour and baryon number in tau lepton decays at LHCb*, Phys.Lett. **B724** (2013) pp. 36–45, arXiv: 1304.4518 [hep-ex].
- [13] C. Biggio and F. Bonnet, *Implementation of the type III seesaw model in FeynRules/MadGraph and prospects for discovery with early LHC data*, The European Physical Journal C **72**.2 (2012), arXiv: 1107.3463 [hep-ph].
- [14] S. P. Martin, *Extra vector-like matter and the lightest Higgs scalar boson mass in low-energy supersymmetry*, Phys. Rev. D **81** (3 2010) p. 035004, arXiv: 0910.2732 [hep-ph].
- [15] P. H. Frampton, P. Q. Hung, and M. Sher, *Quarks and Leptons Beyond the Third Generation*, Physics Reports **330**.5-6 (2000), arXiv: hep-ph/9903387v2 [hep-ph].
- [16] A. Abada et al., $\mu \rightarrow e\gamma$ and $\tau \rightarrow \ell\gamma$ decays in the fermion triplet seesaw model, Phys. Rev. D **78** (3 2008) p. 033007, arXiv: 0803.0481 [hep-ph].
- [17] A. Abada et al., Low energy effects of neutrino masses, JHEP **2007**.12 (2007) p. 061, arXiv: 0707.4058v3 [hep-ph].
- [18] F. del Aguila, J. de Blas, and M. Pérez-Victoria, Effects of new leptons in Electroweak Precision Data, Phys. Rev. D **78** (1 2008) p. 013010, arXiv: 0803.4008 [hep-ph].
- [19] W. Altmannshofer, M. Bauer, and M. Carena, Exotic leptons: Higgs, flavor and collider phenomenology, JHEP **2014**.1 (2014) pp. 60–39, arXiv: 1308.1987 [hep-ph].
- [20] N. Arkani-Hamed et al., 2:1 for naturalness at the LHC?, English, JHEP **2013**.1, 149 (2013).
- [21] J. Alwall et al., The automated computation of tree-level and next-to-leading order differential cross sections, and their matching to parton shower simulations, JHEP **1407** (2014) p. 079, arXiv: 1405.0301 [hep-ph].
- [22] P. M. Nadolsky et al., Implications of CTEQ global analysis for collider observables, Phys. Rev. **D78** (2008) p. 013004, arXiv: 0802.0007 [hep-ph].
- [23] ATLAS Collaboration, ATLAS Run 1 Pythia8 tunes, ATL-PHYS-PUB-2014-021 (2014).
- [24] T. Sjöstrand, S. Mrenna, and P. Skands, A brief introduction to PYTHIA 8.1, Computer Physics Communications **178**.11 (2008) pp. 852–867, arXiv: 0710.3820 [hep-ph].
- [25] P. Meade and M. Reece, BRIDGE: Branching ratio inquiry / decay generated events (2007), arXiv: hep-ph/0703031 [hep-ph].
- [26] K. Olive et al., Review of Particle Physics, Chin.Phys. **C38** (2014) p. 090001.

- [27] T. Junk, *Sensitivity, Exclusion and Discovery with Small Signals, Large Backgrounds, and Large Systematic Uncertainties* (2007) pp. 1–31.
- [28] G. Cowan et al., *Asymptotic formulae for likelihood-based tests of new physics*, Eur. Phys. J. C **71**, 1554 (2011) p. 1554, arXiv: 1007.1727 [physics.data-an].
- [29] A. L. Read, *Presentation of search results: The $CL(s)$ technique*, J.Phys. **G28** (2002) pp. 2693–2704.

Chapter 9

Conclusion

This dissertation has presented two signature-driven searches for new physics using events with three or more charged leptons in pp collisions at $\sqrt{s} = 8 \text{ TeV}$. The dataset was collected by the ATLAS detector at the LHC, with an integrated luminosity of $L = 20.3 \text{ fb}^{-1}$. The first analysis, a model-independent search in final states with three leptons, looked for excesses above background predictions in many signal regions. The search was not optimized around specific models, but rather aimed to be broadly sensitive to nonresonant trilepton production from non-Standard Model sources. The second analysis searched for the resonant production of three electrons or muons via an intermediate Z boson, scanning the trilepton mass spectrum for narrowly peaked excesses. The analysis targeted the pair production of new heavy leptons, using the additional activity from the second heavy lepton to increase the sensitivity.

In both cases, no significant excesses above Standard Model background predictions were observed, and limits were established on a variety of models. The model-independent analysis set competitive limits on a model of doubly charged scalar particles in the case of lepton flavor-violating decays, excluding masses below $\sim 400 \text{ GeV}$ at 95% CL. The trilepton resonance search established limits on the pair production of heavy leptons in the context of a vector-like leptons model and a type III neutrino seesaw model. For the vector-like leptons model, most masses in the range $114 \text{ GeV} - 176 \text{ GeV}$ were excluded. For the type III seesaw model, with significantly higher production cross sections, most masses in the range $100 \text{ GeV} - 468 \text{ GeV}$ were excluded. In addition, both searches presented results in model-independent fashion along with fiducial efficiencies to aid reinterpretations of the results in the context of other models which produce trilepton final states.

Significant gains in sensitivity can be expected in the coming years. Following a three-year-long shutdown period, the LHC has resumed pp collisions with a center-of-mass collision energy of $\sqrt{s} = 13 \text{ TeV}$. The increase in collision energy from $\sqrt{s} = 8 \text{ TeV}$ to 13 TeV greatly enhances the sensitivity to new phenomena; for example, the pair production cross section of vector-like leptons with $m_{L^\pm} = 200 \text{ GeV}$ more than doubles. With targeted integrated luminosities of $75 \text{ fb}^{-1} - 100 \text{ fb}^{-1}$ by 2018 and $\sim 350 \text{ fb}^{-1}$ by 2022, the coming data will be sensitive to new phenomena well beyond the limits set in the first data-taking run.

Appendix A

Author Contributions

The LHC and the ATLAS experiment are projects of tremendous scale, and much of this dissertation covers the combined effort of thousands of contributors over the past twenty years. My own work is concentrated in chapters 4, 6, 7, and 8. I was initially involved in the luminosity measurement effort, with a focus on methods using vertices reconstructed using inner detector data. After using vertices at high z to constrain the presence of satellite bunches, protons in the beams outside the nominal RF buckets, I developed a luminosity measurement method using vertex counting (section 4.6). Much of this effort involved understanding the effect of pileup on the reconstruction efficiency. Vertex counting has proved useful for measuring the luminosity in low pileup scenarios, such as the van der Meer scans and the measurement of the total inelastic cross section with the ALFA detector.

The latter part of my dissertation work involved two searches for new phenomena using events with three or more charged leptons. The Standard Model backgrounds are sufficiently small that backgrounds from non-prompt sources, such as misidentified jets or semileptonic heavy flavor decays, can make significant contributions. I provided the data-driven estimate of the non-prompt electron backgrounds in the context of the model-independent trilepton search (section 6.2.3). Starting from the model-independent search's framework, I then helped to develop the trilepton resonance search. I contributed to most aspects of the analysis, including the event selection, the signal and control region definitions, the non-prompt background estimation, the systematic uncertainties, and the parametrization of the background using the analytical fit functions.

Appendix B

Trilepton Resonance Search

B.0.2 Signal Fit Details

Tables B.1-B.4 show the results of fitting the Voigtian plus Landau function to each signal point for the type III seesaw and vector-like leptons models. The fits are performed in the inclusive category in $Z + e$ and $Z + \mu$ flavor channels.

Mass [GeV]	m_V [GeV]	γ_V [GeV]	σ_V [GeV]	m_L [GeV]	σ_L [GeV]	Ratio
100	8.7222 ± 0.015	0.131 ± 0.04	0.32 ± 0.03	36.1 ± 0.7	10.9 ± 0.355118	0.34
120	28.5035 ± 0.024	0.594 ± 0.12	0.72 ± 0.06	34.1 ± 0.8	10.2 ± 0.391391	0.59
160	68.3224 ± 0.037	1.34 ± 0.15	1.13 ± 0.08	45.9 ± 0.7	15.3 ± 0.392333	0.57
200	108.294 ± 0.052	1.86 ± 0.20	1.59 ± 0.10	59.1 ± 1.1	21.3 ± 0.568737	0.58
250	158.039 ± 0.090	3.08 ± 0.37	1.48 ± 0.26	75.6 ± 2.1	27.6 ± 1.10452	0.59
300	207.856 ± 0.129	2.96 ± 0.45	2.75 ± 0.23	92.3 ± 2.6	35.7 ± 1.39974	0.55
350	257.775 ± 0.169	4.52 ± 0.63	3.21 ± 0.33	106.8 ± 3.4	41.6 ± 1.85383	0.57
400	308.066 ± 0.198	6.84 ± 0.77	2.77 ± 0.48	129.7 ± 4.2	51.3 ± 2.34715	0.55
450	357.463 ± 0.277	7.37 ± 1.05	3.91 ± 0.61	142.1 ± 5.3	58.3 ± 3.06396	0.54
500	407.731 ± 0.262	5.39 ± 1.02	5.26 ± 0.53	179.9 ± 6.1	71.5 ± 3.65063	0.52

Table B.1: Fit parameters for the type III seesaw model in the $Z + e$ flavor channel and inclusive category. m_V , γ_V , and σ_V represent the mean, Lorentzian width, and Gaussian width of the Voigt function, and m_L and σ_L represent the mean and width of the Landau function. Note that the absence of the intrinsic width of the Z boson in the simulation leads to smaller values than expected for the width of the Voigtian peak for masses below ~ 250 GeV.

B.0.3 Additional Kinematic Distributions

This section shows the $m_{3\ell}$, $\Delta R(Z, \ell_3)$, m_T^W , and E_T^{miss} distributions in each of the signal regions (the primary distributions are shown in section 8.6).

Mass [GeV]	m_V [GeV]	γ_V [GeV]	σ_V [GeV]	m_L [GeV]	σ_L [GeV]	Ratio
100	8.78 ± 0.01	0.1 ± 0.0	0.176 ± 0.01	35.6 ± 0.5	10.6 ± 0.3	0.45
120	28.71 ± 0.01	0.28 ± 0.057	0.62 ± 0.02	31.2 ± 0.5	8.7 ± 0.2	0.60
160	68.56 ± 0.03	1.86 ± 0.14	1.18 ± 0.08	44.7 ± 0.6	15.3 ± 0.3	0.60
200	108.3 ± 0.05	3.10 ± 0.25	1.99 ± 0.13	56.6 ± 0.9	19.4 ± 0.5	0.61
250	158.1 ± 0.1	4.36 ± 0.61	3.64 ± 0.31	73.6 ± 1.9	27.0 ± 1.0	0.61
300	207.7 ± 0.1	8.17 ± 0.84	3.87 ± 0.46	86.2 ± 2.4	32.3 ± 1.3	0.61
350	258.3 ± 0.2	10.04 ± 1.44	6.15 ± 0.75	103.1 ± 3.2	40.2 ± 1.7	0.59
400	307.2 ± 0.3	13.09 ± 1.69	6.39 ± 0.98	120.9 ± 4.2	50.2 ± 2.3	0.58
450	357.4 ± 0.5	18.08 ± 3.05	8.86 ± 1.64	137.7 ± 5.9	57.9 ± 3.4	0.56
500	407.6 ± 0.5	14.20 ± 3.10	12.2 ± 1.44	166.7 ± 6.1	67.9 ± 3.6	0.53

Table B.2: Fit parameters for the type III seesaw model in the $Z + \mu$ flavor channel and inclusive category. m_V , γ_V , and σ_V represent the mean, Lorentzian width, and Gaussian width of the Voigt function, and m_L and σ_L represent the mean and width of the Landau function. Note that the absence of the intrinsic width of the Z boson in the simulation leads to smaller values than expected for the width of the Voigtian peak for masses below ~ 250 GeV.

Mass [GeV]	m_V [GeV]	γ_V [GeV]	σ_V [GeV]	m_L [GeV]	σ_L [GeV]	Ratio
100	10.77 ± 0.18	0.1 ± 0.1	2.5 ± 0.2	34.3 ± 1.5	12.12 ± 0.47	0.37
110	18.54 ± 0.04	1.9 ± 0.2	1.0 ± 0.1	34.1 ± 1.8	10.08 ± 0.51	0.69
120	28.25 ± 0.04	2.7 ± 0.4	0.7 ± 0.2	35.8 ± 3.0	10.95 ± 1.02	0.75
130	38.18 ± 0.04	2.2 ± 0.2	1.2 ± 0.1	31.0 ± 0.6	9.40 ± 0.32	0.71
140	48.07 ± 0.04	2.2 ± 0.2	1.5 ± 0.1	33.4 ± 0.6	10.29 ± 0.28	0.69
160	68.00 ± 0.04	3.0 ± 0.2	1.4 ± 0.1	37.0 ± 0.7	11.52 ± 0.32	0.70
180	87.97 ± 0.05	3.2 ± 0.2	1.6 ± 0.1	43.8 ± 0.7	14.05 ± 0.35	0.67
200	107.89 ± 0.05	3.0 ± 0.2	2.0 ± 0.1	49.7 ± 0.8	16.38 ± 0.39	0.65
250	157.75 ± 0.06	3.2 ± 0.2	2.6 ± 0.2	66.2 ± 0.9	22.76 ± 0.47	0.59
300	207.57 ± 0.07	3.4 ± 0.3	3.3 ± 0.2	83.9 ± 1.1	29.64 ± 0.58	0.57
400	307.53 ± 0.09	4.2 ± 0.3	4.4 ± 0.2	118.9 ± 1.7	46.42 ± 0.93	0.53

Table B.3: Fit parameters for the VLL model in the $Z + e$ flavor channel and inclusive category. m_V , γ_V , and σ_V represent the mean, Lorentzian width, and Gaussian width of the Voigt function, and m_L and σ_L represent the mean and width of the Landau function.

Mass [GeV]	m_V [GeV]	γ_V [GeV]	σ_V [GeV]	m_L [GeV]	σ_L [GeV]	Ratio
100	10.9 ± 0.13	0.1 ± 0.05	2.85 ± 0.10	35.63 ± 1.21	11.98 ± 0.40	0.44
110	18.7 ± 0.03	2.13 ± 0.16	0.73 ± 0.11	32.88 ± 1.55	9.47 ± 0.46	0.74
120	28.5 ± 0.03	2.26 ± 0.19	0.78 ± 0.11	30.72 ± 1.17	9.44 ± 0.59	0.75
130	38.4 ± 0.03	2.23 ± 0.16	1.07 ± 0.09	29.40 ± 0.48	8.83 ± 0.26	0.73
140	48.5 ± 0.03	2.38 ± 0.16	1.26 ± 0.09	30.57 ± 0.50	9.31 ± 0.25	0.73
160	68.5 ± 0.05	2.71 ± 0.19	1.74 ± 0.10	33.97 ± 0.55	10.45 ± 0.27	0.71
180	88.3 ± 0.05	2.73 ± 0.21	2.19 ± 0.11	40.06 ± 0.62	12.76 ± 0.30	0.68
200	108.4 ± 0.1	3.34 ± 0.26	2.81 ± 0.14	45.44 ± 0.65	14.28 ± 0.32	0.66
250	158.2 ± 0.1	4.45 ± 0.34	3.89 ± 0.17	61.10 ± 0.85	20.71 ± 0.42	0.62
300	208.0 ± 0.1	6.21 ± 0.48	5.26 ± 0.25	76.50 ± 1.01	26.62 ± 0.51	0.58
400	307.9 ± 0.2	9.12 ± 0.84	8.63 ± 0.40	114.84 ± 1.60	42.99 ± 0.85	0.53

Table B.4: Fit parameters for the VLL model in the $Z + \mu$ flavor channel and inclusive category. m_V , γ_V , and σ_V represent the mean, Lorentzian width, and Gaussian width of the Voigt function, and m_L and σ_L represent the mean and width of the Landau function.

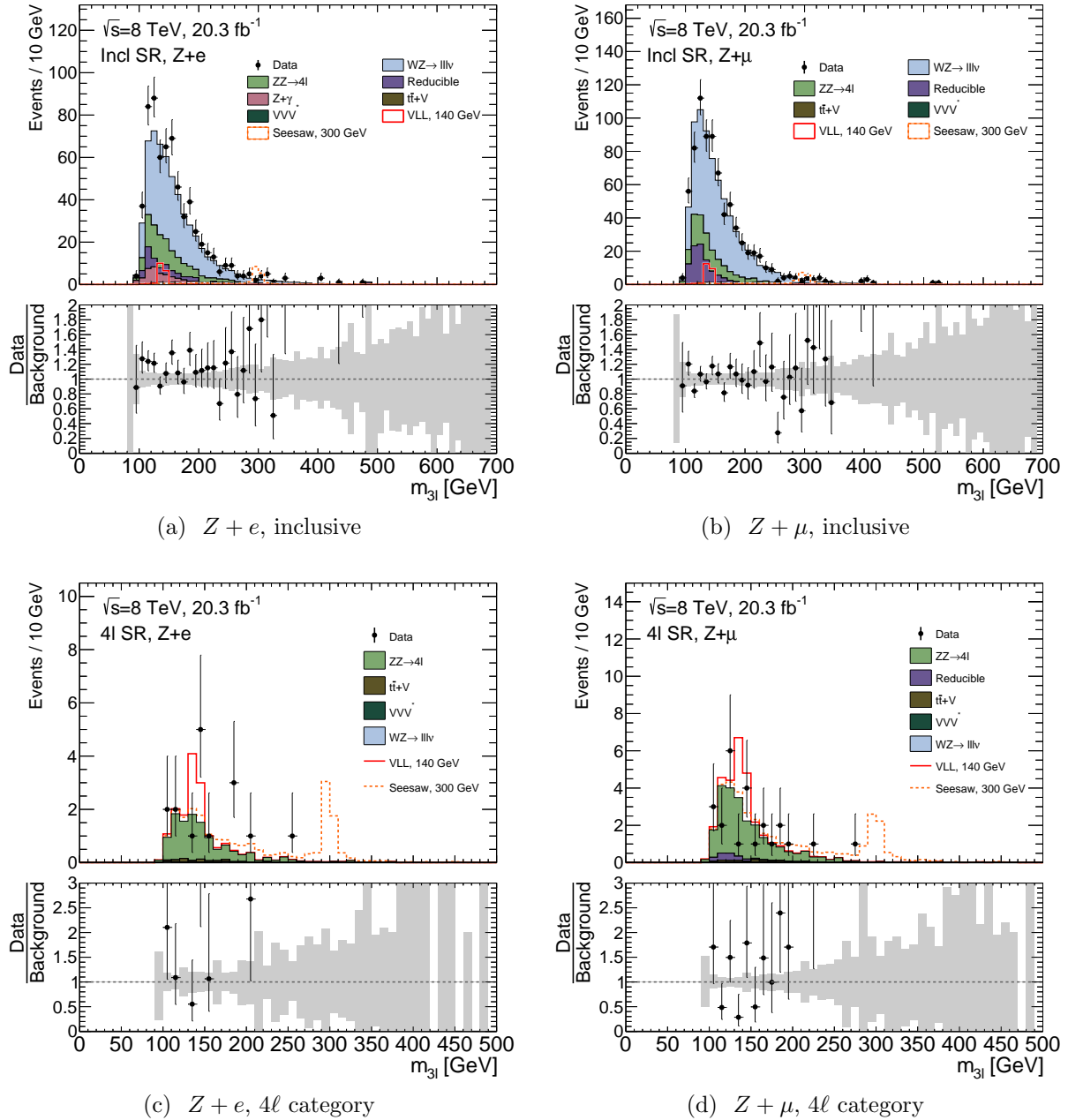


Figure B.1: $m_{3\ell}$ distributions for $Z + e$ and $Z + \mu$ candidates, for the inclusive and 4ℓ signal regions (linear scale).

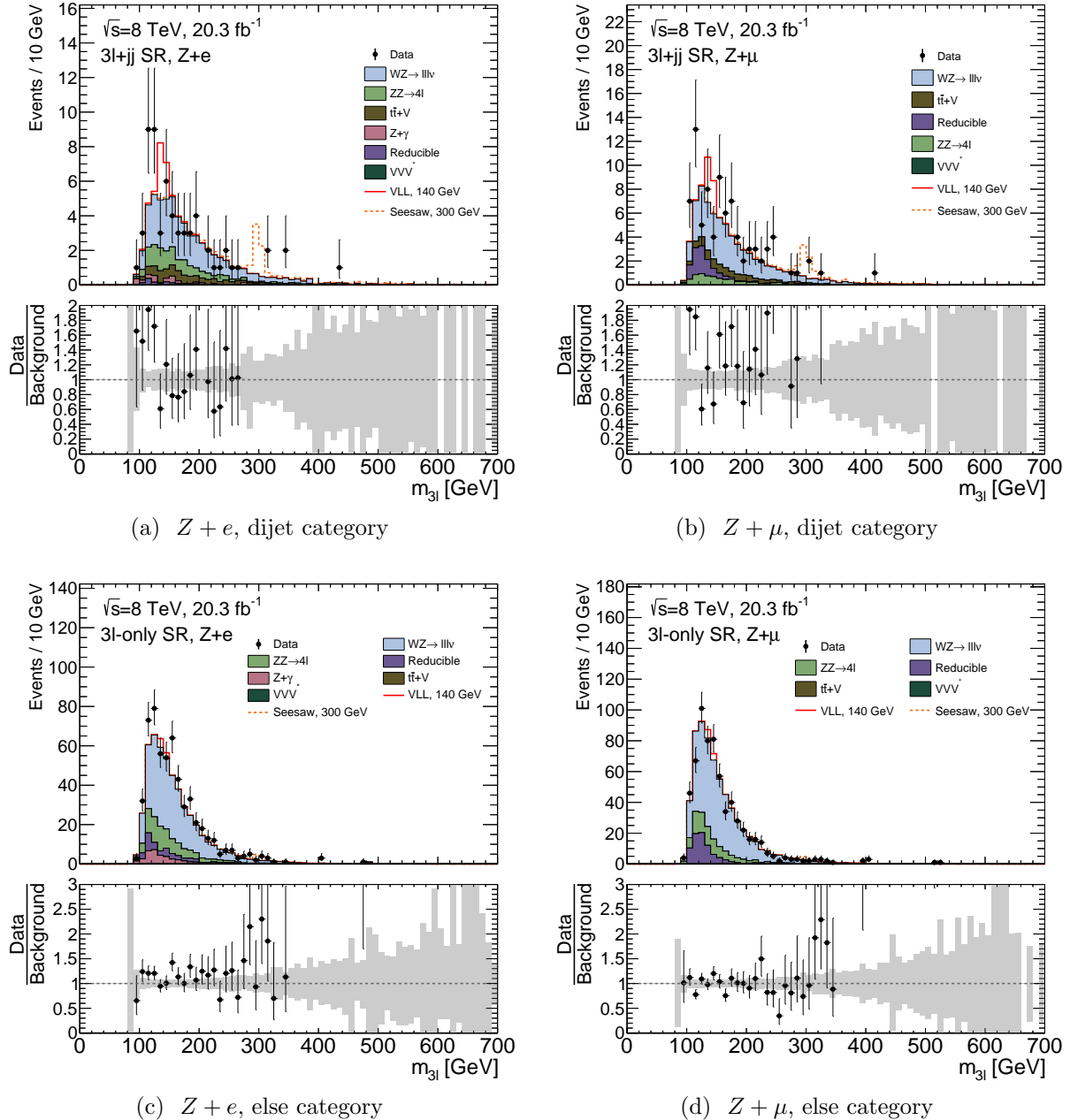


Figure B.2: $m_{3\ell}$ distributions for $Z + e$ and $Z + \mu$ candidates, for the $3\ell + jj$ and 3ℓ -only signal regions (linear scale).

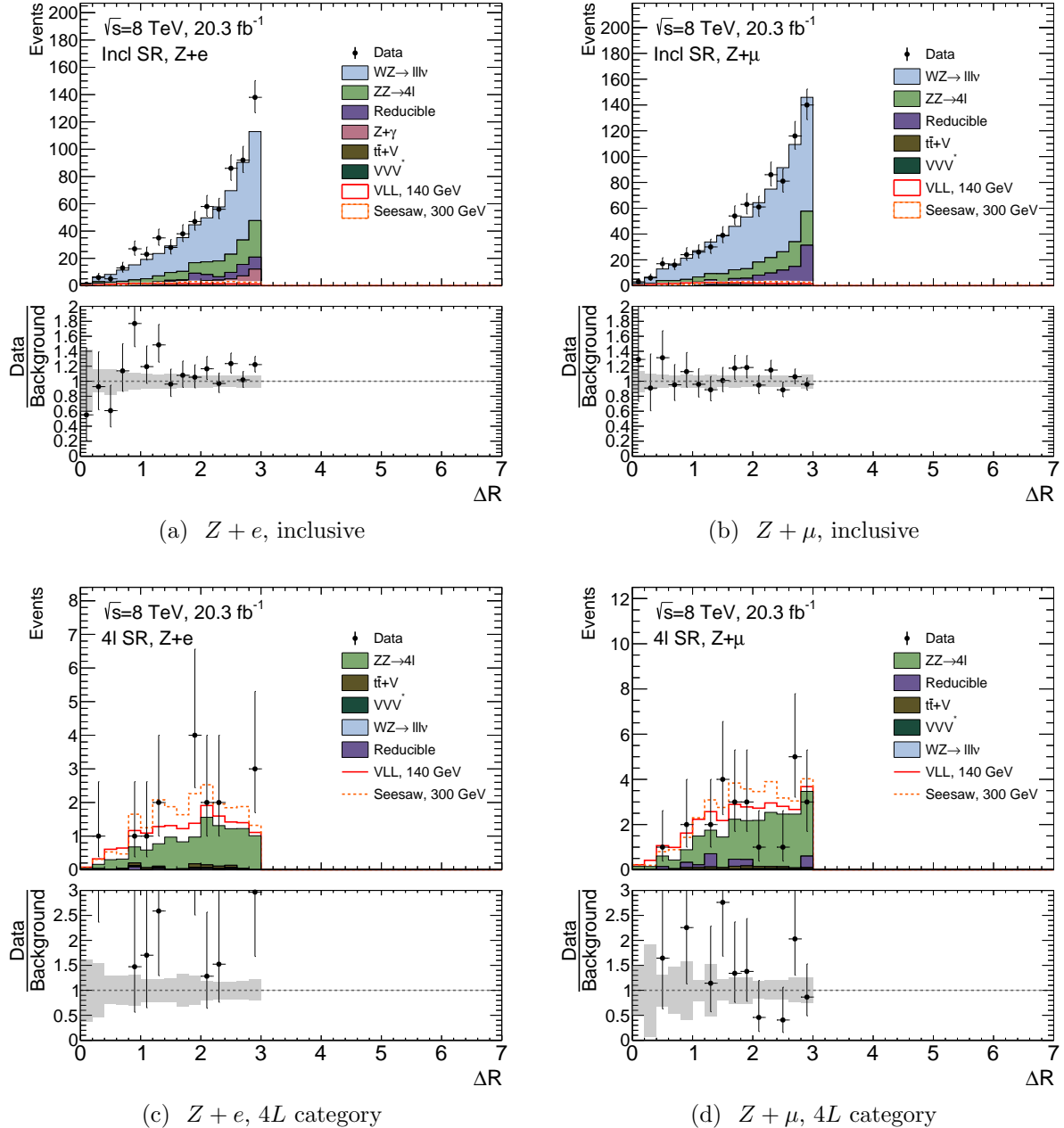


Figure B.3: $\Delta R(Z, \ell_3)$ distributions for $Z + e$ and $Z + \mu$ candidates, for the inclusive and 4ℓ signal regions (linear scale).

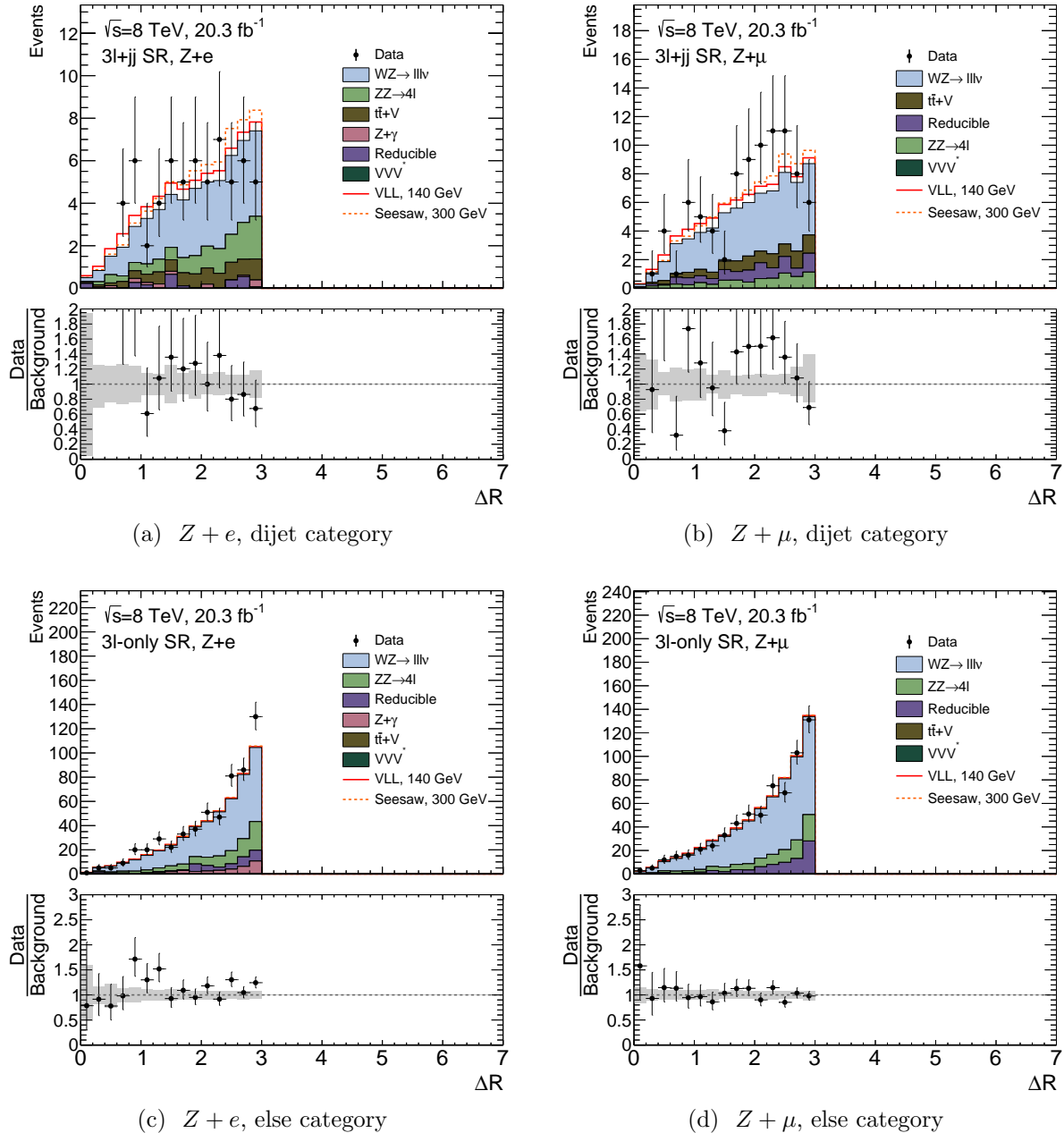


Figure B.4: $\Delta R(Z, \ell_3)$ distributions for $Z + e$ and $Z + \mu$ candidates, for the $3\ell + jj$ and 3ℓ -only signal regions (linear scale).

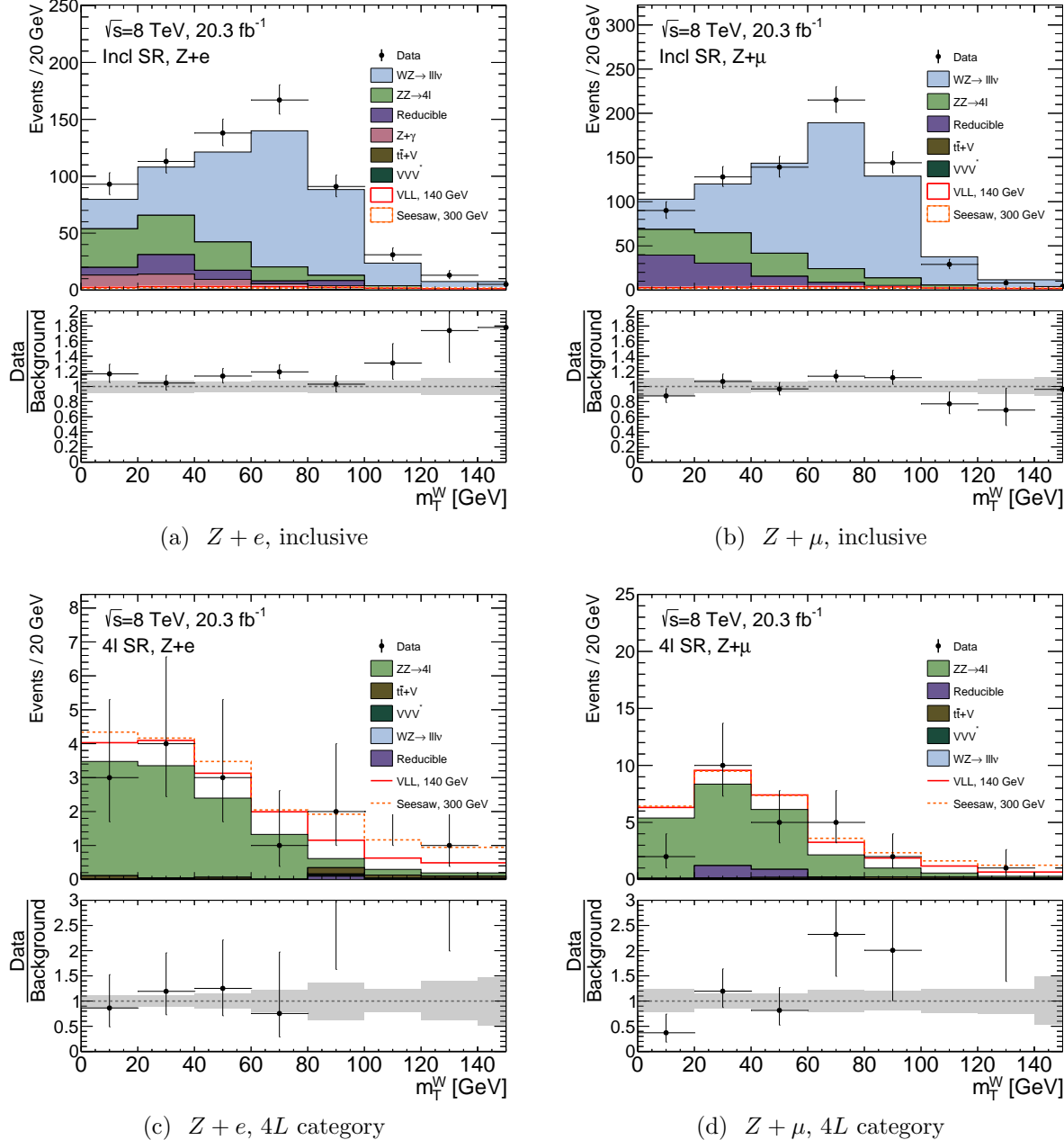


Figure B.5: Transverse mass of the missing energy and bachelor lepton (m_T^W) for $Z + e$ and $Z + \mu$ candidates, for the inclusive and 4ℓ signal regions.

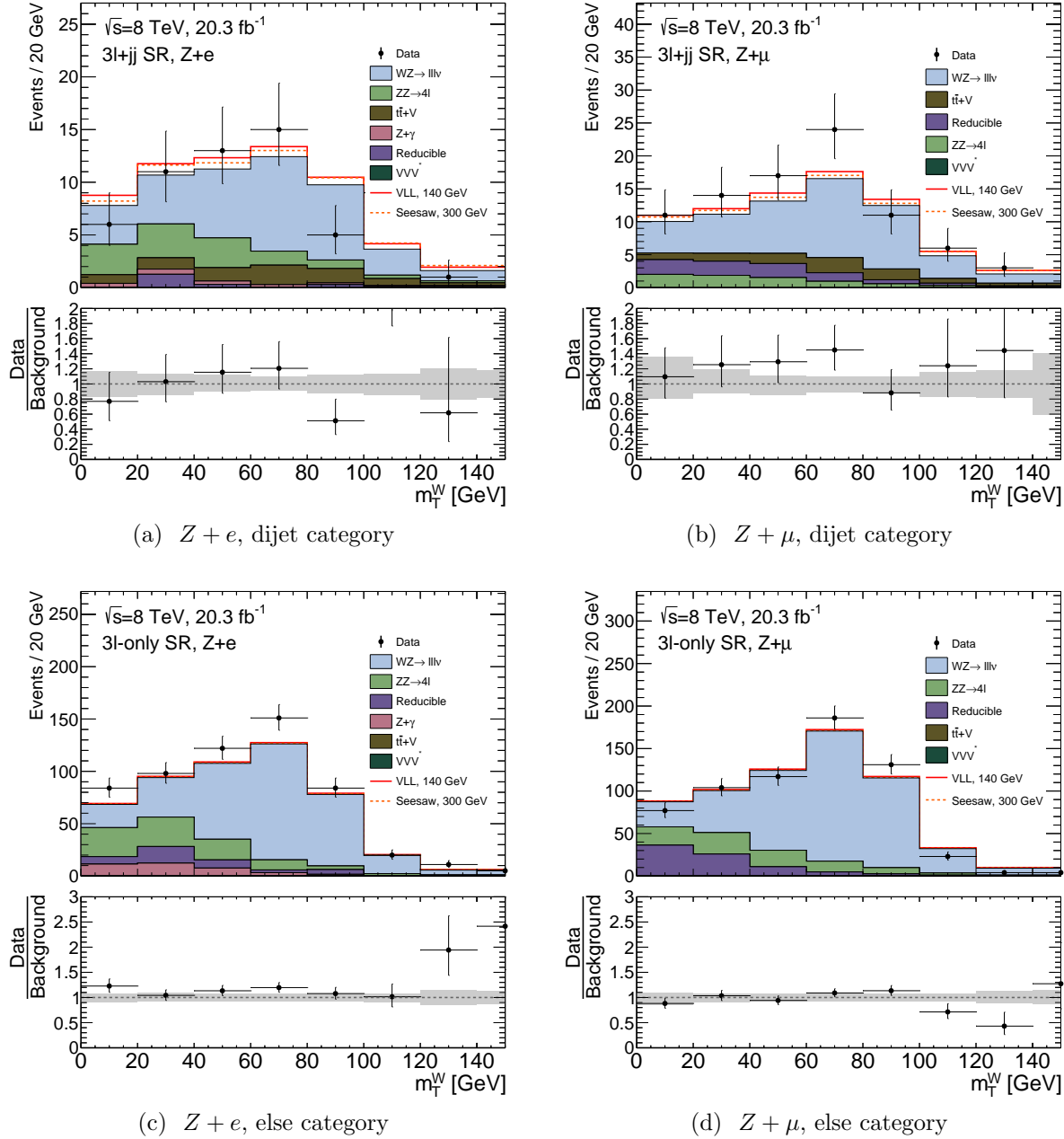


Figure B.6: Transverse mass of the missing energy and bachelor lepton (m_T^W) for $Z + e$ and $Z + \mu$ candidates, for the $3\ell + jj$ and 3ℓ -only signal regions.

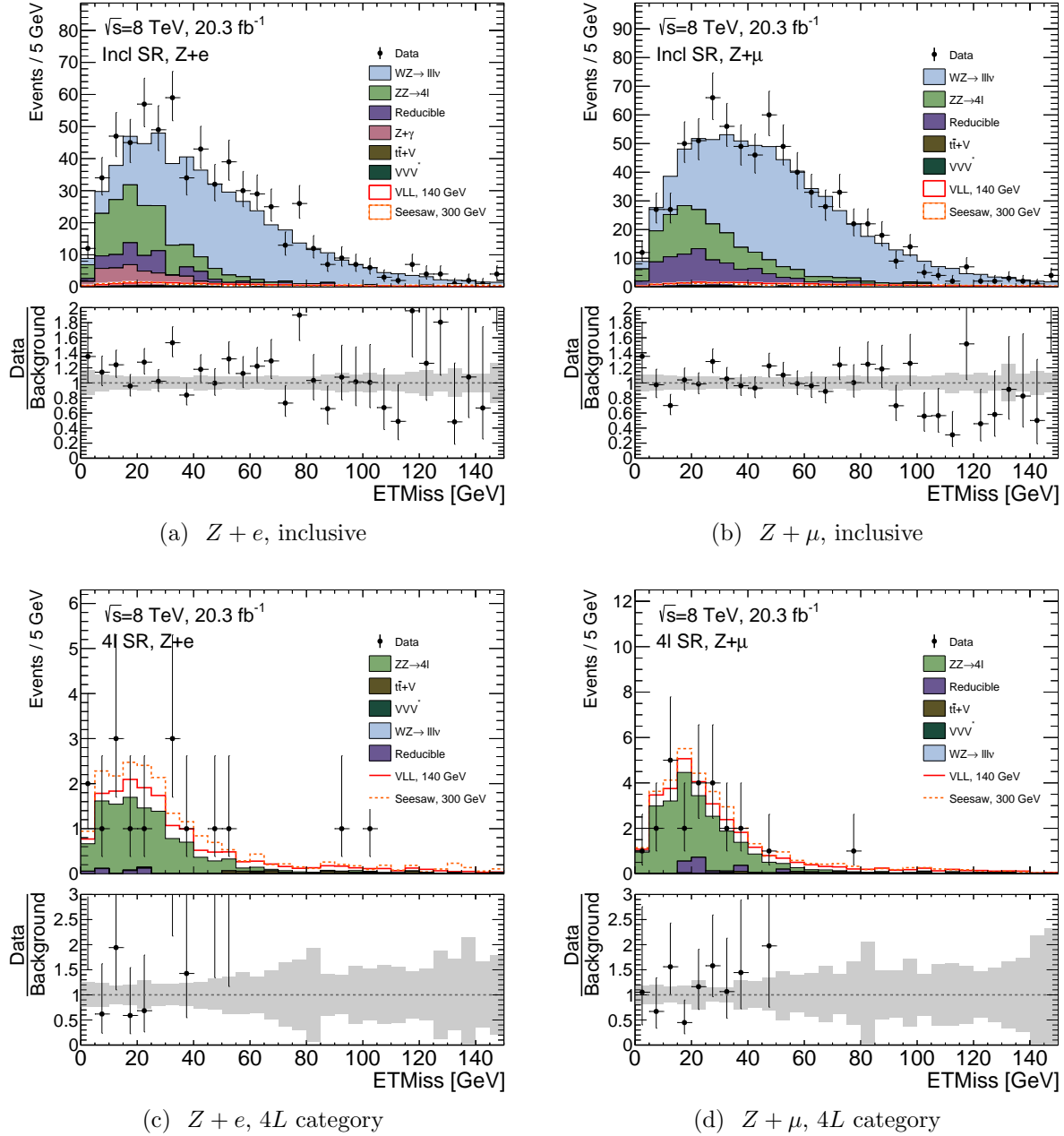


Figure B.7: Missing energy (E_T^{miss}) for $Z + e$ and $Z + \mu$ candidates, for the inclusive and 4ℓ signal regions.

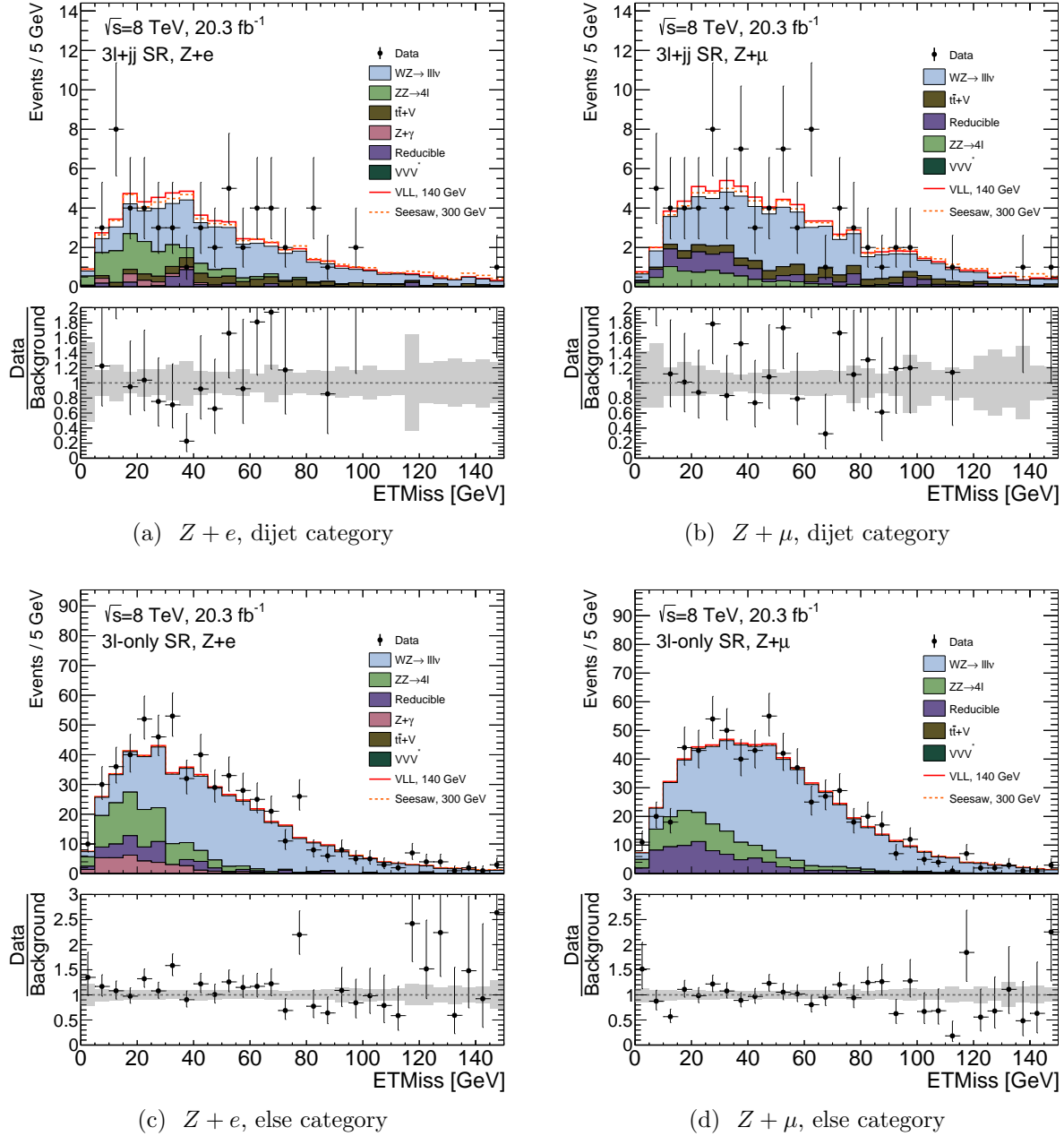


Figure B.8: Missing energy (E_T^{miss}) for $Z + e$ and $Z + \mu$ candidates, for the $3\ell + jj$ and 3ℓ -only signal regions.

Appendix C

Statistical Methods

The analyses presented in chapters 7 and 8 both employ a modified frequentist approach to the statistical limit setting known as the CL_s method [1]. The goal of the method is to compare the data against the signal plus background hypothesis versus the background-only hypothesis. In the case of searches, the signal plus background hypothesis is assumed to predict an excess of events above the background-only hypothesis.

The first step is to define a *test statistic*, \tilde{q}_μ , which distinguishes a background-like data sample from a signal plus background-like sample. Here μ is a parameter representing the signal strength; $\mu = 1$ corresponds to the signal hypothesis ($S + B$), while $\mu = 0$ corresponds to background only (B). The test statistic is based on the profile likelihood method. In the case of binned data, i.e. a histogram with N bins, the likelihood is given by,

$$\mathcal{L} = \left(\prod_{i=1}^N \frac{\mu s_i + b_i}{n_i!} e^{-(\mu s_i + b_i)} \right) \times \rho(\tilde{\theta}|\theta), \quad (\text{C.1})$$

where s_i and b_i are the expected number of signal and background events in bin i and n_i is the number of observed events in bin i . The systematic uncertainties are parametrized by a set of nuisance parameters, θ , with nominal values $\tilde{\theta}$; the $\rho(\tilde{\theta}|\theta)$ are frequentist auxiliary measurement probability distribution functions (pdfs) of the nuisance parameters, which are taken to be Gaussian for most sources of uncertainty considered here. This likelihood is used for the model-independent trilepton search, where the data is binned into the various signal regions.

In the case of unbinned data, $\{x_i\}_{i \in [1,k]}$, the likelihood is given by,

$$\mathcal{L} = \frac{1}{k} \left(\prod_{i=1}^k (\mu S f_s(x_i) + B f_b(x_i)) \times e^{-(\mu S + B)} \right) \times \rho(\tilde{\theta}|\theta), \quad (\text{C.2})$$

where S and B are the total expected number of signal and background events, and $f_s(x_i)$ and $f_b(x_i)$ are the signal and background pdfs for the data x_i . This formalism applied to the trilepton resonance search, where the signal and background are parametrized by analytical functions.

The test statistic is taken to be the negative log likelihood ratio,

$$\tilde{q}_\mu = -2 \log \left(\frac{\mathcal{L}(\text{data}|\mu, \hat{\theta}_\mu)}{\mathcal{L}(\text{data}|\hat{\mu}, \hat{\theta})} \right). \quad (\text{C.3})$$

Greater values correspond to more background-like observations, and lesser values correspond to more signal-like observations. Here, $\hat{\theta}_\mu$ is a conditional maximum likelihood estimator (MLE) of the nuisance parameters θ given the data for fixed μ , and $\hat{\mu}$ and $\hat{\theta}$ are global MLEs of the signal strength and nuisance parameters. The value of $\hat{\mu}$ is restricted to be in the range $[0, \mu]$; the lower bound enforces the expectation that the signal produces an excess, while the upper bound guarantees a one-sided confidence interval, ensuring that an upwards fluctuation beyond μ would not count against the signal plus background hypothesis.

To find the observed limit on μ , pdfs are derived for \tilde{q}_μ under the $S+B$ and B hypotheses ($f(\tilde{q}_\mu|\mu, \hat{\theta}_\mu^{\text{obs}})$ and $f(\tilde{q}_\mu|0, \hat{\theta}_0^{\text{obs}})$) using toy Monte Carlo pseudoexperiments. The nuisance parameters are fixed to the maximum likelihood estimates, $\hat{\theta}_\mu^{\text{obs}}$ and $\hat{\theta}_0^{\text{obs}}$ for the $S+B$ and B hypotheses, respectively. Example pdfs are shown in figure C.1.

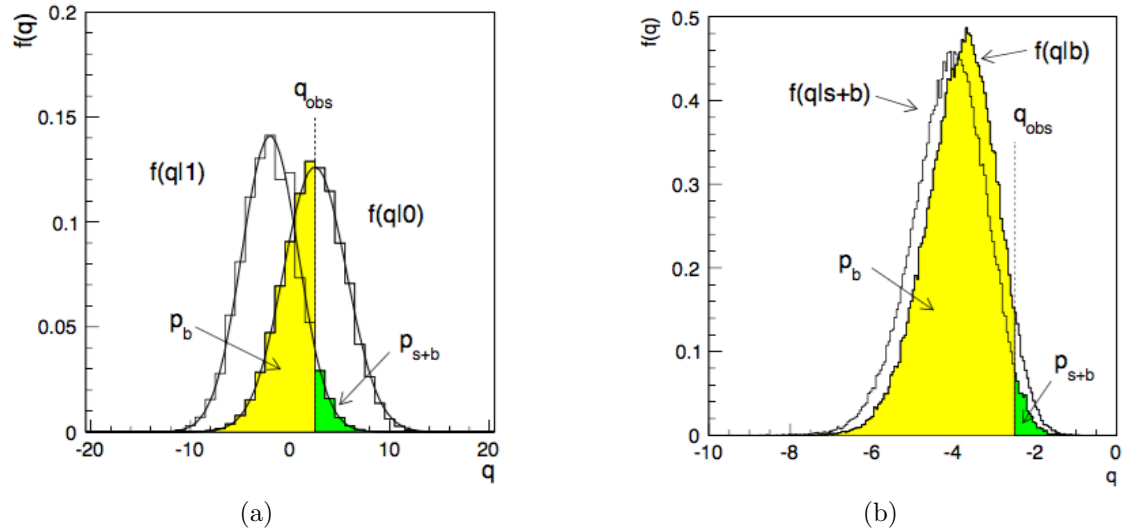


Figure C.1: Two example of pdfs for \tilde{q}_μ for the $S+B$ and B hypotheses [2]. The left plot shows pdfs where the two hypotheses are well separated, while the right plot shows a case where the experiment has little sensitivity to the signal.

Given an observed test statistic $\tilde{q}_\mu^{\text{obs}}$, the pdfs are used to derive p -values for the $S+B$ and B hypotheses:

$$p_0 = P(\tilde{q}_\mu \leq \tilde{q}_\mu^{\text{obs}} | B) = \int_{\tilde{q}_\mu^{\text{obs}}}^{\infty} f(\tilde{q}_\mu | 0) d\tilde{q}_\mu \quad (\text{C.4})$$

$$p_\mu = P(\tilde{q}_\mu \geq \tilde{q}_\mu^{\text{obs}} | S + B) = \int_{\tilde{q}_\mu^{\text{obs}}}^{\infty} f(\tilde{q}_\mu | \mu) d\tilde{q}_\mu. \quad (\text{C.5})$$

$$(\text{C.6})$$

The p_0 value gives the probability of obtaining a test statistic equal to or more signal-like than observed, assuming the background-only hypothesis. Similarly, the p_μ value gives the probability of obtaining a test statistic equal to or more background-like than observed, assuming the signal plus background hypothesis.

Finally, the CL_s method defines the criterion used to exclude a model [1]. The CL_s value is constructed to avoid the problem of excluding models to which the experiment has little sensitivity, like that shown in figure C.1b; for example, a large downward fluctuation can result in the $p_\mu \equiv \text{CL}_{s+b}$ value excluding $\mu = 0$, even if the experiment has no sensitivity to the signal. A model with signal strength μ is considered excluded at confidence level $1 - \alpha$ if:

$$\text{CL}_s \equiv \frac{p_\mu}{1 - p_0} < \alpha. \quad (\text{C.7})$$

Note that the CL_s value is not itself a p -value, but satisfies $\text{CL}_s > p_\mu \equiv \text{CL}_{s+b}$, and hence is more conservative than CL_{s+b} . The 95% confidence level observed exclusion is determined by solving for the μ value which yields $\text{CL}_s = 0.05$.

Bibliography

- [1] A. L. Read, *Presentation of search results: The $CL(s)$ technique*, J.Phys. **G28** (2002) pp. 2693–2704.
- [2] ATLAS Statistics Forum, *The CL_s method: information for conference speakers* (2011).